Modeling Ocean Dynamics and Vegetation-Climate Interactions Under Evolving CO_2 During the Late Paleozoic Ice Age

by

Sophia I. Macarewich

A dissertation submitted in partial fulfillment
of the requirements for the degree of
Doctor of Philosophy
(Earth and Environmental Sciences)
in the University of Michigan
2021

Doctoral Committee:

Professor Christopher J. Poulsen, Chair
Professor Xianglei Huang
Professor Isabel P. Montañez, University of California, Davis
Associate Professor Benjamin H. Passey
Assistant Professor Selena Y. Smith

Sophia I. Macarewich

sophmaca@umich.edu

ORCID iD: 0000-0002-6263-3044

Dedication

To Michael, my partner and *everything*, who's love, encouragement, and humor helps me grow. And to my parents, Mike and Laura, who every day inspire me to work hard and keep learning. None of this would have been possible without your support.

Acknowledgements

This dissertation is the product of the scientific expertise and emotional encouragement from a number of incredibly thoughtful, supportive individuals. It took an immense amount of work and I have all of them to thank for their contributions to my dissertation. First, to my advisor Chris Poulsen. Thank you for giving me the freedom and support to explore the scientific topics that I am interested in. You have always treated me as a peer, and I really appreciate that. Your mentorship throughout graduate school has given me the space to grow into the independent researcher I am today. Thank you to Isabel Montañez, my collaborator and dissertation committee member, for continuously inviting me into your research and actively fostering my professional growth over the years. Thank you to my other committee members: Xianglei Huang, Ben Passey, and Selena Smith. Your diverse expertise and thoughtful feedback on my dissertation have broadened my perspective of research. To my co-authors: Chris Poulsen, Isabel Montañez, Will Matthaeus, Jon Richey, Joseph White, Bill DiMichele, Michael Hren, Jenny McElwain, and Jon Wilson. Your constructive feedback and exciting scientific ideas have expanded the impact of my research as an early career scientist. Developing ongoing collaborations with all of you has been one of the most rewarding parts of my experience in academia. I would also like to acknowledge my funding sources, the Rackham Merit Fellowship and National Science Foundation award 1338200, as well as high-performance computing support from Cheyenne (doi:10.5065/D6RX99HX) provided by the National Center for Atmospheric Research's Computational and Information Systems Laboratory, also sponsored by the National Science Foundation.

I feel very fortunate to have been a part of the Earth and Environmental Sciences Department at the University of Michigan and have many people to thank for supporting me in graduate school. To my lab mates from the beginning through the end, Alex and Phoebe, thank you for your friendship and honest feedback on my work throughout the years. Our silly banter in the lab (and even Zoom) has meant more to me than you know ('conodont' forget me!). To some Poulsen lab alumni: Clay, Jiang, J.B., and Ran, thank you for patiently answering a

seemingly endless stream of emails from me about CESM errors. To the rest of the Poulsen Lab Group, recent past and present: Jeremy, Daeun, Emily, Paul, Julia, Dora, Andrew, Chris, Rich, and Chana, I appreciate our comradery very much. To my graduate cohort and incoming Earth class of 2016: Sha, Alessio, Becca, Aaron, Alex, Juli, Billy, Nik, Kierstin, James, Bekah, Kirk, and Bian, thank you for the fabulous memories from the past five years. I am very fortunate to have learned from and taught with a brilliant group of educators over two summers at Camp Davis. To my co-GSIs, Alex and Bekah, thank you for creating a supportive and fun environment to teach in. I also want to thank Anne Hudon who has always been there to help me navigate the important logistics of graduate school.

Several people at the University of Michigan served a particularly important role in my mental wellness over the years. To my therapist from Counseling and Psychological Services, Danielle, thank you for helping me embrace my authentic self. One piece of your wisdom about perfectionism that has helped me so much: *It's okay to set high standards, it's how you treat yourself for being imperfect that matters*. To Rick Harris, thank you for introducing me to meditation and mindfulness. These practices have helped me immensely in managing stress and uncertainty in life. To the members of the Meditation and Mindfulness CommuniTEA, Juli, Derek, Jenan, and Maria, thank you for creating a space to have honest and nonjudgmental discussions about mental health and imposter feelings.

Lastly, I want to thank my support network of family and friends who have encouraged me throughout the years. To Randy Hudson, my Marine Ecology teacher at Dana Hills High School, thank you for showing me that 'the more you know, the more you see' (Aldous Huxley). Your passion for teaching inspired me to pursue a career in science. To Leila Carvalho, my undergraduate research mentor at UC Santa Barbara, thank you for cultivating a sense of belonging in research and encouraging me to pursue graduate school before I believed I could do it. To my mom and dad, thank you for enthusiastic support and engagement with my research. To my brother Stefan, thank you for setting an example of paving your own career path. It inspires me to do the same. To my little tuxedo cats, Nai Palm and Hannibal, thank you for grounding me in the present moment. And to my partner and best friend, Michael, your love and support has meant more to me than I could ever express in words. Your strength, resilience, and compassion inspire me every day. I'm so grateful to have finished graduate school as a team.

Table of Contents

List of Tables

List of Figures

Abstract

Icehouses, such as the current glacial state and Late Paleozoic Ice Age (LPIA; ~340 to 290 million years ago), make up less than 25% of the past billion years of Earth's history and are associated with major environmental change. Thus, exploring climate dynamics during the LPIA expands our view of the climate system and improves our confidence in future climate projections. Despite major advancement in our understanding of CO_2-induced changes in supercontinental glaciation during the LPIA, far less is known about how the superocean and biosphere factored into the climate system. This dissertation presents new understanding of regional and global ocean dynamics and tropical vegetation-climate feedbacks under evolving atmospheric pCO_2 during the LPIA by simulating these processes in an Earth system model framework. The chapters in this dissertation integrate novel Earth system model simulations with environmental proxy data to better understand how climate dynamics drove marine and terrestrial change during the LPIA.

Chapters 2 and 3 investigate glacial-interglacial changes in ocean circulation and temperature from the global to regional scale to better constrain the nature and role of the superocean in the LPIA. Chapter 2 explores the effects of changing CO_2, sea level, and high-latitude ice extent on global ocean circulation, salinity, and temperature patterns. Results from this chapter represent the first global estimates of surface currents and thermohaline circulation for the LPIA and connect insights from coastal proxy records to large-scale ocean dynamics. Chapter 3 refines the spatial scale of interest by investigating the patterns of seawater oxygen isotopic composition, temperature, and circulation in the North American Midcontinent Sea. Results from this chapter demonstrate that local variations in runoff contribute to much of the high spatial variability observed in oxygen isotopic records from the sea. This chapter demonstrates how isotope-enabled Earth system models can be used to constrain local processes in semi-restricted ancient inland seas, and thus improve proxy-based interpretations of seawater temperature and chemistry related to large-scale paleoceanographic events.

Chapter 4 shifts from the marine to terrestrial realm and explores vegetation-climate interactions across low-latitude Pangaea to better understand the role of paleo-plant physiology in paleotropical climate change. This chapter presents the first methodology for translating Pennsylvanian fossil leaf characteristics and insights from process-based ecosystem modeling into extinct plant types in an Earth system model. Using novel paleo-plant types that represent key Pennsylvanian tropical plants and their modern plant analogs, this chapter explores tropical vegetation-climate feedbacks under different levels of CO_2 as well as wetland and dryland tropical forests. Results from this chapter show that paleo-plants transpire more water overall and respond differently to elevated CO_2 compared to modern plants, leading to regional variations in low-latitude precipitation and soil water that better capture the tropical moisture gradient inferred from terrestrial proxy records. This chapter highlights the important role that age-specific paleo-plant physiology plays in vegetation-climate interactions in deep time.

In sum, findings from this dissertation demonstrate the importance of atmospheric pCO_2 in driving past icehouse climate dynamics and the utility of integrating Earth system models and proxy records in deep time.

Chapter 1 Introduction

1.1 Overview and motivation

1.1.1 Introduction to the Late Paleozoic Ice Age

The Late Paleozoic Ice Age (LPIA; ~340 to 290 Mya) was a dynamic icehouse, defined by episodic glacial events separated by periods of reduced ice volume in the Southern Hemisphere (Fielding et al., 2008a; Isbell et al., 2003, 2012). A number of major environmental changes developed during the LPIA, including the assembly of the supercontinent Pangaea, formation and partial erosion of a southwest-northeast trending equatorial mountain range called the Central Pangaean Mountains, a rise to anomalously high atmospheric O_2 (up to 30%) coupled with fluctuating but overall low CO_2 concentrations (~180 to 740 ppm; Berner, 2006; Montañez et al., 2016; Richey et al., 2020a), and the evolution and expansion of the oldest and most extensive paleotropical forests (Cleal and Thomas, 2005). The superocean, known as the Panthalassic Ocean, surrounded Pangaea, covered an entire hemisphere of the Earth, and periodically flooded low-elevation regions. These shallow inland seas extended far into the interior of continents and supported the diversification of cartilaginous and bony fish (Friedman and Sallan, 2012; Long et al., 2019) as well as marine invertebrates (Fan et al., 2020; Shi et al., 2021). While major environmental, climatic, and biological transitions are documented through the LPIA, our understanding of the factors driving these changes is incomplete. This dissertation addresses some of the important drivers of these environmental changes and the most fundamental uncertainties about LPIA climate conditions.

Icehouses, such as the current glacial state and LPIA, make up less than 25% of the past billion years of Earth's history (Montañez et al., 2011). The LPIA thus documents a unique convergence of major fluctuations in atmospheric CO_2, glaciation, and ecosystems far outside of the world we inhabit. A comprehensive understanding of climate change during the LPIA would expand our view of the climate system and enhance our confidence in projecting future climate under increasing CO_2, particularly as the Earth system evolves beyond the climate state captured

in modern and historical observations. Decades of studies point to a strong link between atmospheric CO_2 and glacial-interglacial transitions during the LPIA (Horton et al., 2010, 2012; Montanez et al., 2007; Richey et al., 2020a), but far less is known about how the role of the superocean and terrestrial biosphere in late Paleozoic climate change (Montañez and Poulsen, 2013). This dissertation investigates the impact of evolving atmospheric pCO_2 on regional to global superocean dynamics and tropical vegetation-climate feedbacks during the Pennsylvanian–early Permian apex of glaciation by simulating these processes in an Earth system model framework.

Our understanding of the LPIA has evolved substantially from a period of long-term stability to one of dynamic change that documents the climate and ecosystem response to repeated glacial-interglacial transitions. For most of the 20th century, the LPIA was interpreted as a period of protracted supercontinental-scale glaciation due to the widespread distribution of Gondwanan glacial deposits and long record of sea level change preserved in cyclic low-latitude sedimentary deposits (Crowley and Baum, 1991; Veevers and Powell, 1987). The volume of this single, massive ice sheet was thought to be determined by the drift of Gondwana relative to the austral pole over tens of millions of years (Caputo and Crowell, 1985). More recent evidence, primarily from the 21st century, has challenged several aspects of this traditional view. Near-field (ice-proximal) studies of glacial deposits have found evidence for multiple 10 Myr glacial hiatuses and indicate that not all regions of Gondwana were glaciated at the same time (Fielding et al., 2008b, 2008a; Griffis et al., 2021, 2019b; Isbell et al., 2003, 2012; Isbell and Lenaker, 2003). In addition, a synthesis of low-latitude sea level estimates supports that the magnitudes of inferred sea-level changes are consistent with a more dynamic view of glaciation (Rygel et al., 2008). The LPIA is now understood as a series of discrete (<1 to ~8 million years) and asynchronous glacial events, with small- to moderate-size ice sheets emanating from multiple ice centers, separated by periods of substantially reduced ice volume or ice-free conditions, collectively called glacial-interglacial cycles (Fielding et al., 2008a; Isbell et al., 2003, 2012). Continental drift can account for some of the glacial transitions, but it cannot account for all the inferred glaciation and associated climate change (Fielding et al., 2008b; Isbell et al., 2012; Lowry et al., 2014). Among the additional drivers proposed for glacial-interglacial cycles, atmospheric CO_2 has emerged as a leading factor (Montañez and Poulsen, 2013).

Recent advancements in the temporal resolution of atmospheric pCO_2 reconstructions during the LPIA confirm the hypothesized strong CO_2–glaciation relationship and document synchroneity between pCO_2 changes and transformations in terrestrial and marine environments (Montanez et al., 2007; Montañez et al., 2016; Richey et al., 2020a). During the Pennsylvanian (~323–299 Ma), atmospheric pCO_2 fluctuated between relatively high concentrations (482 to 713 ppm) during eccentricity scale (~400 kyr) interglacial intervals and low concentrations during glacial periods (161 to 299 ppm). Over Pangaea, these glacial-interglacial pCO_2 variations were accompanied by repeated and dynamic restructuring of paleotropical forests between relatively wet- and dry-adapted floras (Montañez et al., 2016). Glacial-interglacial changes in pCO_2 were superimposed on a multimillion-year trend of declining pCO_2 through the Pennsylvanian into the earliest Permian, during which paleotropical wetland and dryland forests were broadly restructured with more drought-tolerant vegetation (DiMichele et al., 2009; Montañez et al., 2016; Pfefferkorn and Thomson, 1982; Phillips et al., 1974; Tabor et al., 2013). Relatively elevated atmospheric CO_2 levels during the late Pennsylvanian (~515 ppm) dropped substantially across the Carboniferous–Permian boundary (i.e., 298.9 Ma) to a 10 Myr nadir (~300–290 Ma) with CO_2 concentrations varying between ~180 and 400 ppm (Richey et al., 2020a). Over the Carboniferous–Permian transition, the paleogeographic distribution and geochemistry of some climate-sensitive marine invertebrates (i.e., shallow-water benthic bivalves called brachiopods) support seawater cooling and a contraction of warm, subtropical surface currents (Angiolini et al., 2007; Grossman et al., 2008; Waterhouse and Shi, 2010). This low CO_2 interval in the earliest Permian also coincides with renewed glaciation to a maximum ice sheet extent (Fielding et al., 2008b; Isbell et al., 2012; Montañez and Poulsen, 2013; Soreghan et al., 2019) and a drawdown of sea level archived in successions across the paleotropics (Eros et al., 2012), marking the apex of the LPIA. The remainder of the early Permian is defined by a long-term rise in pCO_2 to peak values of up to ~740 ppm and progressive Gondwanan deglaciation (Fielding et al., 2008b; Isbell et al., 2003), marking the demise of the LPIA and transition to the mid-late Permian greenhouse climate.

Reconstructing the complex interconnections between pCO_2, climate, and ecosystems during the LPIA is limited by the availability of late Paleozoic proxy records. For example, our knowledge of the Panthalassic Ocean is largely inferred from sedimentary successions deposited in shallow inland (epicontinental) seas because subduction has destroyed virtually all open-

marine deposits formed before the Jurassic (~200 Ma) (Brand et al., 2009). As a result, temperatures and circulation patterns inferred from marine proxy records over the LPIA are restricted to shallow coastal regions. Furthermore, if proxy records are from an inland sea that was semi-restricted from the open ocean, then they may be subject to local processes such as freshwater input and seawater circulation that can alter their chemical composition and obscure inferred changes in seawater temperature or pCO_2 related to global climate events (Brand et al., 2009; Holmden et al., 1998; Jimenez et al., 2019; Joachimski and Lambert, 2015; Montañez et al., 2018; Narkiewicz et al., 2017; Panchuk et al., 2006; Rosenau et al., 2014; Woodard et al., 2013). To understand the influence of pCO_2 on the late Paleozoic marine environment, constraints on local processes in epicontinental seas and estimates of temperature and circulation beyond coastal settings are needed. Climate models address these gaps in knowledge by providing global, physically based depictions of the Earth system that can be used to connect environmental inferences from spatially discontinuous proxy records to large-scale climate dynamics.

1.1.2 A brief history of Late Paleozoic climate modeling

Early modeling studies used a highly idealized, hemispherically symmetric Pangaean landmass to simulate large-scale atmospheric and ocean circulation. These studies provided some of the first characterizations of Pangaean climate under varying pCO_2 levels, including intense megamonsoons (Kutzbach and Gallimore, 1989), the influence of Earth's orbit on terrestrial precipitation and runoff (Kutzbach, 1994), and surface currents and overturning circulation in the Panthalassic (Kutzbach et al., 1990). Nevertheless, these simplified modeling frameworks highlight the need to incorporate key aspects of the late Paleozoic climate system, such as shallow inland seas, vegetation cover, and a more realistic paleogeography, to capture the environmental changes inferred from marine and terrestrial proxy records over time (Kutzbach and Ziegler, 1993).

Modeling studies have since included more complex representations of the climate system and been used to explore the role of pCO_2 variations in the evolution of terrestrial and marine environments during the late Paleozoic. Many climate–ice sheet simulations have supported the idea that the initiation and expansion of Gondwanan ice sheets are highly sensitive to the atmospheric CO_2 level (Crowley and Baum, 1992; Horton et al., 2007, 2010; Horton and Poulsen, 2009; Hyde et al., 1999; Lowry et al., 2014). Several modeling studies of tropical

hydroclimate have demonstrated that pCO_2 affects precipitation over low latitude Pangaea and likely influenced the composition of paleotropical forests over the Pennsylvanian, yet the phasing of precipitation variability with pCO_2 differs between simulations (Heavens et al., 2012, 2015; Peyser and Poulsen, 2008; Poulsen et al., 2007). This disagreement between climate simulations partly reflects the focus of previous studies on the role of climate forcings (e.g., sea level, Gondwanan ice sheet extent, Earth's orbital configuration) as opposed to vegetation dynamics (e.g., biome restructuring, paleophysiology) in modulating tropical vegetation-climate feedbacks under varying pCO_2. With respect to the late Paleozoic marine environment, virtually all modeling studies of the Panthalassic Ocean have focused on the mid-late Permian greenhouse interval (Kiehl and Shields, 2005; Osen et al., 2013; Winguth et al., 2002, 2012; Winguth and Winguth, 2012). These studies make it apparent that pCO_2 plays an important role in Panthalassic circulation and temperature, but also highlight the dependence of ocean dynamics on the geographic configuration of Pangaea. As a result, the role of tropical vegetation and ocean dynamics in LPIA climate change remains uncertain.

This dissertation presents new Earth system modeling results and applications that investigate the influence of atmospheric pCO_2 on superocean dynamics as well as tropical vegetation-climate interactions during the Pennsylvanian–early Permian. The first two data chapters of this dissertation address how changes in atmospheric pCO_2 influence global patterns of ocean circulation and temperature (Chapter 2) and the physical and chemical characteristics of an epicontinental sea relative to the nearby open ocean (Chapter 3). Chapter 4 constrains the role of paleo-plant physiology in tropical vegetation-climate interactions under changing pCO_2. Taken together, findings from this dissertation highlight the importance of atmospheric pCO_2 in driving past icehouse climate dynamics.

1.2 Novel approaches to combining Earth system models and proxy data

This dissertation leverages the complementary strengths of Earth system models and environmental proxy data to better understand the role of ocean dynamics and the terrestrial biosphere in Pennsylvanian–early Permian climate change under different levels of pCO_2. I use the National Center for Atmospheric Research's Community Earth System Model version 1.2 (CESM), which consists of component models representing the atmosphere, land surface, ocean, and cryosphere, that are connected through a central coupler (Hurrell et al., 2013). CESM is ideal

for simulation of the late Paleozoic Earth system because it (1) produces some of the most realistic modern climate estimates when compared to other Earth system models developed by scientists across the world (Knutti et al., 2013) and (2) is developed with code and dataset modifications necessary for the simulation of deep time paleoclimate states. A community of scientists is dedicated to applying CESM to paleoclimate intervals, whereas other Earth system models are exclusively used to simulate present and near-future climate states.

The boundary conditions (e.g., continental distribution, topography, ice sheets) and external climate forcing (e.g., solar irradiance, greenhouse gases) needed to simulate the late Paleozoic climate system with CESM are based on a diverse compilation of geologic and environmental proxy data. For the land surface, paleolatitudes of continents that make up Pangaea are primarily inferred from paleomagnetic records (Domeier and Torsvik, 2014), the location and extent of Gondwanan ice sheets are based on stratigraphic glacial features and deposits (Griffis et al., 2019a, 2019b), and vegetation is designated based on the paleogeographic distribution of available plant fossil remains (Wilson et al., 2017), typically using the most appropriate modern plant analog (i.e., for lycopsids, I use the 'tropical broadleaf evergreen tree' plant type). For the atmosphere, the concentration of CO_2 is based on 10^5-year resolution estimates from a combination of fossil leaf and soil geochemistry (Montanez et al., 2007; Richey et al., 2020a). Nevertheless, there is uncertainty associated with using geologic data to infer environmental conditions from ~300 Mya, such as mountain elevation and ocean depth, that are known to affect climate. These uncertainties are addressed with CESM by using sensitivity experiments with multiple potential environmental scenarios. Each scenario is constrained by endmembers inferred from environmental proxy data (e.g., CESM simulations that include mountains with 2000 and 4000 m peak elevation or continental shelves with 60 and 120 m depth) to systematically assess the impact of these environmental factors on the climate feature of interest. In the chapters of this dissertation, I use a variety of CESM configurations, including full Earth system coupling (Hurrell et al., 2013) and stable water isotope-enabled (Brady et al., 2019) versions, to investigate ocean dynamics and land-atmosphere interactions during the Pennsylvanian–early Permian.

The main strength of CESM is the ability to provide a simplified, physically based depiction of the Earth system that can be used to differentiate the environmental processes responsible for regional to global climate events. In Chapters 2 and 3, we use this approach to

provide physical mechanisms that link local environmental conditions archived by marine fossils, primarily brachiopods, to regional and global climate change. Marine fossils from the LPIA are limited to shallow inland seas, and thus many proxy studies have assumed that epicontinental seas are representative of the nearby open ocean to reconstruct large-scale palaeoceanographic events. For example, geochemical data from the Russian platform support ocean cooling and a pCO_2 decline during the early Permian apex of glaciation (Grossman et al., 2008; Korte et al., 2005; Mii et al., 2001). On the other hand, epicontinental records from North America do not provide clear evidence for this temperature and pCO_2 change and exhibit high spatial variability (Grossman et al., 2008). The ratio of relatively heavy (^{18}O) to light (^{16}O) oxygen isotopes in well-preserved marine fossils integrates the temperature and oxygen isotopic composition of seawater in which the fossil was formed, and thus serves as a robust proxy of ocean temperature if the local seawater isotopic composition is well constrained. The oxygen isotopic composition of seawater, however, integrates a complex interplay of global ice volume, local balance of precipitation and runoff to evaporation, and exchange of oxygen between water and silicate rocks (Veizer and Prokoph, 2015), and is not well constrained in ancient inland seas. Mounting evidence suggests that local environmental factors, such as freshwater input and seawater circulation, can alter the oxygen isotopic composition of seawater in semi-restricted epicontinental seas and thus obscure the temperature signal archived in marine fossils (Brand et al., 2009; Holmden et al., 1998; Jimenez et al., 2019; Joachimski and Lambert, 2015; Montañez et al., 2018; Narkiewicz et al., 2017; Panchuk et al., 2006; Rosenau et al., 2014; Woodard et al., 2013). CESM can be used to connect epicontinental proxy records to large-scale ocean dynamics during the LPIA by (1) simulating global patterns of ocean circulation and temperature with time-specific boundary conditions and climate forcing, and then (2) focusing on local circulation and temperature in an epicontinental sea under multiple potential environmental scenarios.

Uncertainties do exist regarding the necessary simplification of the late Paleozoic Earth system in CESM that can be improved using environmental proxy records. In Chapter 4, we use Pennsylvanian plant fossil remains, among the most completely studied plants of the fossil record, to enhance the representation of paleo-vegetation in CESM. Pennsylvanian terrestrial ecosystems were considerably different from those of the recent past and present with the notable absence of angiosperms, the most diverse and ecologically dominant modern plant group. Nevertheless, previously limited knowledge of extinct plant ecophysiology has required

modeling studies to use modern angiosperms and conifers as physiological analogs for plants in deep time (Beerling, 1998; Heavens et al., 2015; Kutzbach and Ziegler, 1993; Poulsen et al., 2007; Rees et al., 2002; Wade et al., 2019). Recent studies reveal that Pennsylvanian plants are morphologically and functionally distinct from their extant relatives, particularly in terms of their leaf conductance and hydraulic capacity (McAdam and Brodribb, 2012; Wilson et al., 2015, 2017), which could translate into much broader-scale changes in climate and continental runoff. Advancements in process-based ecosystem modeling (Richey et al., 2020b; White et al., 2020) and a wealth of paleobotanical material—particularly fossil records that provide constraints on leaf traits and morphologies (Boyce and Knoll, 2002; Peppe et al., 2011, 2014; Taylor and Taylor, 2009) and cuticular chemistry (Gupta et al., 2006; Montañez et al., 2016; Mösle et al., 1998; Richey et al., 2020b; Royer and Hren, 2017)—have provided numerical constraints on the physiological capacity and ecosystem function of Pennsylvanian plant communities. These fossil-based numerical constraints provide the information necessary for CESM to simulate the role of plants in modulating paleotropical vegetation-climate interactions under evolving pCO_2.

1.3 Dissertation chapter summaries

This dissertation is comprised of three studies (chapters 2-4) that combine new CESM simulations and published proxy records to investigate the influence of atmospheric pCO_2 on ocean dynamics and vegetation-climate interactions during the Pennsylvanian–early Permian. These studies provide mechanistic linkages between the multitude of complex local environmental processes archived by proxy records and regional and global climate change. Results and conclusions from these chapters help constrain the roles of the superocean and extinct plant communities in mediating LPIA climate change by leveraging the complementary strengths of Earth system models and environmental proxy data.

Chapters 2 and 3 focus on glacial-interglacial changes in ocean circulation and temperature from the global to epicontinental scale. Late Paleozoic modeling studies have provided global estimates of temperature, heat transport, and circulation in the Panthalassic Ocean, revealing a wide range of ocean dynamics with varying atmospheric pCO_2 and paleogeography of superocean basins (Kiehl and Shields, 2005; Kutzbach and Ziegler, 1993; Smith et al., 2004; Winguth et al., 2002, 2012; Zhang et al., 2001). Nevertheless, virtually all modeling studies have focused primarily on large-scale mechanisms for the Permo-Triassic mass

extinction, and thus have spatial resolution that is too coarse to resolve shallow inland seas and model boundary conditions specific to the mid-late Permian greenhouse. These chapters use isotope-enabled CESM to provide time-specific insight into the influence of glacial-interglacial changes in CO_2, sea level, and high-latitude ice extent on ocean circulation, temperature, and oxygen isotopic composition. Together, these chapters address the spatial discrepancy between marine fossils restricted to shallow inland seas and Earth system models that capture large-scale ocean dynamics.

Chapter 2 (in preparation) connects proxy-inferred coastal ocean currents and temperatures to global ocean patterns during the late Pennsylvanian–early Permian by providing the first time-specific estimates of wind-driven and thermohaline circulation as well as temperature from a fully coupled Earth system model. The CESM simulations presented in this chapter represent mean glacial and interglacial states during the Pennsylvanian–early Permian with differing atmospheric CO_2, sea level, and high-latitude ice extent to examine differences in ocean circulation and temperature. We find that wind-driven surface currents, upwelling intensity, and thermohaline circulation are stronger overall under glacial conditions compared to interglacial conditions. Glacial and interglacial latitudinal temperature gradients are similar overall in the open ocean, but glacial temperature gradients are notably enhanced over continental shelves where proxy records are located. Enhanced coastal temperature gradients and reduced continental runoff from relatively warm interglacial to cool glacial conditions could have promoted marine biodiversity over the latest Pennsylvanian–earliest Permian by increasing marine provincialism and forming oligotrophic water masses in coastal environments, respectively. These simulations provide the first potential climatic mechanisms for the Pennsylvanian–earliest Permian increase in marine biodiversity and highlight the importance of understanding physical processes in shallow coastal marine environments for environmental interpretations based on the marine fossil record.

Chapter 3 (published in *Earth and Planetary Science Letters*; Macarewich et al., 2021) focuses on circulation, temperature, and oxygen isotopic variation in one particular epicontinental sea, the North American Midcontinent Sea. This location is particularly important because fossil records from this region contribute disproportionally to late Pennsylvanian isotope secular curves and reconstructions of ocean temperature and sea level over time (Grossman et al., 2008; Henkes et al., 2018). Based on multiple sensitivity simulations and proxy-model

comparisons, we find that the late Pennsylvanian–early Permian North American Midcontinent Sea had a mean depth of ~50 m and Central Pangaean Mountains had a peak elevation of ~2000 m. These regional mountains generated intense runoff and decreased the oxygen isotopic composition of seawater in the sea, particularly under elevated pCO_2 with high sea level. Estuarine-like circulation patterns in the sea under elevated pCO_2 at high sea level break down with relatively low sea level. Results from this chapter show high spatial variability of oxygen isotopic composition in the sea and suggest that caution should be taken when interpreting regional oxygen isotope records as proxies of temperature or sea level. These isotope-enabled CESM simulations are the first to resolve variations in seawater isotopic composition for the LPIA.

Chapter 4 (in preparation) investigates terrestrial biosphere-hydroclimate interactions under evolving pCO_2 and focuses on Pennsylvanian paleotropical forests because these plants are among the most completely studied plants of the fossil record. This chapter presents the methodology for using fossil leaf characteristics and process-based ecosystem modeling to integrate Pennsylvanian plants in the land component of CESM. These are the first Earth system model simulations that include time-specific extinct plant physiology. CESM sensitivity simulations capture tropical vegetation-climate interactions with novel paleo-plant types and modern plant analogs, high and low pCO_2, as well as wetland- and dryland-dominated paleotropical forests. We find that the response of stomatal conductance to elevated pCO_2 is regionally dependent and controls the response of precipitation across the Pangaean tropics. Vegetated regions with suppressed (enhanced) stomatal conductance and thus transpiration rates under elevated pCO_2 are associated with atmospheric and soil wetting (drying). These two vegetation-climate feedbacks are consistent between paleo-plants and modern plant analogs, but modern plant analogs consistently underestimate the drying feedback because of overall lower stomatal conductance rates. This work highlights the important role that paleo-plant physiology plays in vegetation-climate interactions in deep time.

This dissertation does not address all the remaining questions about LPIA climate change, but it represents a substantial step forward in our understanding of the climate dynamics that drove marine and terrestrial change during the LPIA. Still, many unanswered questions remain about deep time climate dynamics, so this dissertation ends with Chapter 5, a summary of

important findings and contributions from this work as well as additional areas to pursue in future research.

1.4 References

Angiolini, L., Mangiagalli, V., Muttoni, G., Stephenson, M. H. and Zanchi, A.: Tethyan oceanic currents and climate gradients 300 m.y. ago, Geology, 35(12), 1071–1074, doi:10.1130/G24031A.1, 2007.

Beerling, D. J.: The influence of Carboniferous palaeo-atmospheres on plant function: An experimental and modelling assessment, Philos. Trans. R. Soc. B Biol. Sci., 353(1365), 131–140, doi:10.1098/rstb.1998.0196, 1998.

Berner, R. A.: GEOCARBSULF: A combined model for Phanerozoic atmospheric O_2 and CO_2, Geochim. Cosmochim. Acta, 70(23 SPEC. ISS.), 5653–5664, doi:10.1016/j.gca.2005.11.032, 2006.

Boyce, C. K. and Knoll, A. H.: Evolution of developmental potential and the multiple independent origins of leaves in Paleozoic vascular plants, Paleobiology, 28(1), 70–100, doi:10.1666/0094-8373(2002)028<0070:eodpat>2.0.co;2, 2002.

Brady, E., Stevenson, S., Bailey, D., Liu, Z., Noone, D., Nusbaumer, J., Otto-Bliesner, B. L., Tabor, C., Tomas, R., Wong, T., Zhang, J. and Zhu, J.: The connected isotopic water cycle in the Community Earth System Model Version 1, J. Adv. Model. Earth Syst., 11(8), 2547–2566, doi:10.1029/2019MS001663, 2019.

Brand, U., Tazawa, J. I., Sano, H., Azmy, K. and Lee, X.: Is mid-late Paleozoic ocean-water chemistry coupled with epeiric seawater isotope records?, Geology, 37(9), 823–826, doi:10.1130/G30038A.1, 2009.

Caputo, M. V. and Crowell, J. C.: Migration of glacial centers across Gondwana during Paleozoic Era, Geol. Soc. Am. Bull., 96(8), 1020–1036, doi:10.1130/0016-7606(1985)96<1020:MOGCAG>2.0.CO;2, 1985.

Cleal, C. J. and Thomas, B. A.: Palaeozoic tropical rainforests and their effect on global climates: Is the past the key to the present?, Geobiology, 3(1), 13–31, doi:10.1111/j.1472-4669.2005.00043.x, 2005.

Crowley, T. J. and Baum, S. K.: Estimating Carboniferous sea-level fluctuations from Gondwanan ice extent, Geology, (October), 975–977, 1991.

Crowley, T. J. and Baum, S. K.: Modeling late Paleozoic glaciation, Geology, 20, 507–510, 1992.

DiMichele, W. A., Montanez, I. P., Poulsen, C. J. and Tabor, N. J.: Climate and vegetational regime shifts in the late Paleozoic ice age earth, Geobiology, 7(2), 200–226, doi:10.1111/j.1472-4669.2009.00192.x, 2009.

Domeier, M. and Torsvik, T. H.: Plate tectonics in the Late Paleozoic, Geosci. Front., 5(3), 303–350, doi:10.1016/j.gsf.2014.01.002, 2014.

Eros, J. M., Montañez, I. P., Davydov, V. I., Osleger, D. A., Nemyrovska, T. I., Poletaev, V. I. and Zhykalyak, M. V.: Sequence stratigraphy and onlap history of the Donets Basin, Ukraine: Insight into Carboniferous icehouse dynamics, Palaeogeogr. Palaeoclimatol. Palaeoecol., 363–364, 187–191, doi:10.1016/j.palaeo.2012.09.013, 2012.

Fan, J., Shen, S., Erwin, D. H., Sadler, P. M., MacLeod, N., Cheng, Q., Hou, X., Yang, J., Wang, X., Wang, Y., Zhang, H., Chen, X., Li, G., Zhang, Y., Shi, Y., Yuan, D., Chen, Q., Zhang, L., Li, C. and Zhao, Y.: A high-resolution summary of Cambrian to Early Triassic marine invertebrate biodiversity, Science, 277(January), 272–277, 2020.

Fielding, C. R., Frank, T. D., Birgenheier, L. P., Rygel, M. C., Jones, A. T. and Roberts, J.: Stratigraphic record and facies associations of the late Paleozoic ice age in eastern Australia (New South Wales and Queensland), in Geological Society of America Special Papers, vol. 2441, pp. 41–57., 2008a.

Fielding, C. R., Frank, T. D. and Isbell, J. L.: The late Paleozoic ice age—A review of current understanding and synthesis of global climate patterns, Spec. Pap. 441 Resolv. Late Paleoz. Ice Age Time Sp., 2441(24), 343–354, doi:10.1130/2008.2441(24), 2008b.

Friedman, M. and Sallan, L. C.: Five hundred million years of extinction and recovery: A phanerozoic survey of large-scale diversity patterns in fishes, Palaeontology, 55(4), 707–742, doi:10.1111/j.1475-4983.2012.01165.x, 2012.

Griffis, N., Montañez, I., Mundil, R., Heron, D. Le, Dietrich, P., Kettler, C., Linol, B., Mottin, T., Vesely, F., Iannuzzi, R., Huyskens, M., Yin, Q. and Griffis, N.: High-latitude ice and climate control on sediment supply across SW Gondwana during the late Carboniferous and early Permian, , 1–12, doi:10.1130/B35852.1, 2021.

Griffis, N. P., Montanez, I. P., Mundil, R., Richey, J., Isbell, J., Fedorchuk, N., Linol, B., Iannuzzi, R., Vesely, F., Mottin, T., da Rosa, E., Keller, B. and Yin, Q. Z.: Coupled stratigraphic and U-Pb zircon age constraints on the late Paleozoic icehouse-to-greenhouse turnover in south-central gondwana, Geology, 47(12), 1146–1150, doi:10.1130/G46740.1, 2019a.

Griffis, N. P., Montañez, I. P., Fedorchuk, N., Isbell, J., Mundil, R., Vesely, F., Weinshultz, L., Iannuzzi, R., Gulbranson, E., Taboada, A., Pagani, A., Sanborn, M. E., Huyskens, M., Wimpenny, J., Linol, B. and Yin, Q. Z.: Isotopes to ice: Constraining provenance of glacial deposits and ice centers in west-central Gondwana, Palaeogeogr. Palaeoclimatol. Palaeoecol., 531(108745), 31–182, doi:10.1016/j.palaeo.2018.04.020, 2019b.

Grossman, E. L., Yancey, T. E., Jones, T. E., Bruckschen, P., Chuvashov, B., Mazzullo, S. J. and Mii, H.: Glaciation, aridification, and carbon sequestration in the Permo-Carboniferous: The isotopic record from low latitudes, Palaeogeogr. Palaeoclimatol. Palaeoecol., 268(3–4), 222–233, doi:10.1016/j.palaeo.2008.03.053, 2008.

Gupta, N. S., Collinson, M. E., Briggs, D. E. G., Evershed, R. P., Pancost, R. D., Paleobiology, S. and Summer, N.: Reinvestigation of the Occurrence of Cutan in Plants: Implications for the Leaf Fossil Record Published by: Cambridge University Press Stable URL: https://www.jstor.org/stable/4096960, 32(3), 432–449, 2006.

Heavens, N. G., Mahowald, N. M., Soreghan, G. S., Soreghan, M. J. and Shields, C. a.: Glacial-interglacial variability in Tropical Pangaean Precipitation during the Late Paleozoic Ice Age: simulations with the Community Climate System Model, Clim. Past Discuss., 8(3), 1915–1972, doi:10.5194/cpd-8-1915-2012, 2012.

Heavens, N. G., Mahowald, N. M., Soreghan, G. S., Soreghan, M. J. and Shields, C. A.: A model-based evaluation of tropical climate in Pangaea during the late Palaeozoic icehouse, Palaeogeogr. Palaeoclimatol. Palaeoecol., 425, 109–127, doi:10.1016/j.palaeo.2015.02.024, 2015.

Henkes, G. A., Passey, B. H., Grossman, E. L., Shenton, B. J., Yancey, T. E. and Pérez-Huerta, A.: Temperature evolution and the oxygen isotope composition of Phanerozoic oceans from carbonate clumped isotope thermometry, Earth Planet. Sci. Lett., 490, 40–50, doi:10.1016/j.epsl.2018.02.001, 2018.

Holmden, C., Creaser, R. A., Muehlenbachs, K., Leslie, S. A. and Bergström, S. M.: Isotopic evidence for geochemical decoupling between ancient epeiric seas and bordering oceans: implications for secular curves, Geology, 26(6), 567–570, doi:10.1130/0091-7613(1998)026<0567:IEFGDB>2.3.CO;2, 1998.

Horton, D. E. and Poulsen, C. J.: Paradox of late Paleozoic glacioeustasy, Geology, 37(8), 715–718, doi:10.1130/G30016A.1, 2009.

Horton, D. E., Poulsen, C. J. and Pollard, D.: Orbital and CO_2 forcing of late Paleozoic continental ice sheets, Geophys. Res. Lett., 34(19), 2–7, doi:10.1029/2007GL031188, 2007.

Horton, D. E., Poulsen, C. J. and Pollard, D.: Influence of high-latitude vegetation feedbacks on late Palaeozoic glacial cycles, Nat. Geosci., 3(8), 572–577, doi:10.1038/ngeo922, 2010.

Horton, D. E., Poulsen, C. J., Montañez, I. P. and DiMichele, W. A.: Eccentricity-paced late Paleozoic climate change, Palaeogeogr. Palaeoclimatol. Palaeoecol., 331–332, 150–161, doi:10.1016/j.palaeo.2012.03.014, 2012.

Hurrell, J. W., Holland, M. M., Gent, P. R., Ghan, S., Kay, J. E., Kushner, P. J., Lamarque, J. F.,

Large, W. G., Lawrence, D., Lindsay, K., Lipscomb, W. H., Long, M. C., Mahowald, N., Marsh, D. R., Neale, R. B., Rasch, P., Vavrus, S., Vertenstein, M., Bader, D., Collins, W. D., Hack, J. J., Kiehl, J. and Marshall, S.: The community earth system model: A framework for collaborative research, Bull. Am. Meteorol. Soc., 94(9), 1339–1360, doi:10.1175/BAMS-D-12-00121.1, 2013.

Hyde, W. T., Crowley, T. J., Tarasov, L. and Peltier, W. R.: The Pangean ice age: studies with a coupled climate-ice sheet model, Clim. Dyn., 15(9), 619–629, doi:10.1007/s003820050305, 1999.

Isbell, J. L. and Lenaker, P. A.: Reevaluation of the timing and extent of late Paleozoic glaciation in Gondwana: Role of the Transantarctic Mountains, Geology, 31(11), 977–980, 2003.

Isbell, J. L., Miller, M. F., Wolfe, K. L. and Lenaker, P. A.: Timing of late Paleozoic glaciation in Gondwana: Was glaciation responsible for the development of Northern Hemisphere cyclothems?, Geol. Soc. Am. Spec. Pap. 370, 370, 5–24, doi:10.1130/0-8137-2370-1.5, 2003.

Isbell, J. L., Henry, L. C., Gulbranson, E. L., Limarino, C. O., Fraiser, M. L., Koch, Z. J., Ciccioli, P. L. and Dineen, A. A.: Glacial paradoxes during the late Paleozoic ice age: Evaluating the equilibrium line altitude as a control on glaciation, Gondwana Res., 22(1), 1–19, doi:10.1016/j.gr.2011.11.005, 2012.

Jimenez, M. Y., Ivany, L. C., Judd, E. J. and Henkes, G. A.: Low and seasonally variable salinity in the Pennsylvanian equatorial Appalachian Basin, Earth Planet. Sci. Lett., 519, 182–191, doi:10.1016/j.epsl.2019.04.051, 2019.

Joachimski, M. M. and Lambert, L. L.: Salinity contrast in the US Midcontinent Sea during Pennsylvanian glacio-eustatic highstands: Evidence from conodont apatite $\delta^{18}O$, Palaeogeogr. Palaeoclimatol. Palaeoecol., 433, 71–80, doi:10.1016/j.palaeo.2015.05.014, 2015.

Kiehl, J. T. and Shields, C. A.: Climate simulation of the latest Permian: Implications for mass extinction, Geology, (9), 757–760, doi:10.1130/G21654.1, 2005.

Knutti, R., Masson, D. and Gettelman, A.: Climate model genealogy: Generation CMIP5 and how we got there, Geophys. Res. Lett., 40(6), 1194–1199, doi:10.1002/grl.50256, 2013.

Korte, C., Jasper, T., Kozur, H. W. and Veizer, J.: $\delta^{18}O$ and $\delta^{13}C$ of Permian brachiopods: A record of seawater evolution and continental glaciation, Palaeogeogr. Palaeoclimatol. Palaeoecol., 224(4), 333–351, doi:10.1016/j.palaeo.2005.03.015, 2005.

Kutzbach, J. E.: Idealized Pangean climates: Sensitivity to orbital change, in Pangea: Paleoclimate, Tectonics, and Sedimentation During Accretion, Zenith, and Breakup of a Supercontinent, vol. 288, edited by G. O. Klein, p. 0, Geological Society of America., 1994.

Kutzbach, J. E. and Gallimore, R. G.: Pangaean climates: megamonsoons of the megacontinent, J. Geophys. Res., 94(D3), 3341–3357, doi:10.1029/JD094iD03p03341, 1989.

Kutzbach, J. E. and Ziegler, A. M.: Simulation of late Permian climate and biomes with an atmosphere- ocean model: comparisons with observations, Philos. Trans. - R. Soc. London, B, 341(1297), 327–340, doi:10.1098/rstb.1993.0118, 1993.

Kutzbach, J. E., Guetter, P. J. and Washington, W. M.: Simulated circulation of an idealized ocean for Pangaean time, Paleoceanography, 5(3), 299–317, doi:10.1029/PA005i003p00299, 1990.

Long, J. A., Choo, B. and Clement, A.: The Evolution of Fishes through Geological Time, in Evolution and Development of Fishes, pp. 3–29, Cambridge University Press., 2019.

Lowry, D. P., Poulsen, C. J., Horton, D. E., Torsvik, T. H. and Pollard, D.: Thresholds for Paleozoic ice sheet initiation, Geology, 42(7), 627–630, doi:10.1130/G35615.1, 2014.

Macarewich, S., Poulsen, C. J. and Montañez, I. P.: Simulation of oxygen isotopes and circulation in a late Carboniferous epicontinental sea with implications for proxy records, Earth Planet. Sci. Lett., 559, 116770, doi:10.1016/j.epsl.2021.116770, 2021.

McAdam, S. A. M. and Brodribb, T. J.: Stomatal innovation and the rise of seed plants, Ecol. Lett., 15(1), 1–8, doi:10.1111/j.1461-0248.2011.01700.x, 2012.

Mii, H. S., Grossman, E. L., Yancey, T. E., Chuvashov, B. and Egorov, A.: Isotopic records of brachiopod shells from the Russian Platform - Evidence for the onset of mid-Carboniferous glaciation, Chem. Geol., 175(1–2), 133–147, doi:10.1016/S0009-2541(00)00366-1, 2001.

Montanez, I. P., Tabor, N. J., Niemeier, D., DiMichele, W. A., Frank, T. D., Fielding, C. R., Isbell, J. L., Birgenheier, L. P. and Rygel, M. C.: CO_2-Forced Climate and Vegetation Instability During Late Paleozoic Deglaciation, Science (80-.)., 315(5808), 87–91, doi:10.1126/science.1134207, 2007.

Montañez, I. P. and Poulsen, C. J.: The Late Paleozoic Ice Age: An Evolving Paradigm, Annu. Rev. Earth Planet. Sci., 41(1), 629–656, doi:10.1146/annurev.earth.031208.100118, 2013.

Montañez, I. P., Norris, R. D., Algeo, T., Chandler, M. A., Johnson, K. R., Kennedy, M. J., Kent, D. V., Kiehl, J. T., Kump, L. R., Ravelo, A. C. and Turekian, K. K.: Understanding Earth's Deep Past: Lessons for Our Climate Future, National Academies Press., 2011.

Montañez, I. P., McElwain, J. C., Poulsen, C. J., White, J. D., DiMichele, W. A., Wilson, J. P., Griggs, G. and Hren, M. T.: Climate, pCO_2 and terrestrial carbon cycle linkages during late Palaeozoic glacial–interglacial cycles, Nat. Geosci., 9(11), 824–828,

doi:10.1038/ngeo2822, 2016.

Montañez, I. P., Osleger, D. J., Chen, J., Wortham, B. E., Stamm, R. G., Nemyrovska, T. I., Griffin, J. M., Poletaev, V. I. and Wardlaw, B. R.: Carboniferous climate teleconnections archived in coupled bioapatite $\delta^{18}O_{PO4}$ and $^{87}Sr/^{86}Sr$ records from the epicontinental Donets Basin, Ukraine, Earth Planet. Sci. Lett., 492, 89–101, doi:10.1016/j.epsl.2018.03.051, 2018.

Mösle, B., Collinson, M. E., Finch, P., Stankiewicz, B. A., Scott, A. C. and Wilson, R.: Factors influencing the preservation of plant cuticles: A comparison of morphology and chemical composition of modern and fossil examples, Org. Geochem., 29(5–7), 1369–1380, doi:10.1016/S0146-6380(98)00080-1, 1998.

Narkiewicz, M., Narkiewicz, K., Krzeminska, E. and Kruchek, S. A.: Oxygen Isotopic Composition of Conodont Apatite in the Equatorial Epeiric Belarussian Basin (Eifelian)–Relationship To Fluctuating Seawater Salinity and Temperature, Palaios, 32(7), 439–447, doi:10.2110/palo.2016.059, 2017.

Osen, A. K., Winguth, A. M. E., Winguth, C. and Scotese, C. R.: Sensitivity of Late Permian climate to bathymetric features and implications for the mass extinction, Glob. Planet. Change, 105, 171–179, doi:10.1016/j.gloplacha.2012.01.011, 2013.

Panchuk, K. M., Holmden, C. E. and Leslie, S. A.: Local controls on carbon cycling in the Ordovician Midcontinent region of North America, with implications for carbon isotope secular curves, J. Sediment. Res., 76(2), 200–211, doi:10.2110/jsr.2006.017, 2006.

Peppe, D. J., Royer, D. L., Cariglino, B., Oliver, S. Y., Newman, S., Leight, E., Enikolopov, G., Fernandez-Burgos, M., Herrera, F., Adams, J. M., Correa, E., Currano, E. D., Erickson, J. M., Hinojosa, L. F., Hoganson, J. W., Iglesias, A., Jaramillo, C. A., Johnson, K. R., Jordan, G. J., Kraft, N. J. B., Lovelock, E. C., Lusk, C. H., Niinemets, Ü., Peñuelas, J., Rapson, G., Wing, S. L. and Wright, I. J.: Sensitivity of leaf size and shape to climate: Global patterns and paleoclimatic applications, New Phytol., 190(3), 724–739, doi:10.1111/j.1469-8137.2010.03615.x, 2011.

Peppe, D. J., Lemons, C. R., Royer, D. L., Wing, S. L., Wright, I. J., Lusk, C. H. and Rhoden, C. H.: Biomechanical and leaf-climate relationships: A comparison of ferns and seed plants, Am. J. Bot., 101(2), 338–347, doi:10.3732/ajb.1300220, 2014.

Peyser, C. E. and Poulsen, C. J.: Controls on Permo-Carboniferous precipitation over tropical Pangaea: A GCM sensitivity study, Palaeogeogr. Palaeoclimatol. Palaeoecol., 268(3–4), 181–192, doi:10.1016/j.palaeo.2008.03.048, 2008.

Pfefferkorn, H. W. and Thomson, M. C.: Changes in dominance patterns in upper Carboniferous plant-fossil assemblages, Geology, 10(12), 641–644, doi:10.1130/0091-7613(1982)10<641:CIDPIU>2.0.CO;2, 1982.

Phillips, T. L., Peppers, R. A., Avcin, M. J. and Laughnan, P. F.: Fossil plants and coal: Patterns of change in Pennsylvanian coal swamps of the Illinois Basin, Science, 184(4144), 1367–1369, doi:10.1126/science.184.4144.1367, 1974.

Poulsen, C. J., Pollard, D., Montanez, I. P. and Rowley, D.: Late Paleozoic tropical climate response to Gondwanan deglaciation, Geology, 35(9), 771–774, doi:10.1130/G23841A.1, 2007.

Rees, P. M., Ziegler, A. M., Gibbs, M. T., Kutzbach, J. E., Behling, P. J. and Rowley, D. B.: Permian Phytogeographic Patterns and Climate Data/Model Comparisons Permian Phytogeographic Patterns and Climate, J. Geol., 110(January), 1–31, 2002.

Richey, J. D., Montañez, I. P., Goddéris, Y., Looy, C. V., Griffis, N. P. and Dimichele, W. A.: Influence of temporally varying weatherability on CO_2-climate coupling and ecosystem change in the late Paleozoic, Clim. Past, 16(5), 1759–1775, doi:10.5194/cp-16-1759-2020, 2020a.

Richey, J. D., Montañez, I. P., White, J. D., DiMichele, W. A., Matthaeus, W. J., Poulsen, C. J., Macarewich, S. I. and Looy, C. V.: Modeled physiological mechanisms for observed changes in the late Paleozoic plant fossil record, Palaeogeogr. Palaeoclimatol. Palaeoecol., doi:10.1016/j.palaeo.2020.110056, 2020b.

Rosenau, N. A., Tabor, N. J. and Herrmann, A. D.: Assessing the paleoenvironmental significance of middle-late Pennsylvanian conodont apatite ^{18}O values in the Illinois Basin, Palaios, 29(6), 250–265, doi:10.2110/palo.2013.112, 2014.

Royer, D. L. and Hren, M. T.: Carbon isotopic fractionation between whole leaves and cuticle, Palaios, 32(4), 199–205, doi:10.2110/palo.2016.073, 2017.

Rygel, M. C., Fielding, C. R., Frank, T. D. and Birgenheier, L. P.: The Magnitude of Late Paleozoic Glacioeustatic Fluctuations: A Synthesis, J. Sediment. Res., 78(8), 500–511, doi:10.2110/jsr.2008.058, 2008.

Shi, Y., Wang, X., Fan, J., Huang, H., Xu, H. and Zhao, Y.: Carboniferous-earliest Permian marine biodiversification event (CPBE) during the Late Paleozoic Ice Age, Earth-Science Rev., 220(April), 2021.

Smith, R. S., Dubois, C. and Marotzke, J.: Ocean circulation and climate in an idealised Pangean OAGCM, Geophys. Res. Lett., 31(18), 1–4, doi:10.1029/2004GL020643, 2004.

Soreghan, G. S., Soreghan, M. J. and Heavens, N. G.: Explosive volcanism as a key driver of the late Paleozoic ice age, Geology, 47(7), 600–604, doi:10.1130/G46349.1, 2019.

Tabor, N. J., DiMichele, W. A., Montañez, I. P. and Chaney, D. S.: Late Paleozoic continental warming of a cold tropical basin and floristic change in western Pangea, Int. J. Coal Geol., 119, 177–186, doi:10.1016/j.coal.2013.07.009, 2013.

Taylor, E. L. and Taylor, T. N.: Seed ferns from the late Paleozoic and Mesozoic: Any angiosperm ancestors lurking there?, Am. J. Bot., 96(1), 237–251, doi:10.3732/ajb.0800202, 2009.

Veevers, J. J. and Powell, C. M.: Late Paleozoic glacial episodes in Gondwanaland reflected in transgressive- regressive depositional sequences in Euramerica, Geol. Soc. Am. Bull., 98(4), 475–487, doi:10.1130/0016-7606(1987)98<475:LPGEIG>2.0.CO;2, 1987.

Veizer, J. and Prokoph, A.: Temperatures and oxygen isotopic composition of Phanerozoic oceans, Earth-Science Rev., 146, 92–104, doi:10.1016/j.earscirev.2015.03.008, 2015.

Wade, D. C., Luke Abraham, N., Farnsworth, A., Valdes, P. J., Bragg, F. and Archibald, A. T.: Simulating the climate response to atmospheric oxygen variability in the Phanerozoic: A focus on the Holocene, Cretaceous and Permian, Clim. Past, 15(4), 1463–1483, doi:10.5194/cp-15-1463-2019, 2019.

Waterhouse, J. B. and Shi, G. R.: Evolution in a cold climate, Palaeogeogr. Palaeoclimatol. Palaeoecol., 298(1–2), 17–30, doi:10.1016/j.palaeo.2010.08.022, 2010.

White, J. D., Montanez, I. P., Wilson, J. P., Poulsen, C. J., Mcelwain, J. C., DiMichele, W. A., Hren, M. T., Macarewich, S., Richey, J. D. and Matthaeus, W. J.: A process-based ecosystem model (*Paleo*-BGC) to simulate the dynamic response of Late Carboniferous plants to elevated O_2 and aridification, Am. J. Sci., 320(September), 122–136, doi:10.2475/09.2020.01, 2020.

Wilson, J. P., White, J. D., Dimichele, W. A., Hren, M. T., Poulsen, C. J., McElwain, J. C. and Montañez, I. P.: Reconstructing Extinct Plant Water Use for Understanding Vegetation–Climate Feedbacks: Methods, Synthesis, and a Case Study Using the Paleozoic-Era Medullosan Seed Ferns, Paleontol. Soc. Pap., 21, 167–196, doi:10.1017/s1089332600003004, 2015.

Wilson, J. P., Montañez, I. P., White, J. D., DiMichele, W. A., McElwain, J. C., Poulsen, C. J. and Hren, M. T.: Dynamic Carboniferous tropical forests: new views of plant function and potential for physiological forcing of climate, New Phytol., 215(4), 1333–1353, doi:10.1111/nph.14700, 2017.

Winguth, A. M. E., Heinze, C., Kutzbach, J. E., Maier-Reimer, E., Mikolajewicz, U., Rowley, D., Rees, A. and Ziegler, A. M.: Simulated warm polar currents during the middle Permian, Paleoceanography, 17(4), 9-1-9–18, doi:10.1029/2001pa000646, 2002.

Winguth, A. M. E., Thomas, E. and Winguth, C.: Global decline in ocean ventilation, oxygenation, and productivity during the Paleocene-Eocene Thermal Maximum: Implications for the benthic extinction, Geology, 40(3), 263–266, doi:10.1130/G32529.1, 2012.

Winguth, C. and Winguth, A. M. E.: Simulating Permian–Triassic oceanic anoxia distribution : Implications for species extinction and recovery, Geology, (2), 127–130, doi:10.1130/G32453.1, 2012.

Woodard, S. C., Thomas, D. J., Grossman, E. L., Olszewski, T. D., Yancey, T. E., Miller, B. V., Raymond, A., Olszewski, T. D., Yancey, T. E., Grossman, E. L., Woodard, S. C. and Raymond, A.: Radiogenic isotope composition of Carboniferous seawater from North American epicontinental seas, Palaeogeogr. Palaeoclimatol. Palaeoecol., 370, 51–63, doi:10.1016/j.palaeo.2012.11.018, 2013.

Zhang, R., Follows, M. J., Grotzinger, J. P. and Marshall, J.: Could the Late Permian deep ocean have been anoxic?, Paleoceanography, 16(3), 317–329, 2001.

Chapter 2 Glacial-interglacial Controls on Ocean Circulation and Temperature During the Permo-Carboniferous

Co-author: Christopher J. Poulsen

2.1 Abstract

The apex of Earth's penultimate icehouse during the latest Carboniferous to early Permian coincided with dramatic glacial-interglacial fluctuations in atmospheric CO_2, sea level, and high-latitude ice. Global transformations in marine fauna also occurred during this interval, including a rise to peak foraminiferal diversity, suggesting that glacial-interglacial climate change impacted marine ecosystems. Nevertheless, changes in glacial-interglacial ocean circulation and temperature over the Permo-Carboniferous and their influence on marine ecosystem change are largely unknown. Here, we present simulations of glacial and interglacial phases of the latest Carboniferous to early Permian using the Community Earth System Model version 1.2 to provide estimates of global superocean circulation and temperature during this interval. We characterize general patterns of glacial and interglacial surface ocean circulation, temperature, and salinity, and compare them to the documented abundance and distribution of Permo-Carboniferous marine fauna as well as a pre-industrial climate simulation. We then explore how glacial-interglacial changes in atmospheric CO_2, sea level, and high-latitude ice extent impact thermohaline circulation. We find that glacial-interglacial changes in equatorial surface temperatures are consistently ~3–6°C, supporting the notion of climatically buffered tropics (25°C±5°C) as opposed to substantially cooler glacial tropical oceans (up to 10°C) compared to the Late Pleistocene icehouse. Ocean circulation is stronger overall in the glacial simulation, particularly as lower atmospheric CO_2 enables deep convection in the Northern Hemisphere. Wind-driven circulation, heat transport, and upwelling intensity are stronger overall in the late Pennsylvanian superocean relative to the pre-industrial oceans at the same level of atmospheric CO_2. We also find that CO_2-induced glacial conditions of the early Permian may

have promoted foraminiferal diversity through increased thermal gradients and suppressed riverine input in marine shelf environments.

2.2 Introduction

During the Late Paleozoic Ice Age (LPIA; ~340 to 290 Ma), the Earth's penultimate icehouse, proxy reconstructions document a broad synchroneity between shifts in atmospheric pCO_2, high-latitude glaciation, glacioeustasy, and restructuring of paleotropical biomes across the supercontinent Pangaea, supporting hypothesized greenhouse gas forcing of sub-million-year glacial-interglacial cycles during this interval (Montañez et al., 2016; Richey et al., 2020). Relatively elevated late Pennsylvanian atmospheric CO_2 levels (~515 ppm) dropped substantially across the Carboniferous–Permian boundary (i.e., 298.9 Ma) to a 10 Myr nadir (~300–290 Ma) with CO_2 concentrations of ~180 to < 400 ppm (Richey et al., 2020). This low CO_2 interval in the earliest Permian coincides with renewed glaciation and maximum ice sheet extent, marking the apex of the late Paleozoic glaciation (Fielding et al., 2008; Isbell et al., 2012; Montañez and Poulsen, 2013; Soreghan et al., 2019) and an associated drawdown of sea level archived in paleotropical successions world-wide (Eros et al., 2012).

Glacial-interglacial changes in surface ocean circulation, temperature, and seasonality of the late Pennsylvanian–early Permian have been inferred from paleogeographic distributions and geochemistry of climate-sensitive marine fauna (e.g., Clapham, 2010; Reid et al., 2007). Global distributions of Permian brachiopod genera have been used to identify three major global marine biomes, including polar, temperate, and tropical, that are each characterized by a distinct association of biota and reflect the first-order control of regional climate and latitudinal temperature gradients on their distribution (Magazine, 1976; Shi and Waterhouse, 2010; Waterhouse and Bonham-Carter, 1975). The aerial expansion and contraction of these three biomes over time has been qualitatively related to secular changes in ocean temperature and thus the waxing and waning of high-latitude ice sheets (Shi and Waterhouse, 2010). Nevertheless, the response of equatorial sea surface temperatures (SSTs) to changes in high-latitude glaciation during the Permo-Carboniferous remains debated, with some records of brachiopod $\delta^{18}O$ supporting climatically buffered tropical oceans with less seasonality (Powell et al., 2009), while other brachiopod Mg/Ca and $\delta^{18}O$ values have been used to argue for tropical SSTs that were significantly colder (up to 10°C) than their modern counterparts (Giles, 2012). These proxy records suggest that tropical SSTs during the LPIA experienced much larger oscillations than

during glacial-interglacial cycles of the Late Pleistocene (~2–3°C ± 0.5°C) (Ballantyne et al., 2005; Monteagudo et al., 2021). Reconstructing palaeoceanographic events from the fossil record, however, is limited by relatively poor correlation between temperature changes and biotic reorganizations (Boersma and Premoli Silva, 1983), as minor reductions in surface temperature can represent a several-fold increase in trophic resources (Hallock et al., 1991), and by the fragmentary paleogeographic distribution of fossil remains that are often restricted to shallow coastal environments (Peters and Husson, 2017). These limitations complicate the interpretation of marine proxy records and may contribute to the difficulty of relating climate change to region-to-global trends in marine biodiversity during the LPIA.

Contrary to earlier theories of sustained low biodiversity and evolutionary turnover rates in marine ecosystems during the LPIA (McGhee et al., 2012; Powell, 2005; Stanley and Powell, 2003), high temporal resolution marine biodiversity curves indicate a dramatic increase in marine species and genus richness from the late Visean of the Carboniferous to a peak value in the early Permian (Asselian; ~294.19 Ma), now known as the Carboniferous–earliest Permian marine Biodiversification Event (CPBE) (Fan et al., 2020; Shi et al., 2021). The main radiation episode of the CPBE (i.e., Bashkirian–late Asselian) during which species richness quickly increased by 140% and climatic shift into the 10-Myr CO_2 nadir with peak late Paleozoic glacial conditions are broadly contemporaneous. Nevertheless, published information about the influence of climate change on marine ecosystems during the latest Carboniferous–early Permian is limited.

The superocean surrounding the Pangaean supercontinent, the Panthalassic Ocean, has been the focus of many climate modeling studies that propose mechanisms for the Permo-Triassic mass extinction (Kiehl and Shields, 2005; Kutzbach and Ziegler, 1993; Smith et al., 2004; Winguth et al., 2002, 2012; Zhang et al., 2001). These studies have provided estimates of ocean temperatures, heat transport, and circulation patterns in the Panthalassic Ocean over a wide range of atmospheric pCO_2. Nevertheless, they highlight the dependence of simulated Pangaean ocean dynamics on the model configuration and boundary conditions (e.g., ocean basin shape), suggesting that patterns of circulation and temperature with a single, hemispherically symmetrical landmass or under more realistic mid-late Permian environmental conditions differ from that of the late Paleozoic icehouse. While the latest Carboniferous–early Permian has been a focal period for paleoclimate simulations, most studies have employed climate model

configurations with slab ocean components that simulate ocean heat transport but do not incorporate a complete representation of ocean dynamics (e.g., Horton et al., 2010; Poulsen et al., 2007). The few previous climate modeling studies that have discussed ocean circulation during the LPIA have focused on specific coastal regions for proxy-model comparison (Macarewich et al., 2021; Sardar Abadi et al., 2019) or changes in ocean heat transport under changing atmospheric pCO_2 and pO_2 (Wade et al., 2019).

Here, we present Earth system model simulations of glacial and interglacial phases of the latest Carboniferous–early Permian that not only reproduce the temperature and circulation patterns inferred from Permo-Carboniferous marine fauna, but also provide potential climatic mechanisms for marine faunal diversification during this interval. We first compare simulated spatial variations in surface ocean temperature and circulation with published work on the distribution and abundance of climate-sensitive marine fauna over the globe. We then explore the response of global runoff, salinity, and thermohaline circulation to glacial-interglacial changes in atmospheric CO_2, sea level, and high-latitude ice extent. Finally, we propose a climatic mechanism for foraminiferal diversification during the Permo-Carboniferous.

2.3 Methods

2.3.1 Model description

The simulations are performed with the fully coupled Community Earth System Model version 1.2 (CESM), a global climate model that has been widely used for future climate prediction and modern climate studies (Hurrell et al., 2013). Coupled simulations using CESM version 1.2 have been found to compare well to temperature proxies from the Last Glacial Maximum (Zhu et al., 2021) and even an improvement in temperature proxy-model agreement compared to prior climate simulations of the Eocene (Zhu et al., 2019). The fully coupled configuration of CESM includes the Community Atmosphere Model version 5 (CAM), Community Land Model version 4 (CLM), Parallel Ocean Model version 2 (POP), and Sea Ice Model version 4 (CICE) components (Brady et al., 2019). CAM and CLM have a 1.9°×2.5° horizontal resolution with 30 vertical levels. POP and CICE have a nominal 1° horizontal resolution. iPOP has 60 vertical levels with 10 m resolution in the top 15 levels that increase to 250 m resolution for the deepest ocean. Vertical mixing is represented using the modified K-

Profile Parameterization scheme (Danabasoglu et al., 2006) with a horizontally constant background diffusivity of 0.1×10^{-4} m^2 s^{-1} to accommodate the deep time paleogeography. The Gent-McWilliams scheme with diagnostically evaluated isopycnal diffusivity, as described in Danabasoglu et al. (2012), is used as the lateral closure with upper ocean isopycnal diffusivity values up to 3000 m^2 s^{-1}. The horizontal diffusivity coefficient is also set to 3000 m^2 s^{-1} in the surface diabatic layer. A detailed description of the ocean model can be found in Danabasoglu et al. (2012).

2.3.2 Experimental design

We perform two simulations of late Pennsylvanian glacial and interglacial simulations that are each run for ~2,500 years with a fully dynamic ocean model (POP). At the end of the integration, the simulations have reached quasi-equilibrium in the deep ocean, as characterized by time series of temperature and meridional overturning circulation (MOC; Figure S2.1). The glacial and interglacial simulations include the same continental distribution of a late Pennsylvanian (300 Ma) paleogeography (Domeier and Torsvik, 2014), deep ocean bathymetry, treatment of aerosols, and solar luminosity. Deep ocean bathymetry includes an idealized mid-ocean ridge system defined by accretion zones in the Gplates tectonic reconstruction at 300 Ma (www.gplates.com; Figure 2.1). Mid-ocean ridge crests have a uniform depth of 2,500 m based on the present-day global average (NOAA, 2021). Elsewhere the abyssal seafloor has a uniform depth of 4,000 m and continental shelves at 60 m depth. Aerosol distributions are zonally averaged separately for land and ocean from pre-industrial levels following the procedure outlined by Heavens et al. (2012). We use a modern Earth orbital configuration, and the total incoming solar irradiance is reduced to a late Pennsylvanian value of 1333 W m^{-2} (97.5% of present), following Gough (1981).

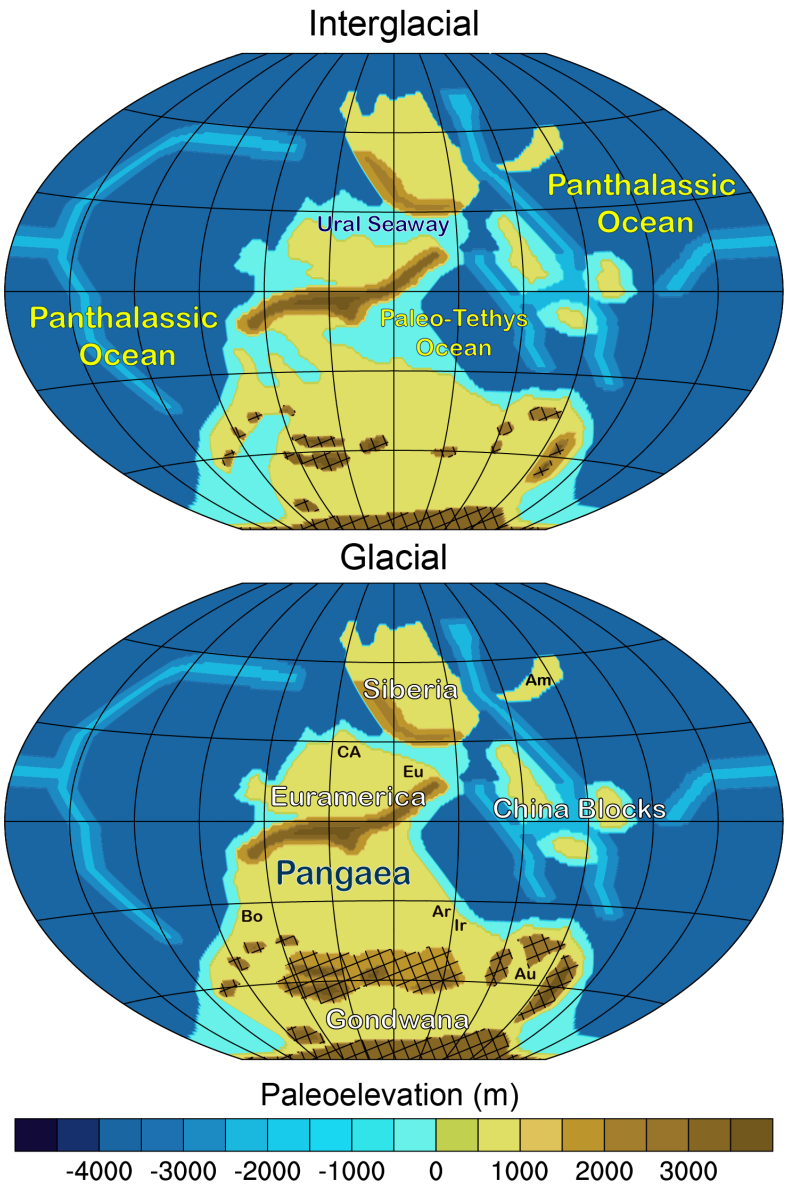

Figure 2.1 Paleogeographic reconstruction used in the glacial and interglacial simulations. Reconstructions are based on Domeier and Torsvik (2014). Cross-hatched areas indicate regions with prescribed land ice. Abbreviated continental units: Amuria, Am; Canadian Artic, CA; Europe, Eu; Bolivia, Bo; Arabia, Ar; Iran, Ir; Australia, Au.

The late Pennsylvanian glacial and interglacial simulations differ with respect to atmospheric pCO_2, tropical vegetation, ice sheets, and sea level to represent key differences between interglacial highstand and glacial lowstand conditions during the late Pennsylvanian. Interglacial and glacial atmospheric CO_2 concentrations were specified as 560 ppm and 280 ppm, respectively, based on a multi-proxy (10^3–10^4 yr resolution) CO_2 reconstruction (Montañez et al., 2016; Richey et al., 2020). In the absence of proxy data, other greenhouse gas concentrations

are set to their pre-industrial values. The distribution of prescribed vegetation follows the mid-late Pennsylvanian biomes for interglacial and glacial phases (Wilson et al., 2017), where the closest possible composition of modern plant functional types is chosen to represent each biome. The prescribed land ice geographies for glacial and interglacial simulations are based on reconstructions of paleo-glacier extent and ice stream pathways constrained by Carboniferous glacial features and deposits from high-latitude southern Gondwana as well as their and detrital zircon U-Pb geochronology (Griffis et al., 2018, 2019). We compare the late Pennsylvanian glacial and interglacial simulations with a published pre-industrial simulation using the same version of CESM (Zhu et al., 2019) to evaluate differences in late Pennsylvanian climate, including temperature patterns, ocean circulation, and meridional heat transport, from the present day.

To differentiate the influences of atmospheric CO_2, sea level, and Gondwanan ice extent on the surface climate factors that control deep-water formation in the South Panthalassic Ocean, we ran four additional simulations for 60 years with a slab ocean model (SOM). The glacial–SOM and interglacial–SOM simulations are identical to the fully-coupled glacial and interglacial simulations, respectively, except for the replacement of a dynamic ocean with the SOM. These two simulations capture the same general surface climate as the fully coupled glacial and interglacial simulations, including SSTs and near-surface zonal winds (Figure S3). We compare these cases with two sensitivity simulations: interglacial–SOM–lowSL simulation, which includes the same boundary conditions as the interglacial–SOM run with the exception that sea level is lowered as in the glacial–SOM run, and glacial–SOM–2×CO_2, which includes the same boundary conditions as the glacial–SOM run with the exception that atmospheric CO_2 is 560 ppm as in the interglacial–SOM run. Differences between interglacial–SOM and interglacial–SOM–lowSL isolate the impact of sea level, and specifically the land-ocean configuration, on surface climate. Similarly, differences between glacial–SOM and interglacial–SOM–2×CO_2 isolate the impact of atmospheric CO_2 on surface climate.

Results presented in the following sections are averaged over the last 100 years of glacial and interglacial simulations to provide climatologies that remove interannual and interdecadal variability. Results from the SOM simulations are averaged over the last 30 years. We first describe general characteristics of the surface climate, ocean heat transport, and wind-driven circulation and compare each aspect with an analogous pre-industrial simulation. We then

characterize glacial-interglacial changes in thermohaline circulation and major water masses. We then compare our results with previous late Paleozoic modeling studies as well as surface current configurations and temperatures reconstructed from climate-sensitive marine fauna. Finally, we propose some potential climatic mechanisms for marine biodiversification over the latest Carboniferous–earliest Permian.

2.4 Results

2.4.1 Surface climate and ocean heat transport

The global-average surface ocean (upper 100 m) temperature of the glacial and interglacial simulations reaches 15.8 and 20.5°C, respectively. Mean annual SSTs are uniformly ~3–6°C warmer in the interglacial case than in the glacial case (Figure S2.2), and thus the glacial and interglacial equator-to-pole upper ocean temperature differences are similar (~23 and 25°C, respectively; Figure S2.6). The global-average SST in the pre-industrial simulation (16.8°C) is comparable to the glacial case due to similar levels of atmospheric CO_2 (~280 ppm), but slightly warmer due to ~2.5% enhanced solar luminosity. The glacial case has a smaller equator-to-pole ocean temperature difference than the pre-industrial case (~28°C) because of cooler equatorial SSTs associated with an expanded equatorial cold tongue. Like the modern equatorial Pacific, trade wind divergence in the eastern equatorial Panthalassic drives coastal upwelling along the coast of western Pangaea, forming an east-west temperature gradient with a cold tongue of SSTs in the eastern equatorial Panthalassic and warm pool in the western equatorial Panthalassic and Paleo-Tethys (Figure 2a and d). The glacial Panthalassic equatorial cold tongue is expanded compared to that of the pre-industrial Pacific because of overall stronger low-latitude wind stress (Figure S2.14). The Paleo-Tethys warm pool has maximum upper ocean temperatures of 27.9 and 33.1°C in the glacial and interglacial simulations, respectively, compared to upper ocean temperatures of up to 29.6°C in the Pacific warm pool of the pre-industrial simulation.

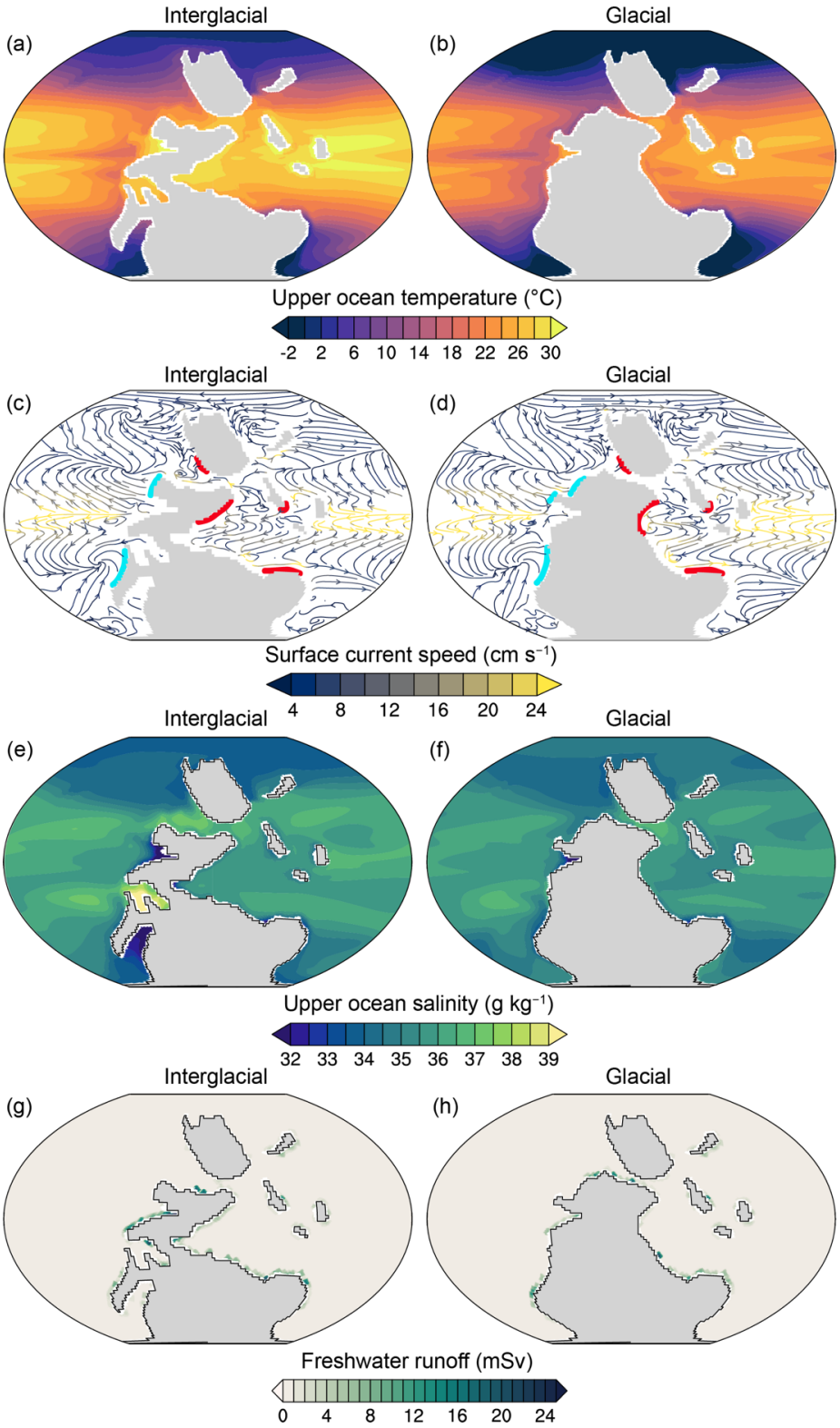

Figure 2.2 Mean annual conditions in the upper ocean (top 100 m). Upper ocean temperatures (a, b), surface current streamlines and speed (colors), continuous (light blue) and seasonal (red) coastal upwelling zones indicated with thick lines (c, d), upper ocean salinity (e, f), and freshwater runoff (g, h) in the glacial and interglacial cases, respectively.

Oceans react to excess radiation at low latitudes and the deficit at high latitudes by transporting heat from the equator towards the poles. Ocean heat transport is primarily driven by wind-driven gyres and deep circulation associated high-latitude convection (Ferrari and Ferreira, 2011). The Earth's climate is very sensitive to perturbations in ocean heat transport, as relatively small increases in ocean heat transport can cause tropical cooling, polar warming, loss of sea ice, and flatter meridional temperature gradients (Herweijer et al., 2005; Pollard and Thompson, 1993; Smith et al., 2004). In our simulations, ocean heat transport in the Southern Hemisphere is similar between the glacial and interglacial simulations, whereas more heat is transported northward in the glacial case between ~20–60°N due to both stronger wind-driven subtropical gyre circulation (Figure S2.6) and deep convection (Figure 2.3d) in the North Panthalassic. While the glacial and pre-industrial simulations have similar meridional heat transport in the North Hemisphere, the pre-industrial case transports ~50% less heat in the Southern Hemisphere. The size of the ocean basin does not account for this difference in heat transport, as a relatively higher proportion of land in the Southern Hemisphere during the late Pennsylvanian results in ~32% smaller ocean volume in the glacial case compared to the pre-industrial. Rather, relatively stronger subtropical gyre circulation (Figure S2.6) and deep convection (Figure 2.3d) in the Southern Hemisphere of the glacial case likely account for stronger southward heat transport in the ocean. Global patterns of surface circulation are generally similar between the glacial and interglacial simulations, with some key differences in the northern polar latitudes as described below.

2.4.2 Tropical gyres, subtropical gyres, and upwelling zones

Prevailing equatorial easterlies and westerlies near 50°N and S form a set of subtropical gyres in the Panthalassic Ocean in each case (Figure 2.2a and b), where the barotropic stream function is 10–20 Sv stronger in the glacial case compared to the interglacial case (Figure S2.12). The Panthalassic Ocean spans an entire hemisphere (i.e., ~2.3× the area of the Pacific Ocean) and produces subtropical gyres that are >40 Sv stronger than that of the pre-industrial Pacific or Atlantic. Eastern boundary currents along the coasts of northwest Pangaea and western Gondwana coincide with robust upwelling zones in the glacial and interglacial simulations (Figure 2c and d), as indicated by meridional wind stress values of up to –18.9 and –19.8 N m^{-2} along northwest Pangaea and 22.2 and 15.3 N m^{-2} along western Gondwana, respectively (Figure

S2.14f and h). Although upwelling intensity is relatively stronger in the late Pennsylvanian cases compared to the pre-industrial, coastal upwelling along western Africa is comparable to northwest Pangaea, with meridional wind stress values of up to –17.0 and 16.6 N m^{-2} along western and southern Africa, respectively (Figure S2.14e, f, g).

In the Paleo-Tethys Ocean, equatorial winds drive two relatively smaller tropical gyres. The southern tropical gyre in the Paleo-Tethys Ocean features a strong western boundary current (~60 cm s^{-1}) that carries warm equatorial surface waters (~20°C and ~24°C in the glacial and interglacial cases, respectively) southward along the northeastern margin of Gondwana (present-day central Iran; Figure 2.2). Conversely, the relatively weaker eastern boundary current of the South Panthalassic Ocean transports cool polar waters (~12°C and ~18°C in the glacial and interglacial cases, respectively) along the southwestern coast of Gondwana (present-day Bolivia) towards the equatorial realm. At the same general paleolatitude (~30°S), these regional differences in ocean circulation produce mean annual glacial and interglacial SST differences of 8°C and 6°C, respectively, between the eastern and western coasts of southern Gondwana. Following the direction of circulation in the southern gyre, relatively warm waters in the eastern Paleo-Tethys transition to cold waters along the southeastern margin of Gondwana (present-day India and Australia) in the glacial and interglacial cases due to the presence of strong seasonal upwelling along the southern margin of the Paleo-Tethys Ocean (Figure 2.2c and d). Zonal wind stress values of up to 29.9 and 25.2 N m^{-2} drive upwelling along the coast of northeastern Australia during austral winter (Figure S2.14b). In the North Paleo-Tethys, warm equatorial surface waters are transported towards the northwest North American craton, leading to mixing with relatively cold paleo-Artic waters in the Ural Seaway in the interglacial case (Figure 2.2c). In the glacial case, relatively low sea level and weak easterly wind stress in the region inhibits the westward transport of warm waters from the Paleo-Tethys across the Ural Seaway.

2.4.3 Subpolar gyres, polar gyres, and meridional overturning circulation

The poleward transport of salt towards sites of deep convection is an important source of climate variability, as changes in regional buoyancy and density stratification can influence the formation of dense waters which form the lower limb of thermohaline circulation (Koul et al., 2020). With respect to the modern North Atlantic, the size and strength of subpolar gyre circulation has emerged as one of the most important sources of interannual to decadal variations in regional salinity (Koul et al., 2020). The strength and size of the subpolar gyre impacts

regional salinity by modulating the proportion of subpolar and subtropical waters reaching the subpolar sites of deep convection in the North Atlantic. As a result, local air-sea fluxes (Holliday, 2003) and the Atlantic MOC (Häkkinen et al., 2011) play a minor role in regional salinity variations. During the late Pennsylvanian, the mechanisms controlling salinity variations in sites of deep convection have not been studied.

In our glacial and interglacial simulations, cyclonic wind stress curl due to the change in wind direction from westerlies at ~50°N and S to polar easterlies drives subpolar gyres in the North and South Panthalassic. In the southern subpolar gyre, the mean annual depth-integrated volume transport is ~10 Sv stronger in the glacial case compared to the interglacial case (Figure S2.12). Cool waters in the South Panthalassic (60–90°S) of the glacial (interglacial) simulation allow for the formation of annual (seasonal) sea ice cover along the southern coast of Gondwana. Relatively higher runoff enters the polar region of the South Panthalassic in the interglacial case (annual total of 149.1 mSv compared to 75.6 mSv) and thus mean annual sea surface salinity over continental shelfs from 60–90°S is 33.63 g kg^{-1} compared to 34.99 g kg^{-1} in the glacial case (Figure 2.1). Despite higher freshwater runoff, weaker subpolar gyre circulation in the interglacial case enhances the southward transport of warm, salty equatorial waters by the subtropical gyre to the polar region (Figure S2.8a and b), resulting in higher open ocean salinities in the interglacial compared to the glacial case (i.e., mean annual sea surface salinities of 35.03 g kg^{-1} and 34.64 g kg^{-1} in the open ocean from 60–90°S, respectively). A temperature- and salt-advection feedback causes a winter-spring deepening of the mixed-layer depth associated with a large area of deep-water formation along the continental shelf of southern Gondwana (Figure S2.8c and d). The relatively higher open ocean salinities of the interglacial case reduce surface buoyancy and stratification, driving more robust deep-water formation in terms of areal extent, duration, and depth reached by sinking waters compared to the interglacial case (Figure S2.7). Sinking waters in the South Panthalassic drive a strong overturning cell in the Southern Hemisphere, with a maximum of ~18 Sv (16 Sv) around 65°S and 2000 m depth, and whose lower limb extends to approximately 30°N (30°S) at depths of ~3,500 m in the interglacial (glacial) case (Figure 2.3c and d). The magnitude of the southern MOC cell is similar to that of the North Atlantic MOC in the pre-industrial simulation (~18 Sv; Figure 2.3e). This link between the spatiotemporal extent of deep-water formation and the subpolar gyre strength in the late

Pennsylvanian simulations is reminiscent of that in the modern North Atlantic (e.g., Koul et al., 2020).

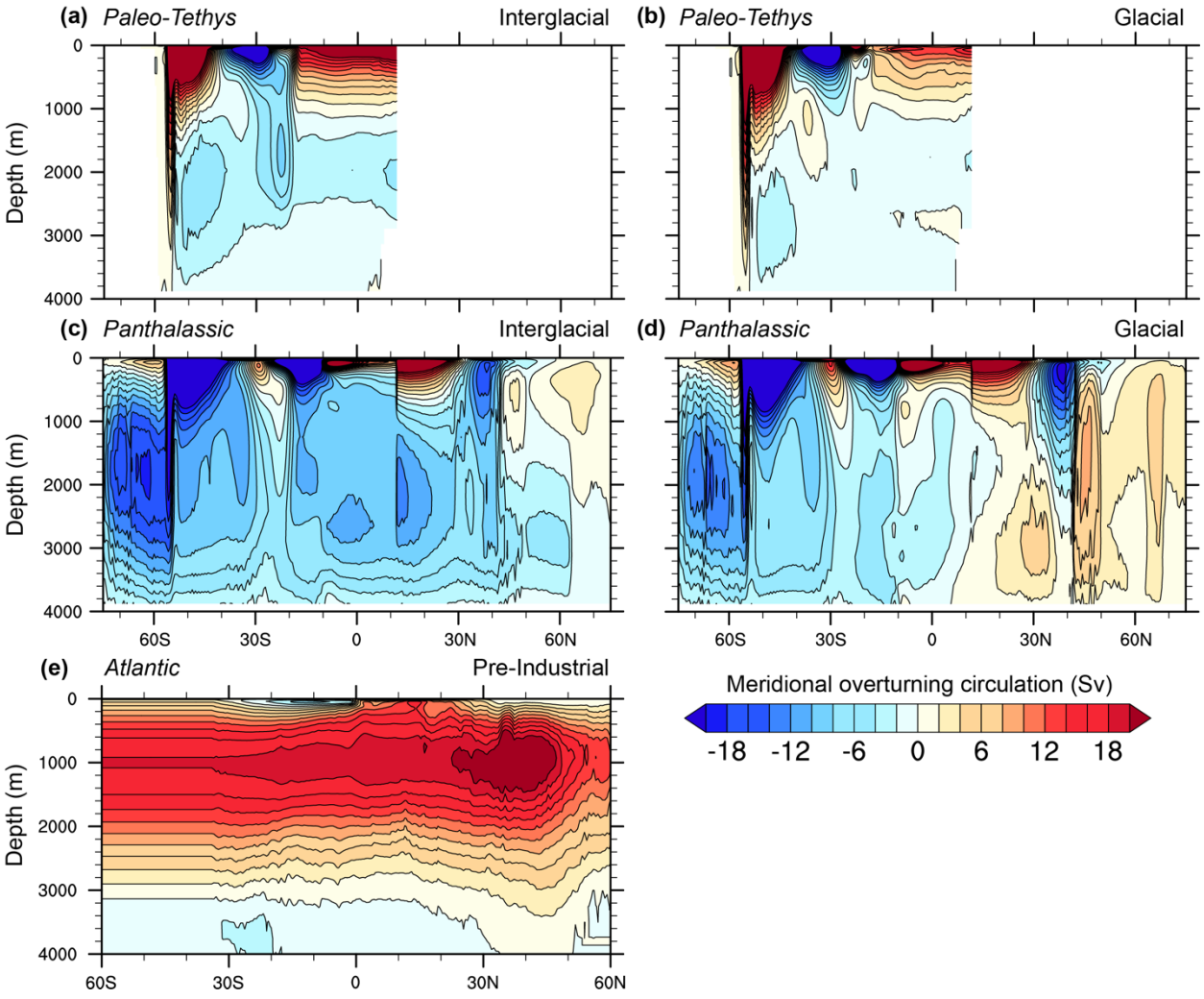

Figure 2.3 Meridional overturning circulation (MOC). MOC in the Paleo-Tethys Ocean (a, b) and Panthalassic Ocean (c, d) for the interglacial and glacial cases, respectively. MOC in the Atlantic Ocean (e) for the pre-industrial case.

As in the present-day North Atlantic, the strength of the South Panthalassic subpolar gyre is driven primarily by the variability in wind stress curl above the subpolar South Panthalassic. To determine the mechanism responsible for a stronger subpolar gyre and thus weaker South Panthalassic deep-water formation in the glacial case, we compare the strength of the prevailing westerly winds at 35–40°S between glacial–SOM, interglacial–SOM, glacial–SOM–2×CO_2, and interglacial–SOM–lowSL (Figure S2.3c). As in the fully coupled simulations, glacial–SOM exhibits stronger surface winds at 35–40°S than the interglacial–SOM simulation (Figure S3b).

Nearly identical surface wind patterns at 35–40°S between glacial–SOM and glacial–SOM–2×CO_2 simulations indicate that atmospheric CO_2 level plays a minor role in subpolar gyre strength (Figure S3c). The interglacial–SOM–lowSL case has wind speeds that are similar to those in the glacial–SOM case, suggesting that lower sea level (i.e., higher land-to-sea ratio) in the glacial simulation is the primary cause of the strong winds and subpolar gyre in the South Panthalassic.

In the northern subpolar gyre, the barotropic stream function is ~20–30 Sv stronger in the glacial case compared to the interglacial case (Figure S2.12). In the absence of a landmass over the North Pole, a polar gyre also forms but with cyclonic and anticyclonic circulation in the glacial and interglacial cases, respectively (Figure 2.2c and d). Annual sea ice cover forms over the North Pole in the glacial case and extends to ~60°N during the winter, whereas relatively warm surface waters (>0°C) in the interglacial case prevent the North Panthalassic from freezing (Figure S2.9a and b). A semi-permanent low-pressure center over the North Pole drives cyclonic winds in the glacial and interglacial cases (Figure S2.5). A lower meridional temperature gradient in the atmosphere of the interglacial case (Figure S2.6) produces weaker cyclonic winds at the North Pole relative to the glacial case, allowing for the formation of an anticyclonic polar gyre. In addition to the absence of sea ice and relatively higher precipitation over the ocean, relatively low sea surface salinities in the northern polar region of the interglacial case (i.e., mean annual surface salinities from 60–90°N of 33.87 g kg^{-1} and 34.38 g kg^{-1} in the interglacial and glacial cases, respectively) are promoted by Ekman pumping of anticyclonic circulation that creates a freshwater reservoir near the North Pole (like the Beaufort Gyre in the present-day Arctic Ocean). Low polar salinities in the interglacial case increase the surface buoyancy and stratification, preventing deep convection from occurring in the North Panthalassic. As a result, Panthalassic MOC is comprised of one large overturning cell driven by sinking water in the Southern Hemisphere (Figure 2.3d). In the glacial case, relatively high polar salinities and cold temperatures lead to two regions of deep-water formation in the North Panthalassic Ocean, one over the North Pole and one along the northern coast of Amuria (present-day northeast Asia; Figure S2.9d). Sinking North Panthalassic waters in these two regions drive two overturning cells in the Northern Hemisphere, with maximum values of 8 and 10 Sv around 65°S and 45°S, respectively, at ~1,500 m depth (Figure 2.3c).

Simulated glacial-interglacial changes in ocean circulation produce differences in the composition and structure of major oceanic water masses. Using a temperature-salinity analysis of the glacial and interglacial simulations, we identify two major intermediate water masses (1,500–2,500 m depth): (1) North Panthalassic Intermediate Water (NPIW) with a salinity of 34.85–35.06 g kg^{-1} (34.95–35.13 g kg^{-1}) and temperature of −1 to 1°C (~4 to 7°C) in the glacial (interglacial) case and (2) South Panthalassic Intermediate Water (SPIW) with a salinity of 34.90–35.09 g kg^{-1} (34.91–35.11 g kg^{-1}) and temperature of −1 to 1°C (~3.5–6°C) in the glacial (interglacial) case. NPIW and SPIW form at ~45°N and 45°S, respectively. We also identify two major deep-water masses (2,500–4,000 m depth): (1) Panthalassic Deep Water (PDW) with a salinity of ~34.9–35 g kg^{-1} in both cases and a temperature of −1.6°C (4°C) in the glacial (interglacial) case and (2) Panthalassic Bottom Water (PBW) with a salinity of ~34.8–34.9 g kg^{-1} in both cases and a temperature of approximately −1.6°C in the glacial case (Figure S2.10). PBW is only present in the glacial case because it is formed by spring-winter time deep convection near Amuria and over the North Pole (Figure S2.9d). PBW travels southward and mixes with PDW near the equator. In the interglacial case, PDW formed in the South Panthalassic flows northward to the deep ocean of the Northern Hemisphere (Figure 2.4). The temperature and salinity ranges of major deep-water masses in the Paleo-Tethys completely overlap with PDW and PBW, suggesting that these deep-water masses formed by cooling in the polar regions flow into the Paleo-Tethys at depth (Figure S2.10).

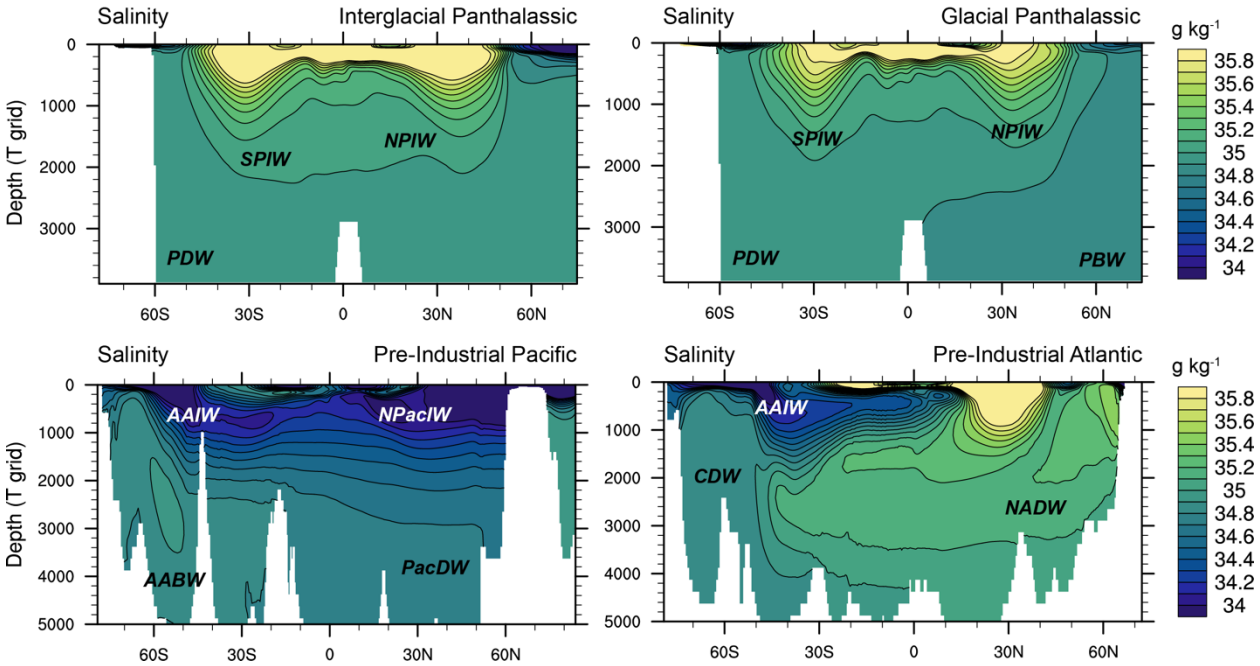

Figure 2.4 Major water masses in the glacial and interglacial simulations. Mean annual salinity (g kg^{-1}) in the Panthalassic Ocean in the glacial and interglacial simulations (top). PDW = Panthalassic Deep Water (34.9–35 g kg^{-1}), PBW = Panthalassic Bottom Water (34.8–34.9 g kg^{-1}), NPIW = North Panthalassic Intermediate Water (~35–35.1 g kg^{-1}), SPIW = South Panthalassic Intermediate Water (~35–35.1 g kg^{-1}). Mean annual salinity (g kg^{-1}) for the Pacific Ocean and Atlantic Ocean in the pre-industrial simulation (bottom). AABW = Antarctic Bottom Water, PacDW = Pacific Deep Water, NADW = North Atlantic Deep Water, AAIW = Antarctic Intermediate Water, NPacIW = North Pacific Intermediate Water.

2.5 Discussion

2.5.1 Comparison to previous modeling results

Patterns of ocean circulation captured in our simulations are broadly consistent with idealized models of Pangaean ocean dynamics that feature a strong westward flowing equatorial current, tropical anticyclonic gyres in the Paleo-Tethys (i.e., when the China Blocks are included), and subpolar cyclonic and subtropical anticyclonic gyres in Panthalassic Ocean (Kiessling et al., 1999; Kutzbach et al., 1990). Idealized ocean simulations with a single, uniform landmass produce overturning circulation that is hemispherically symmetrical (Kutzbach et al., 1990; Smith et al., 2004), whereas a realistic Pangaean configuration has been found to produce highly asymmetrical ocean circulation (Winguth et al., 2002; Winguth and Maier-Reimer, 2005; Zhang et al., 2001). Two general modes of Pangaean thermohaline circulation have been

identified: a vigorous “thermal mode” driven by cooling in the southern polar latitudes during icehouse climate states and a weaker “haline mode” driven by evaporation from the subtropics during greenhouse climate states (Winguth and Maier-Reimer, 2005; Zhang et al., 2001). Our glacial and interglacial simulations support the former “thermal mode” as MOC is driven primarily by a temperature- and salt-advection feedback linked to winter-spring deepening of the mixed-layer depth in the polar regions (Figures S2.8 and S2.9). The glacial case features a relatively stronger southern MOC cell (i.e., comparable in magnitude to pre-industrial MOC in the North Atlantic) compared to that of the North Panthalassic (Figure 2.3), whereas our interglacial simulation features a single, vigorous overturning cell driven by cooling in the Southern Panthalassic. Notably, our glacial and interglacial simulations do not capture the formation of a relatively warm, salty deep-water mass in the subtropics. Deep-water masses formed in the North and South Panthalassic Ocean flow from the polar regions into the Paleo-Tethys and broader equatorial region (Figure S2.10). While the general patterns of ocean circulation captured in our simulations align with previous studies, the response of thermohaline circulation to atmospheric CO_2 exhibits some key differences.

Mid-Permian (Wordian) simulations with a coupled atmosphere-ocean model of intermediate complexity (i.e., atmospheric energy balance model, or EBM, and large-scale geostrophic ocean general circulation model, or LSG) feature stronger MOC with increasing atmospheric CO_2 (Winguth et al., 2002). While relatively cooler SSTs and expanded sea ice in the North Panthalassic allow for deep convection in our glacial case (280 ppm CO_2), large sea ice coverage in the North Panthalassic prevents deepwater formation in the Wordian simulation with 280 ppm CO_2. Wordian simulations with ≥560 ppm CO_2 and relatively less sea ice allow for deepwater formation in the North Panthalassic because of increased sea-to-air heat exchange in the polar region (Winguth et al., 2002). One potential explanation for this discrepancy is that feedback processes associated with the hydrological cycle are not considered in the coupled LSG/EBM (i.e., freshwater flux forcing of the ocean is one-way) (Mikolajewicz and Crowley, 1997). In our glacial simulation, the influences of reduced high-latitude freshwater flux and brine rejection with annual sea ice formation that increase surface salinities and reduce surface buoyancy are essential for deepwater formation in the Northern Panthalassic. Therefore, Northern Panthalassic deepwater formation in the coupled LSG/EBM is primarily produced by thermal feedbacks and does not account for the influence of sea ice on surface salinity or

regional freshwater influx. This discrepancy in the response of thermohaline circulation to atmospheric CO_2 shows the importance of incorporating a more complete representation of Earth system feedbacks in ancient ocean simulations.

Under relatively similar levels of radiative forcing, our late Pennsylvanian glacial and pre-industrial simulations indicate that a superocean produces overall stronger wind-driven circulation, enhanced ocean heat transport, and cooler equatorial temperatures relative to the present-day ocean configuration. Higher surface wind stress drives stronger wind-driven circulation in the glacial Panthalassic compared to the pre-industrial Pacific and Atlantic (Figures S2.12 and S2.14). Nevertheless, circulation strength of the polar gyre in the North Panthalassic is comparable to the pre-industrial Antarctic Circumpolar Current due to the absence of any landmasses that would block their trajectory. In the Southern Hemisphere, ocean heat transport in is up to 0.8 PW greater in the glacial simulation than the pre-industrial simulation (Figure S2.4). More robust deep circulation connected to high-latitude convection in the glacial simulation likely contributes to this increased meridional heat transport (Ferrari and Ferreira, 2011). Ocean simulations of the mid-Permian with 280 ppm CO_2 also support enhanced heat transport in the Southern Hemisphere, with 1.1 PW stronger ocean heat transport at 30°S compared to an analogous present-day simulation (Winguth et al., 2002). The mean annual SST is ~1°C cooler (i.e., in the upper 100 m and 10 m surface layer) in the glacial compared to the pre-industrial simulation, in part because higher equatorial wind stress produces a more extensive tongue of cool SSTs in the glacial case. The mid-Permian simulation with 280 ppm CO_2 also supports cooler SSTs with a superocean, yet the mean annual SST is 3.9°C lower than present-day (Winguth et al., 2002). With relatively similar high-latitude temperatures in the glacial and pre-industrial cases, cooler equatorial SSTs in the glacial simulation produce a lower equator-to-pole temperature difference (Figure S2.6). Nevertheless, the late Paleozoic simulations incorporate reduced solar luminosity (2.5% and 2.1% lower than present-day for the Pennsylvanian and mid-Permian, respectively) with pre-industrial levels of atmospheric CO_2, and thus lower radiative forcing may also play a role in relatively cooler ocean temperatures.

2.5.2 Comparison with climate-sensitive sediments: reconstructions of marine biomes

Global distributions of brachiopod genera have been used to reconstruct three major global marine biomes from the latest Carboniferous through the Permian: tropical, warm temperate, and cold temperate to glacial (Figure 2.5c and d; e.g., Waterhouse, 1977; Waterhouse

and Bonham-Carter, 1975). An assessment of two million brachiopod fossil occurrences has been used to characterize each biome based on a distinct association of biota, shared to some degree with other biomes (Shi and Waterhouse, 2010). The spatial disposition of these marine biomes is broadly parallel to the climatic zonation pattern of the earth at the time, and thus reflects the first-order control of global climate and latitudinal temperature gradients on their distribution, as in the modern ocean. The three biomes expanded and contracted in area over time, a pattern that has been attributed to secular changes in global ocean temperature and thus the waxing and waning of high-latitude ice sheets (Waterhouse, 1977). Over the latest Carboniferous–early Permian transition to the apex of LPIA glaciation, the cold temperate to polar biome expanded towards the equator (from ~50°S to 20°S) and the tropical biome contracted, particularly in the Southern Hemisphere (Figure 2.5c and d). In the Northern Hemisphere, the warm temperate biome covered much of the high-latitudes and shifted southward with cooling as the cold temperate to polar biome stretched down to ~60°N. Our glacial and interglacial simulations generally support the contraction of the tropical biome and expansion of the northern cold temperate to polar biome as zonal mean SSTs cool by ~5°C in the low and northern high latitudes, respectively (Figure S2.6). Furthermore, interglacial SSTs in the North Panthalassic are >0°C and thus do not support sea ice formation (Figure S2.9a). In the glacial simulation, SSTs in this region decrease to below 0°C as far south as ~60°N in the glacial case, supporting widespread annual sea ice formation in the region (Figure S2.9b). Nevertheless, our simulations do not capture overall cooler SSTs in the Southern Hemisphere compared to the Northern Hemisphere, as indicated by more dramatic shifts in marine biomes along the coasts of Gondwana.

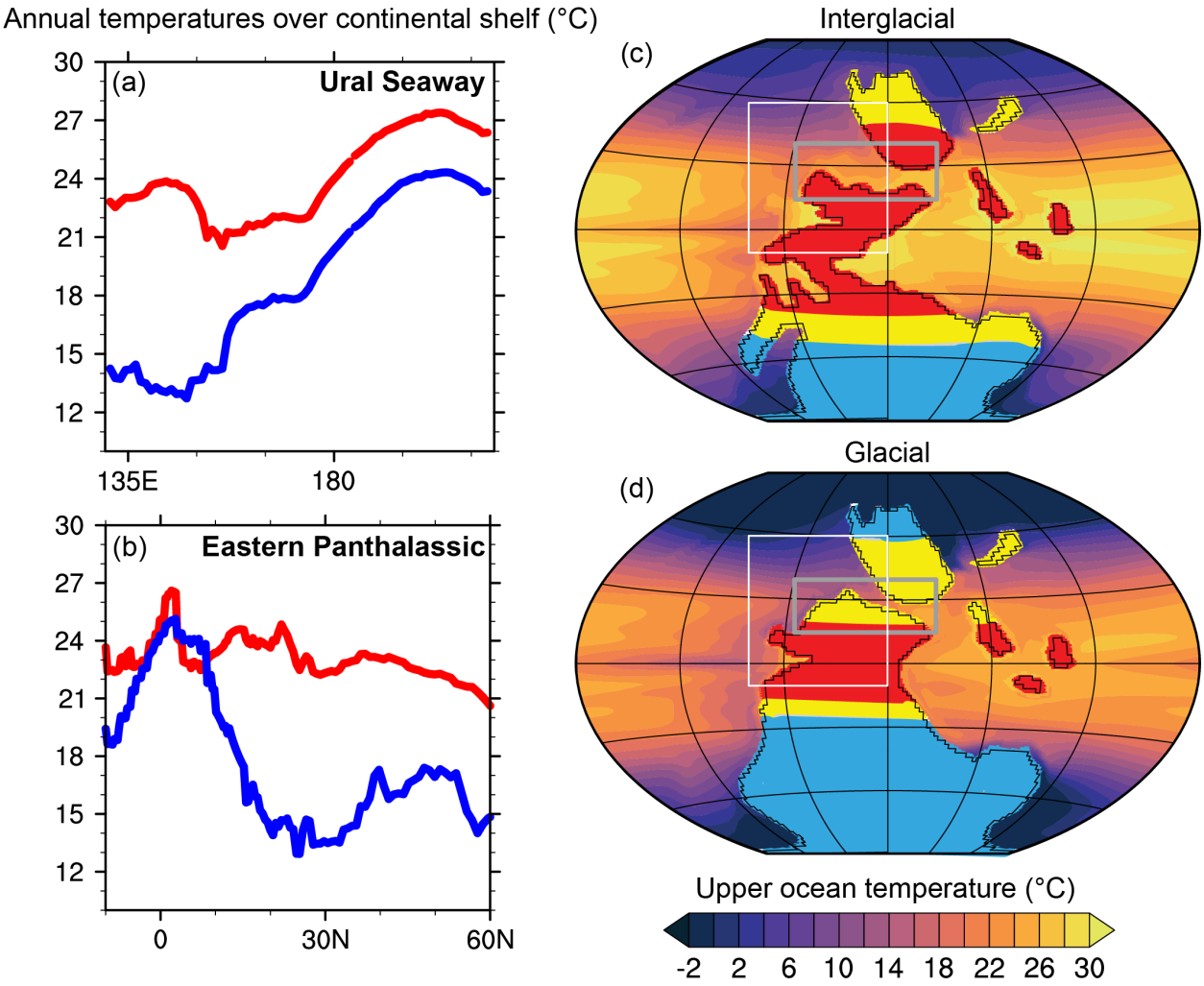

Figure 2.5 Annual temperature patterns over continental shelves. (a) Meridional mean temperatures (°C) in the Ural Seaway for the glacial (blue) and interglacial (red) cases. (b) Zonal mean temperatures (°C) over continental shelves in the eastern Panthalassic Ocean in the glacial (blue) and interglacial (red) cases. Mean annual upper-ocean (top 100 m) temperatures in the (c) interglacial and (b) glacial simulations. Glacial and interglacial land masses are colored according to the palaeolatitudinal extent of the three major marine biomes inferred from brachiopods across the latest Pennsylvanian–early Permian, including tropical (red), warm temperate (yellow), and cold temperate to glacial (blue) (see Figure 2b from Shi and Waterhouse, 2010; Waterhouse, 1977). Boxes outline regions where continental shelf temperatures are averaged (a-b), with the Ural Seaway region shown with gray boxes and eastern Panthalassic region shown with white boxes in the interglacial (c) and glacial (d) cases.

Interhemispheric temperature asymmetry has been acknowledged as an important feature of climate change during the LPIA as most land masses were distributed in the Southern Hemisphere and glaciation was likely restricted to Gondwana (Chumakov and Zharkov, 2003; Shi and Waterhouse, 2010). Our glacial and interglacial simulations capture surface air

temperatures in the southern high-latitudes (60–90°S) that are ~20°C and 30°C colder than that of the northern high-latitudes, respectively, supporting an interhemispheric temperature asymmetry in the atmosphere (Figure S2.6). However, simulated meridional upper (100 m) ocean temperatures, which capture the depth habitat of brachiopods, are roughly symmetric with respect to the palaeoequator (Figure S2.6). If we only consider waters over continental shelves, which may more closely reflect the coastal habitats of the brachiopod genera used to reconstruct major marine biomes (Figure 2.5c and d), upper ocean temperatures in the southern high-latitudes are 1.5°C and 4.7°C cooler than the northern high-latitudes in the glacial and interglacial cases, respectively. Relatively larger shifts in marine biomes in the Southern Hemisphere could also be explained by interhemispheric differences in temperature gradients over continental shelves. In the glacial simulation, water masses over continental shelves in the Southern Panthalassic exhibit an overall lower meridional temperature gradient compared to those in the Northern Panthalassic (Figure S2.13), suggesting that brachiopods of the cold temperate to polar biome in the Southern Hemisphere may have more easily migrated equatorward.

2.5.3 Comparison with climate-sensitive sediments: reconstructions of ocean circulation and temperature

Faunal migration patterns inferred from paleogeographic distributions of climate-sensitive marine fauna, primarily brachiopods and foraminifera, have been used to reconstruct surface spatial temperature patterns and current configurations during the latest Carboniferous–early Permian (e.g., Angiolini et al., 2007; Clapham, 2010; Reid et al., 2007). Relatively small changes in low-latitude shallow-water temperatures inferred from some fossil $\delta^{18}O$ compositions over the Permo-Carboniferous support the hypothesis that the tropics remained climatically buffered throughout this interval (e.g., Angiolini et al., 2009; Buggisch et al., 2008; Mii et al., 2001). These records support the hypothesis that the tropics remained climatically buffered (25°C±5°C), even during the early Permian apex of late Paleozoic glaciation (Montañez and Poulsen, 2013). Alternatively, Permo-Carboniferous brachiopod Mg/Ca and $\delta^{18}O$ values have been used to argue for shallow-water temperatures in the glacial tropics that were significantly colder (up to 10°C) than their modern counterparts (Giles, 2012; Powell et al., 2009). These cooler SSTs would suggest much larger oscillations in surface temperatures during the LPIA than during glacial-interglacial cycles of the Late Pleistocene (~2–3°C±0.5°C) (Ballantyne et al.,

2005; Monteagudo et al., 2021). Our simulations indicate that glacial-interglacial changes in upper ocean temperature in the low-latitudes were consistently ~3–6°C, supporting smaller SST variations in tropical oceans during the LPIA. The only notable exception to this range of glacial-interglacial temperature change is the North America Midcontinent Sea (Figure S2.2). Regional upper ocean temperatures are very similar in the glacial and interglacial simulations, and relatively cool in the interglacial case compared to temperatures along the same latitude, because estuarine-like circulation patterns in the interglacial case that pull cool, upwelled marine waters from the eastern Panthalassic Ocean onto the continental shelf (Macarewich et al., 2021). Ocean temperatures and circulation patterns have also been inferred from paleogeographic patterns of biodiversity during the LPIA.

Functional and taxonomic diversity of marine ecosystems has long been recognized to decline with increasing paleolatitude (Hillebrand, 2004; Willig et al., 2003). A strong positive coupling also exists between biodiversity and temperature changes in present-day marine ecosystems (Antão et al., 2020). As a result, ocean temperatures and currents have been inferred from the paleogeographic distribution of climate-sensitive marine fauna during the late Paleozoic based on the assumption that spatial patterns of biodiversity are primarily driven by temperature variations associated with regional ocean circulation patterns. In the low-latitudes, apparent discrepancies in the distribution of shallow-water benthic foraminifera between North America and Paleo-Tethys basins has been attributed to a strong zonal SST gradient. In the eastern Panthalassic, North American shelves were located at low paleolatitudes during the Pennsylvanian and Permian time but appear to have had temperate paleoclimates as indicated by significantly lower foraminiferal diversity than coeval warm-water faunas in the Paleo-Tethys (Davydov, 2014; Groves and Wang, 2009). Our glacial and interglacial simulations support a strong zonal gradient in equatorial SSTs of ~11°C formed by equatorial winds that drive upwelling and an equatorial Panthalassic cold tongue in the east and a Paleo-Tethys warm pool in the west (Figure 2.2a and d). In the Ural Seaway, brachiopod taxa found in the Sverdrup Basin (present-day northern Canada) as well as European Russia are not found in southwestern North America (Carter and Poletaev, 1998), suggesting that east to west currents in the Ural Seaway influenced the dispersion of brachiopod faunas during the latest Carboniferous (Reid et al., 2007). Our interglacial simulation captures this east to west current that carries relatively warm tropical water from the Paleo-Tethys towards the Arctic (Figure 2.1c).

In the subtropics of the Southern Hemisphere, spatial contrasts in latest Pennsylvanian–early Permian carbonate platforms on the coasts of eastern and western Gondwana have been observed along ~30°S (Sardar Abadi et al., 2019). Carbonate platforms in southwestern Paleo-Tethys (present-day Iran) are defined by warm, shallow-water carbonates as indicated by highly diversified chlorozoan carbonate ecosystems, whereas coeval platforms in the southeastern Panthalassic (present-day Bolivia) contain cool-water carbonates preserving a low-diversity brachiopod and bryozoan assemblage (Sardar Abadi et al., 2019). Sardar Abadi et al. (2019) use fully coupled climate simulations of early Permian glacial environments with a <3.6° ocean grid resolution to propose that contrasting directions of regional ocean circulation produce relatively cold upper-ocean temperatures along western Gondwana compared to that of eastern Gondwana at the same paleolatitude (~30°S). In the climate simulation with 280 ppm CO_2, the western boundary current in the South Paleo-Tethys is relatively weak (~30 cm s^{-1}) but strengthens to 60 cm s^{-1} in simulations with lower global surface temperatures (i.e., lower pCO_2 or higher ice sheet volume), resembling the present-day Gulf Stream. Our glacial and interglacial simulations also capture these regional differences in ocean circulation at ~30°S (Figure 2.2c and d). However, our glacial simulation (280 ppm CO_2) resolves the western boundary current with a magnitude of ~60 cm s^{-1} at relatively higher surface temperatures (Figure S2.11), likely due to finer horizontal grid resolution in the ocean component (~1°). A coarser grid size requires large horizontal momentum diffusion that produces somewhat sluggish ocean circulation in modern simulations when compared to observations (Meehl et al., 1982).

Distributions of early Permian brachiopod assemblages in the Paleo-Tethys, with warm-water taxa along northeastern Gondwana (present-day northern Iran) and coeval cold-water, poorly diversified taxa in eastern Gondwana (present-day Western Australia, India, Oman), have also been used to reconstruct a contracted tropical gyre in the South Paleo-Tethys and a cold surface current along the glaciated northeastern Gondwanan margin (Angiolini et al., 2007). Our glacial and interglacial simulations support the presence of a warm tropical surface current gyre with relatively cold SSTs along the glaciated northeastern Gondwanan margin, but do not capture an opposing cold surface current in the region. Alternatively, we attribute cold SSTs along the glaciated northeastern Gondwanan margin to a coastal upwelling system driven by prevailing westerlies as part of the southern branch of the South Paleo-Tethys subtropical gyre (Figure 2.3a and b). Oceanic upwelling in the region is supported by the dominant macrofossils

of Australian carbonate communities from the early Permian, which comprise a calcitic, fully heterozoan assemblage typical of cold-water carbonate systems, as well as oxygen isotope-based brachiopod temperatures of <9°C that agree well with simulated upper-ocean temperatures in the glacial simulation (Frank et al., 2012). This upwelling hypothesis also aligns with the prolonged deposition of cold-climate indicators in the eastern Australian Permian despite an apparent post-Sakmarian warming elsewhere in Gondwana.

Glacioeugenic sedimentary deposits record the history of glaciation across Gondwana. A suite of dropstones, interpreted as ice-rafted debris, and glendonites throughout the Permian succession of eastern Australia (northeastern Gondwana) indicates that small accumulations of ice persisted in the region after the deglaciation of the rest of Gondwana (Veevers and Powell, 1987). Glendonites in Permian strata of eastern Australia are interpreted to have formed originally in the sediments as the mineral ikaite (Carr et al., 1989). Ikaite formation is prompted by the upwelling of cold, high alkalinity waters that interact with organic rich sediment like those contained within Permian strata deposited along the paleo-coastline of eastern Australia (Isbell et al., 2012; Jones et al., 2006). Simulations of Permian surface wind and ocean circulation patterns have indicated that oceanic upwelling was the cause of locally lowered SSTs (Gibbs et al., 2002; Winguth et al., 2002). However, intermediate complexity climate model simulations that include an LSG ocean component do not explicitly resolve upwelling along the coast southeastern Gondwana because the horizontal resolution (3.5°×3.5°) is too coarse (e.g., Winguth et al., 2002). Our glacial and interglacial simulations capture westerly surface winds that drive upwelling in the region, providing a physical mechanism for the persistence of relatively cold climate in western Australia.

2.5.4 Influence of late Paleozoic climate on the diversification of foraminifera

The CPBE extended for 42.1 Myr from the late Visean to Asselian, with 246% species richness increase dominated by fusulinid foraminifera (Shi et al., 2021). The late Paleozoic biodiversity curve is comprised of fossil records that span a broad paleolatitudinal range, including the China tectonic blocks, Europe, and North America (Groves and Wang, 2009; Shi et al., 2021). The CPBE coincided with the LPIA, and in particular the late Asselian (294.19 Ma) diversity peak coincided with the acme of the LPIA (Fan et al., 2020), suggesting that climatic cooling promoted foraminiferal diversity during this time. However, global compilations of environmental proxies (e.g., $^{87}Sr/^{86}Sr$ ratio, $\delta^{13}C$, $\delta^{18}O$, continental fragmentation index) do not

exhibit compelling trends with diversity and the CPBE stands in contrast to the modern association between warm climates and diversity (Fan et al., 2020). As a result, previous studies have focused on non-climatic mechanisms for the CPBE. Higher evolutionary rates during this time have been attributed to the advent of algal symbiosis of fusulinids, which enabled them to reside in the low-nutrient (oligotrophic) environments, generating more offspring and experimenting to suit more niches in warm and shallow water (Groves and Wang, 2009). Environmental changes associated with the closure of a subequatorial gateway in the Late Mississippian (~325 Ma) during the assembly of Pangaea, such as glacial episodes, suppressed marine circulation, and fragmented niches, have also been proposed as mechanisms for the CPBE (Shi et al., 2021). Our simulations indicate that climatic cooling over the late Pennsylvanian–earliest Permian may have also contributed to the main radiation episode of the CPBE.

A transition from interglacial to glacial conditions, marked by decreased atmospheric CO_2, expansion of Gondwanan ice sheets, and lowered sea level, is associated with changes in coastal temperature gradients that may have increased marine provinciality. Marine provinciality, caused by plate tectonics via continent fragmentation and climate change via enhanced meridional SST gradients, has been invoked as a fundamental driver of global biodiversity during the last 250 million years (Kocsis et al., 2021). Although our glacial and interglacial simulations capture relatively similar latitudinal temperature gradients in the open ocean, the transition from interglacial to glacial conditions leads to increased temperature gradients in coastal shallow-water regions where the CPBE is archived. The simulated latitudinal temperature gradient increases in over continental shelf regions of the northeastern Panthalassic (i.e., present-day North America), particularly from ~10–25°N (Figure 2.5b). In addition, the longitudinal temperature gradient is enhanced across the Ural Seaway (i.e., present-day Canada and Europe; Figure 2.5a). Increased coastal temperature gradients may have caused habitat fragmentation in these regions and thus promoted evolution of many different kinds of foraminifera (Groves and Wang, 2009). In addition to stronger thermal gradients in coastal regions, changes in terrestrial runoff may have enabled the widespread development of oligotrophic shelf environments.

Oligotrophic and highly oligotrophic environments can be finely partitioned by symbiont-bearing k-strategists such as fusulinids capable of specialization to narrow ranges of light intensity (Hallock et al., 1991). As a result, the widespread development of oligotrophic,

carbonate platform and shelf environments would have promoted fusulinoidean diversification (Groves and Wang, 2009). Our simulations indicate overall stronger oceanic mixing in the cooler glacial case compared to the interglacial case, which is typically associated with more evenly distributed nutrients and a reduction in the geographic extent of oligotrophic environments (Groves and Wang, 2009). However, simulated glacial cooling also decreases precipitation over the ocean and reduces riverine input to the coastal regions of North America, Europe, and the China tectonic blocks (Figure 2.2g and h). As a result, global runoff decreases by ~35% from the interglacial to glacial simulation. A reduction in riverine runoff could reduce nutrient input to coastal regions and promote the formation of oligotrophic shallow water masses (Hallock et al., 1991).

The dominance of Arctic-Eurasian diversity compared to that of North America has been interpreted to indicate that the Tethyan Realm was a biogeographic center of origination for the CPBE (Douglass, 1977; Groves and Wang, 2009; Mamet, 1977). Our glacial and interglacial simulations support a robust upwelling system along western Pangaea that supplies cold, nutrient-rich waters to the paleo-coastline of North America that would have potentially suppressed foraminiferal diversification relative to the Paleo-Tethys. Estuarine-like circulation patterns in the North American Midcontinent Sea likely transported nutrient-rich upwelled waters further inland during some glacioeustatic highstands (interglacial intervals) of the Pennsylvanian (Algeo et al., 2008; Turner et al., 2019). During glacial intervals, a lowering of sea level and reduction of riverine runoff may have caused estuarine-like circulation to break down (Macarewich et al., 2021). Changes in regional ocean circulation and decreased riverine input would have reduced nutrient input to the North American region during glacial conditions compared to interglacial conditions, providing a climatic mechanism that could also have impacted North America foraminiferal diversity during the Permo-Carboniferous.

2.6 Conclusions

Our CESM simulations of glacial and interglacial phases during latest Pennsylvanian–earliest Permian demonstrate significant changes in thermohaline circulation, temperatures in continental shelf regions, and riverine runoff due to the combined effects of atmospheric CO_2, sea level, and Gondwanan ice extent. Small glacial-interglacial changes in upper-ocean temperatures (~3–6°C) in the equatorial region provide more support for temperature proxies that indicate that tropical oceans were climatically buffered during the LPIA. Our simulations capture

glacial and interglacial ocean circulation and temperature patterns that compare well overall with previous modeling studies. Nevertheless, the relatively high spatial resolution of our simulations increases the speed of western boundary currents along the coast of Pangaea and resolves wind-driven coastal upwelling along northwestern Australia inferred from environmental proxies that have not been captured in previous modeling studies. The glacial simulation captures overall stronger wind-driven ocean circulation compared to the interglacial simulation and deep convection in the North Panthalassic driven by cooler SSTs and brine rejection from expansive sea ice formation in the region. In the interglacial case, warm polar SSTs (>0°C) prevent deep-water formation in the Northern Hemisphere, yet relatively weaker subpolar gyre circulation and thus greater poleward salt transport in the Southern Hemisphere produces stronger South Panthalassic MOC.

Comparisons between our Pennsylvanian glacial simulation and a pre-industrial simulation with a similar level of radiative forcing reveal the impact of a superocean on ocean temperatures, circulation, and heat transport. Relatively stronger wind stress in the glacial simulation produces overall stronger wind-driven circulation, enhanced coastal upwelling systems, and a more expansive cold tongue of equatorial SSTs compared to the pre-industrial ocean basin configuration. In the glacial simulation, cooler mean zonal SSTs near the equator result in a lower latitudinal SST gradient than the pre-industrial case. In addition, the magnitude of South Panthalassic MOC captured in the glacial simulation is comparable to the pre-industrial Atlantic MOC, which drives stronger heat transport in the Southern Hemisphere of the glacial simulation compared to the pre-industrial case.

Our glacial and interglacial simulations also reveal some climatic mechanisms that may have contributed to the CPBE. Despite overall stronger circulation and mixing with glacial conditions on a global scale, diversification of symbiont-bearing foraminifera during the CPBE could have been promoted in shallow coastal environments where marine fossil records are located during this interval. The glacial simulation features enhanced temperature gradients over continental shelves regions of North America and the Ural Seaway, which could have caused habitat fragmentation and promoted higher evolutionary rates. Additionally, a reduction in coastal runoff with glacial cooling may have contributed to the formation of oligotrophic water masses in continental shelf regions, allowing fusulinids to finely partition the oligotrophic niches to which they are uniquely specialized. Ultimately, our work highlights the critical impacts of

changing atmospheric CO_2, sea level, and Gondwanan ice sheets on Permo-Carboniferous ocean dynamics and marine fauna.

2.7 Acknowledgements and funding

This work was supported by the National Science Foundation (NSF) award 1338200. We also acknowledge high-performance computing support from Cheyenne (doi:10.5065/D6RX99HX) provided by the National Center for Atmospheric Research's Computational and Information Systems Laboratory, sponsored by NSF.

2.8 References

Algeo, T. J., Heckel, P. H., Maynard, J. B., Blakey, R. C. and Rowe, H.: Modern and ancient epeiric seas and the super-estuarine circulation model of marine anoxia, Spec. Pap. - Geol. Assoc. Canada, (48), 7–38, 2008.

Angiolini, L., Mangiagalli, V., Muttoni, G., Stephenson, M. H. and Zanchi, A.: Tethyan oceanic currents and climate gradients 300 m.y. ago, Geology, 35(12), 1071–1074, doi:10.1130/G24031A.1, 2007.

Angiolini, L., Jadoul, F., Leng, M. J., Stephenson, M. H., Rushton, J., Chenery, S. and Crippa, G.: How cold were the Early Permian glacial tropics? Testing sea-surface temperature using the oxygen isotope composition of rigorously screened brachiopod shells, J. Geol. Soc. London., 166(5), 933–945, doi:10.1144/0016-76492008-096R, 2009.

Antão, L. H., Bates, A. E., Blowes, S. A., Waldock, C., Supp, S. R., Magurran, A. E., Dornelas, M. and Schipper, A. M.: Temperature-related biodiversity change across temperate marine and terrestrial systems, Nat. Ecol. Evol., 4(7), 927–933, doi:10.1038/s41559-020-1185-7, 2020.

Ballantyne, A. P., Lavine, M., Crowley, T. J., Liu, J. and Baker, P. B.: Meta-analysis of tropical surface temperatures during the Last Glacial Maximum, Geophys. Res. Lett., 32(5), 1–4, doi:10.1029/2004GL021217, 2005.

Boersma, A. and Premoli Silva, I.: Paleocene planktonic foraminiferal biogeography and the paleoceanography of the Atlantic Ocean, Micropaleontology, 29(4), 355–381, doi:10.2307/1485514, 1983.

Brady, E., Stevenson, S., Bailey, D., Liu, Z., Noone, D., Nusbaumer, J., Otto-Bliesner, B. L., Tabor, C., Tomas, R., Wong, T., Zhang, J. and Zhu, J.: The connected isotopic water cycle in the Community Earth System Model Version 1, J. Adv. Model. Earth Syst., 11(8), 2547–2566, doi:10.1029/2019MS001663, 2019.

Buggisch, W., Joachimski, M. M., Sevastopulo, G. and Morrow, J. R.: Mississippian d13Ccarb and conodont apatite $\delta^{18}O$ records - Their relation to the Late Palaeozoic Glaciation,

Palaeogeogr. Palaeoclimatol. Palaeoecol., 268(3–4), 273–292, doi:10.1016/j.palaeo.2008.03.043, 2008.

Carr, P. F., Jones, B. G. and Middleton, R. G.: Precursor and formation of glendonites in the Sydney Basin, Aust. Mineral., 4, 3–12, 1989.

Carter, J. L. and Poletaev, V. I.: Atokan (late Bashkirian or early Moscovian) brachiopods from the Hare Fiord Formation of Ellesmere Island, Canadian Arctic Archipelago, Ann. Carnegie Museum, 67(1), 1998.

Chumakov, N. M. and Zharkov, M. A.: Climate during the Permian-Triassic biosphere reorganizations. Article 2. Climate of the Late Permian and Early Triassic: General inferences, Stratigr. Geol. Correl., 11(4), 361–375, 2003.

Clapham, M. E.: Faunal evidence for a cool boundary current and decoupled regional climate cooling in the Permian of western Laurentia, Palaeogeogr. Palaeoclimatol. Palaeoecol., 298(3–4), 348–359, doi:10.1016/j.palaeo.2010.10.019, 2010.

Danabasoglu, G., Large, W. G., Tribbia, J. J., Gent, P. R., Briegleb, B. P. and McWilliams, J. C.: Diurnal coupling in the tropical oceans of CCSM3, J. Clim., 19(11), 2347–2365, doi:10.1175/JCLI3739.1, 2006.

Danabasoglu, G., Bates, S. C., Briegleb, B. P., Jayne, S. R., Jochum, M., Large, W. G., Peacock, S. and Yeager, S. G.: The CCSM4 ocean component, J. Clim., 25(5), 1361–1389, doi:10.1175/JCLI-D-11-00091.1, 2012.

Davydov, V.: Warm water benthic foraminifera document the Pennsylvanian-Permian warming and cooling events - The record from the Western Pangea tropical shelves, Palaeogeogr. Palaeoclimatol. Palaeoecol., 414, 284–295, doi:10.1016/j.palaeo.2014.09.013, 2014.

Domeier, M. and Torsvik, T. H.: Plate tectonics in the Late Paleozoic, Geosci. Front., 5(3), 303–350, doi:10.1016/j.gsf.2014.01.002, 2014.

Douglass, R. C.: The development of fusulinid biostratigraphy, in Concepts and methods of biostratigraphy (Kauffman, E. G. and Hazel, J. E.), pp. 463–482., 1977.

Eros, J. M., Montañez, I. P., Davydov, V. I., Osleger, D. A., Nemyrovska, T. I., Poletaev, V. I. and Zhykalyak, M. V.: Sequence stratigraphy and onlap history of the Donets Basin, Ukraine: Insight into Carboniferous icehouse dynamics, Palaeogeogr. Palaeoclimatol. Palaeoecol., 363–364, 187–191, doi:10.1016/j.palaeo.2012.09.013, 2012.

Fan, J., Shen, S., Erwin, D. H., Sadler, P. M., MacLeod, N., Cheng, Q., Hou, X., Yang, J., Wang, X., Wang, Y., Zhang, H., Chen, X., Li, G., Zhang, Y., Shi, Y., Yuan, D., Chen, Q., Zhang, L., Li, C. and Zhao, Y.: A high-resolution summary of Cambrian to Early Triassic marine invertebrate biodiversity, Science., 277(January), 272–277, 2020.

Ferrari, R. and Ferreira, D.: What processes drive the ocean heat transport?, Ocean Model., 38(3–4), 171–186, doi:10.1016/j.ocemod.2011.02.013, 2011.

Fielding, C. R., Frank, T. D. and Isbell, J. L.: The late Paleozoic ice age; a review of current understanding and synthesis of global climate patterns, Geol. Soc. Am. Spec. Pap. 441 Resolv. Late Paleoz. Ice Age Time Sp., 441(24), 343–354, doi:10.1130/2008.2441(24)., 2008.

Frank, T. D., Pritchard, J. M., Fielding, C. R. and Mory, A. J.: Cold-water carbonate deposition in a high-latitude, glacially influenced permian seaway (southern carnarvon basin, Western Australia), Aust. J. Earth Sci., 59(4), 479–494, doi:10.1080/08120099.2012.672932, 2012.

Gibbs, M. T., Rees, P. M., Kutzbach, J. E., Ziegler, A. M., Pat, J., Rowley, D. B., The, S., January, N., Gibbs, M. T., Rees, P. M., Kutzbach, J. E., Ziegler, A. M., Behling, P. J. and Rowley, D. B.: Simulations of Permian Climate and Comparisons with Climate - Sensitive Sediments Published by : The University of Chicago Press Simulations of Permian Climate and Comparisons with Climate-Sensitive Sediments, , 110(1), 33–55, 2002.

Giles, P. S.: Low-latitude Ordovician to Triassic brachiopod habitat temperatures (BHTs) determined from $\delta^{18}O$ [brachiopod calcite]: A cold hard look at ice-house tropical oceans, Palaeogeogr. Palaeoclimatol. Palaeoecol., 317–318, 134–152, doi:10.1016/j.palaeo.2012.01.002, 2012.

Gough, D. O.: Solar interior structure and luminosity variations, Sol. Phys., 74(1), 21–34, doi:10.1007/BF00151270, 1981.

Griffis, N. P., Montañez, I. P., Isbell, J., Mundil, R., Vesely, F., Iannuzzi, R., Gulbranson, E., Taboada, A., Pagani, A., Sanborn, M. E., Huyskens, M., Wimpenny, J., Linol, B., Yin, Q., Isbell, J., Mundil, R., Vesely, F., Weinshultz, L., Huyskens, M., Wimpenny, J., Linol, B. and Yin, Q.: Isotopes to ice: Constraining provenance of glacial deposits and ice centers in west-central Gondwana, Palaeogeogr. Palaeoclimatol. Palaeoecol., #pagerange#, doi:10.1016/j.palaeo.2018.04.020, 2018.

Griffis, N. P., Montañez, I. P., Fedorchuk, N., Isbell, J., Mundil, R., Vesely, F., Weinshultz, L., Iannuzzi, R., Gulbranson, E., Taboada, A., Pagani, A., Sanborn, M. E., Huyskens, M., Wimpenny, J., Linol, B. and Yin, Q. Z.: Isotopes to ice: Constraining provenance of glacial deposits and ice centers in west-central Gondwana, Palaeogeogr. Palaeoclimatol. Palaeoecol., 531(108745), 31–182, doi:10.1016/j.palaeo.2018.04.020, 2019.

Groves, J. R. and Wang, Y.: Foraminiferal diversification during the late Paleozoic ice age, Paleobiology, 35(3), 367–392, doi:10.1666/0094-8373-35.3.367, 2009.

Häkkinen, S., Rhines, P. B. and Worthen, D. L.: Warm and saline events embedded in the meridional circulation of the northern North Atlantic, J. Geophys. Res. Ocean., 116(3),

1–13, doi:10.1029/2010JC006275, 2011.

Hallock, P., Premoli Silva, I. and Boersma, A.: Similarities between planktonic and larger foraminiferal evolutionary trends through Paleogene paleoceanographic changes, Palaeogeogr. Palaeoclimatol. Palaeoecol., 83(1–3), 49–64, doi:10.1016/0031-0182(91)90075-3, 1991.

Heavens, N. G., Shields, C. A. and Mahowald, N. M.: A paleogeographic approach to aerosol prescription in simulations of deep time climate, J. Adv. Model. Earth Syst., 4(11), doi:10.1029/2012MS000166, 2012.

Herweijer, C., Seager, R., Winton, M. and Clement, A.: Why ocean heat transport warms the global mean climate, Tellus A Dyn. Meteorol. Oceanogr., 57(4), 662–675, doi:10.3402/tellusa.v57i4.14708, 2005.

Hillebrand, H.: On the generality of the latitudinal diversity gradient, Am. Nat., 163(2), 192–211, doi:10.1086/381004, 2004.

Holliday, N. P.: Air-sea interaction and circulation changes in the northeast Atlantic, J. Geophys. Res. Ocean., 108(8), 1–11, doi:10.1029/2002jc001344, 2003.

Horton, D. E., Poulsen, C. J. and Pollard, D.: Influence of high-latitude vegetation feedbacks on late Palaeozoic glacial cycles, Nat. Geosci., 3(8), 572–577, doi:10.1038/ngeo922, 2010.

Hurrell, J. W., Holland, M. M., Gent, P. R., Ghan, S., Kay, J. E., Kushner, P. J., Lamarque, J. F., Large, W. G., Lawrence, D., Lindsay, K., Lipscomb, W. H., Long, M. C., Mahowald, N., Marsh, D. R., Neale, R. B., Rasch, P., Vavrus, S., Vertenstein, M., Bader, D., Collins, W. D., Hack, J. J., Kiehl, J. and Marshall, S.: The community earth system model: A framework for collaborative research, Bull. Am. Meteorol. Soc., 94(9), 1339–1360, doi:10.1175/BAMS-D-12-00121.1, 2013.

Isbell, J. L., Henry, L. C., Gulbranson, E. L., Limarino, C. O., Fraiser, M. L., Koch, Z. J., Ciccioli, P. L. and Dineen, A. A.: Glacial paradoxes during the late Paleozoic ice age: Evaluating the equilibrium line altitude as a control on glaciation, Gondwana Res., 22(1), 1–19, doi:10.1016/j.gr.2011.11.005, 2012.

Jones, A. T., Frank, T. D. and Fielding, C. R.: Cold climate in the eastern Australian mid to late Permian may reflect cold upwelling waters, Palaeogeogr. Palaeoclimatol. Palaeoecol., 237(2–4), 370–377, doi:10.1016/j.palaeo.2005.12.009, 2006.

Kiehl, J. T. and Shields, C. A.: Climate simulation of the latest Permian: Implications for mass extinction, Geology, (9), 757–760, doi:10.1130/G21654.1, 2005.

Kiessling, W., Flügel, E. and Golonka, J.: Paleoreef maps: Evaluation of a Comprehensive Database on Phanerozoic Reefs, Am. Assoc. Pet. Geol. Bull., 83(10), 1552–1587, doi:10.1306/e4fd4215-1732-11d7-8645000102c1865d, 1999.

Kocsis, Á. T., Reddin, C. J., Scotese, C. R., Valdes, P. J. and Kiessling, W.: Increase in marine provinciality over the last 250 million years governed more by climate change than plate tectonics, Proc. R. Soc. B Biol. Sci., 288(1957), 20211342, doi:10.1098/rspb.2021.1342, 2021.

Koul, V., Tesdal, J. E., Bersch, M., Hátún, H., Brune, S., Borchert, L., Haak, H., Schrum, C. and Baehr, J.: Unraveling the choice of the north Atlantic subpolar gyre index, Sci. Rep., 10(1), 1–12, doi:10.1038/s41598-020-57790-5, 2020.

Kutzbach, J. E. and Ziegler, A. M.: Simulation of late Permian climate and biomes with an atmosphere- ocean model: comparisons with observations, Philos. Trans. - R. Soc. London, B, 341(1297), 327–340, doi:10.1098/rstb.1993.0118, 1993.

Kutzbach, J. E., Guetter, P. J. and Washington, W. M.: Simulated circulation of an idealized ocean for Pangaean time, Paleoceanography, 5(3), 299–317, doi:10.1029/PA005i003p00299, 1990.

Macarewich, S., Poulsen, C. J. and Montañez, I. P.: Simulation of oxygen isotopes and circulation in a late Carboniferous epicontinental sea with implications for proxy records, Earth Planet. Sci. Lett., 559, 116770, doi:10.1016/j.epsl.2021.116770, 2021.

Magazine, G.: brachiopod families through Permian Period, , 113(5), 1976.

Mamet, B. L.: Foraminiferal zonation of the Lower Carboniferous: methods and stratigraphic implications, in Concepts and methods of biostratigraphy (Kauffman, E. G. and Hazel, J. E.), pp. 445–462, Dowden, Hutchinson & Ross ; Distributed by Halsted Press, Stroudsburg, Pa.; [New York]., 1977.

McGhee, G. R., Sheehan, P. M., Bottjer, D. J. and Droser, M. L.: Ecological ranking of Phanerozoic biodiversity crises: The Serpukhovian (early carboniferous) crisis had a greater ecological impact than the end-ordovician, Geology, 40(2), 147–150, doi:10.1130/G32679.1, 2012.

Meehl, G. A., Washington, W. M. and Jr., A. J. S.: Experiments with a Global Ocean Model Driven by Observed Atmospheric Forcing, J. Phys. Oceanogr., 12, 301–312, doi:https://doi.org/10.1175/1520-0485(1982)012<0301:EWAGOM>2.0.CO;2, 1982.

Mii, H. S., Grossman, E. L., Yancey, T. E., Chuvashov, B. and Egorov, A.: Isotopic records of brachiopod shells from the Russian Platform - Evidence for the onset of mid-Carboniferous glaciation, Chem. Geol., 175(1–2), 133–147, doi:10.1016/S0009-2541(00)00366-1, 2001.

Mikolajewicz, U. and Crowley, T. S.: Response of a coupled ocean/energy balance model to restricted flow through the Central American Isthmus, Paleoceanography, 12(3), 429–441, doi:10.1029/96PA03542, 1997.

Montañez, I. P. and Poulsen, C. J.: The Late Paleozoic Ice Age: An Evolving Paradigm, Annu. Rev. Earth Planet. Sci., 41(1), 629–656, doi:10.1146/annurev.earth.031208.100118, 2013.

Montañez, I. P., McElwain, J. C., Poulsen, C. J., White, J. D., DiMichele, W. A., Wilson, J. P., Griggs, G. and Hren, M. T.: Climate, pCO_2 and terrestrial carbon cycle linkages during late Palaeozoic glacial–interglacial cycles, Nat. Geosci., 9(11), 824–828, doi:10.1038/ngeo2822, 2016.

Monteagudo, M. M., Lynch-Stieglitz, J., Marchitto, T. M. and Schmidt, M. W.: Central Equatorial Pacific Cooling During the Last Glacial Maximum, Geophys. Res. Lett., 48(3), 1–10, doi:10.1029/2020GL088592, 2021.

NOAA: What is the mid-ocean ridge?, Natl. Ocean. Atmos. Adm. [online] Available from: https://oceanexplorer.noaa.gov/facts/mid-ocean-ridge.html, 2021.

Peters, S. E. and Husson, J. M.: Sediment cycling on continental and oceanic crust, Geology, 45(4), 323–326, doi:10.1130/G38861.1, 2017.

Pollard, D. and Thompson, S.: Past climate and the role of ocean heat transport : model simulations for the cretaceous, Science (80-.)., 8(6), 785–798, 1993.

Poulsen, C. J., Pollard, D., Montanez, I. P. and Rowley, D.: Late Paleozoic tropical climate response to Gondwanan deglaciation, Geology, 35(9), 771–774, doi:10.1130/G23841A.1, 2007.

Powell, M. G.: Climatic basis for sluggish macroevolution during the late Paleozoic ice age, Geology, 33(5), 381–384, doi:10.1130/G21155.1, 2005.

Powell, M. G., Schöne, B. R. and Jacob, D. E.: Tropical marine climate during the late Paleozoic ice age using trace element analyses of brachiopods, Palaeogeogr. Palaeoclimatol. Palaeoecol., 280(1–2), 143–149, doi:10.1016/j.palaeo.2009.06.003, 2009.

Reid, C. M., James, N. P., Beauchamp, B. and Kyser, T. K.: Faunal turnover and changing oceanography: Late Palaeozoic warm-to-cool water carbonates, Sverdrup Basin, Canadian Arctic Archipelago, Palaeogeogr. Palaeoclimatol. Palaeoecol., 249(1–2), 128–159, doi:10.1016/j.palaeo.2007.01.007, 2007.

Richey, J. D., Montañez, I. P., Goddéris, Y., Looy, C. V., Griffis, N. P. and Dimichele, W. A.: Influence of temporally varying weatherability on CO_2-climate coupling and ecosystem change in the late Paleozoic, Clim. Past, 16(5), 1759–1775, doi:10.5194/cp-16-1759-2020, 2020.

Sardar Abadi, M., Soreghan, G. S., Heavens, N. G., Voeten, D. F. A. E. and Ivanova, R. M.: Warm-water carbonates in proximity to Gondwanan ice–sheets: A record from the Upper

Paleozoic of Iran, Palaeogeogr. Palaeoclimatol. Palaeoecol., 531(September 2018), 108914, doi:10.1016/j.palaeo.2018.09.008, 2019.

Shi, G. R. and Waterhouse, J. B.: Late Palaeozoic global changes affecting high-latitude environments and biotas: An introduction, Palaeogeogr. Palaeoclimatol. Palaeoecol., 298(1–2), 1–16, doi:10.1016/j.palaeo.2010.07.021, 2010.

Shi, Y., Wang, X., Fan, J., Huang, H., Xu, H. and Zhao, Y.: Carboniferous-earliest Permian marine biodiversification event (CPBE) during the Late Paleozoic Ice Age, Earth-Science Rev., 220(April), 2021.

Smith, R. S., Dubois, C. and Marotzke, J.: Ocean circulation and climate in an idealised Pangean OAGCM, Geophys. Res. Lett., 31(18), 1–4, doi:10.1029/2004GL020643, 2004.

Soreghan, G. S., Soreghan, M. J. and Heavens, N. G.: Explosive volcanism as a key driver of the late Paleozoic ice age, Geology, 47(7), 600–604, doi:10.1130/G46349.1, 2019.

Stanley, S. M. and Powell, M. G.: Depressed rates of origination and extinction during the late Paleozoic ice age: A new state for the global marine ecosystem, Geology, 31(10), 877–880, doi:10.1130/G19654R.1, 2003.

Turner, A. C. E., Algeo, T. J., Peng, Y. and Herrmann, A. D.: Circulation patterns in the Late Pennsylvanian North American Midcontinent Sea inferred from spatial gradients in sediment chemistry and mineralogy, Palaeogeogr. Palaeoclimatol. Palaeoecol., (November), 0–1, doi:10.1016/j.palaeo.2018.12.008, 2019.

Veevers, J. J. and Powell, C. M.: Late Paleozoic glacial episodes in Gondwanaland reflected in transgressive- regressive depositional sequences in Euramerica, Geol. Soc. Am. Bull., 98(4), 475–487, doi:10.1130/0016-7606(1987)98<475:LPGEIG>2.0.CO;2, 1987.

Wade, D. C., Luke Abraham, N., Farnsworth, A., Valdes, P. J., Bragg, F. and Archibald, A. T.: Simulating the climate response to atmospheric oxygen variability in the Phanerozoic: A focus on the Holocene, Cretaceous and Permian, Clim. Past, 15(4), 1463–1483, doi:10.5194/cp-15-1463-2019, 2019.

Waterhouse, J. B.: What's the time, Mr. Wolf?, Univ. of Queensland Press, Queensland., 1977.

Waterhouse, J. B. and Bonham-Carter, G. F.: Global Distribution and Character of Permian Biomes Based on Brachiopod Assemblages, Can. J. Earth Sci., 12(7), 1085–1146, doi:10.1038/2031227a0, 1975.

Willig, M. R., Kaufman, D. M. and Stevens, R. D.: Latitudinal Gradients of Biodiversity: Pattern, Process, Scale, and Synthesis, Annu. Rev. Ecol. Evol. Syst., 34, 273–309, doi:10.1146/annurev.ecolsys.34.012103.144032, 2003.

Wilson, J. P., Montañez, I. P., White, J. D., DiMichele, W. A., McElwain, J. C., Poulsen, C. J.

and Hren, M. T.: Dynamic Carboniferous tropical forests: new views of plant function and potential for physiological forcing of climate, New Phytol., 215(4), 1333–1353, doi:10.1111/nph.14700, 2017.

Winguth, A. M. E. and Maier-Reimer, E.: Causes of the marine productivity and oxygen changes associated with the Permian-Triassic boundary: A reevaluation with ocean general circulation models, Mar. Geol., 217(3–4), 283–304, doi:10.1016/j.margeo.2005.02.011, 2005.

Winguth, A. M. E., Heinze, C., Kutzbach, J. E., Maier-Reimer, E., Mikolajewicz, U., Rowley, D., Rees, A. and Ziegler, A. M.: Simulated warm polar currents during the middle Permian, Paleoceanography, 17(4), 9-1-9–18, doi:10.1029/2001pa000646, 2002.

Winguth, A. M. E., Thomas, E. and Winguth, C.: Global decline in ocean ventilation, oxygenation, and productivity during the Paleocene-Eocene Thermal Maximum: Implications for the benthic extinction, Geology, 40(3), 263–266, doi:10.1130/G32529.1, 2012.

Zhang, R., Follows, M. J., Grotzinger, J. P. and Marshall, J.: Could the Late Permian deep ocean have been anoxic?, Paleoceanography, 16(3), 317–329, 2001.

Zhu, J., Poulsen, C. J. and Tierney, J. E.: Simulation of Eocene extreme warmth and high climate sensitivity through cloud feedbacks, Sci. Adv., 5(9), 1–11, doi:10.1126/sciadv.aax1874, 2019.

Zhu, J., Otto-Bliesner, B. L., Brady, E. C., Poulsen, C. J., Tierney, J. E., Lofverstrom, M. and DiNezio, P.: Assessment of Equilibrium Climate Sensitivity of the Community Earth System Model Version 2 Through Simulation of the Last Glacial Maximum, Geophys. Res. Lett., 48(3), doi:10.1029/2020GL091220, 2021.

2.9 Supplementary information

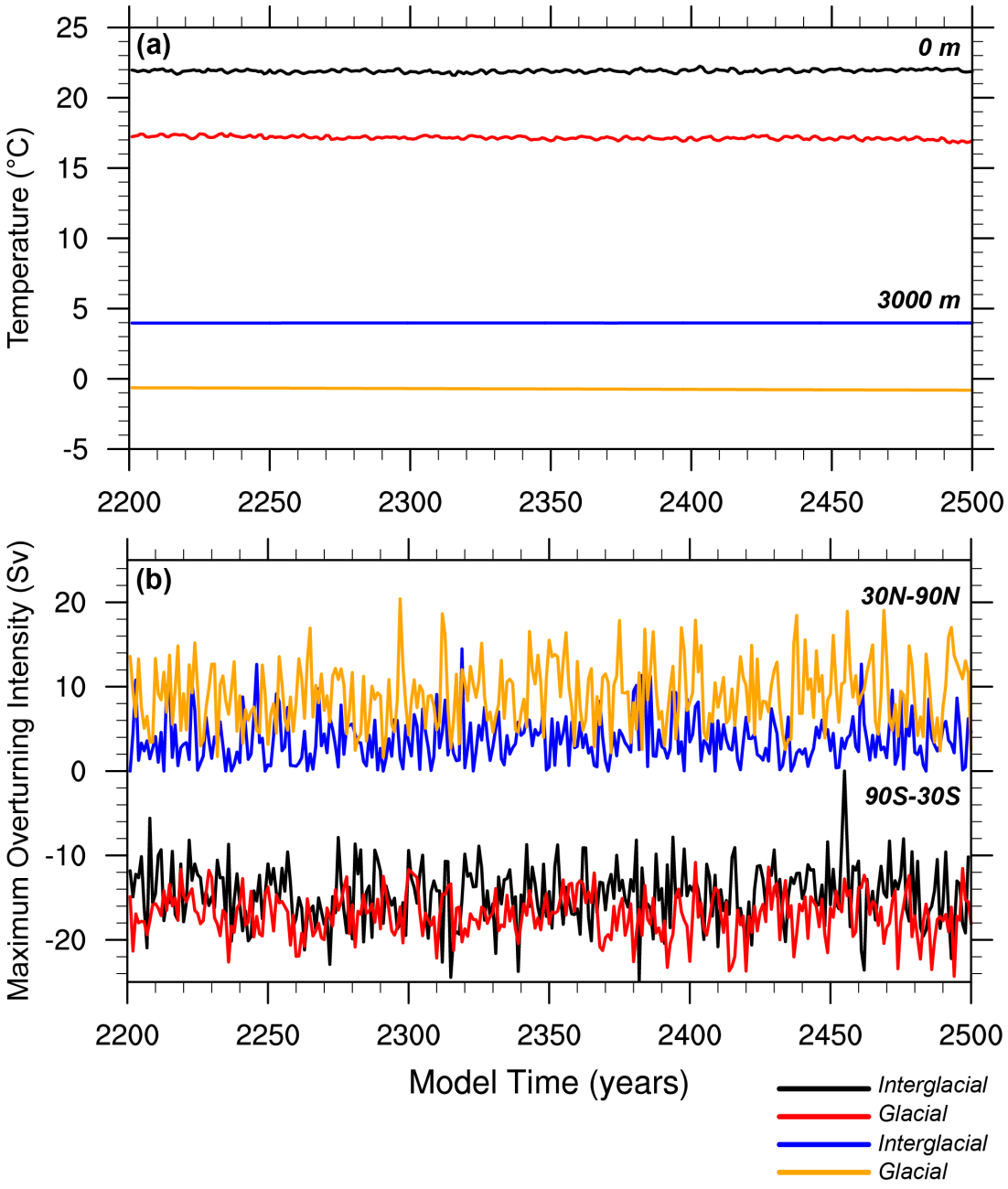

Figure S2.1 Timeseries of temperature and overturning circulation at the end of each simulation. (a) global annual-average surface and bottom temperatures (°C) and (b) meridional overturning intensity (Sv) over the last 300 years of the interglacial and glacial simulations.

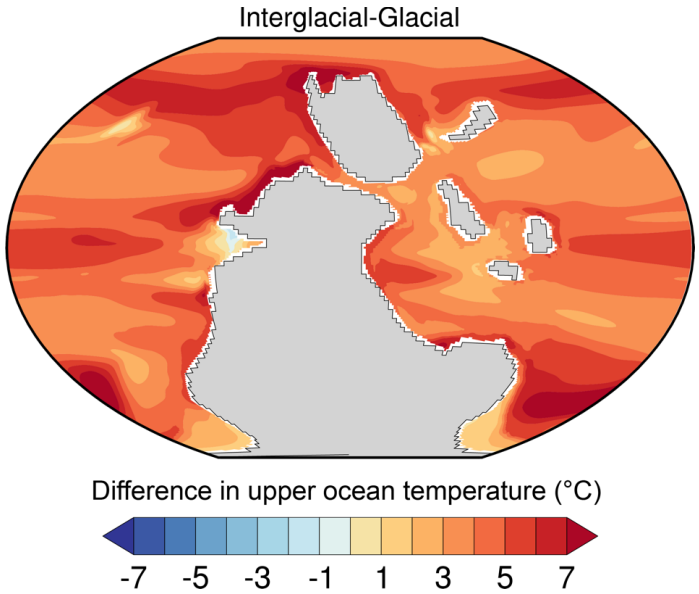

Figure S2.2 Global surface (upper 100 m) temperature difference between the glacial and interglacial simulations.

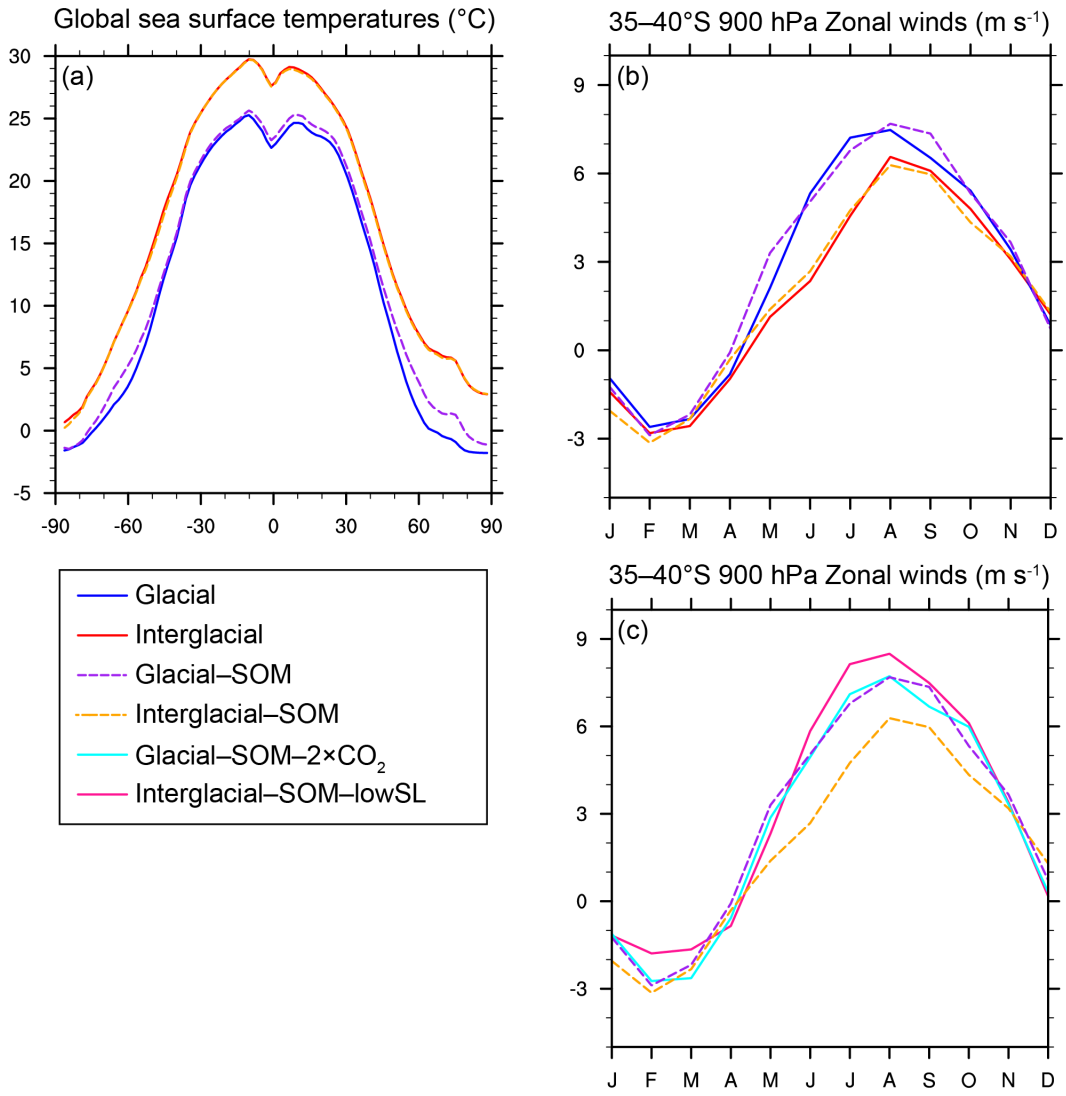

Figure S2.3 Mean surface temperature and winds in the slab ocean model (SOM) simulations. Global annual sea surface temperatures (a) and monthly mean zonal wind speed at 900 hPa from 35–40°S over the ocean (b) for the glacial, interglacial, glacial–SOM, and interglacial–SOM simulations. (c) Monthly mean zonal wind speed at 900 hPa from 35–40°S over the ocean is also shown for the glacial–SOM, interglacial–SOM, glacial–SOM–2×CO_2, and interglacial–SOM–lowSL simulations. Output from the fully-coupled glacial and interglacial simulations are included to show that (a) mean annual sea surface temperatures and (b) zonal wind speeds are nearly identical between the glacial and glacial–SOM as well as interglacial and interglacial–SOM simulations, respectively.

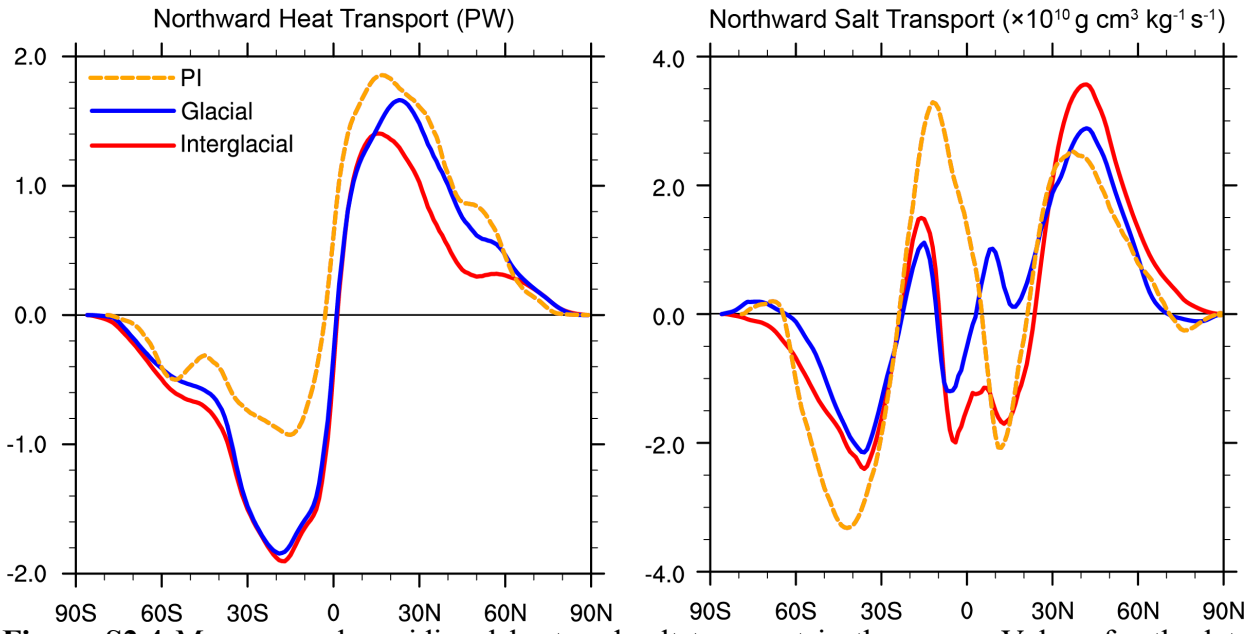

Figure S2.4 Mean annual meridional heat and salt transport in the ocean. Values for the late Pennsylvanian glacial (blue) and interglacial (red) simulations as well as the pre-industrial (PI; orange) simulation. Positive (negative) values correspond to net northward (southward) movement.

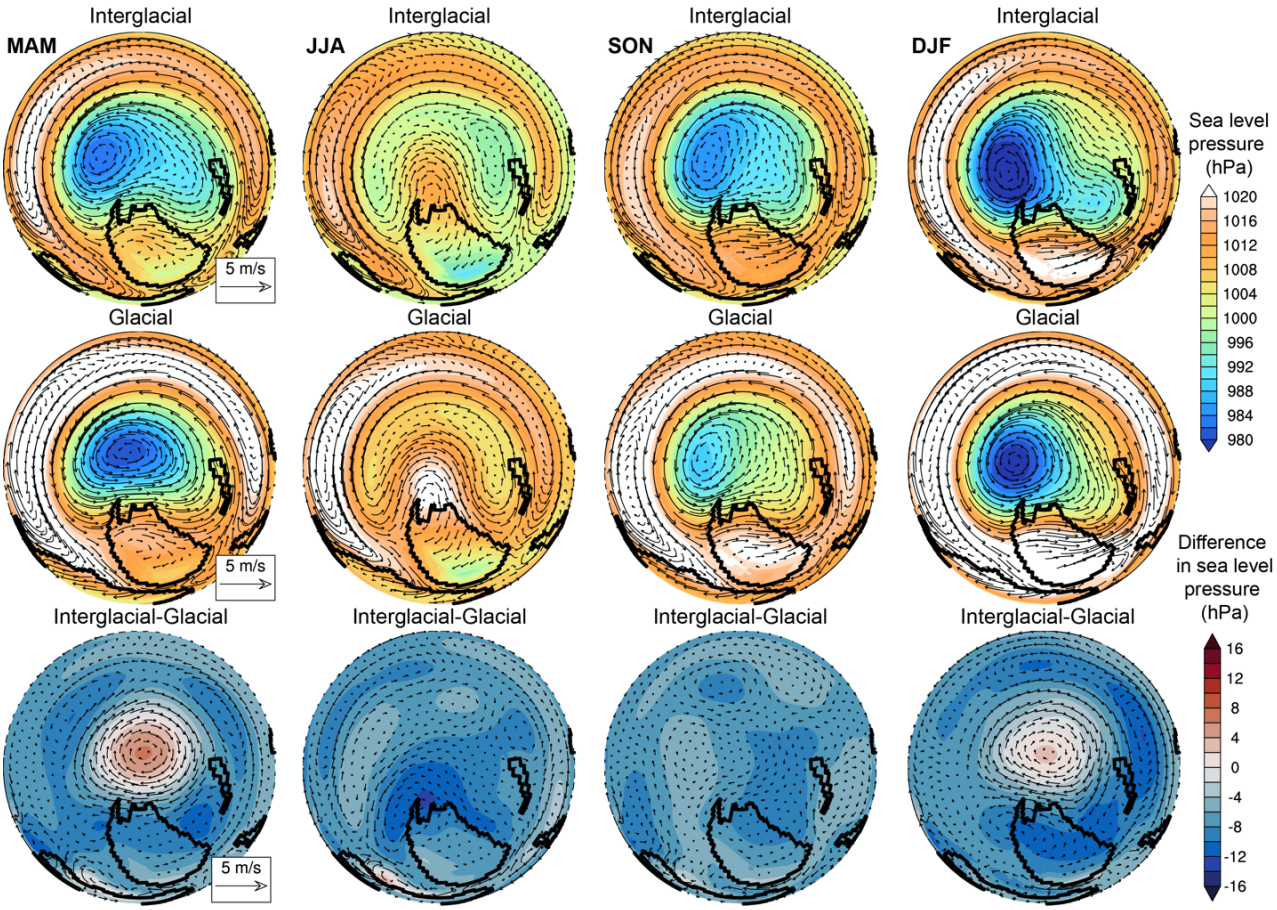

Figure S2.5 Seasonal sea level pressure and winds at 900 hPa in the Northern Hemisphere of the glacial and interglacial cases. MAM = March-April-May, JJA = June-July-August, SON = September-October-November, DJF = December-January-February.

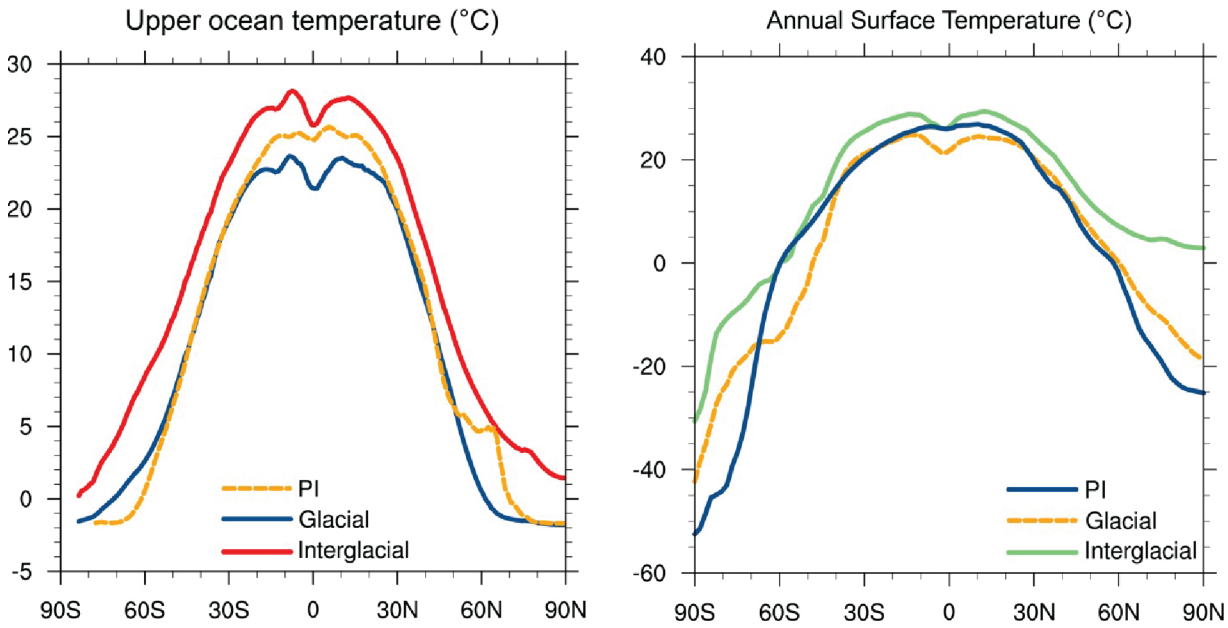

Figure S2.6 Mean annual oceanic (upper 100 m) and atmospheric surface temperatures. Annual ocean values shown for the interglacial (red), glacial (blue), and pre-industrial (orange) and atmosphere values for the interglacial (green), glacial (orange), and pre-industrial (blue) cases.

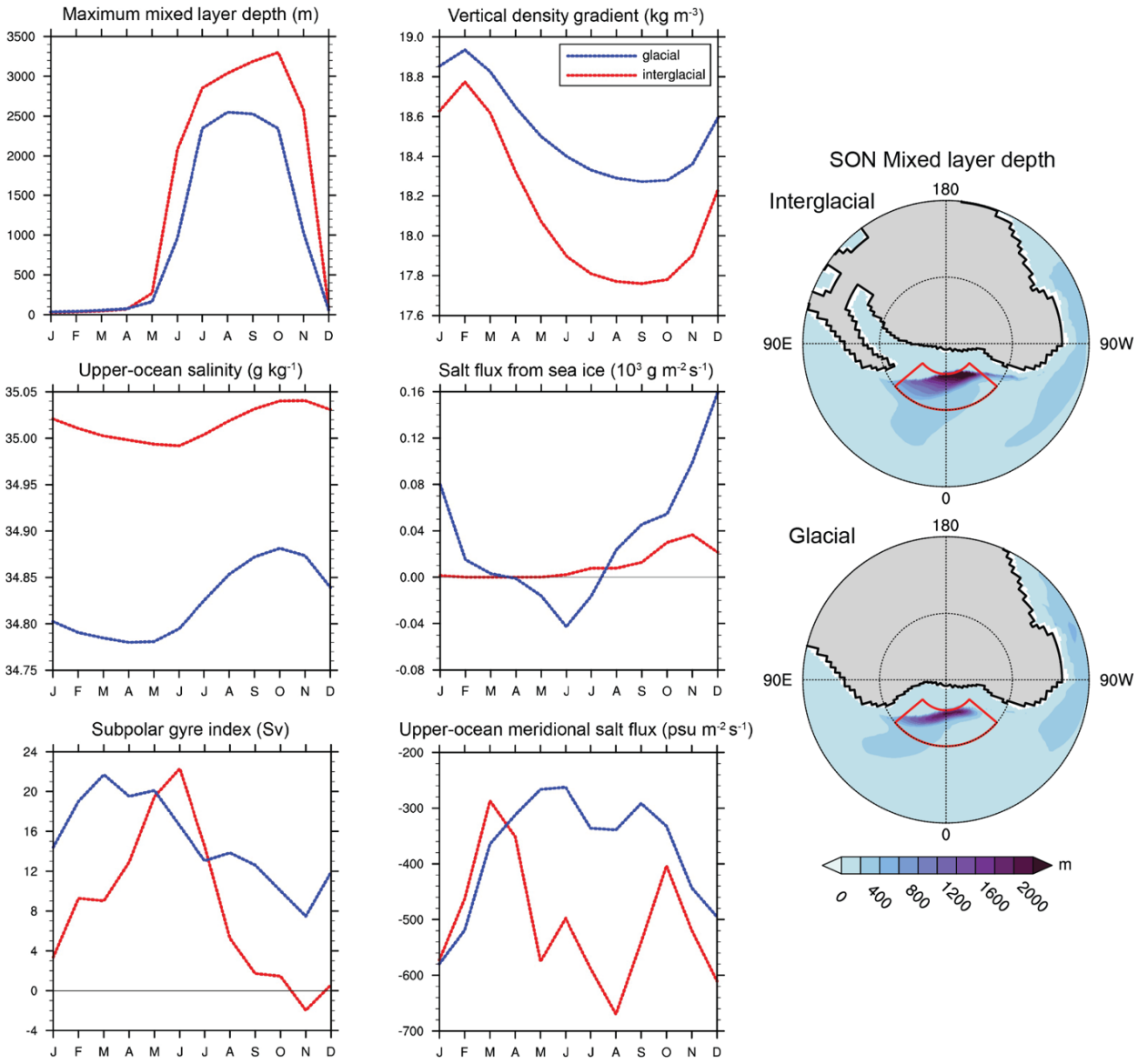

Figure S2.7 Monthly conditions in Southern Panthalassic deep-water formation regions. Deep-water formation regions (red boxes) in the Southern Hemisphere defined over the springtime maximum mixed-layer depths in the glacial and interglacial simulations. Maximum mixed layer depth (m), vertical density gradient (kg m^{-3}), upper-ocean salinity (g kg^{-1}), salt flux from sea ice (10^3 g m^2 s), subpolar gyre index (Sv), and upper-ocean meridional salt flux (psu m^2 s) in the deep-water formation regions for each case.

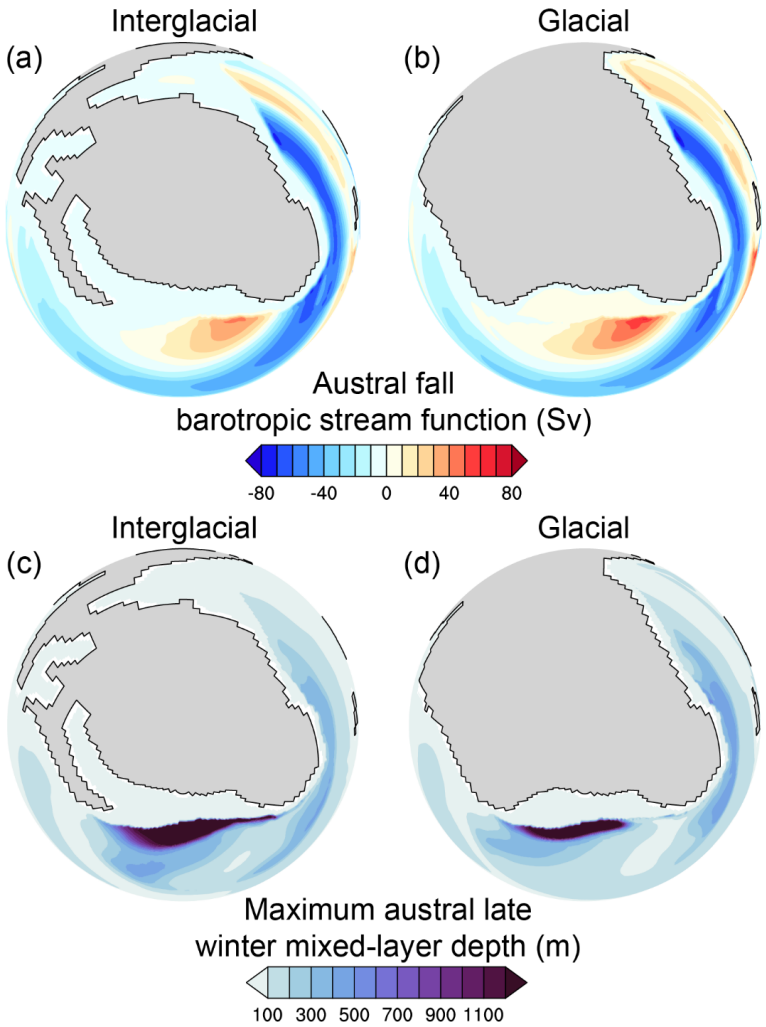

Figure S2.8 Southern polar plots of the barotropic stream function and maximum mixed-layer depth. Southern polar plots of the austral fall (March-April-May) barotropic stream function (a-b) and maximum austral late winter (September) mixed-layer depth (c-d) are shown for the interglacial and glacial cases, respectively.

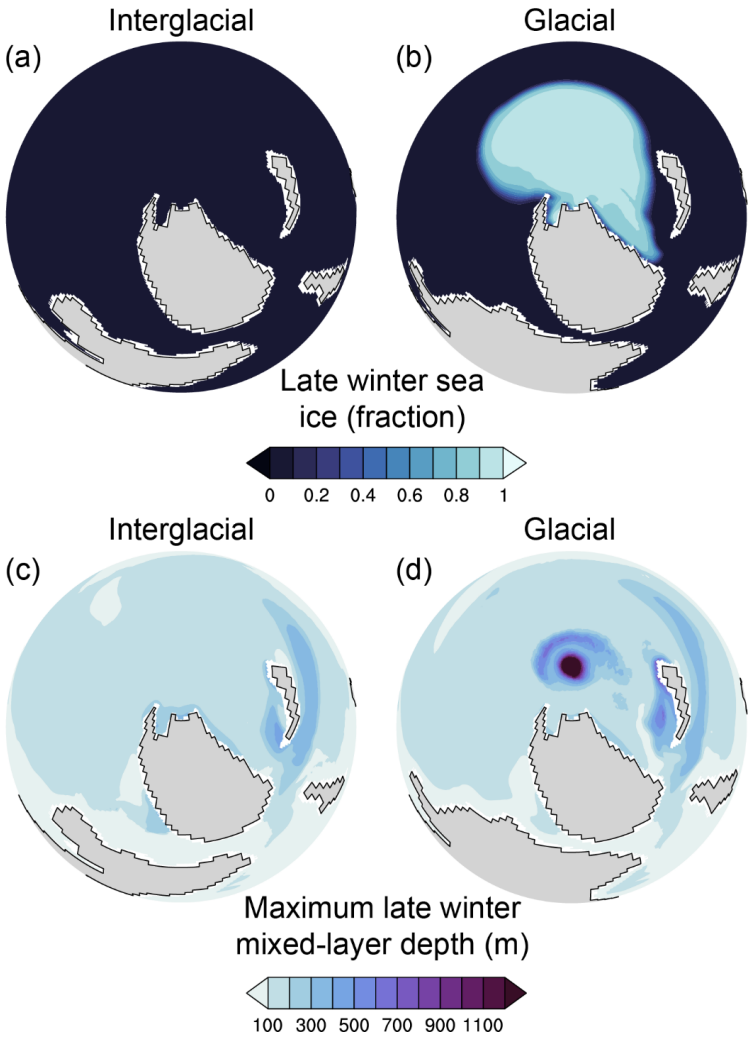

Figure S2.9 Northern polar plots of sea ice fraction and maximum mixed-layer depth. Northern polar plots of the late winter (March) sea ice (a-b) and maximum austral late winter (March) mixed-layer depth (c-d) in the interglacial and glacial cases, respectively.

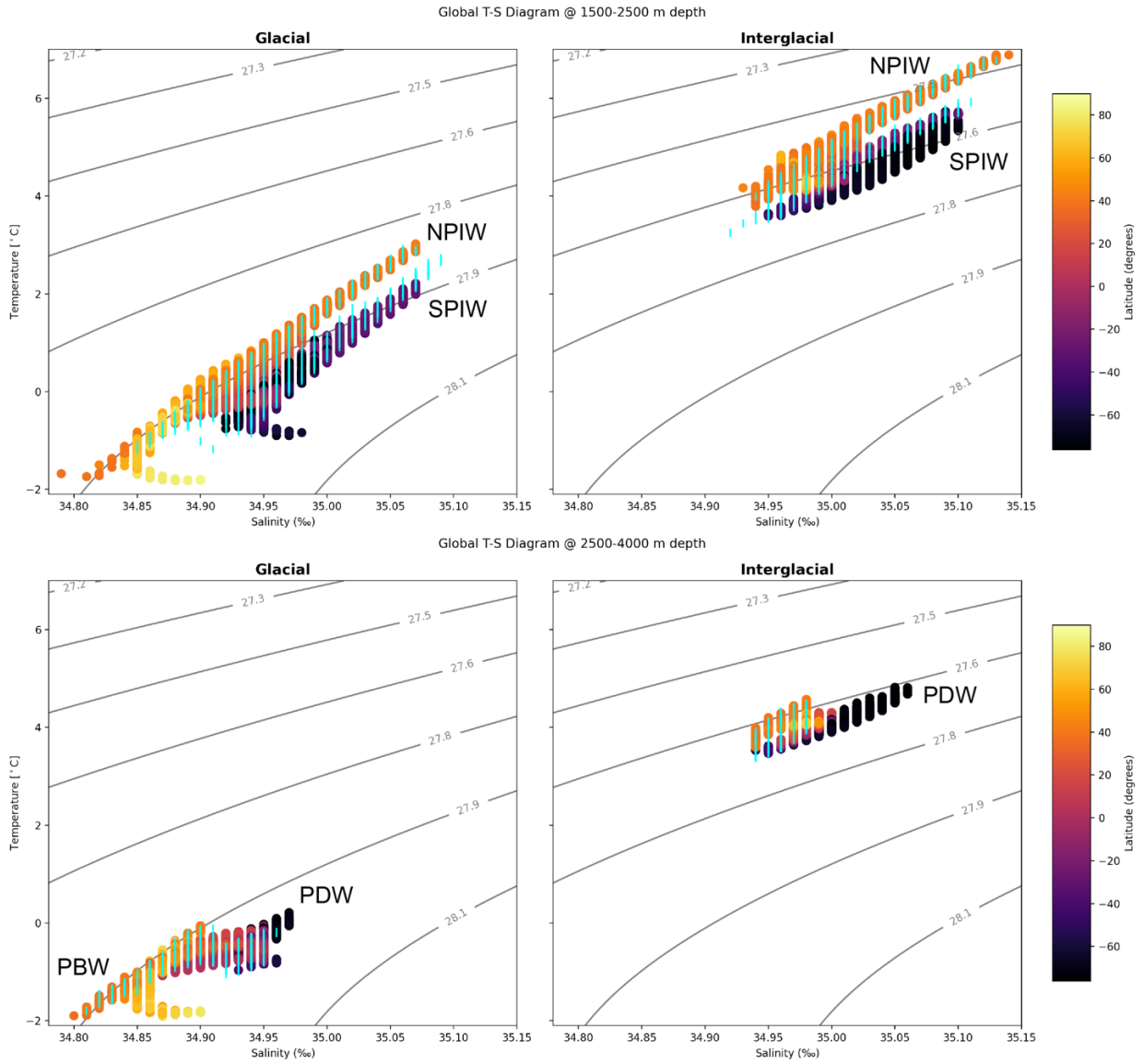

Figure S2.10 Global temperature-salinity (T-S) diagrams for major water masses in the glacial and interglacial simulations. T-S diagrams for major intermediate (1500–2500 m depth; top) and deep (2500–4000 m depth; bottom) water masses across the entire globe in the glacial and interglacial simulations. T-S values in the Panthalassic Ocean are shown with circle markers that are colored by latitude. T-S values in the Paleo-Tethys Ocean are shown with light blue line markers. From 1500 to 2500 m depth, North and South Panthalassic Intermediate Water forms in the glacial and interglacial cases around 45°N and 45°S (see also Figure S4.10). In the glacial and interglacial cases, North Panthalassic Intermediate Water (NPIW; glacial: −1 to 1°C, 34.85–35.06 g kg^{-1}; interglacial: ~4 to 7°C, 34.95–35.13 g kg^{-1}) is shown in a line of orange circle markers and South Panthalassic Intermediate Water (SPIW; glacial: −1 to 1°C, 34.90–35.09 g kg^{-1}; interglacial: ~3.5–6°C, 34.91–35.11 g kg^{-1}) is shown in a line of dark purple circles. Mixing between SPIW and NWIP occurs near the equator with pink circle markers in the glacial and interglacial cases. Approximately overlapping ranges of T-S markers between the Panthalassic and Paleo-Tethys indicate that the Paleo-Tethys intermediate water masses are

relatively similar to the SPIW and NPIW. Mixing between the SPIW and NPIW occurs with relatively cooler, fresher deep-water masses. In the glacial case, the three tales of T-S circles (orange, yellow, and deep purple) indicate three deepwater masses: the orange and yellow tales show two regions of Panthalassic Bottom Water (PBW; −1.6°C, 34.9–35 g kg^{-1}) formation in the Northern Panthalassic (North Pole and Amuria) and the deep purple tale shows Panthalassic Deep Water formation in the Southern Panthalassic (PDW; −1.6°C, 34.9–35 g kg^{-1}). Approximately overlapping ranges of T-S markers between the Panthalassic and Paleo-Tethys from 2500 to 4000 m depth indicate that PBW formed in Amuria around 45°N around (as opposed to the North Pole) mix with PDW in the Paleo-Tethys. In the interglacial case, T-S points from 2500 to 4000 m depth cover a smaller range as PDW (~4°C, 34.95–35.05 g kg^{-1}) formed in the Southern Panthalassic is the only major deep-water mass and flows into the Paleo-Tethys at depth. Notably, neither our glacial nor interglacial simulations capture the formation of a relatively warm, salty deep-water mass in the subtropics, and thus support the "thermal mode" of overturning circulation driven by cooling in the southern polar latitudes and not the "haline mode" that has been found in previous studies.

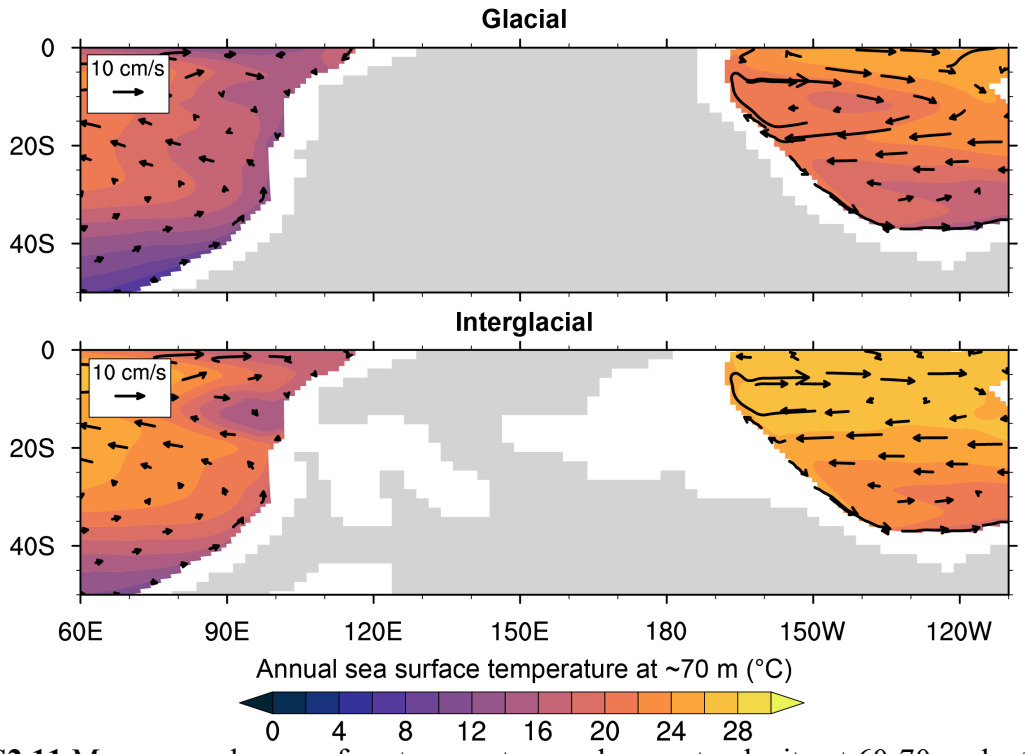

Figure S2.11 Mean annual sea surface temperature and current velocity at 60-70 m depth for the glacial and interglacial simulations. Surface temperature (°C) and current velocity (cm/s) values are shown with colored contours and vectors, respectively. Note the relatively cool sea temperatures along the western coast Gondwana compared to that of northeastern Gondwana.

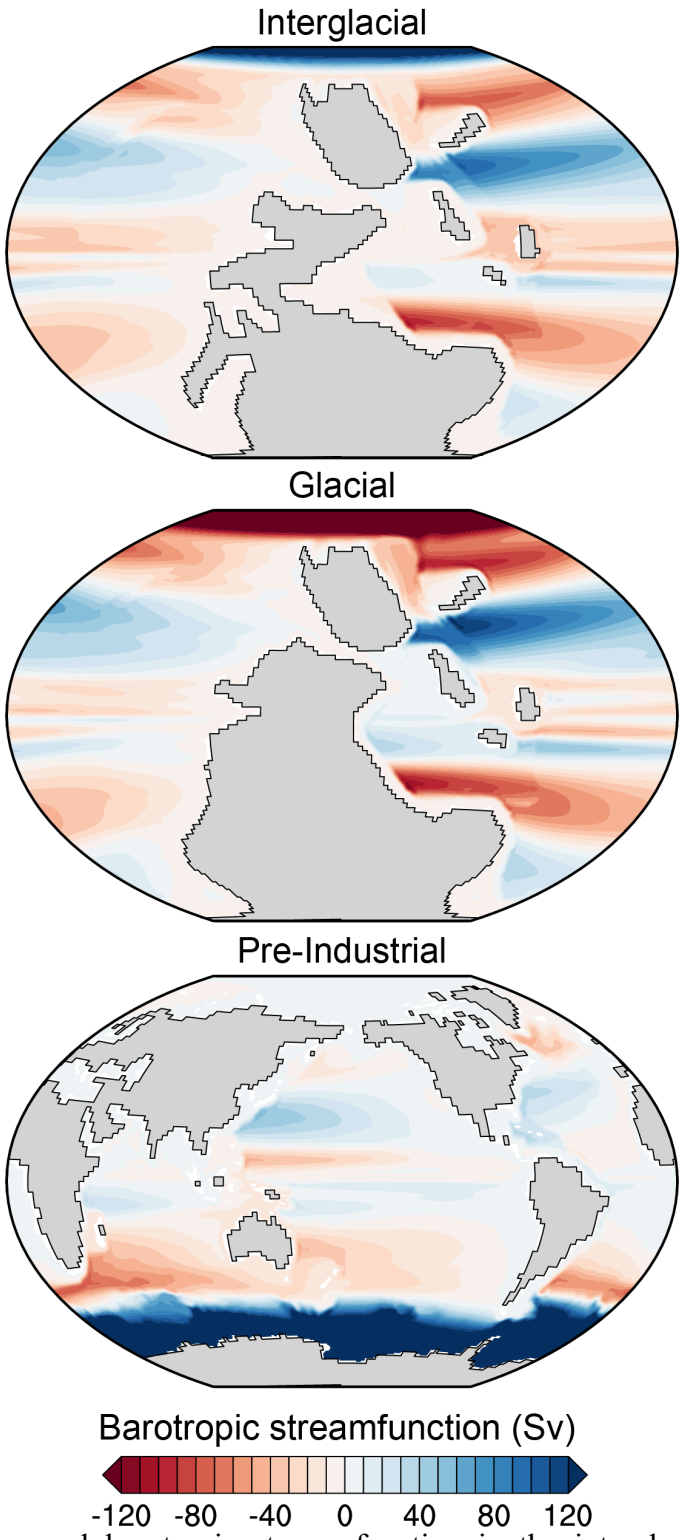

Figure S2.12 Mean annual barotropic stream function in the interglacial, glacial, and pre-industrial simulations. The barotropic stream function is defined as the depth-integrated volume transport and illustrates the position of the subpolar and subtropical gyre.

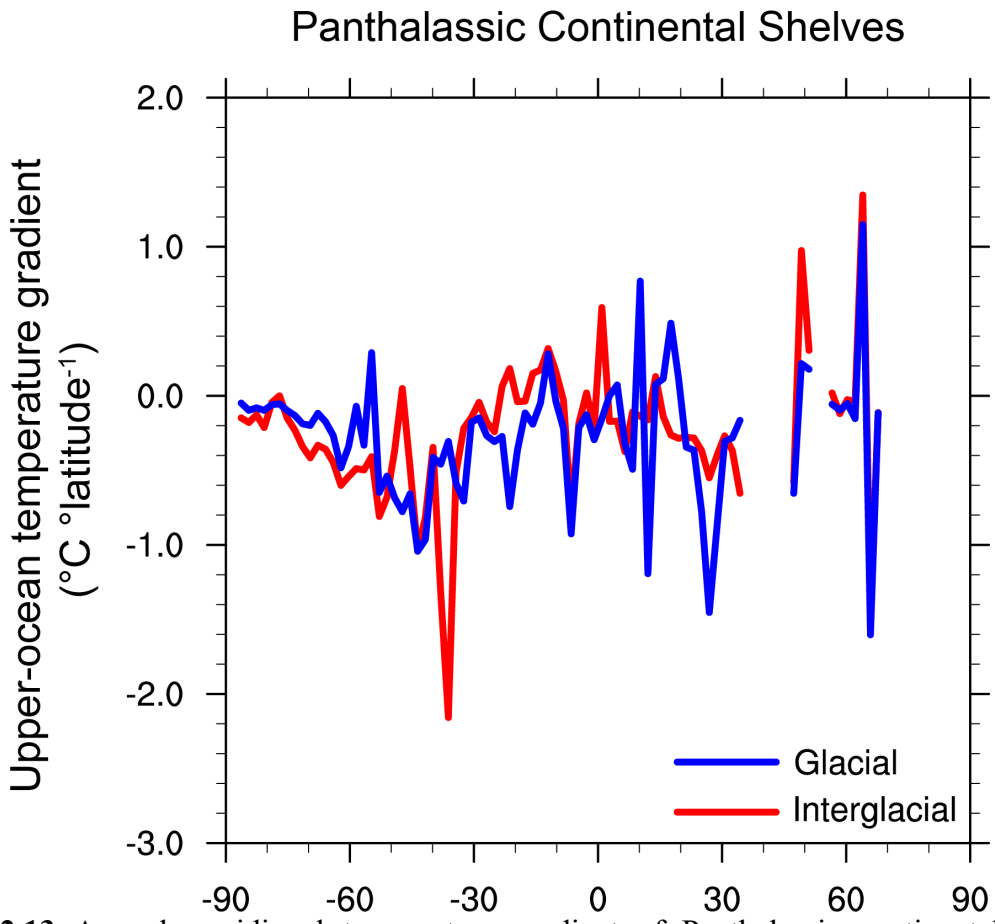

Figure S2.13 Annual meridional temperature gradient of Panthalassic continental shelves. Continental meridional gradients (°C per °latitude) are shown in the Panthalassic Ocean for the in the glacial (blue) and interglacial (red) simulations.

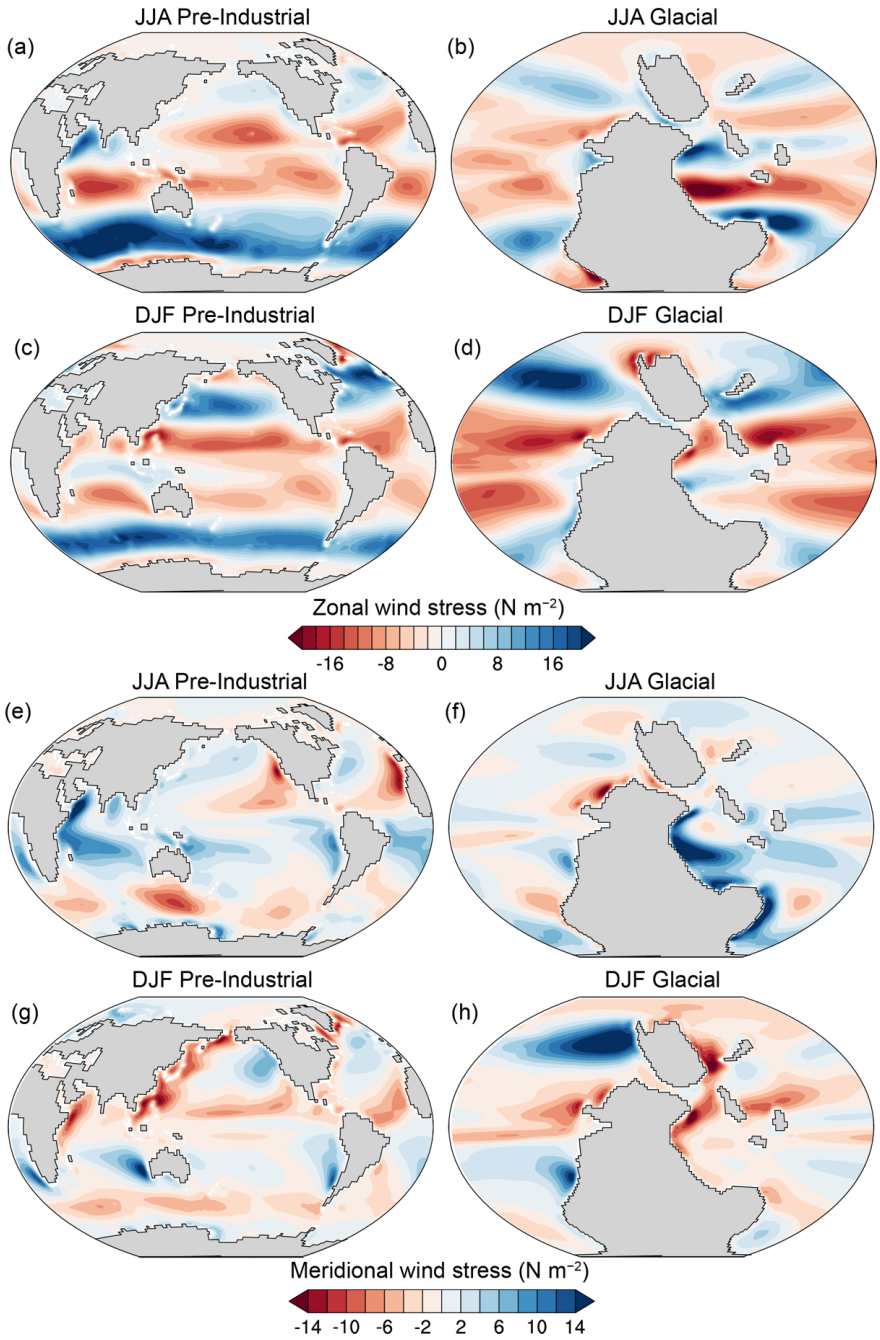

Figure S2.14 Seasonal zonal and meridional wind stress. Mean June-July-August (JJA) and December-January-February (DJF) values of zonal and meridional wind stress (N m^{-2}) are shown for the pre-industrial (a, c, e, g) and late Paleozoic glacial (b, d, f, h) simulations.

References

Domeier, M. and Torsvik, T. H.: Plate tectonics in the Late Paleozoic, Geosci. Front., 5(3), 303–350, doi:10.1016/j.gsf.2014.01.002, 2014.

Chapter 3 Simulation of Oxygen Isotopes and Circulation in a Late Carboniferous Epicontinental Sea with Implications for Proxy Records[1]

Co-authors: Christopher J. Poulsen and Isabel P. Montañez

3.1 Abstract

Reconstructions of ancient ocean chemistry are largely based on geochemical proxies obtained from epicontinental seas. Mounting evidence suggests that these shallow inland seas were chemically distinct from the nearby open ocean, decoupling epicontinental records from broader ocean conditions. Here we use the isotope-enabled Community Earth System Model to evaluate the extent to which the oxygen isotopic composition of the late Carboniferous epicontinental sea, the North American Midcontinent Sea (NAMS), reflects the chemistry of its open-ocean sources and connect epicontinental isotope variability in the sea to large-scale ocean-atmosphere processes. Model results support estuarine-like circulation patterns demonstrated by past empirical studies and suggest that orographic runoff produced decreases in surface seawater $\delta^{18}O$ ($\delta^{18}O_w$) of up to ~3‰ between the NAMS and the bordering ocean. Simulated sea surface temperatures are relatively constant across the sea and broadly reproduced from proxy-based $\delta^{18}O$ paleotemperatures for which model-based values of epicontinental $\delta^{18}O_w$ are used, indicating that offshore-onshore variability in surface proxy $\delta^{18}O$ is primarily influenced by seawater freshening. Simulated bottom water temperatures in the NAMS are also reproduced from biogenic calcite $\delta^{18}O$ using model-based values of epicontinental $\delta^{18}O_w$, suggesting that benthic marine fossil $\delta^{18}O$ is also influenced by seawater freshening and coastal upwelling. In addition, glacial-interglacial variations in nearshore seawater freshening counteract the effects of temperature on marine biogenic $\delta^{18}O$ values, suggesting that salinity effects should be considered

[1] Published as: Macarewich, S.I., Poulsen, C.J., Montañez, I.P. (2021) Simulation of Oxygen Isotopes and Circulation in a Late Carboniferous Epicontinental Sea with Implications for Proxy Records, Earth and Planetary Science Letters, doi: 10.1016/j.epsl.2021.116770.

in $\delta^{18}O$-based estimates of glacioeustatic sea level change from nearshore regions of the NAMS. Our results emphasize the importance of constraining epicontinental dynamics for interpretations of marine biogenic $\delta^{18}O$ as proxies of paleotemperature, salinity, and glacioeustasy.

3.2 Introduction

Our knowledge of ancient oceans is largely inferred from sedimentary successions deposited in shallow inland seas (i.e. epicontinental, epeiric, marginal, and intracratonic seas; herein referred to as 'epicontinental') reflecting that ~75% of sedimentary deposits preserved on Earth come from such environments (Peters and Husson, 2017). For the pre-Jurassic (earlier than ~200 Ma), the only preserved marine archives are epicontinental due to the subduction of open-marine deposits. The $\delta^{18}O$ value of biogenic minerals is dependent on both the oxygen isotopic composition and temperature of seawater from which those minerals grew, and thus has been used to construct the history of ocean temperature, sea level, and ice sheet volume over the Phanerozoic and beyond (Mii et al., 2001; van Geldern et al., 2006). Long-term variation in global compositions of biogenic $\delta^{18}O$ has further fueled debate over whether this trend records a shift in ocean temperatures, the influence of diagenetic alteration, or the evolution of global seawater $\delta^{18}O$ ($\delta^{18}O_w$) driven mainly by high-temperature water–rock interactions at mid-ocean ridges (e.g., Gregory and Taylor, 1981; Veizer and Prokoph, 2015). At any timescale, the reconstruction of an oxygen isotope secular curve from epicontinental deposits assumes that these environments were representative of more open-ocean settings. However, these paleo-seas were much broader than deep (<< 200 m) and often semi-restricted, and thus local environmental factors such as climate, freshwater input, and seawater circulation likely altered the chemistry and isotopic composition of these small volumes of seawater relative to contemporaneous oceans (Holmden et al., 1998; Panchuk et al., 2006; Brand et al., 2009; Woodard et al., 2013; Rosenau et al., 2014; Joachimski and Lambert, 2015; Narkiewicz et al., 2017; Montañez et al., 2018; Jimenez et al., 2019). Consequently, local-scale differences in seawater isotopic composition may have been superimposed on the global oxygen isotope secular curve.

Geochemical discrepancies between carbonate sediments from epicontinental and more open-marine settings have motivated investigation of the local environmental dynamics that form distinct shallow inland water masses (Holmden et al., 1998; Panchuk et al., 2006; Brand et al., 2009). Numerical constraints, using coupled epeiric sea-ocean carbon box models and salinity

mixing models, have helped discern the relative importance of carbon and water fluxes in epicontinental seas and emphasize that observed isotopic variations cannot be reproduced without some terrestrial influence and/or restricted exchange with the open ocean (Panchuk et al., 2005; Roark et al., 2017). The water fluxes that determine values of epicontinental $\delta^{18}O_w$ depend on local surface processes (evaporation and precipitation), freshwater inputs via runoff, and seawater circulation and exchange with the bordering ocean, which are quantities that cannot be directly inferred from biogenic isotope records or box models.

The advantage of applying Earth system models to studies of ancient epicontinental seas is that they can explicitly resolve these hydrologic processes through the physical representation of major components of the Earth system (i.e. atmosphere, ocean, land surface, and sea ice). Simulated patterns of precipitation, temperature, and salinity from Earth system models have been compared with geochemical records from epicontinental seaways to relate local isotopic variations to large-scale climate features, such as monsoonal circulation in the late Paleozoic Donets Sea (Montañez et al., 2018) and orographic precipitation in the Cretaceous Western Interior Seaway (Petersen et al., 2016). Water isotope-enabled Earth system models have the added ability to track the isotopic composition of water through the climate system, providing simulated estimates of $\delta^{18}O_w$, which can be directly compared with marine biogenic $\delta^{18}O$ values for deriving estimates of temperature, salinity, or glacioeustasy.

The North American Midcontinent Sea (NAMS) was an extensive epicontinental sea that extended from ~10ºS–15ºN and periodically flooded $>2\times10^6$ km^2 of the Laurentian Craton during glacioeustatic highstands of the Carboniferous and early Permian (Heckel, 1977; Algeo and Heckel, 2008). Circulation in the sea has long been hypothesized as estuarine, with a low-salinity surface layer positioned over a cooler saltwater wedge, based on multiple lines of geologic evidence, including patterns of total organic carbon and redox-sensitive trace elements, faunal diversity and distribution, and radiogenic isotopes (Algeo and Heckel, 2008; Roark et al., 2017; Turner et al., 2019). The NAMS is an ideal case study for epicontinental sea dynamics because stable isotope records from this region contribute disproportionally to late Carboniferous secular curves and paleoclimate reconstructions (e.g., Grossman et al., 2008; Henkes et al., 2018).

Here we use an isotope-enabled Earth system model to link variations in $\delta^{18}O_w$, temperature, and salinity to the degree of freshwater influence and coastal upwelling in the

NAMS. We resolve broad patterns of superestuarine circulation and specifically address the sensitivity of seawater freshening and upwelling influence to changes in regional topography and water column depth, respectively. We compare simulated values and patterns of $\delta^{18}O_w$ and sea temperature with proxy-based paleotemperatures to evaluate the primary environmental drivers of spatial variability in marine biogenic $\delta^{18}O$. We further compare simulated patterns of circulation, temperature, and $\delta^{18}O_w$ in the NAMS simulated for a glacioeustatic highstand and for a lowstand to constrain glacial-interglacial changes in ambient temperature and seawater freshening. To our knowledge, this study is the first to synthesize isotope-enabled Earth system modeling and published geochemical proxy data to constrain the regional controls on isotopic compositions and circulation in an ancient epicontinental sea.

3.3 Methods

3.3.1 Model setup

We employ the fully coupled isotope-enabled Community Earth System Model version 1.2 (iCESM), a global climate model that has been widely used for future climate prediction and modern climate studies (Hurrell et al., 2013). Coupled simulations using iCESM have been found to compare well to present day observations and paleoclimate records (Zhu et al., 2017; Tabor et al., 2018; Brady et al., 2019; Ladant et al., 2020; Zhu et al., 2020). CESM has been shown to accurately reproduce modern SST differences between marginal seas and the open ocean in the same latitudinal band, providing support for the use of CESM in studies of ancient epicontinental seas (Judd et al., 2020). The fully coupled configuration of iCESM includes the Community Atmosphere Model version 5 (iCAM), Community Land Model version 4 (iCLM), Parallel Ocean Model version 2 (iPOP), and Sea Ice Model version 4 (iCICE) components (Brady et al., 2019). iCAM and iCLM have a 1.9° × 2.5° horizontal resolution with 30 vertical levels. iPOP and iCICE have a nominal 1° horizontal resolution.

The ocean component of iCESM, iPOP, features an orthogonal grid with an enhancement of meridional resolution near the equator to more precisely simulate low-latitude ocean dynamics such as the El-Niño Southern Oscillation (Griffies et al., 2000). This equatorial grid refinement corresponds to a 0.3° × 1° horizontal resolution in the NAMS region. iPOP has 60 vertical levels with 10 m resolution in the top 15 levels and is stretched to 250 m resolution for the deepest

ocean. In the NAMS, due to the shallow depths of the epicontinental seaway, a maximum of 12 vertical levels (i.e. up to 120 m depth) are used. The iPOP grid resolution captures large-scale features of climate and ocean circulation and relies on parameterizations for unresolved physics, such as upper ocean mixing processes. Vertical mixing is represented using the modified K-Profile Parameterization (KPP) scheme (Danabasoglu et al., 2006) with a horizontally constant background diffusivity of 0.1×10^{-4} m^2 s^{-1} to accommodate the deep time paleogeography. The Gent-McWilliams scheme with diagnostically evaluated isopycnal diffusivity, as described in Danabasoglu et al. (2012), is used as the lateral closure with upper ocean isopycnal diffusivity values up to 3000 m^2 s^{-1}. The horizontal diffusivity coefficient is also set to 3000 m^2 s^{-1} in the surface diabatic layer. A detailed description of the ocean model can be found in Danabasoglu et al. (2012).

Riverine discharge is introduced into iPOP with zero salinity as an additional surface flux over a specified region surrounding the actual river mouth, implicitly neglecting any estuarine mixing or exchange (Griffies et al., 2005; Tseng et al., 2016). We implement several changes to the treatment of riverine discharge in iPOP that have been found to improve unresolved estuarine processes and reduce near-shore salinity biases, including (1) removing the contribution of river runoff to the surface buoyancy flux in the KPP and (2) using local salinity and $\delta^{18}O_w$ as reference values in the virtual flux formulations (Sun et al., 2019; Tseng et al., 2016).

3.3.2 Experimental design

The simulations presented in this study are branched for 200 years from late Carboniferous interglacial and glacial simulations (not shown here) that were each integrated for ~1,500 years to near equilibrium with a 100-yr mean top-of-atmosphere net energy flux of −0.01 and −0.16 Wm^{-2}, respectively. We use the same continental distribution of a late Pennsylvanian (300 Ma) paleogeography (Domeier and Torsvik, 2014), deep ocean bathymetry, treatment of aerosols, and solar luminosity between the interglacial highstand and glacial lowstand simulations. Deep ocean bathymetry is flat with a basic mid-ocean ridge system defined by accretion zones in the Gplates tectonic reconstruction at 300 Ma (www.gplates.com). Aerosol distributions are zonally averaged separately for land and ocean from pre-industrial levels following the procedure outlined by Heavens et al. (2012). Solar luminosity is reduced to 97.5% of the modern value, in accordance with traditional solar evolution models (Gough, 1981). The

simulations differ with respect to atmospheric CO_2, tropical vegetation, ice sheets, sea level, and global mean $\delta^{18}O_w$ to represent key differences between interglacial highstand and glacial lowstand conditions. A multi-proxy (10^3–10^4 yr resolution) CO_2 reconstruction was used to specify constant interglacial and glacial atmospheric CO_2 concentrations of 560 ppm and 280 ppm, respectively (Montañez et al., 2016; Richey et al., 2020). The distribution of prescribed vegetation follows the mid-late Pennsylvanian biomes for interglacial and glacial phases (Wilson et al., 2017), where the closest possible composition of modern plant functional types is chosen to represent each biome. The prescribed land ice geographies for interglacial and glacial simulations are based on reconstructions of paleo-glacier extent and ice stream pathways constrained by Carboniferous glacial features and deposits from high-latitude southern Gondwana as well as their and detrital zircon U-Pb geochronology (Griffis et al., 2018, 2019). The ocean was initialized with a uniform $\delta^{18}O_w$ of 0‰, and final values of the interglacial simulations are offset by −0.5‰ to account for reduced land ice.

Case	NAMS Depth	CPM Maximum Elevation
ShallowSeaLowMtn	Uniform 60 m	2000 m
SlopeSeaLowMtn	Mean 50 m	2000 m
DeepSeaHighMtn	Uniform 120 m	4000 m
DeepSeaLowMtn	Uniform 120 m	2000 m

Table 3.1 Differences in model boundary conditions between glacioeustatic highstand simulations. The only differences include NAMS water column depth and elevation of the Central Pangaean Mountains (CPM). Note that the elevation of the CPM is uniformly increased by 100% from *DeepSeaLowMtn* to *DeepSeaHighMtn*. Case names are used to refer to each sensitivity experiment.

To constrain $\delta^{18}O_w$ and circulation patterns in the NAMS during a glacioeustatic highstand, we ran four global climate simulations with different scenarios of regional bathymetry and topography in the NAMS (Table 3.1). The boundary conditions of the four sensitivity simulations are identical to the late Carboniferous simulation apart from water column depth in the NAMS and regional topographic elevations which are not well constrained. More recent estimates suggest that epicontinental sea depths were on the order of 10s of meters (Algeo &

Heckel, 2008) as opposed to 100s of meters (Heckel, 1994, 1977). Accordingly, two of our experiments, *DeepSeaLowMtn* and *ShallowSeaLowMtn*, have uniform depths of 120 and 60 m, respectively. A third experiment, *SlopeSeaLowMtn*, has depths that grade from 30 to 80 m with a mean of ~50 m that most closely reflects current proxy-based estimates (Algeo & Heckel, 2008; Roark et al., 2017). A SW−NE trending equatorial mountain chain, collectively referred to as the Central Pangaean Mountains (CPM), bordered the southern margin of the NAMS. Height estimates of the CPM range from ~2,000–4,000 m (Ziegler, 1985). To account for this range of estimates, we raise the elevation of the CPM by 2× in a fourth experiment, *DeepSeaHighMtn*, that corresponds to an increase in peak elevation from 2,000 to 4,000 m. A fifth experiment of a glacioeustatic lowstand scenario of *SlopeSeaLowMtn* (referred to as *Glacial-SlopeSeaLowMtn*) is produced to constrain differences in epicontinental temperature, $\delta^{18}O_w$, and circulation patterns during glacial phases of the Pennsylvanian. The CPM height of *Glacial-SlopeSeaLowMtn* is identical to *SlopeSeaLowMtn*. The NAMS depth is reduced by ½ from that of *SlopeSeaLowMtn* to a mean depth of ~25 m in *Glacial-SlopeSeaLowMtn*.

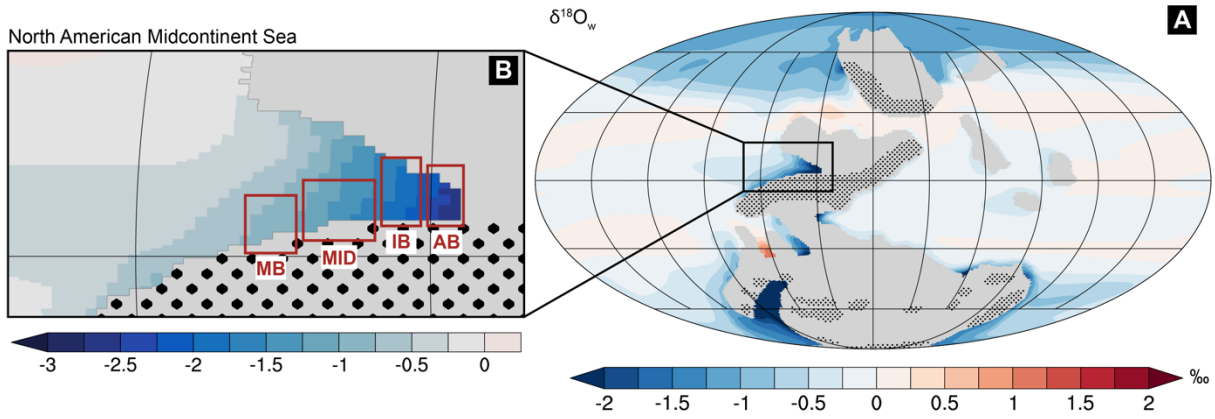

Figure 3.1 Global mean annual seawater $\delta^{18}O$ ($\delta^{18}O_w$). (A) with a closeup view of the North American Midcontinent Sea (B). Locations of regional domains are marked with red boxes, including the Midland Basin (MB), Midcontinent Shelf (MID), Illinois Basin (IB), and Appalachian Basin (AB). Stippled shading indicates elevations >500 m.

We focus on four domains in the NAMS that capture east-west variation in the sea (i.e. onshore to offshore trends within the sea; herein referred to as onshore-offshore) (Figure 3.1A) and use modeled differences in $\delta^{18}O_w$, temperature, and circulation between *DeepSeaLowMtn*,

SlopeSeaLowMtn, and *ShallowSeaLowMtn* cases to capture the effect of epicontinental sea depth on the influence of upwelled marine water. Differences between *DeepSeaLowMtn* and *DeepSeaHighMtn* cases capture the influence of CPM height on seawater freshening. *Glacial-SlopeSeaLowMtn* and *SlopeSeaLowMtn* are compared to assess glacial-interglacial variability in the NAMS. To equilibrate the upper layers of the ocean, each sensitivity simulation was run for 200 years with the last 50 years used in the analysis presented here (Figure S3.1).

3.5 Results & Discussion

3.5.1 NAMS climate conditions

In our glacioeustatic highstand simulations, prevailing upper-level northeasterly winds drive upwelling offshore of the NAMS continental margin. Low-level winds bring moist air from the bordering Panthalassic Ocean to the CPM and produce large amounts of orographic precipitation, particularly from March–November when the wind direction shifts from north to west (Figure S3.2). The NAMS receives an annual cumulative runoff of ~1.7 Sv with ~27% and 10% entering the Appalachian Basin (AB) and Midland Basin (MB), respectively; resulting in surface salinities that range from 25–27‰ in the AB and 32–33‰ in the MB (Figure S3.3). The ranges of seasonal surface salinity are similar in *DeepSeaLowTopo*, *ShallowSeaLowTopo*, and *SlopeSeaLowTopo* (i.e. the scenarios with identical CPMs) due to similar patterns of regional precipitation and runoff (Table S3.1). The bottom water salinities of *ShallowSeaLowTopo* and *SlopeSeaLowTopo* exhibit seasonal variations that are comparable to their surface waters, whereas the bottom water salinity of *DeepSeaLowTopo* remains at a near-constant marine value of 35‰, reflecting the absence of any freshwater influence at depth with a deeper epicontinental sea (120 m). Despite the seasonality of regional precipitation patterns, concomitant changes in basin-scale salinities are low overall because freshwater inputs are integrated into much larger ocean regions. For example, $\sim 1.2 \times 10^{10}$ m^3 of total annual runoff and direct precipitation enter the AB in *ShallowSeaLowTopo*. The upper 30 m of the AB has a volume of $\sim 7.5 \times 10^{12}$ m^3, so the surface ocean region is roughly 625× larger than the volume of annual freshwater input. Thus, we focus on mean annual seawater conditions (Table S3.1). Sea surface temperatures (SSTs) are also relatively stable through the seasons and across the sea, varying between 28 to 31°C.

3.5.2 Continental runoff and water column depth control spatial patterns of epicontinental $\delta^{18}O_w$

Orographic precipitation from the CPM produces ^{18}O-depleted runoff that flows into the NAMS to produce a laterally extensive surface layer of reduced $\delta^{18}O_w$ (Figure 3.1B). Runoff $\delta^{18}O$ is influenced by CPM height such that higher elevations produce lower values of runoff $\delta^{18}O$ and surface $\delta^{18}O_w$ (Figure 3.2A and B). In *DeepSeaLowMtn*, the MB and AB receive runoff with mean annual $\delta^{18}O$ values of −6.0‰ and −11.0‰ that produce surface $\delta^{18}O_w$ values of −0.8‰ and −1.8‰, respectively. A doubling of CPM elevation in *DeepSeaHighMtn* decreases runoff $\delta^{18}O$ by −3.0 and −5.0‰ and surface $\delta^{18}O_w$ by −0.4 and −1.3‰ in the MB and AB, respectively. The onshore-offshore increase in surface $\delta^{18}O_w$ captured in our simulations is comparable to observed variations in conodont $\delta^{18}O$ from highstand deposits inferred to have formed during climatically wetter conditions (Joachimski and Lambert, 2015).

Epicontinental sea depth controls the degree of mixing between upwelled marine water and coastal freshwater runoff in the NAMS, and thus offshore-onshore gradients of bottom $\delta^{18}O_w$. Upwelled marine water, with a $\delta^{18}O_w$ of −0.2‰, is enriched relative to local runoff. A deep shelf in *DeepSeaLowMtn* allows upwelled water to flow freely into the sea such that the bottom layer (90–120 m) is almost entirely marine (Figure 3.2A). Shallower depths in S*hallowSeaLowMtn* inhibit the advection of marine water causing bottom water $\delta^{18}O_w$ to be lower by −0.5‰ in the MB and −1.1‰ in the AB (Figure 3.2C). Marine water in *SlopeSeaLowMtn* flows inland without freshwater mixing until the edge of the Midcontinent Shelf where a water column depth of ~60 m is reached, resulting in $\delta^{18}O_w$ similar to the nearby ocean seaward of the shelf edge, whereas interior basins on the shelf (Illinois and Appalachian basins) with shallower depths have lower $\delta^{18}O_w$ (Figure 3.2D). For *ShallowSeaLowMtn* and *SlopeSeaLowMtn*, this produces differences in bottom $\delta^{18}O_w$ between the AB and Midcontinent Shelf regions (of ~0.4‰ and 1.4‰, respectively) that are comparable to that of well-preserved calcite brachiopod and aragonitic mollusk $\delta^{18}O$ over the same geographic extent (Jimenez et al., 2019; Roark et al., 2017).

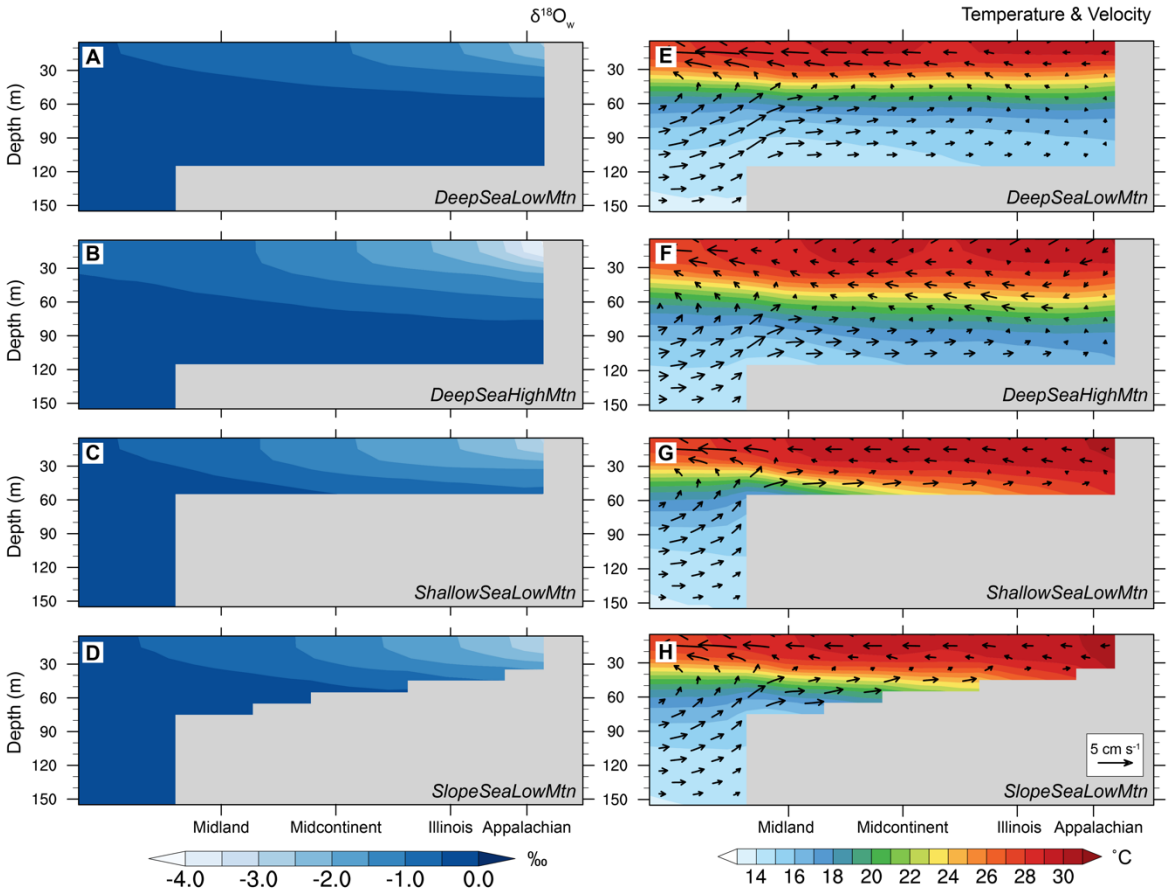

Figure 3.2 Longitude-depth cross sections of seawater $\delta^{18}O$ ($\delta^{18}O_w$) (A–D) and temperature and velocity (E–H) in the NAMS for each glacioeustatic highstand case. Averages are annual and calculated from 0–10°N. Note that the vertical component of the velocity has been multiplied by a scalar (5,000 cm s^{-1}). The continental shelf is in gray. The surface layer is defined as 0–30 m depth in all cases (based on the mean depth of the regional pycnocline, see Figure S2.5), whereas the bottom layer is the greatest 30 m of depth in each case, which is 30–60 m in *ShallowSeaLowMtn*, 90–120 m in *DeepSeaLowMtn* and *DeepSeaHighMtn*, and shallows from 50–80 m to 10–40 m towards the eastern coast in *SlopeSeaLowMtn*.

3.5.3 Reconstructing superestuarine circulation

Our simulations generally confirm superestuarine circulation in the NAMS—characterized by estuarine circulation, halocline formation, lateral advection of oxygen-deficient marine deepwater, and a persistent counterclockwise surface gyre (Algeo and Heckel, 2008; Turner et al., 2019). A continent-margin upwelling system draws deeper marine water onto the continental shelf (Figure 3.2E, F, G, H). High riverine inflow to the eastern end of the sea produces an offshore increase in seawater density that directs counterclockwise circulation of

surface waters (Figure S3.4). The organization of warmer brackish surface water over cooler marine water forms a highly stratified water column in *DeepSeaLowMtn* and *DeepSeaHighMtn* with vertical temperature gradients of >15°C (Figure 3.2E and F). Conversely, a reduction of marine influence in *ShallowSeaLowMtn* and *SlopeSeaLowMtn* produces lower vertical temperature gradients of ~3–5°C (Figure 3.2G and H) that match well with paleotemperatures inferred from coeval conodont and brachiopod $\delta^{18}O$ in the AB (Roark et al., 2017).

The formation of extensive black shales in the NAMS has been attributed to low-oxygen bottom waters formed from superestuarine circulation during highstands (Algeo and Heckel, 2008). The depth at which vertical stratification is stable and can form bottom water anoxia is poorly constrained (Montañez and Poulsen, 2013). Our simulations indicate that consistent freshwater input forms a stable pycnocline at a minimum depth of ~20–40 m across the NAMS in all cases (Figure S3.5). The regional pycnocline extends to the seafloor in the IB and AB of *SlopeSeaLowMtn*, whereas subpycnoclinal waters in the Midcontinent Shelf and MB approach a marine density of ~1027 kg m^{-3}. The presence of subpycnoclinal marine water in the Midcontinent Shelf of *SlopeSeaLowMtn* most closely reflects differences found in trace metal enrichment factors between black shale facies of the Midcontinent Shelf and IB (Algeo and Herrmann, 2018). The persistence of a stable pycnocline over the Midcontinent Shelf indicates that water depths of >100 m and approaching depths of the oceanic pycnocline are not necessary for the deposition of black shales.

3.5.4 Proxy-based paleotemperatures using simulated $\delta^{18}O_w$

Paleo-sea temperature reconstructions using the $\delta^{18}O$ thermometer are complicated by the uncertainty of $\delta^{18}O_w$ in the past. Carbonate clumped isotope measurements are a promising technique for constraining $\delta^{18}O_w$ independently from temperature, but so far have been minimally applied to Late Paleozoic records (Henkes et al., 2018). Without independent constraints on the isotopic composition of ancient seawater, variations in biogenic carbonate and apatite $\delta^{18}O$ have been interpreted with the assumption that epicontinental $\delta^{18}O_w$ was similar to open ocean values, such as –0.5‰ for an interglacial world (e.g., Adlis et al., 1988; Mii et al., 1999). However, if applied to paleotemperature equations this assumption produces temperatures of up to 44°C from highstand deposits in the AB (Figure 3.3A), exceeding the lethal limit of most animal phyla (Pörtner, 2002). Several studies have suggested that variations of

Pennsylvanian biogenic carbonate and apatite $\delta^{18}O$ at least partially reflect local salinity changes and cannot be exclusively attributed to temperature and/or high-latitude ice volume (Brand, 1987; Joachimski and Lambert, 2015; Roark et al., 2017; Montañez et al., 2018; Jimenez et al., 2019). However, the degree to which marine biogenic $\delta^{18}O$ values were influenced by seawater freshening has not been quantitatively examined.

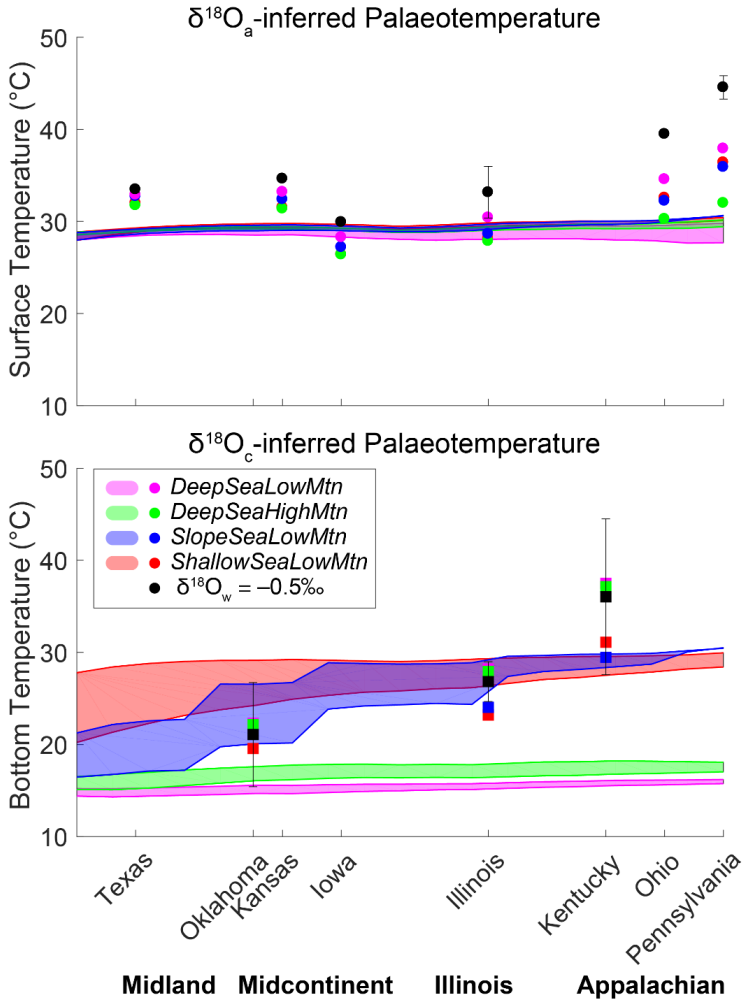

Figure 3.3 Comparison of proxy-based and simulated paleotemperatures. Proxy-based paleotemperatures calculated using an open-ocean $\delta^{18}O_w$ = –0.5‰ (black points) and simulated $\delta^{18}O_w$ values (colored points) are compared with simulated sea temperatures from each case (shaded regions). Shaded temperature regions are averages from 0–10°N at the longitudes of each locality. (A) Conodont data ($\delta^{18}O_S$) (Joachimski and Lambert, 2015; Rosenau et al., 2014) are compared to surface temperatures (shaded from 0–30 m depth) using the Pucéat et al. (2010) equation. (B) Brachiopod and mollusk data ($\delta^{18}O_B$) (Brand, 1987, 1981; Grossman et al., 2008;

Jimenez et al., 2019; Mii et al., 1999) are compared with bottom temperatures (same depths as in Figure 3.2 caption) using the Hays and Grossman (1991) equation. Mollusk values are adjusted by –0.8‰ to directly combine with brachiopod data (see Jimenez et al., 2019). Error bars on the black points are ±1σ of paleotemperatures derived from proxy data.

Our simulations provide physical representations of $\delta^{18}O_w$ and temperature that can be used to constrain the proportion of biogenic carbonate and apatite $\delta^{18}O$ variation that is associated with seawater freshening. To illustrate this, we compare onshore-offshore trends in paleotemperatures inferred from Pennsylvanian planktonic conodont and benthic brachiopod and mollusk $\delta^{18}O$ values using simulated $\delta^{18}O_w$ values from each sample locality versus a constant 'open ocean' $\delta^{18}O_w$ value (–0.5‰) and, in turn, evaluate the fit between these paleotemperature estimates with simulated temperature patterns. Paleotemperatures calculated with simulated $\delta^{18}O_w$ values indicate that SSTs were lower than paleotemperature based on using the constant marine $\delta^{18}O_w$ value and are generally uniform across the NAMS (Figure 3.3). Using simulated $\delta^{18}O_w$ values also improves the agreement between conodont-based paleotemperatures and simulated SSTs. For example, the root mean square error (RMSE) is reduced from 7.6°C to 2.4°C when paleotemperatures are calculated using the $\delta^{18}O_w$ values from *SlopeSeaLowMtn* (Table S3.2). Notably, the largest SST changes and greatest improvements in model-data fit occur in the AB where runoff is greatest and $\delta^{18}O_w$ is the lowest.

Simulated onshore-offshore variations in $\delta^{18}O_w$ and temperature of near-bottom seawater are controlled by both seawater freshening and upwelled marine water, with marine influence increasing as a function of epicontinental sea depth. Despite similar onshore-offshore trends of $\delta^{18}O_w$ between *ShallowSeaLowMtn* and *SlopeSeaLowMtn*, the simulated bottom water temperatures of *SlopeSeaLowMtn* are cooler in the MB and Midcontinent Shelf because the seafloor is deeper. The bottom layers of *DeepSeaLowMtn* and *DeepSeaHighMtn* are entirely marine with a near-constant $\delta^{18}O_w$ and temperature and therefore cannot account for the observed variation in benthic mollusk and brachiopod $\delta^{18}O$ (Figure 3.3B). As a result, agreement between simulated bottom water temperatures and proxy-based paleotemperatures using model-based $\delta^{18}O_w$ is best in *SlopeSeaLowMtn*, as shown by a reduction of RMSE of inferred bottom temperatures from 4.2°C to 2.0°C (Table S3.2). Simulated differences in bottom water conditions between the Midcontinent Shelf and the AB in *SlopeSeaLowMtn* indicate that ~1.4‰ (or 30%) of the onshore-offshore increase in mollusk and brachiopod $\delta^{18}O$ of ~5.0‰ is from

decreased seawater freshening and the remainder is from decreased temperatures with greater depths.

Remaining data-model discrepancies may be due to uncertainty of model boundary conditions in deep time and/or model grid resolution. The eastern NAMS, particularly the IB and AB, may have been located to the south of the equator between 310 and 298 Ma (Matthews et al., 2016), rather than flanking the northern margin of the paleoequator as in our experiments. Additionally, the Ancestral Rocky Mountains, located in the northwest of the NAMS, are not included in the simulations presented here. In an additional experiment that assesses the uncertainty in these boundary conditions, we found comparable values of $\delta^{18}O_w$ and temperature (Figure S3.6) as well as circulation patterns in the NAMS (Figure S3.7). Based on these results, we argue that paleogeographic modifications within the uncertainty of the reconstructions are likely of secondary importance (Lowry et al., 2014). Sub-grid scale paleobathymetric features, such as the Mississippi River Arch (Heckel, 1977), are not resolved at the grid resolution of our simulations, and may lead to local deviations in temperature, $\delta^{18}O_w$, or circulation at individual proxy sites from larger-scale patterns in the NAMS. That said, broad agreement between simulated temperatures and $\delta^{18}O$ paleotemperatures using model-based $\delta^{18}O_w$ suggest that our simulations sufficiently capture first-order patterns of temperature, $\delta^{18}O_w$, and circulation in the NAMS.

3.5.5 Glacial-interglacial changes in nearshore seawater freshening rival effects of temperature

Variations of marine biogenic $\delta^{18}O$ in Pennsylvanian cyclothems from the NAMS have been used to infer a wide range of sea level fluctuations (30 to 170+ m) (e.g., Adlis et al., 1988; Joachimski et al., 2006; Mazzullo et al., 2007; Rygel et al., 2008; Elrick and Scott, 2010). Differences in marine biogenic $\delta^{18}O$ between highstand and lowstand deposits integrate changes in global average $\delta^{18}O_w$, temperature, and local freshwater input over glacial-interglacial cycles that are challenging to differentiate from geochemical data alone. Generally, both high-latitude ice-sheet accumulation and seawater cooling associated with glacial periods produce higher proxy $\delta^{18}O$ values, whereas increased ambient seawater freshening causes a decrease in marine biogenic $\delta^{18}O$. To estimate the contribution of high-latitude ice-sheet volume, and thus glacioeustatic sea level fluctuation, to changes of marine biogenic $\delta^{18}O$, past studies have assumed that glacial-interglacial SST variations were similar to those in the Pleistocene (~2–

4°C) (Waelbroeck et al., 2009) and/or the effects of ambient seawater freshening were negligible (Elrick and Scott, 2010; Joachimski et al., 2006; Adlis et al., 1988). However, these assumptions may not be appropriate for Late Paleozoic glacial-interglacial changes in epicontinental SST and $\delta^{18}O_w$.

Differences between *Glacial-SlopeSeaLowMtn* and (interglacial) *SlopeSeaLowMtn* provide an estimate of glacial-interglacial changes in temperature and seawater freshening across the NAMS during the Pennsylvanian. SSTs cool by ~4°C in the NAMS from the interglacial *SlopeSeaLowMtn* simulation to the *Glacial-SlopeSeaLowMtn* simulation (Figure 3.4D), which is on the upper end of Pleistocene glacial-interglacial SST differences and would correspond to a ~0.8‰ increase in conodont $\delta^{18}O$ (Elrick and Scott, 2010; Joachimski et al., 2006). Glacial-interglacial differences in epicontinental $\delta^{18}O_w$ caused by changes in local seawater freshening are spatially disparate, with a slight increase of ~0.1‰ in the MB and decrease of ~0.7‰ in the Midcontinent Shelf between interglacial and glacial simulations (i.e., *SlopeSeaLowMtn* versus *Glacial-SlopeSeaLowMtn*; Figure 3.4C). Although the total amount of freshwater runoff received by the NAMS is ~25% less in *Glacial-SlopeSeaLowMtn*, the degree of seawater freshening is higher in the Midcontinent Shelf in the glacioeustatic lowstand case because a relatively larger amount of cumulative annual runoff (~860 mSv) is directed into this region. Superestuarine circulation patterns break down in the *Glacial-SlopeSeaLowMtn* simulation with a net onshore transport of surface waters that prevents the oceanward flow of nearshore low-salinity surface waters (Figure 3.4D), resulting in slightly higher $\delta^{18}O_w$ in the MB than for the interglacial simulation *SlopeSeaLowMtn*. The contribution of local seawater freshening to isotopic variation in more offshore regions such as the MB may have been relatively small. Importantly, results from the Midcontinent Shelf suggest that increases in marine biogenic $\delta^{18}O$ due to ambient seawater cooling could be almost equally opposed by concomitant decreases in marine biogenic $\delta^{18}O$ associated with seawater freshening. These results stress that glacial-interglacial variations in local seawater freshening should be considered in addition to temperature for nearshore regions of epicontinental seas such as the NAMS as such variations in surface $\delta^{18}O_w$ could potentially contribute to increased spread in $\delta^{18}O$-based estimates of glacioeustasy.

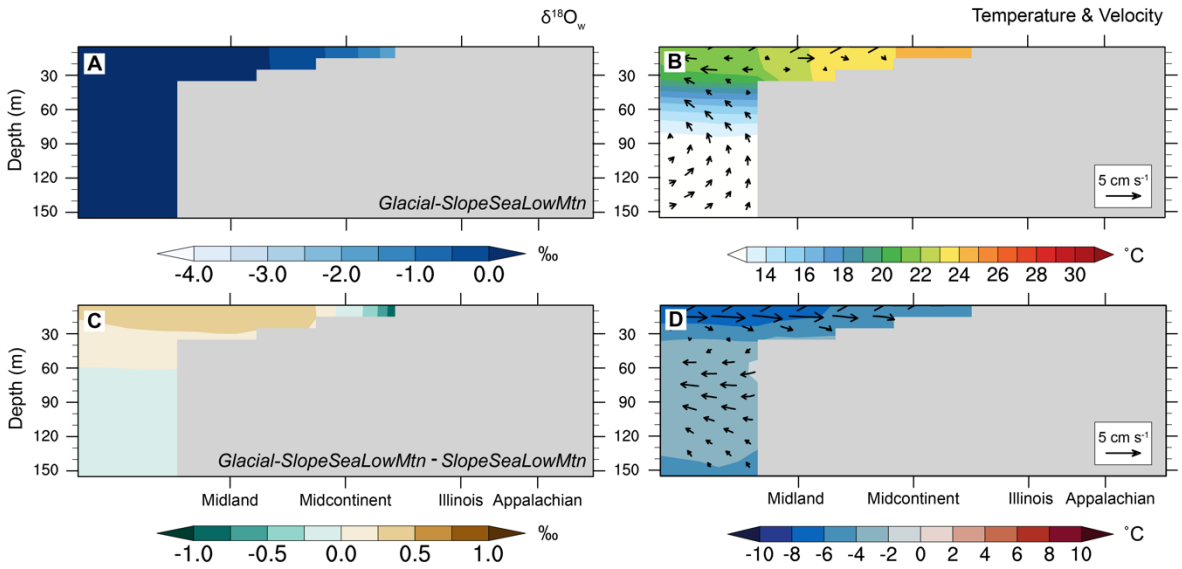

Figure 3.4 Longitude-depth cross sections in the NAMS for a glacioeustatic lowstand. Longitude-depth cross sections of mean annual (A) seawater $\delta^{18}O$ ($\delta^{18}O_w$; ‰) and (B) temperature (°C) and velocity (cm s^{-1}) in the NAMS for a glacioeustatic lowstand (glacial) scenario of *SlopeSeaLowMtn*, or *Glacial-SlopeSeaLowMtn*. Values are calculated as an average from 0–10°N. Note that the vertical component of the velocity has been multiplied by a scalar (5,000 cm s^{-1}) and that the Illinois and Appalachian Basins are above sea level in this case. Differences in mean annual (C) $\delta^{18}O_w$ (due to changes in ambient seawater freshening only) and (D) temperature (°C) and velocity (cm s^{-1}) between *SlopeSeaLowMtn* and *Glacial-SlopeSeaLowMtn* are also shown. The continental shelf is in gray.

3.6 Modeling limitations

This study represents an important first step in understanding epicontinental sea circulation and oxygen isotopic composition. We have shown that isotope-enabled Earth system models such as iCESM are a valuable tool for constraining the local environmental factors that potentially influenced epicontinental $\delta^{18}O_w$, temperature, and circulation in the NAMS and should be considered for investigating other ancient epicontinental seas. It is important to note, however, that our implementation of iCESM has some limitations. High-resolution regional ocean models are able to better represent epicontinental seas by including flow-topography interactions (e.g. bathymetric sills), tidal and near-surface wind-driven mixing processes in estuaries, and other non-steady dynamics. The treatment of riverine freshwater in iPOP as a vertical flux of "augmented precipitation" that is spread over a large region surrounding the river mouth omits any estuarine mixing or exchange processes, and modifications to these river input

methods can have an appreciable influence on coastal ocean salinity and stratification (Tseng et al., 2016). The resolution in the upper ocean corresponds to at most 12 vertical levels in the NAMS for the simulations presented here, which may be inadequate for resolving steep vertical gradients in salinity, temperature, and $\delta^{18}O_w$. Consequently, nesting a regional ocean model in an Earth system model or implementing a high-resolution version of iPOP will provide a more complete representation of ancient epicontinental seas. Given the computational cost of high-resolution simulations and the large uncertainty surrounding the NAMS bathymetry, we determined that the ability to run multiple sensitivity simulations in a globally integrated framework (i.e. allowing for dynamic interactions between the open ocean, terrestrial hydrologic cycle, and the NAMS) outweighed the benefit of higher spatial resolution in this first-time modeling study of the NAMS. While the limitations described above may affect the details of our results, we do not believe that they influence the important conclusions of this study.

3.7 Conclusions and Implications

Orographic precipitation from the CPM produces large amounts of freshwater runoff that feed into the NAMS, producing offshore-onshore patterns of decreasing $\delta^{18}O_w$ and superestuarine circulation during glacioeustatic highstands. Offshore-onshore decreases in surface $\delta^{18}O_w$ are enhanced by higher CPM due to the combination of increased continental runoff and decreased values of runoff $\delta^{18}O$. Epicontinental sea depth modifies the degree of mixing between upwelled marine water and surface brackish water, with greater depths enhancing the influence of marine water in the NAMS and thus increasing values of near-bottom $\delta^{18}O_w$. Proxy-based $\delta^{18}O$ paleotemperatures using simulated values of epicontinental $\delta^{18}O_w$ support that offshore-onshore variation in conodont $\delta^{18}O$ is primarily driven by increased proximity to freshwater runoff, whereas brachiopod and mollusk $\delta^{18}O$ values are influenced by seawater freshening as well as the presence of upwelled marine water in regions offshore of the Midcontinent Shelf. Glacial-interglacial variation in epicontinental $\delta^{18}O_w$ due to local seawater freshening may be as important as the changes in ambient seawater temperature on marine biogenic $\delta^{18}O$, and thus should be considered in $\delta^{18}O$-based inferences of glacioeustasy from nearshore regions of the NAMS and other comparable epicontinental seas. Notably, patterns of $\delta^{18}O_w$, salinity, and temperature from a simulation with shallow epicontinental depths that

deepen towards the continental margin and relatively low-elevation CPM (i.e. *SlopeSeaLowMtn*) most closely capture the seawater characteristics inferred from published geochemical evidence, and thus provide support for relatively shallow depth in the NAMS.

Negative deviations of low-latitude epicontinental $\delta^{18}O_w$ compared to the nearby open ocean may be relevant to interpretations of the Phanerozoic oxygen isotope secular curve. Records of marine calcite $\delta^{18}O$ reveal an ~8‰ increase over the past half billion years with two first-order and long debated hypotheses for the origin of this long-term $\delta^{18}O$ trend (e.g., Meuhlenbachs and Clayton, 1976; Gregory and Taylor, 1981; Veizer and Prokoph, 2015; Bergmann et al., 2018; Ryb and Eiler, 2018). The first is the progressive increased influence of diagenesis in more deeply buried sedimentary deposits over time (e.g., Land, 1995). The second is a secular increase in global $\delta^{18}O_w$ over the Phanerozoic driven in large part by high-temperature isotopic exchange between seawater and seafloor at mid-ocean ridges (Gregory and Taylor, 1981; Veizer and Prokoph, 2015). In the Phanerozoic, the range of low-latitude calcite $\delta^{18}O$ values increases from between ~0 to –4.0‰ during the Jurassic and Cretaceous to 0 to –12.0‰ around ~200 Mya, with the maximum value remaining ~0‰ through time. Oceanic crust older than ~200 Mya is not preserved, and thus pre-Jurassic records of calcite $\delta^{18}O$ are primarily from low-latitude epicontinental seas (Veizer & Prokoph, 2015). We hypothesize that open-ocean $\delta^{18}O_w$ has remained relatively constant over the past ~500 Ma, as evidenced by the absence of values greater than 0‰, and in line with recent studies of clumped isotopes (Bergmann et al., 2018; Ryb and Eiler, 2018). We further suggest that the growing range of calcite $\delta^{18}O$ and more negatives values (prior to ~200 Mya) reflect the outsized influence of low-latitude epicontinental seas in marine records that have been impacted by freshwater runoff and diagenetic overprinting. Furthermore, we show that spatial variation of bottom $\delta^{18}O_w$ and temperature in a low-latitude epicontinental sea such as the NAMS can account for calcite $\delta^{18}O$ values as low as –5.0‰. Even lower values of $\delta^{18}O_w$ in epicontinental seas could result from shallower sea depths than used for our simulations due to increased seawater freshening. That said, biogenic calcite $\delta^{18}O$ values less than −5.0‰ are challenging to argue as archiving seawater conditions and rather likely carry the overprinting signature of diagenetic alteration.

3.8 Acknowledgements and funding

This work was supported by the National Science Foundation (NSF) awards 1338200 (C.J.P.) and 1338281 (I.P.M.). We thank members of the Poulsen lab for helpful discussion. We also acknowledge high-performance computing support from Cheyenne (doi:10.5065/D6RX99HX) provided by the National Center for Atmospheric Research's Computational and Information Systems Laboratory, sponsored by NSF.

3.9 References

Adlis, D.S., Grossman, E.L., Yancey, T.E., McLerran, R.D., 1988. Isotope stratigraphy and paleodepth changes of Pennsylvanian cyclical sedimentary deposits. Palaios 3, 487–506. https://doi.org/10.2307/3514722

Algeo, T.J., Heckel, P.H., 2008. The Late Pennsylvanian Midcontinent Sea of North America: A review. Palaeogeogr. Palaeoclimatol. Palaeoecol. 268, 205–221. https://doi.org/10.1016/j.palaeo.2008.03.049

Algeo, T.J., Herrmann, A.D., 2018. An ancient estuarine-circulation nutrient trap: The Late Pennsylvanian Midcontinent Sea of North America. Geology 46, 143–146. https://doi.org/10.1130/G39804.1

Bergmann, K.D., Finnegan, S., Creel, R., Eiler, J.M., Hughes, N.C., Popov, L.E., Fischer, W.W., 2018. A paired apatite and calcite clumped isotope thermometry approach to estimating Cambro-Ordovician seawater temperatures and isotopic composition. Geochim. Cosmochim. Acta 224, 18–41. https://doi.org/10.1016/j.gca.2017.11.015

Brady, E., Stevenson, S., Bailey, D., Liu, Z., Noone, D., Nusbaumer, J., Otto-Bliesner, B.L., Tabor, C., Tomas, R., Wong, T., Zhang, J., Zhu, J., 2019. The connected isotopic water cycle in the Community Earth System Model Version 1. J. Adv. Model. Earth Syst. 11, 2547–2566. https://doi.org/10.1029/2019MS001663

Brand, U., 1987. Depositional analysis of the Breathitt Formation's marine horizons, Kentucky, U.S.A.: trace elements and stable isotopes. Chem. Geol. 65, 117–136. https://doi.org/10.1016/0168-9622(87)90068-6

Brand, U., 1981. Mineralogy and chemistry of the lower Pennsylvanian Kendrick fauna, eastern Kentucky: 1. trace elements. Chem. Geol. 32, 1–16. https://doi.org/10.1016/0009-2541(81)90124-8

Brand, U., Tazawa, J.I., Sano, H., Azmy, K., Lee, X., 2009. Is mid-late Paleozoic ocean-water chemistry coupled with epeiric seawater isotope records? Geology 37, 823–826. https://doi.org/10.1130/G30038A.1

Danabasoglu, G., Bates, S.C., Briegleb, B.P., Jayne, S.R., Jochum, M., Large, W.G., Peacock, S., Yeager, S.G., 2012. The CCSM4 ocean component. J. Clim. 25, 1361–1389. https://doi.org/10.1175/JCLI-D-11-00091.1

Danabasoglu, G., Large, W.G., Tribbia, J.J., Gent, P.R., Briegleb, B.P., McWilliams, J.C., 2006. Diurnal coupling in the tropical oceans of CCSM3. J. Clim. 19, 2347–2365. https://doi.org/10.1175/JCLI3739.1

Domeier, M., Torsvik, T.H., 2014. Plate tectonics in the Late Paleozoic. Geosci. Front. 5, 303–350. https://doi.org/10.1016/j.gsf.2014.01.002

Elrick, M., Scott, L.A., 2010. Carbon and oxygen isotope evidence for high-frequency (10^4-10^5 yr) and My-scale glacio-eustasy in Middle Pennsylvanian cyclic carbonates (Gray Mesa Formation), central New Mexico. Palaeogeogr. Palaeoclimatol. Palaeoecol. 285, 307–320. https://doi.org/10.1016/j.palaeo.2009.11.023

Gough, D.O., 1981. Solar interior structure and luminosity variations. Sol. Phys. 74, 21–34. https://doi.org/10.1007/BF00151270

Gregory, R.T., Taylor, H.P., 1981. An Oxygen Isotope Profile in a Section of Cretaceous Oceanic Crust, Samail Ophiolite, Oman: Evidence for $\delta^{18}O$ Buffering of the Oceans by Deep (>5 km) Seawater-Hydrothermal Circulation at Mid-Ocean Ridges. J. Geophys. Res. Solid Earth 86, 2737–2755. https://doi.org/10.1029/jb086ib04p02737

Griffies, S.M., Gnanadesikan, A., Dixon, K.W., Dunne, J.P., Gerdes, R., Harrison, M.J., Rosati, A., Russell, J.L., Samuels, B.L., Spelman, M.J., Winton, M., Zhang, R., 2005. Formulation of an ocean model for global climate simulations. Ocean Sci. 1, 45–79. https://doi.org/10.5194/os-1-45-2005

Griffies, S.M., Pacanowski, R.C., Hallberg, R.W., 2000. Spurious diapycnal mixing associated with advection in a z-coordinate ocean model. Mon. Weather Rev. 128, 538–564. https://doi.org/10.1175/1520-0493(2000)128<0538:SDMAWA>2.0.CO;2

Griffis, N.P., Montañez, I.P., Fedorchuk, N., Isbell, J., Mundil, R., Vesely, F., Weinshultz, L., Iannuzzi, R., Gulbranson, E., Taboada, A., Pagani, A., Sanborn, M.E., Huyskens, M., Wimpenny, J., Linol, B., Yin, Q.Z., 2019. Isotopes to ice: Constraining provenance of glacial deposits and ice centers in west-central Gondwana. Palaeogeogr. Palaeoclimatol. Palaeoecol. 531, 31–182. https://doi.org/10.1016/j.palaeo.2018.04.020

Griffis, N.P., Montañez, I.P., Isbell, J., Mundil, R., Vesely, F., Iannuzzi, R., Gulbranson, E., Taboada, A., Pagani, A., Sanborn, M.E., Huyskens, M., Wimpenny, J., Linol, B., Yin, Q., Isbell, J., Mundil, R., Vesely, F., Weinshultz, L., Huyskens, M., Wimpenny, J., Linol, B., Yin, Q., 2018. Isotopes to ice: Constraining provenance of glacial deposits and ice centers in west-central Gondwana. Palaeogeogr. Palaeoclimatol. Palaeoecol. #pagerange#. https://doi.org/10.1016/j.palaeo.2018.04.020

Grossman, E.L., Yancey, T.E., Jones, T.E., Bruckschen, P., Chuvashov, B., Mazzullo, S.J., Mii, H., 2008. Glaciation, aridification, and carbon sequestration in the Permo-Carboniferous: The isotopic record from low latitudes. Palaeogeogr. Palaeoclimatol. Palaeoecol. 268, 222–233. https://doi.org/10.1016/j.palaeo.2008.03.053

Hays, P.D., Grossman, E.L., 1991. Oxygen isotopes in meteoric calcite cements as indicators of continental paleoclimate. Geology 19, 441–444.

Heavens, N.G., Shields, C.A., Mahowald, N.M., 2012. A paleogeographic approach to aerosol prescription in simulations of deep time climate. J. Adv. Model. Earth Syst. 4. https://doi.org/10.1029/2012MS000166

Heckel, P.H., 1994. Evaluation of evidence for glacio-eustatic control over marine Pennsylvanian cyclothems in North America and consideration of possible tectonic effects, in: Dennison, J.M., Ettensohn, F.R. (Eds.), Tectonic and Eustatic Controls on Sedimentary Cycles. SEPM Society for Sedimentary Geology, pp. 65–87.

Heckel, P.H., 1977. Origin of phosphatic black shale facies in Pennsylvanian cyclothems of Mid-Continent North America. Am. Assoc. Pet. Geol. Bull. 61, 1045–1068.

Henkes, G.A., Passey, B.H., Grossman, E.L., Shenton, B.J., Yancey, T.E., Pérez-Huerta, A., 2018. Temperature evolution and the oxygen isotope composition of Phanerozoic oceans from carbonate clumped isotope thermometry. Earth Planet. Sci. Lett. 490, 40–50. https://doi.org/10.1016/j.epsl.2018.02.001

Holmden, C., Creaser, R.A., Muehlenbachs, K., Leslie, S.A., Bergström, S.M., 1998. Isotopic evidence for geochemical decoupling between ancient epeiric seas and bordering oceans: implications for secular curves. Geology 26, 567–570. https://doi.org/10.1130/0091-7613(1998)026<0567:IEFGDB>2.3.CO;2

Hurrell, J.W., Holland, M.M., Gent, P.R., Ghan, S., Kay, J.E., Kushner, P.J., Lamarque, J.F., Large, W.G., Lawrence, D., Lindsay, K., Lipscomb, W.H., Long, M.C., Mahowald, N., Marsh, D.R., Neale, R.B., Rasch, P., Vavrus, S., Vertenstein, M., Bader, D., Collins, W.D., Hack, J.J., Kiehl, J., Marshall, S., 2013. The community earth system model: A framework for collaborative research. Bull. Am. Meteorol. Soc. 94, 1339–1360. https://doi.org/10.1175/BAMS-D-12-00121.1

Jimenez, M.Y., Ivany, L.C., Judd, E.J., Henkes, G., 2019. Low and seasonally variable salinity in the Pennsylvanian equatorial Appalachian Basin. Earth Planet. Sci. Lett. 519, 182–191. https://doi.org/10.1016/j.epsl.2019.04.051

Joachimski, M.M., Lambert, L.L., 2015. Salinity contrast in the US Midcontinent Sea during Pennsylvanian glacio-eustatic highstands: Evidence from conodont apatite $\delta^{18}O$. Palaeogeogr. Palaeoclimatol. Palaeoecol. 433, 71–80. https://doi.org/10.1016/j.palaeo.2015.05.014

Joachimski, M.M., von Bitter, P.H., Buggisch, W., 2006. Constraints on Pennsylvanian glacioeustatic sea-level changes using oxygen isotopes of conodont apatite. Geology 34, 277–280. https://doi.org/10.1130/G22198.1

Judd, E.J., Bhattacharya, T., Ivany, L.C., 2020. A dynamical framework for interpreting ancient sea surface temperatures. Geophys. Res. Lett. https://doi.org/10.1029/2020GL089044

Ladant, J.B., Poulsen, C.J., Fluteau, F., Tabor, C.R., Macleod, K.G., Martin, E.E., Haynes, S.J., Rostami, M.A., 2020. Paleogeographic controls on the evolution of Late Cretaceous ocean circulation. Clim. Past 16, 973–1006. https://doi.org/10.5194/cp-16-973-2020

Land, L.S., 1995. Comment on "Oxygen and carbon isotopic composition of Ordovician brachiopods: Implications for coeval seawater" by H. Qing and J. Veizer. Geochim. Cosmochim. Acta 59, 2843–2844. https://doi.org/10.1016/0016-7037(95)00176-Z

Lowry, D.P., Poulsen, C.J., Horton, D.E., Torsvik, T.H., Pollard, D., 2014. Thresholds for Paleozoic ice sheet initiation. Geology 42, 627–630. https://doi.org/10.1130/G35615.1

Matthews, K.J., Maloney, K.T., Zahirovic, S., Williams, S.E., Seton, M., Müller, R.D., 2016. Global plate boundary evolution and kinematics since the late Paleozoic. Glob. Planet. Change. https://doi.org/10.1016/j.gloplacha.2016.10.002

Mazzullo, S.J., Boardman, D.R., Grossman, E.L., Dimmick-Wells, K., 2007. Oxygen-carbon isotope stratigraphy of upper Carboniferous to lower Permian marine deposits in Midcontinent U.S.A. (Kansas and NE Oklahoma): Implications for sea water chemistry and depositional cyclicity. Carbonates and Evaporites 22, 55–72. https://doi.org/10.1007/BF03175846

Meuhlenbachs, K., Clayton, R.N., 1976. Oxygen Isotope Composition of the Oceanic Crust and Its Bearing on Seawater. J. Geophys. Res. 81, 4365–4369. https://doi.org/10.1029/JB081i023p04365

Mii, H.S., Grossman, E.L., Yancey, T.E., 1999. Carboniferous isotope stratigraphies of North America: Implications for Carboniferous paleoceanography and Mississippian glaciation. Bull. Geol. Soc. Am. 111, 960–973. https://doi.org/10.1130/0016-7606(1999)111<0960:CISONA>2.3.CO;2

Mii, H.S., Grossman, E.L., Yancey, T.E., Chuvashov, B., Egorov, A., 2001. Isotopic records of brachiopod shells from the Russian Platform - Evidence for the onset of mid-Carboniferous glaciation. Chem. Geol. 175, 133–147. https://doi.org/10.1016/S0009-2541(00)00366-1

Montañez, I.P., McElwain, J.C., Poulsen, C.J., White, J.D., Dimichele, W.A., Wilson, J.P., Griggs, G., Hren, M.T., 2016. Climate, pCO_2 and terrestrial carbon cycle linkages during late Palaeozoic glacial–interglacial cycles. Nat. Geosci. 9, 824–828. https://doi.org/10.1038/ngeo2822

Montañez, I.P., Osleger, D.J., Chen, J., Wortham, B.E., Stamm, R.G., Nemyrovska, T.I., Griffin, J.M., Poletaev, V.I., Wardlaw, B.R., 2018. Carboniferous climate teleconnections archived in coupled bioapatite $\delta^{18}O_{PO4}$ and $^{87}Sr/^{86}Sr$ records from the epicontinental Donets Basin, Ukraine. Earth Planet. Sci. Lett. 492, 89–101. https://doi.org/10.1016/j.epsl.2018.03.051

Montañez, I.P., Poulsen, C.J., 2013. The Late Paleozoic Ice Age: An Evolving Paradigm. Annu. Rev. Earth Planet. Sci. 41, 629–656. https://doi.org/10.1146/annurev.earth.031208.100118

Narkiewicz, M., Narkiewicz, K., Krzeminska, E., Kruchek, S.A., 2017. Oxygen Isotopic Composition of Conodont Apatite in the Equatorial Epeiric Belarussian Basin (Eifelian)–Relationship To Fluctuating Seawater Salinity and Temperature. Palaios 32, 439–447. https://doi.org/10.2110/palo.2016.059

Panchuk, K.M., Holmden, C., Kump, L.R., 2005. Sensitivity of the epeiric sea carbon isotope record to local-scale carbon cycle processes: Tales from the Mohawkian Sea. Palaeogeogr. Palaeoclimatol. Palaeoecol. 228, 320–337. https://doi.org/10.1016/j.palaeo.2005.06.019

Panchuk, K.M., Holmden, C.E., Leslie, S.A., 2006. Local controls on carbon cycling in the Ordovician Midcontinent region of North America, with implications for carbon isotope secular curves. J. Sediment. Res. 76, 200–211. https://doi.org/10.2110/jsr.2006.017

Peters, S.E., Husson, J.M., 2017. Sediment cycling on continental and oceanic crust. Geology 45, 323–326. https://doi.org/10.1130/G38861.1

Petersen, S. V., Tabor, C.R., Lohmann, K.C., Poulsen, C.J., Meyer, K.W., Carpenter, S.J., Erickson, J.M., Matsunaga, K.K.S., Smith, S.Y., Sheldon, N.D., 2016. Temperature and salinity of the late cretaceous western interior seaway. Geology 44, 903–906. https://doi.org/10.1130/G38311.1

Pörtner, H.O., 2002. Climate variations and the physiological basis of temperature dependent biogeography: Systemic to molecular hierarchy of thermal tolerance in animals. Comp. Biochem. Physiol. 132, 739–761. https://doi.org/10.1016/S1095-6433(02)00045-4

Pucéat, E., Joachimski, M.M., Bouilloux, A., Monna, F., Bonin, A., Motreuil, S., Morinière, P., Hénard, S., Mourin, J., Dera, G., Quesne, D., 2010. Revised phosphate-water fractionation equation reassessing paleotemperatures derived from biogenic apatite. Earth Planet. Sci. Lett. 298, 135–142. https://doi.org/10.1016/j.epsl.2010.07.034

Richey, J.D., Montañez, I.P., Goddéris, Y., Looy, C. V, Griffis, N.P., William, A., 2020. Influence of temporally varying weatherability on CO_2–climate coupling and ecosystem change in the late Paleozoic. Clim. Past Discuss. 1–37. https://doi.org/10.5194/cp-2020-50

Roark, A., Flake, R., Grossman, E.L., Olszewski, T., Lebold, J., Thomas, D., Marcantonio, F., Miller, B., Raymond, A., Yancey, T., 2017. Brachiopod geochemical records from across the Carboniferous seas of North America: Evidence for salinity gradients, stratification, and

circulation patterns. Palaeogeogr. Palaeoclimatol. Palaeoecol. 485, 136–153. https://doi.org/10.1016/j.palaeo.2017.06.009

Rosenau, N.A., Tabor, N.J., Herrmann, A.D., 2014. Assessing the paleoenvironmental significance of middle-late Pennsylvanian conodont apatite ^{18}O values in the Illinois Basin. Palaios 29, 250–265. https://doi.org/10.2110/palo.2013.112

Ryb, U., Eiler, J.M., 2018. Oxygen isotope composition of the Phanerozoic ocean and a possible solution to the dolomite problem 115, 1–6. https://doi.org/10.1073/pnas.1719681115

Rygel, M.C., Fielding, C.R., Frank, T.D., Birgenheier, L.P., 2008. The Magnitude of Late Paleozoic Glacioeustatic Fluctuations: A Synthesis. J. Sediment. Res. 78, 500–511. https://doi.org/10.2110/jsr.2008.058

Sun, Q., Whitney, M.M., Bryan, F.O., Tseng, Y. heng, 2019. Assessing the Skill of the Improved Treatment of Riverine Freshwater in the Community Earth System Model (CESM) Relative to a New Salinity Climatology. J. Adv. Model. Earth Syst. 2. https://doi.org/10.1029/2018MS001349

Tabor, C.R., Otto-bliesner, B.L., Brady, E.C., Nusbaumer, J., Erb, M.P., Wong, T.E., Liu, Z., Noone, D., 2018. Interpreting Precession-Driven $\delta^{18}O$ Variability in the South Asian Monsoon Region. J. Geophys. Res. Atmos. 5927–5946. https://doi.org/10.1029/2018JD028424

Tseng, Y. heng, Bryan, F.O., Whitney, M.M., 2016. Impacts of the representation of riverine freshwater input in the community earth system model. Ocean Model. 105, 71–86. https://doi.org/10.1016/j.ocemod.2016.08.002

Turner, A.C.E., Algeo, T.J., Peng, Y., Herrmann, A.D., 2019. Circulation patterns in the Late Pennsylvanian North American Midcontinent Sea inferred from spatial gradients in sediment chemistry and mineralogy. Palaeogeogr. Palaeoclimatol. Palaeoecol. 531. https://doi.org/10.1016/j.palaeo.2018.12.008

van Geldern, R., Joachimski, M.M., Day, J., Jansen, U., Alvarez, F., Yolkin, E.A., Ma, X.P., 2006. Carbon, oxygen and strontium isotope records of Devonian brachiopod shell calcite. Palaeogeogr. Palaeoclimatol. Palaeoecol. https://doi.org/10.1016/j.palaeo.2006.03.045

Veizer, J., Prokoph, A., 2015. Temperatures and oxygen isotopic composition of Phanerozoic oceans. Earth-Science Rev. 146, 92–104. https://doi.org/10.1016/j.earscirev.2015.03.008

Waelbroeck, C., Paul, A., Kucera, M., Rosell-Melé, A., Weinelt, M., Schneider, R., Mix, A.C., Abelmann, A., Armand, L., Bard, E., Barker, S., Barrows, T.T., Benway, H., Cacho, I., Chen, M.T., Cortijo, E., Crosta, X., De Vernal, A., Dokken, T., Duprat, J., Elderfield, H., Eynaud, F., Gersonde, R., Hayes, A., Henry, M., Hillaire-Marcel, C., Huang, C.C., Jansen, E., Juggins, S., Kallel, N., Kiefer, T., Kienast, M., Labeyrie, L., Leclaire, H., Londeix, L., Mangin, S., Matthiessen, J., Marret, F., Meland, M., Morey, A.E., Mulitza, S., Pflaumann,

U., Pisias, N.G., Radi, T., Rochon, A., Rohling, E.J., Sbaffi, L., Schäfer-Neth, C., Solignac, S., Spero, H., Tachikawa, K., Turon, J.L., 2009. Constraints on the magnitude and patterns of ocean cooling at the Last Glacial Maximum. Nat. Geosci. 2, 127–132. https://doi.org/10.1038/ngeo411

Wilson, J.P., Montañez, I.P., White, J.D., DiMichele, W.A., McElwain, J.C., Poulsen, C.J., Hren, M.T., 2017. Dynamic Carboniferous tropical forests: new views of plant function and potential for physiological forcing of climate. New Phytol. 215, 1333–1353. https://doi.org/10.1111/nph.14700

Woodard, S.C., Thomas, D.J., Grossman, E.L., Olszewski, T.D., Yancey, T.E., Miller, B. V., Raymond, A., 2013. Radiogenic isotope composition of Carboniferous seawater from North American epicontinental seas. Palaeogeogr. Palaeoclimatol. Palaeoecol. 370, 51–63. https://doi.org/10.1016/j.palaeo.2012.11.018

Zhu, J., Liu, Z., Brady, E., Otto-Bliesner, B., Zhang, J., Noone, D., Tomas, R., Nusbaumer, J., Wong, T., Jahn, A., Tabor, C., 2017. Reduced ENSO variability at the LGM revealed by an isotope-enabled Earth system model. Geophys. Res. Lett. 44, 6984–6992. https://doi.org/10.1002/2017GL073406

Zhu, J., Poulsen, C.J., Otto-Bliesner, B.L., Liu, Z., Brady, E.C., Noone, D.C., 2020. Simulation of early Eocene water isotopes using an Earth system model and its implication for past climate reconstruction. Earth Planet. Sci. Lett. 537, 116164. https://doi.org/10.1016/j.epsl.2020.116164

Ziegler, A., 1985. Paleogeographic Interpretation: With an Example From the Mid-Cretaceous. Annu. Rev. Earth Planet. Sci. 13, 385–425. https://doi.org/10.1146/annurev.earth.13.1.385

3.10 Supplementary information

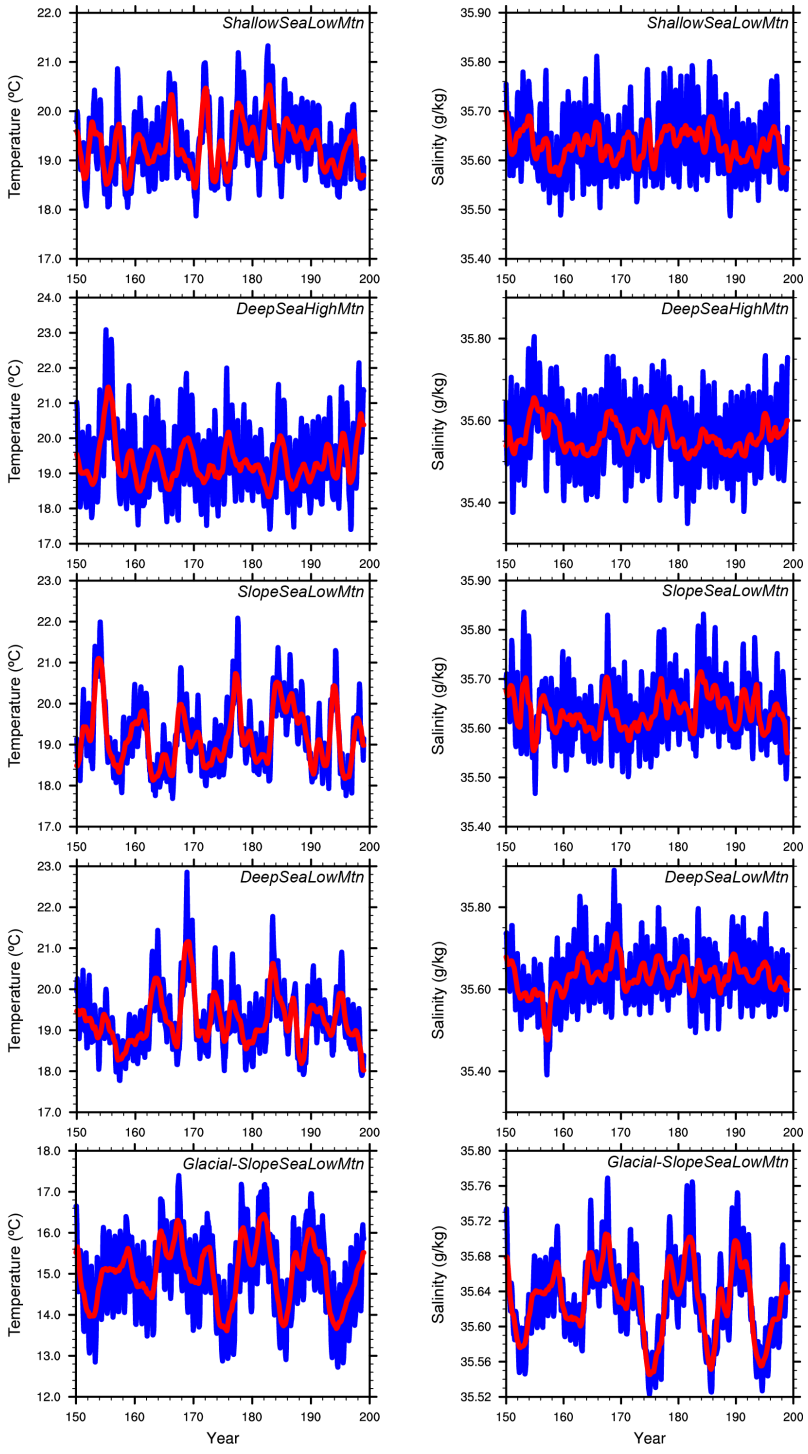

Figure S3.1 North American Midcontinent Sea (NAMS) salinity and temperature from simulation year 150–200. Mean values are plotted for each month (blue) and year (red). Note that mean temperature and salinity are relatively constant.

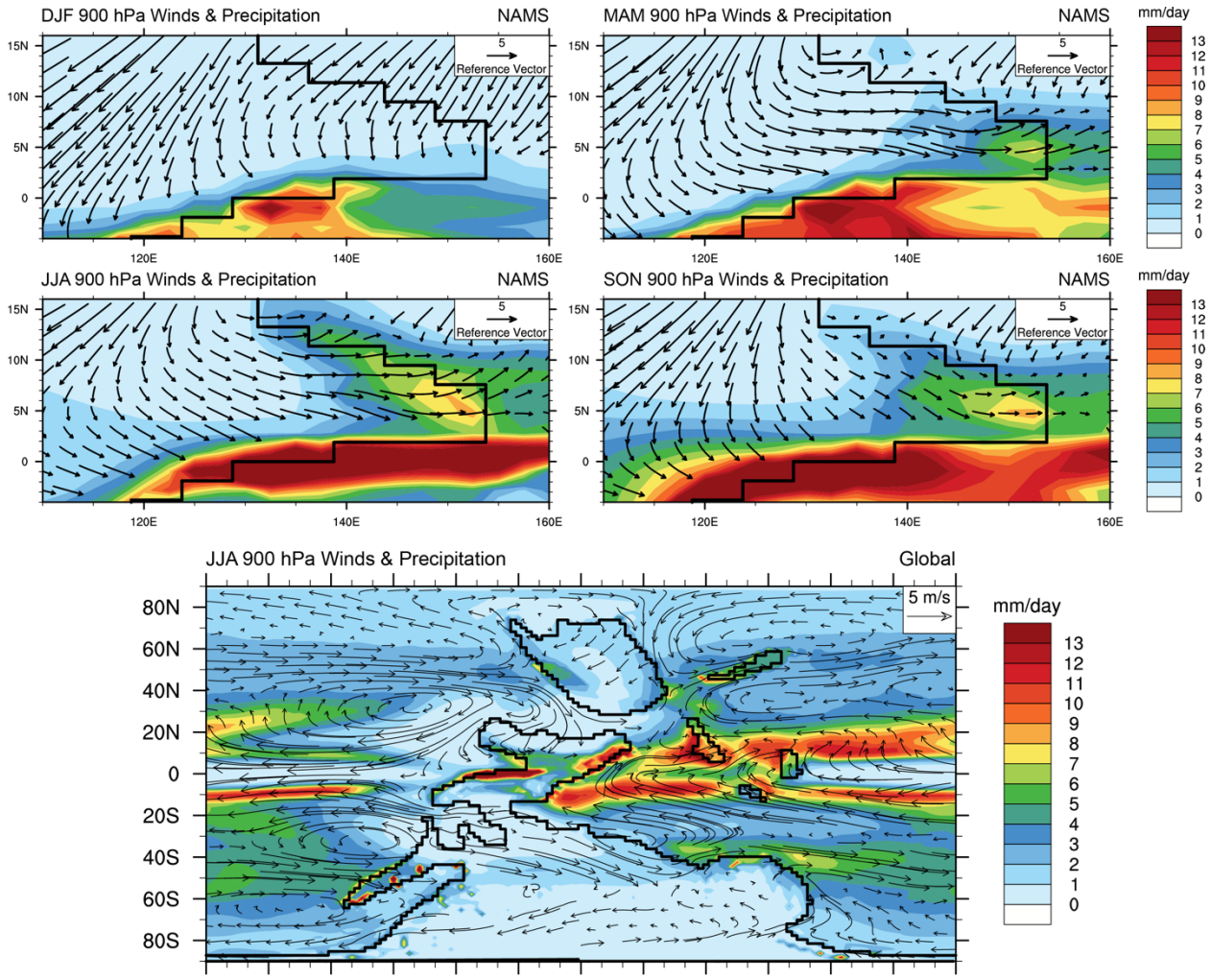

Figure S3.2 Seasonal 900hPa winds and total precipitation over the globe and NAMS region. Maps of mean seasonal winds at 900 hPa (m s^{-1}) and total precipitation (mm day^{-1}) over the NAMS in *DeepSeaHighMtn*. DJF=December-January-February, MAM=March-April-May, JJA=June-July-August, SON=September-October-November. Global mean JJA winds at 900 hPa and total precipitation are also shown in the bottom panel. Wind and precipitation patterns look similar across all simulations, though rainfall amounts over the Central Pangaean Mountains are lower in *DeepSeaLowMtn*, *ShallowSeaLowMtn*, and *SlopeSeaLowMtn*.

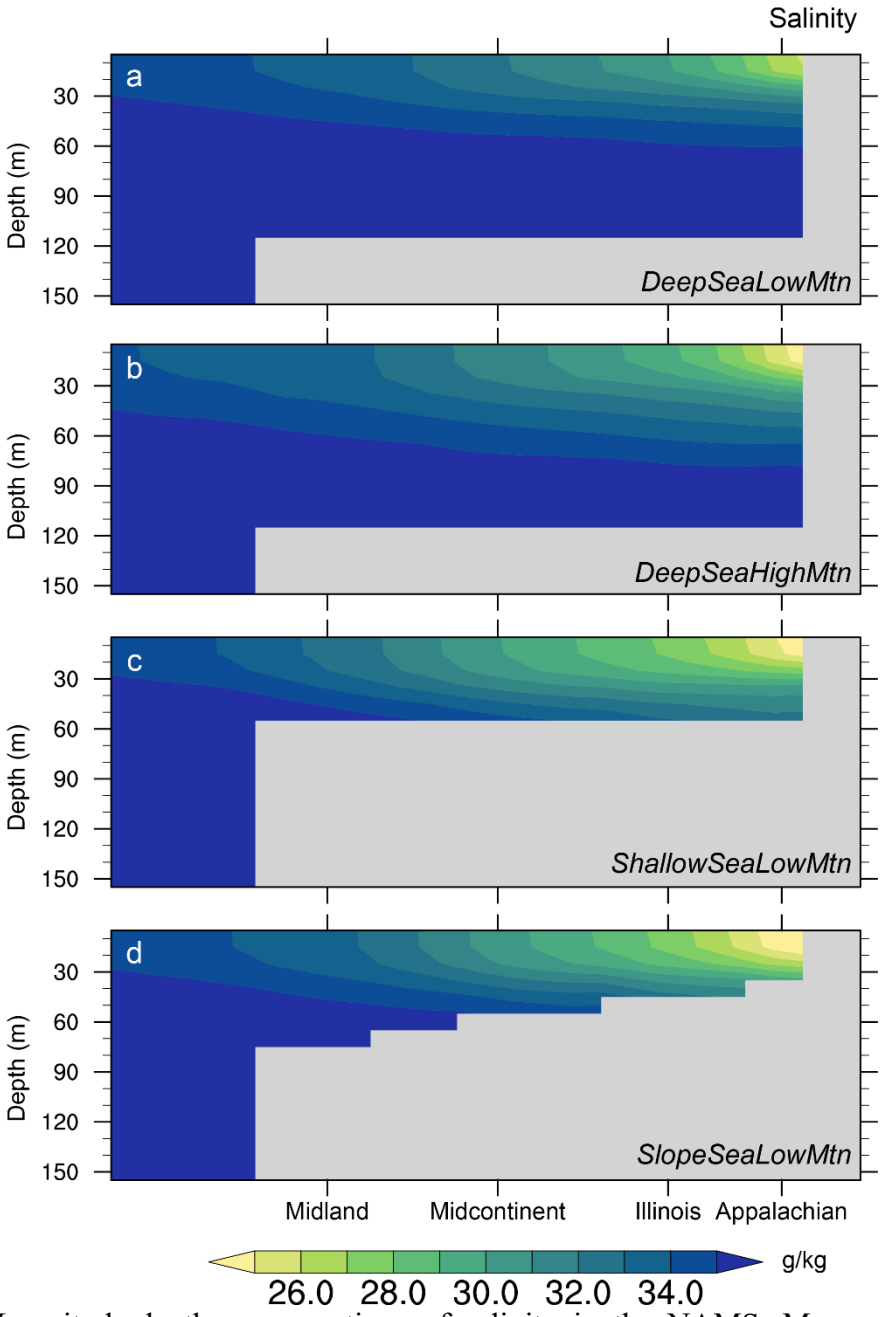

Figure S3.3 Longitude-depth cross sections of salinity in the NAMS. Mean annual salinity (g/kg) values are displayed across longitude (indicated here with regions in the NAMS). Values are calculated as an average from 0 to 10°N. The continental shelf is in gray.

ShallowSeaLowMtn	**$\delta^{18}O_w$ (‰)**		**Salinity (g/kg)**		**Runoff (mSv)**	**Temperature (˚C)**	
	Surface	**Bottom**	**Surface**	**Bottom**		**Surface**	**Bottom**
Appalachian							

Annual	–2.3	–1.1	26.8	31.6	503.2	29.9	28.4
DJF	–2.1	–0.9	27.3	32.6	179.8	29.7	27.8
MAM	–2.3	–1.3	26.3	31.0	94.7	29.6	28.4
JJA	–2.4	–1.2	26.1	31.0	155.3	30.1	28.9
SON	–2.0	–1.1	27.6	31.7	73.4	30.3	28.7
Illinois							
Annual	–1.8	–1.0	28.7	32.0	412.5	29.5	27.2
DJF	–1.8	–0.9	28.6	32.7	117.8	29.2	26.3
MAM	–1.6	–1.1	29.5	31.8	58.4	28.9	27.2
JJA	–1.8	–1.2	28.5	31.2	146.7	29.9	28.2
SON	–1.9	–1.0	28.1	32.2	90.0	30.2	27.3
Midcontinent							
Annual	–1.4	–0.7	30.5	33.4	340.4	29.1	24.8
DJF	–1.4	–0.6	30.4	33.8	87.0	29.0	23.7
MAM	–1.2	–0.8	30.9	32.9	71.9	28.5	25.4
JJA	–1.4	–0.8	30.7	33.1	133.2	29.2	25.9
SON	–1.5	–0.6	30.0	33.8	48.3	29.7	24.3
Midland							
Annual	–0.9	–0.5	32.5	34.7	152.6	28.1	22.0
DJF	–0.9	–0.4	32.5	35.0	32.0	27.7	21.0
MAM	–0.8	–0.5	32.8	34.2	21.7	27.9	23.6
JJA	–0.9	–0.4	32.6	34.7	67.5	27.9	22.3
SON	–1.0	–0.5	32.0	34.7	31.4	28.8	20.9
DeepSeaHighMtn	**$\delta^{18}O_w$ (‰)**		**Salinity (g/kg)**		**Runoff (mSv)**	**Temperature (˚C)**	
	Surface	**Bottom**	**Surface**	**Bottom**		**Surface**	**Bottom**
Appalachian							
Annual	–3.1	–0.2	27.3	35.7	602.8	29.2	17.1
DJF	–2.6	–0.2	28.8	35.8	161.7	27.7	17.0
MAM	–2.9	–0.2	27.8	35.7	126.2	29.2	17.2
JJA	–3.3	–0.2	26.7	35.7	185.1	29.7	17.2
SON	–3.4	–0.2	26.1	35.8	130.1	30.1	17.1
Illinois							
Annual	–1.9	–0.2	30.3	35.7	522.8	28.9	16.8
DJF	–2.0	–0.2	30.1	35.8	95.2	28.1	16.7
MAM	–1.7	–0.2	31.1	35.7	72.2	28.2	16.9
JJA	–1.8	–0.2	30.7	35.8	188.4	29.1	16.8
SON	–2.2	–0.3	29.4	35.7	168.6	30.0	16.8
Midcontinent							
Annual	–1.5	–0.2	31.7	35.8	500.2	29.0	16.5
DJF	–1.7	–0.2	31.0	35.8	104.0	28.5	16.2

MAM	–1.3	–0.2	32.2	35.7	116.3	28.3	16.7
JJA	–1.4	–0.2	32.0	35.8	168.7	29.0	16.5
SON	–1.5	–0.2	31.6	35.7	111.2	30.2	16.5
Midland							
Annual	–1.2	–0.2	32.5	35.8	270.9	28.4	15.9
DJF	–1.3	–0.2	32.2	35.8	51.4	27.8	16.4
MAM	–1.1	–0.2	32.8	35.8	45.4	27.8	16.1
JJA	–1.2	–0.2	32.7	35.8	92.0	28.4	15.7
SON	–1.3	–0.2	32.3	35.8	82.1	29.7	15.5
SlopeSeaLowMtn	**$\delta^{18}O_w$ (‰)**		**Salinity (g/kg)**		**Runoff (mSv)**	**Temperature (˚C)**	
	Surface	**Bottom**	**Surface**	**Bottom**		**Surface**	**Bottom**
Appalachian							
Annual	–2.3	–1.8	26.6	28.5	471.6	30.1	30.0
DJF	–2.2	–1.7	27.1	29.3	163.8	29.8	29.5
MAM	–2.3	–2.0	26.5	27.6	81.7	29.6	29.6
JJA	–2.6	–2.0	25.7	27.8	152.5	30.3	30.3
SON	–2.2	–1.7	27.1	29.1	73.7	30.8	30.4
Illinois							
Annual	–1.7	–1.1	28.9	31.8	392.3	29.1	27.1
DJF	–1.8	–0.9	28.8	32.5	109.3	28.7	25.9
MAM	–1.5	–1.1	29.8	31.6	52.3	28.5	27.1
JJA	–1.8	–1.3	28.9	31.0	139.4	29.6	28.5
SON	–1.9	–1.0	28.3	32.3	91.7	29.8	26.7
Midcontinent							
Annual	–1.2	–0.4	31.3	34.7	311.6	28.6	21.4
DJF	–1.2	–0.4	31.2	35.1	79.1	28.2	20.1
MAM	–1.1	–0.6	31.6	34.2	62.7	28.2	22.4
JJA	–1.2	–0.5	31.4	34.4	123.9	28.6	22.7
SON	–1.3	–0.4	30.8	35.1	46.0	29.2	20.6
Midland							
Annual	–0.8	–0.3	33.0	35.7	141.8	27.7	17.3
DJF	–0.8	–0.2	33.0	35.7	27.2	27.1	17.4
MAM	–0.7	–0.3	33.3	35.6	20.4	27.6	18.5
JJA	–0.8	–0.2	33.1	35.7	64.1	27.4	17.0
SON	–0.9	–0.3	32.5	35.6	30.1	28.7	16.5
DeepSeaLowMtn	**$\delta^{18}O_w$ (‰)**		**Salinity (g/kg)**		**Runoff (mSv)**	**Temperature (˚C)**	
	Surface	**Bottom**	**Surface**	**Bottom**		**Surface**	**Bottom**
Appalachian							
Annual	–1.8	–0.2	28.7	35.9	470.9	28.0	16.0
DJF	–1.8	–0.2	28.8	35.9	171.1	27.6	15.9

MAM	–2.0	–0.2	28.1	35.9	84.5	28.8	16.1
JJA	–1.9	–0.2	28.6	35.9	147.7	28.1	16.0
SON	–1.6	–0.2	29.5	35.9	67.6	27.6	15.9
Illinois							
Annual	–1.2	–0.2	31.1	35.9	388.5	28.1	15.6
DJF	–1.3	–0.2	30.8	35.9	111.6	27.8	15.6
MAM	–1.2	–0.2	31.4	35.9	51.3	27.9	15.8
JJA	–1.3	–0.2	31.0	35.9	140.6	28.6	15.6
SON	–1.2	–0.2	31.1	35.9	85.4	28.1	15.6
Midcontinent							
Annual	–1.0	–0.2	32.3	35.8	313.2	28.1	15.1
DJF	–1.0	–0.2	32.4	35.8	79.9	27.8	15.0
MAM	–0.8	–0.2	32.8	35.8	62.8	27.9	15.3
JJA	–1.1	–0.2	32.2	35.8	125.5	28.2	15.3
SON	–1.1	–0.2	31.9	35.8	44.9	28.6	15.0
Midland							
Annual	–0.8	–0.2	33.3	35.8	140.1	27.6	15.1
DJF	–0.7	–0.2	33.5	35.8	26.2	27.1	15.4
MAM	–0.6	–0.2	33.8	35.8	19.8	27.6	15.7
JJA	–0.8	–0.2	33.3	35.8	64.8	27.0	14.9
SON	–0.9	–0.2	32.5	35.8	29.3	28.6	14.1

Table S3.1 Mean seasonal and annual variables for each NAMS region in each experiment. DJF=December-January-February, MAM=March-April-May, JJA=June-July-August, SON=September-October-November. Surface and bottom refer to averages from 0–30 m depth and the greatest 30 m of each experiment (90–120 m in *DeepSeaLowMtn* and *DeepSeaHighMtn*, 30–60 m in *ShallowSeaLowMtn*, and the greatest 30 m varies in each region in *SlopeSeaLowMtn*).

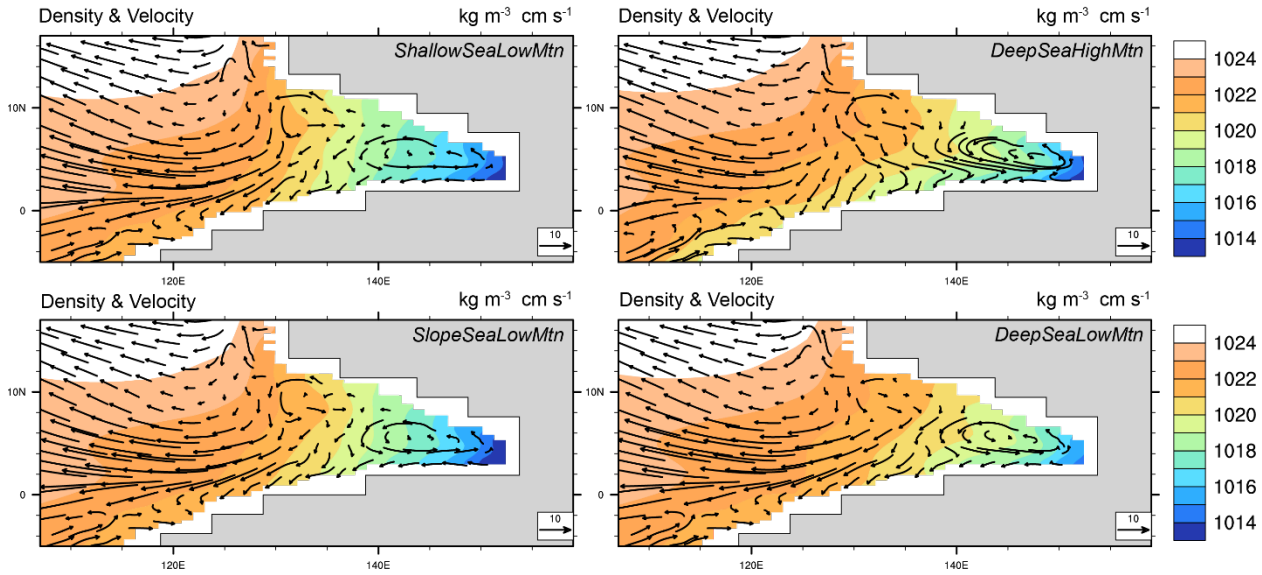

Figure S3.4 Sea surface density and velocity in the NAMS. Maps of mean annual sea surface density (kg m^{-3}) and velocity (cm s^{-1}) in the NAMS for each experiment. Note the counterclockwise circulation pattern in the eastern NAMS that results from an offshore increase in seawater density. Flow intensity increases with the gradient of surface density, which is greatest in *DeepSeaHighMtn*.

Case	Conodont $\delta^{18}O$					
	Annual		JJA		DJF	
	RMSE model	*RMSE cst*	*RMSE model*	*RMSE cst*	*RMSE model*	*RMSE cst*
ShallowSeaLowTopo	3.4	7.7	3.1	7.7	3.5	7.8
DeepSeaHighTopo	**2.1**	8.0	**2.1**	8.0	**3.1**	8.3
SlopeSeaLowTopo	3.2	7.6	3.0	7.6	3.3	7.7
DeepSeaLowTopo	5.1	8.6	4.8	8.4	5.2	8.8
Mean	3.5	8.0	3.3	7.9	3.8	8.2
Case	Brachiopod and Mollusk $\delta^{18}O$					
	Annual		JJA		DJF	
	RMSE model	*RMSE cst*	*RMSE model*	*RMSE cst*	*RMSE model*	*RMSE cst*
ShallowSeaLowTopo	5.1	5.4	5.0	5.2	5.3	5.7
DeepSeaHighTopo	13.3	12.3	13.2	12.2	13.7	12.7
SlopeSeaLowTopo	**2.0**	4.2	**2.5**	3.9	**1.6**	4.5
DeepSeaLowTopo	15.1	13.8	15.1	13.8	15.2	13.9
Mean	8.8	8.9	9.0	8.8	9.0	9.2

Table S3.2 Root mean square errors between simulated sea temperatures and proxy-inferred paleotemperature in Figure 3.3. Root mean square errors (RMSE, in °C) between simulated sea

temperatures and proxy-inferred paleotemperature estimates using spatially-varying model $\delta^{18}O_w$ (*RMSE model*) and a constant $\delta^{18}O_w = –0.5‰$ (*RMSE cst*). RMSE values are reported using mean annual, June-July-August (JJA), and December-January-February (DJF) temperatures and $\delta^{18}O_w$ for each model experiment. Bold values indicate the lowest RMSE value, or best fit between simulated and proxy-inferred temperatures, for each time interval (annual, JJA, and DJF). Note that the lowest RMSE values always coincide with model-based temperatures and proxy-based temperatures calculated with model $\delta^{18}O_w$.

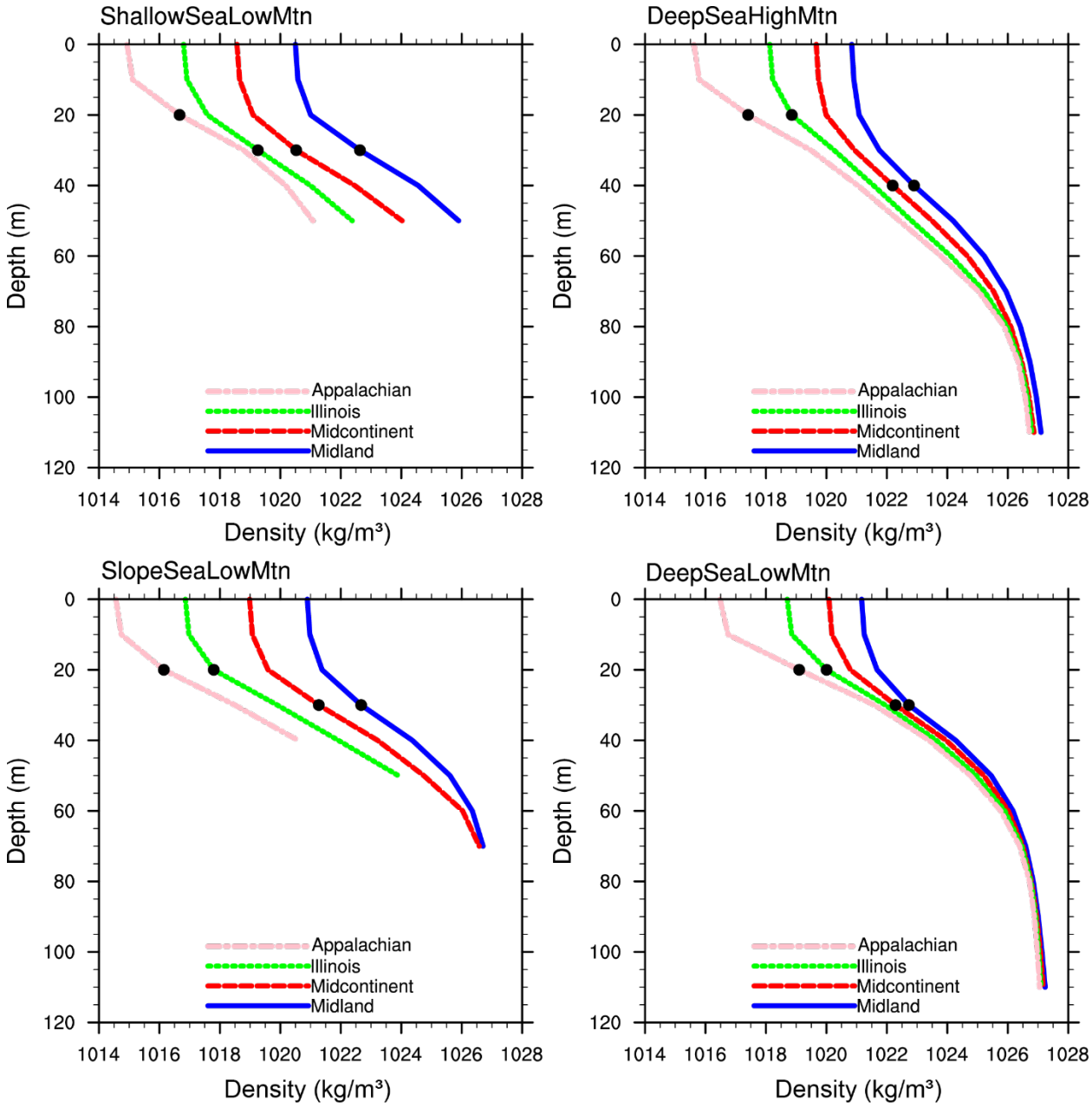

Figure S3.5 Vertical profiles of seawater density for regions across the NAMS. Mean annual profiles of seawater density (kg m^{-3}) for regions across the NAMS (colored lines) in each experiment. The regional pycnocline depth (black points) is defined as the location of the maximum of the first vertical derivative of the density (Kim and Miller, 2007).

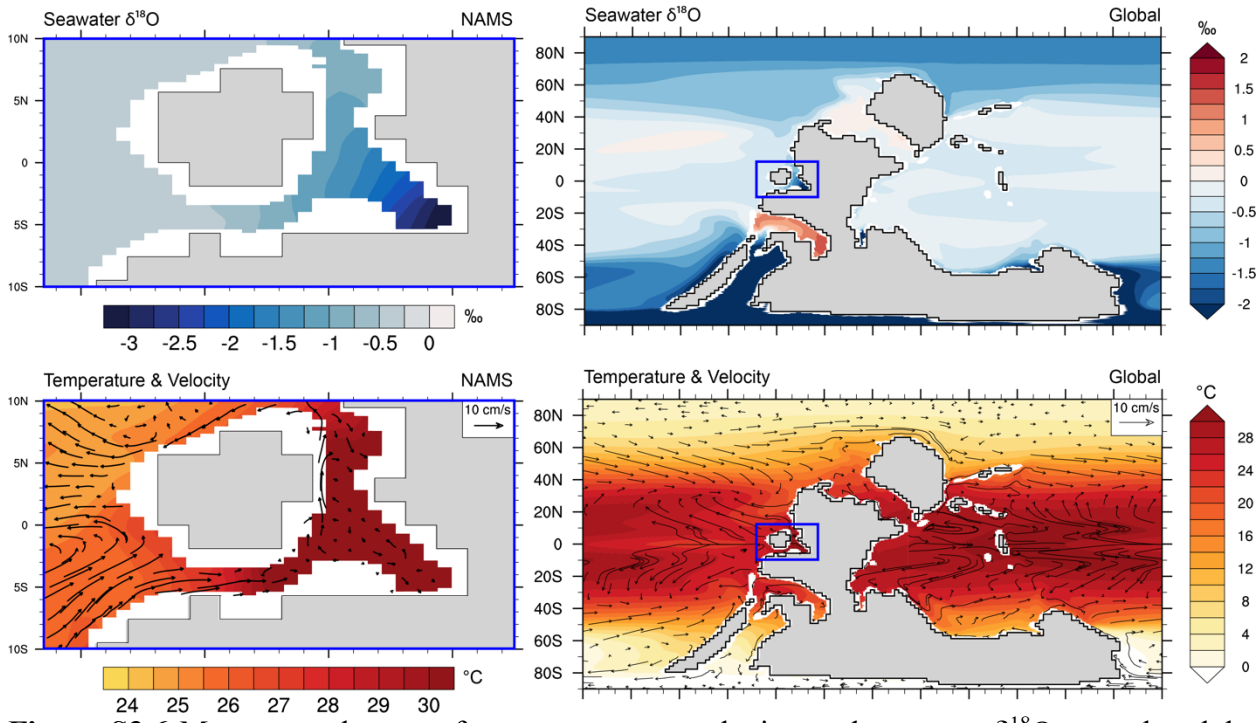

Figure S3.6 Mean annual sea surface temperature, velocity, and seawater $\delta^{18}O$ over the globe and NAMS region for an additional experiment with paleogeographic modifications. Maps of mean annual surface $\delta^{18}O_w$ (‰) (top) and surface temperature (°C) and velocity (cm s^{-1}) (bottom) for an experiment with the equator bisecting the NAMS and the presence of the Ancestral Rocky Mountains (land masses shown in gray, no topography is shown). Blue boxes outline the NAMS region on each of the global maps. The paleogeography used in this experiment is from the PALEOMAP Project (Scotese and Wright, 2018). Note that the magnitude and offshore-onshore gradient of surface $\delta^{18}O_w$ and temperature is similar to the experiments presented in the main text.

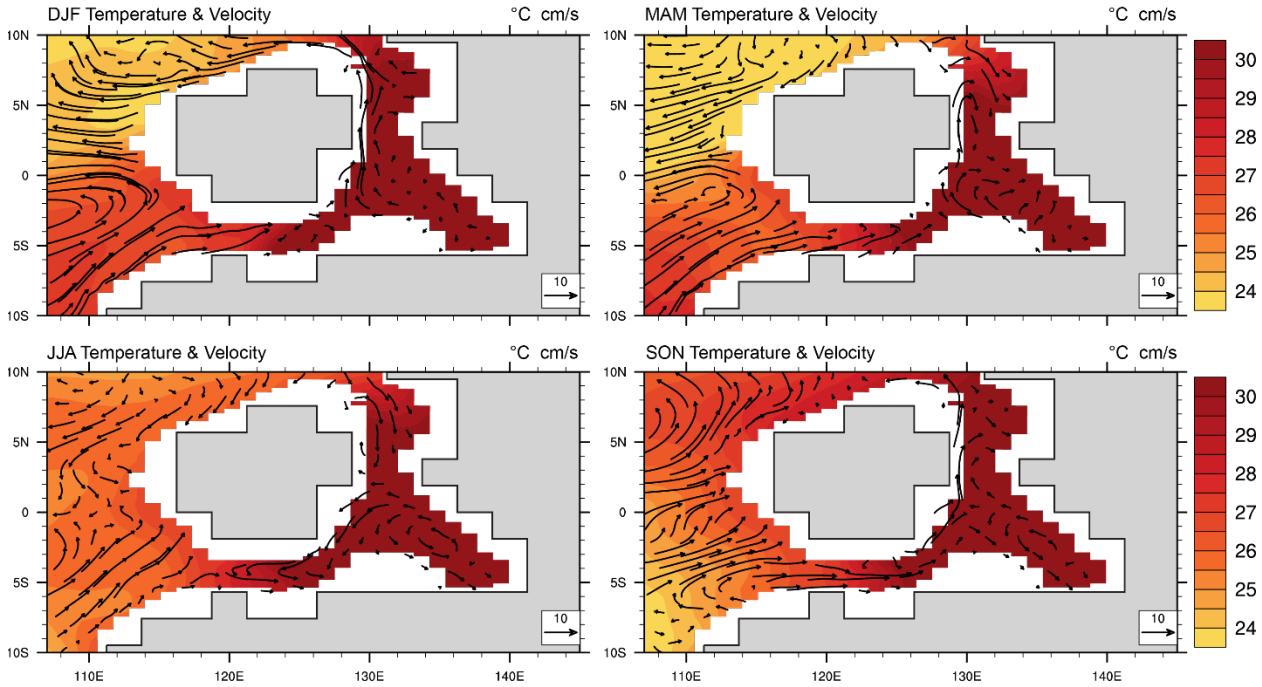

Figure S3.7 Seasonal sea surface temperature and velocity in the NAMS for experiment with paleogeographic modifications. Maps of seasonal sea surface temperature (°C) and velocity (cm s^{-1}) for an experiment with the equator bisecting the NAMS and the presence of the Ancestral Rocky Mountains (land masses shown in gray, no topography is shown). DJF = December-January-February, MAM = March-April-May, JJA = June-July-August, SON = September-October-November. Note that a counterclockwise gyre is present only in JJA and SON.

References

Kim, H.J., and Miller, A.J., 2007, Did the thermocline deepen in the California current after the 1976/77 climate regime shift? Journal of Physical Oceanography, v. 37, p. 1733–1739, doi:10.1175/JPO3058.1.

Scotese, C.R., and Wright, N.M., 2018, PALEOMAP Paleodigital Elevation Models (PaleoDEMS) for the Phanerozoic PALEOMAP Project, https://www.earthbyte.org/paleodem-resource- scotese-and-wright-2018/.

Chapter 4 Ecosystem-to-Global Scale Modeling of Vegetation-Climate Feedbacks During the Late Paleozoic Ice Age with Fossil-Based Plant Functional Types

Co-authors: Christopher J. Poulsen, William J. Matthaeus, Jon D. Richey, Joseph D. White, Isabel P. Montañez, William A. DiMichele, Michael T. Hren, Jennifer C. McElwain, Jonathon P. Wilson

4.1 Abstract

The Late Paleozoic Ice Age (LPIA; ~340 to 290 Ma), Earth's penultimate icehouse, was a time of widespread coal formation, characterized by the evolution and expansion of the oldest and most extensive paleotropical forests. Increasing evidence suggests that repeated restructuring of terrestrial ecosystems during LPIA were tightly coupled with changes in atmospheric CO_2, aridity, and high-latitude ice volume, supporting the hypothesis that pre-angiosperm biomes exerted a strong influence on the climate system. Land surface models have been used to simulate the role of vegetation-climate feedbacks in past climate change, but the representation of plants in those models are typically based on modern plant functional types (PFTs) such as angiosperms and conifers, which may be poor physiological analogs for Late Paleozoic plants. Recent work has quantified key parameters of physiological functioning of extinct plants from well-preserved Pennsylvanian fossils and process-based ecosystem modeling, providing support that ancient plants were functionally distinct from their present-day relatives. Here, we incorporate six experimentally and empirically constrained paleo-floral plant functional types (paleo-PFTs) into the Community Earth System Model to simulate the response of terrestrial climate to Pennsylvanian tropical wetland and seasonally dry biomes under changing atmospheric CO_2. Our results indicate that under the same atmospheric conditions, paleo-PFTs exhibit substantially higher transpiration rates compared to modern PFTs. Tropical vegetation modulates the magnitude of drying and wetting of soil moisture by increasing and decreasing canopy transpiration rates under elevated CO_2, respectively. Modern PFTs almost uniformly suppress transpiration rates under increased CO_2 (in line with most modern vegetation), while

Paleo-PFTs either suppress or enhance regional transpiration rates based on relatively low humidity (increased VPD) or high humidity (decreased VPD), respectively. These differences in water transport by plants lead to substantially drier regions of tropics with paleo-PFTs compared to modern PFTs under elevated CO_2, which better captures the regional drying inferred from paleoclimate proxy records across the Pangaean tropics. Ultimately, this work highlights the importance of accounting for paleo-plant physiology in modeling vegetation-climate feedbacks during past intervals of climate change.

4.2 Introduction

Since their mid-Paleozoic emergence, terrestrial plants have transformed Earth's climate in a multitude of ways including changes to the hydrological cycle, surface energy budget, and global biogeochemical cycles. Global climate models, or more recently Earth system models, have permitted the simulation of the relationship between changes in terrestrial ecosystems and climate in the deep past. The representation of paleo-ecosystems in Earth system models is traditionally based on modern angiosperms and conifers as physiological analogs for extinct plants (Beerling, 1998; Heavens et al., 2015; Kutzbach and Ziegler, 1993; Poulsen et al., 2007; Rees et al., 2002; Wade et al., 2019). Modeling past vegetation-climate interactions using modern plant analogs has been necessary due to limited knowledge of plant ecophysiology in the past. The validity of this approach is likely to diminish with increasing time in the past due to plant evolution. In the deep past, paleo-plants and the ecosystems they comprised differ greatly from those of today, or even of the Cenozoic. Whereas evolution has led to novelty and divergence over time within lineages, the number of phylogenetically distinct, ecologically dominant lineages has decreased through time. Thus, these ancient systems become increasingly distinct (i.e., morphologically and functionally) from the modern with increasing time. Recent efforts to include time-appropriate vegetation (Le Hir et al., 2011; Lenton et al., 2016) have been limited to employing simplistic functional type categorizations (e.g., non-vascular plants, woody plants) rather than using the observed traits of extinct plants to infer paleo-physiology. To better understand vegetation-climate feedbacks throughout the evolutionary history of plants, the representation of paleo-vegetation in Earth system models needs to be improved by incorporating the functional traits of paleo-plants.

Reconstructing paleo-ecophysiology is challenging because these plants no longer exist. Without direct observation of extinct plants, nearest-living relatives and/or modeling processes from structural characteristics based on limited fossil evidence are typically used to infer plant function in deep time. However, recent work has elucidated a much broader spectrum of physiological functioning in extinct plants than previously understood, and thus reveals the limitations of studying nearest-living relatives that bear little developmental, morphological, and/or anatomical resemblance to the extinct plants of interest (Montañez et al., 2016; Wilson et al., 2017, 2020; but see Boyce and Zwieniecki, 2019). Advancements in process-based ecosystem modeling bridge the gap between computational models of plant physiology (Peck, 2004) and the unfeasible, *in vivo* investigation of how ancient flora functioned in their paleoclimatic environment by integrating fossil-derived measurements into the simulation framework (Richey et al., 2020b; White et al., 2020). As a result, mechanistic ecosystem modeling of extinct plants has created a new purpose for the wealth of existing paleobotanical material—particularly fossil records that provide constraints on leaf traits and morphologies (Boyce and Knoll, 2002; Feild et al., 2011; Franks and Beerling, 2009; McElwain et al., 2016; Peppe et al., 2011, 2014; Taylor and Taylor, 2009) and cuticular chemistry (Gupta et al., 2006; Montañez et al., 2016; Mösle et al., 1998; Richey et al., 2020b; Royer and Hren, 2017)—and provided a testing ground for integrating the physiological capacity and ecosystem function of ancient plant communities into the land component of an Earth system model.

Here, we use plant type-specific fossil leaf morphologic and C:N measurements and the process-based ecosystem model *Paleo*-BGC (White et al., 2020) to construct a suite of plant functional types (PFTs) in the Community Land Model (CLM) for deep-time climate simulations using the Community Earth System Model (CESM). This is the first time paleo-PFTs have been derived for CLM (i.e., lycopsids, cordaitaleans, walchian conifers, sphenopsids, marattialean tree ferns, and medullosans) as the representative plant groups that dominated paleotropical forests during the Earth's penultimate icehouse, or the Late Paleozoic Ice Age (LPIA; ~340–290).

The LPIA is characterized by orbital forcing of glacial-interglacial climate and sea-level cycles (Montañez and Poulsen, 2013) under systematically varying but overall low atmospheric pCO_2 (<1000 ppm) (Montañez et al., 2016; Richey et al., 2020a). Pennsylvanian tropical regions of Euramerica were characterized by temporal shifts between wetland and seasonally dry plant communities broadly in sync with changes in low-latitude climate, high-latitude continental ice

sheet extent, and atmospheric pCO_2 (DiMichele, 2014; DiMichele et al., 2009; Montañez, 2016; Montañez et al., 2016). The oldest and potentially most expansive tropical forests evolved and expanded in the low-latitudes of the supercontinent Pangaea during this time (Cleal and Thomas, 2005; DiMichele, 2014), and underwent repeated climate-driven turnovers in the dominance of humid wetland plant assemblages and seasonally dry assemblages over a hierarchy of timescales (10^5–10^7 yr) (Bashforth et al., 2021; DiMichele, 2014; DiMichele et al., 2009). Several modeling studies of tropical hydroclimate have demonstrated that direct and indirect environmental changes associated with the extent of high-latitude glaciation, including atmospheric CO_2, affect precipitation over low latitude Pangaea and likely influenced the composition of paleotropical forests, yet the phasing of precipitation with glacial conditions differs between simulations (Heavens et al., 2012, 2015; Peyser and Poulsen, 2008; Poulsen et al., 2007). This ongoing discussion partly reflects that previous modeling studies have focused on the role of climate forcings as opposed to vegetation (e.g., paleophysiology and vegetation cover) in modulating tropical vegetation-climate interactions during the LPIA. We use the six paleo-floral PFTs to define wetland and seasonally-dry (i.e., dryland) tropical biomes during the Pennsylvanian (323–299 Ma) to simulate vegetation-climate interactions under varying levels of atmospheric CO_2. Using this model setup, we address three fundamental questions:

(1) How does replacing modern PFTs with paleo-PFTs in CESM alter tropical vegetation-climate interactions in Pennsylvanian simulations?
(2) How did paleotropical biomes influence Pangaean surface climate under elevated CO_2?
(3) How did shifts in the distribution of tropical wetland and dryland biomes influence low-latitude hydroclimate over Pangaea?

4.3 Methods

4.3.1 Methodological overview

Major progress in our understanding of the biosphere's role in the climate system over the course of geologic time requires a systems-based approach in which plants are a focal point. In the following Methods sections, we outline the series of steps involved in such a systems-based approach of vegetation-climate interactions in deep time. First, we describe previous foundational work on process-based ecosystem modeling integrated with detailed anatomical and

paleontological data that motivates the Earth system modeling in the current study (Section 4.3.2). Second, we describe the general anatomical structure and abundance of key plant taxa in terrestrial biomes during the period of interest that will be incorporated in the Earth system model (Section 4.3.3). Third, we describe how distinct vegetation types and their interactions with the atmosphere are represented in the Earth system model (Section 4.3.4). Fourth, we describe how leaf fossil measurements, insights from ecosystem modeling, and reconstructions of plant morphology are translated into the parameters that define paleo-plant types in the Earth system model (Section 4.3.5). Fifth, we outline a series of experiments using ecosystem process modeling as well as standalone land and coupled land-atmosphere model configurations to compare the influences of paleo-plant and modern plant physiology on vegetation-climate interactions under varying CO_2 (Section 4.3.6). Collectively, these sections document a complete systems-based approach to studying vegetation-climate interactions in deep time from fossil-derived ecophysiology to Earth system modeling of paleo-floral plant types appropriate for the period of interest. The current study also provides an initial testing ground for future efforts to represent vegetation-climate interactions in deep time.

4.3.2 Rationale for Earth system model selection

Fundamental distinctions between the water-use efficiency of paleo-plants compared to their distant, living relatives (Wilson et al., 2017) has motivated advancements in process-based ecosystem modeling of deep-time ecosystems (Richey et al., 2020b; White et al., 2020). White et al. (2020) modified BIOME-BGC, a mechanistic modeling system with ~45 years of development and testing across modern ecosystems, to include paleo-environmental and fossil-plant structural attributes and functional traits. The model estimates stomatal conductance according to Jarvis (1976) where a mean operational maximum stomatal conductance (g_{smax}) value is reduced by scalars representing environmental constraints (e.g., light, temperature, vapor pressure deficit or VPD, and atmospheric CO_2) and is, therefore, well-suited for paleo-plant simulations as theoretical g_{smax} can be directly measured from leaf fossils (Franks and Beerling, 2009; Montañez et al., 2016) and has been shown to universally scale with g_s (operational g_s:g_{smax} ratio of 0.26 ± 0.11) (Murray et al., 2020). Additionally, the model permits “off-line” modification of the physiological representation of extinct plants as a step towards subsequent integration into fully coupled Earth system models. The modified version of BIOME-BGC,

referred to as *Paleo*-BGC, also shares a historical connection to CLM as the widely-utilized terrestrial ecosystem component of CESM (Hurrell et al., 2013; Thornton et al., 2007), particularly with respect to the photosynthesis and soil carbon/nitrogen cycling routines.

The first studies using *Paleo*-BGC simulated the physiological response of Pennsylvanian wetland and dry-adapted plant types (Figure 4.1) to age-specific atmospheric pCO_2, pO_2, and site-specific meteorology derived from a climate model (Matthaeus et al., 2021; Richey et al., 2020b; White et al., 2020). These studies reveal pCO_2 and precipitation thresholds for paleotropical vegetation viability, the ecophysiological advantages of dryland over wetland plant types to drought conditions, and the capacity for paleo-vegetation to influence surface hydrology. This study builds upon previous *Paleo*-BGC modeling by (1) using fossil measurements, reconstructions of fossil plant morphology, insights from *Paleo*-BGC (e.g., simulated vegetation cover) to define a suite of key extinct plants from Pennsylvanian paleotropical forests, and then (2) integrating these extinct plant types into a coupled land-atmosphere model framework. Given the historical connection of *Paleo*-BGC to CLM and the widespread use of CESM and its predecessor the Community Climate System Model for deep-time climate studies (e.g., Heavens et al., 2015; Kiehl and Shields, 2005; Ladant et al., 2020; Macarewich et al., 2021; Shields and Kiehl, 2018), we use fossil measurements and insights from *Paleo*-BGC to define a suite of key extinct plants from Pennsylvanian paleotropical forests in CLM version 4 that can be simulated in the fully coupled configuration of CESM. Land-atmosphere coupling in CESM simulates heat, moisture, and momentum exchanges between Pennsylvanian land plants and the atmosphere, as well as the thermal and hydrologic processes at the surface and within the interior of near surface soil layer (Bonan et al., 2011; Oleson et al., 2010), and thus completes the land–atmosphere feedback loop needed to simulate the potential impact of paleo-vegetation on the Earth system.

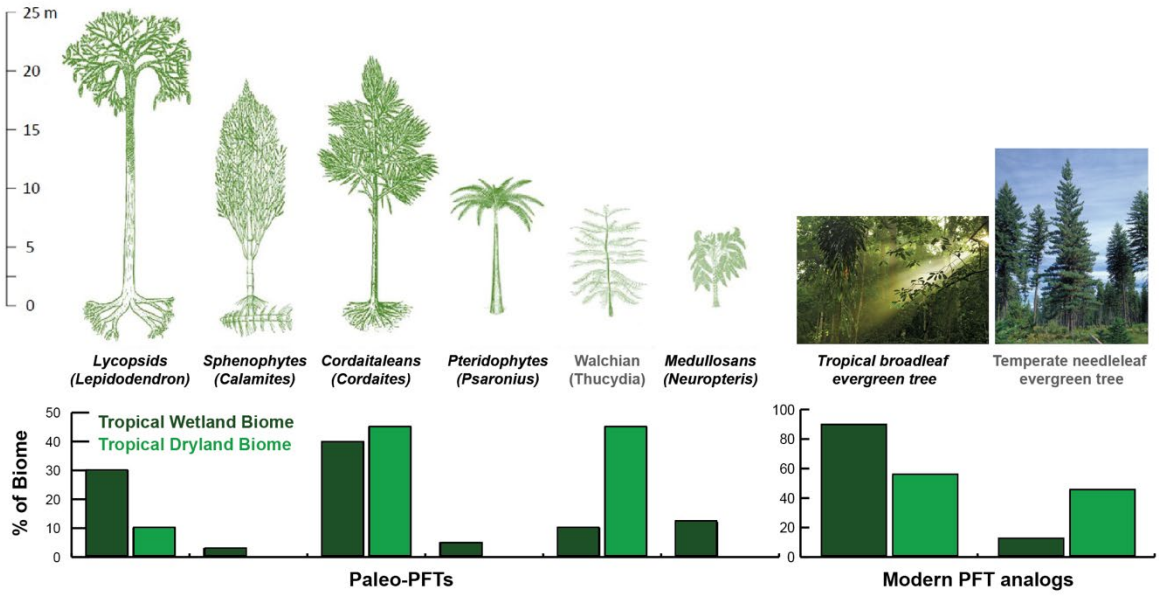

Figure 4.1 Plant functional type (PFT) compositions of the tropical wetland and dryland biomes. In the paleo-PFT simulations, the tropical wetland biome (dark green bars) is based on the relative abundance distribution observed in fossil plant assemblages as follows: 30% lycopsid PFT, 3% sphenopsid PFT, 40% cordaitalean PFT, 5% tree fern PFT, 10% walchian conifer PFT, and 12% medullosan PFT; the dryland biome (light green bars) is 10% lycopsid PFT, 45% cordaitalean PFT, and 45% walchian conifer PFT. In the modern PFT simulations, the tropical wetland biome (dark green bars) is 90% tropical broadleaf evergreen tree PFT and 10% temperate needleleaf evergreen PFT; the dryland biome (light green bars) is 55% tropical broadleaf evergreen tree PFT and 45% temperate needleleaf evergreen PFT. Reconstructions of Pennsylvanian tropical plants and references of modern plants are also included to represent each PFT. Paleo-PFTs with a black (gray) label have the tropical broadleaf evergreen tree (temperate needleleaf evergreen tree) as a modern analog.

4.3.3 Simulated plant taxa from Pennsylvanian tropical wetland and dryland forests

Pennsylvanian tropical regions of Euramerica were characterized by temporal shifts between wetland and seasonally dry plant communities broadly in sync with changes in low-latitude climate, high-latitude continental ice extent, and atmospheric pCO_2 (DiMichele, 2014; DiMichele et al., 2009; Montañez, 2016; Montañez et al., 2016). At the eccentricity (10^5-yr) time scale, there is an oscillatory pattern throughout the Pennsylvanian of wetland floras characteristic of swamp habitats and dry adapted floras (Cecil et al., 2014; DiMichele et al., 2020; Falcon-Lang et al., 2009). During times of sea-level minima (suggesting maximum expansion of high-latitude ice sheets), wetland floras dominated vast portions of central and eastern Pangaea (Matthaeus et al., 2021). At the same time, dry-adapted floras lived in large, interconnected populations in

western Pangaea (Bashforth et al., 2021; DiMichele et al., 2017; Falcon-Lang et al., 2015; Rothwell and Mapes, 1988; Tidwell and Ash, 2003), which was consistently drier, on average, than central and eastern Pangaea (Cecil et al., 2003; Tabor and Montañez, 2002), as well as in disconnected refugia in central and eastern Pangaea (Kerp, 2000; Roscher and Schneider, 2006). During maximum flooding intervals (times of maximum deglaciation) and subsequent stages of lowering sea level (early glacials), dry-adapted floras expanded out of western Pangaea and their mountain refugia to invade lowland basins in central and eastern Pangaea while wet-adapted vegetation retreated into wet refugia (Falcon-lang and DiMichele, 2010; Falcon-Lang et al., 2009; Looy et al., 2014). As the interglacial interval ended and the prevailing climate shifted to more humid conditions, dry-adapted biomes contracted and wet-adapted biomes expanded out of their refugia. Thereby, the glacial-interglacial climate and vegetation cycle was brought back to its glacial starting point (DiMichele et al., 2020). A second, longer-term (10^6–10^7 yr) trend on which the eccentricity scale variability is superimposed, marks a secular change in Pennsylvanian tropical forests towards more drought-tolerant vegetation. In contrast to the Euramerican tropics, wet-adapted flora such as lycopsids remained dominant in the Cathaysian floral province into the Permian (Hilton and Cleal, 2007; Pfefferkorn and Wang, 2007).

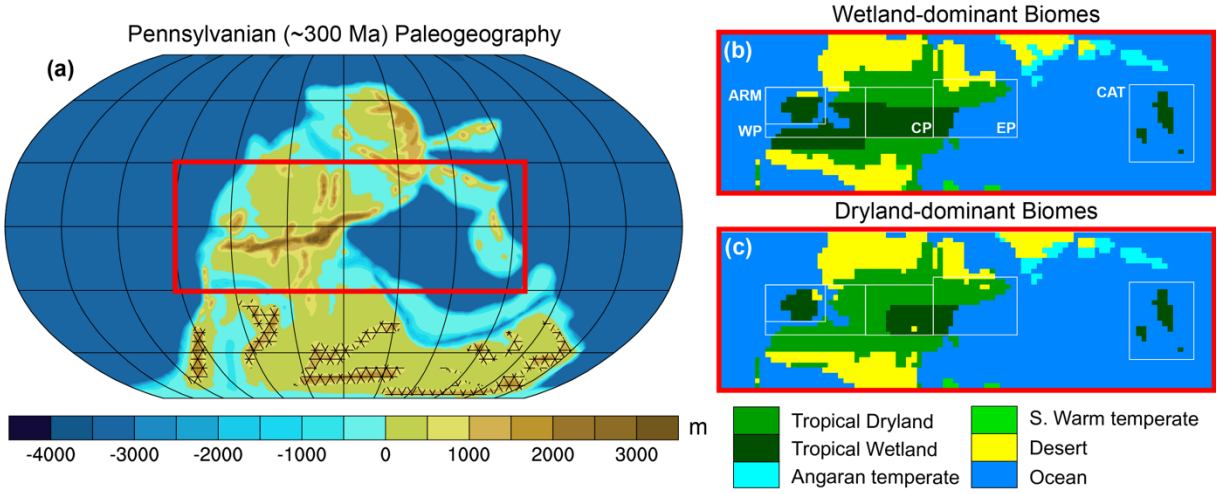

Figure 4.2 Pennsylvanian paleogeography (~300 Ma) and tropical biome distributions used in the simulations. (a) Paleotopography is shown with colored contours, prescribed ice sheets are shown with cross-hatched areas, and the low-latitude domain of biomes is outlined in a red box. (b) Distribution of wetland-dominant biomes and (c) dryland-dominant biomes in the Pangaean tropics with equatorial domains of interest outlined in white boxes. Abbreviated domains: ARM, Ancestral Rocky Mountains; WP, Western Pangaea; CP, Central Pangaea; EP, Eastern Pangaea; CAT, Cathaysian floral province. Note that the paleo-PFTs are only defined in the tropical

dryland (light green) and wetland (dark green) biomes. Modern PFTs are used for the Angaran temperate (cyan) and southern warm temperate (neon green) biomes in all simulations. The desert (yellow) biome is 100% bare ground.

To represent vegetation in the Pangaean tropics, we define two distributions of tropical wetland and dryland biomes associated with glacial and interglacial climates of the Middle Pennsylvanian (Figure 4.2; Wilson et al., 2017). For wetland-dominant phases associated with glacial climate, we prescribe a trans equatorial wetland biome across equatorial Pangaea with the dryland biome along the northern and southern edges of the tropics (Figure 4.2b). For dryland-dominant phases associated with interglacial climate, the dryland biome displaces the wetland biome at the equator with the wetland biome restricted to east and west equatorial coastal regions (Figure 4.2c).

Within these two biomes we assign variable compositions of the six paleo PFTs (Figure 4.1)—including lycopsids (e.g., *Lepidodendron*, *Lepidophloios*, *Ulodendron*), cordaitaleans (e.g., *Cordaites*, *Cordaadaxicutis*, *Cordaabaxicutis*), medullosans (e.g., *Macroneuropteris*, *Neuropteris*), marattialean tree ferns (e.g., *Pecopteris*, *Psaronius*), sphenopsids (specifically *Calamites*), and walchian conifers (specifically *Walchia* and *Thucydia*). The composition and relative abundance of the paleo-PFTs is estimated based on paleotropical observations of Middle Pennsylvanian (~315–307 Ma) tropical wetland and dryland biomes (e.g., DiMichele, 2014; DiMichele et al., 2009; Phillips et al., 1974; Phillips and Peppers, 1984). During this interval, wet-adapted forests in the tropics were co-dominated by arborescent lycopsids and cordaitaleans (Montañez et al., 2016) and thus comprise 30% and 40% of the wetland biome in our simulations, respectively. Arborescent lycopsids are a distant tree-sized relative of the diminutive modern lycopsid *Isoetes.* Cordaitaleans were selected as an early coniferophyte lineage, with a wide range of growth habits, from scrambling forms to small and large trees with trunks that contained dense, pycnoxylic (dense with little parenchyma) wood and bore strap-shaped leaves that could approach a meter in length (Florin, 1951). Cordaitalean trees were abundant within Pangaean wetland flora during the Middle Pennsylvanian (Montañez et al., 2016; Phillips and Peppers, 1984; Raymond et al., 2010). Marattialean tree ferns were present in wetland environments in the late Middle Pennsylvanian (DiMichele and Phillips, 2002; Montañez et al., 2016; Phillips et al., 1974) and represent 5% of the wetland biome in our simulations. In terms of biomass, medullosans were important pteridosperms (i.e., seed ferns) in tropical wetlands,

occurring as subcanopy plants and groundcover, and even forming low canopies in some environments (Raymond and Sloan, 2013; Wilson and Fischer, 2011; Wnuk and Pfefferkorn, 1984), and comprise 12% of the wetland biome in our simulations. Medullosan stems contained high-conductivity xylem cells arranged in anastomosing vascular segments (Basinger et al., 1974; Delevoryas, 1955; Stewart and Delevoryas, 1952; Wilson, 2013; Wilson et al., 2008, 2015) attached to meter- or multi-meter-long compound leaves (Laveine, 1986; Laveine and Belhis, 2007; Wnuk and Pfefferkorn, 1984). Calamitaleans (arborescent sphenopsids), close relatives of the modern Equisetales (horsetails), were often located in streamside and lakeside habitats (DiMichele and Falcon-Lang, 2012) and are well documented from petrified material in coal-swamp settings (Andrews and Agashe, 1965; Spatz et al., 1998) and clastic wetlands (Mencl et al., 2013; Rößler and Noll, 2006). Sphenophytes comprise 3% of the wetland biome in our simulations. Dry-adapted plants, including Walchian conifers, also grew in well drained basinal slopes of the Euramerican equatorial tropics (Rothwell et al., 1997) and make up 10% of the wetland biome in our simulations.

Dryland biomes of the tropics were dominated by cordaitaleans during the late Middle Pennsylvanian (~308 Ma) (Montañez et al., 2016). Dry-adapted cordaitaleans were towering trees (up to 48.5 m tall) with crowns composed of medium to large strap-shaped leaves, which formed a dense, multi-layered closed canopy (Bashforth et al., 2014; Falcon-Lang and Bashforth, 2004, 2005), and make up 45% of the dryland biome. It is important to note that relatively larger forms of cordaitaleans dominated seasonally-dry areas compared to that of wetlands (Falcon-Lang, 2004); these forms are taxonomically distinct. The significant presence of cordaitaleans in both wet and dry habitats indicates that they are among the most widespread and ecologically diverse plant groups of the Pennsylvanian (DiMichele, 2014). However, in the current study the cordaitalean PFT is the same in the wetland and dryland biomes. Walchian conifers were are also prominent dry-adapted flora during this time, varying from small (Hernandez-Castillo et al., 2014) to medium-sized (Bashforth et al., 2014; Looy, 2013) woody trees with a plagiotropic (near-horizontal) branching pattern and growth morphology that resembles certain modern araucarian conifers. At ~307 Ma, seasonally dry biomes shifted from cordaitalean- to walchian-dominance (Richey et al., 2020b) and thus walchian conifers are also 45% of the dryland biome. Plants typically considered wet-adapted are a highly variable component of seasonally dry assemblages (DiMichele, 2014). The lycopsid *Sigillaria* occurs in dryland habitats into the Early

Permian Texas red beds (DiMichele et al., 2006) and thus comprises 10% of the dryland biome. For more information on the key extinct genera used for measurements of fossil roots, stems, and leaves, see Richey et al. (2020b) and White et al. (2020).

4.3.4 Simulated plant taxa from Pennsylvanian tropical wetland and dryland forests

Spatial land surface heterogeneity in CLM is represented as a nested subgrid hierarchy in which grid cells are composed of multiple types of surface cover (i.e., vegetated, glacier, wetland), snow/soil columns, and PFTs (Oleson et al., 2010). For the purposes of this study, we focus on vegetated grid cells comprised of a soil column (without snow) and PFTs. CLM, and terrestrial vegetation models in general, use plant functional types (PFTs) to represent broad groups of plants that share similar biogeophysical and biogeochemical characteristics in terms of their ecosystem function (Wullschleger et al., 2014). While the PFTs defined for our paleoflora are based on specific taxa, in reality the plant types represent a broad group of taxonomically similar plants with assumed similar form and functions as defined by fossil information. In CLM version 4, a single vegetated grid cell can be comprised of up to 15 possible modern PFTs (e.g., tropical broadleaf evergreen tree, temperate needleleaf evergreen tree) plus bare ground and a soil column with 15 vertical layers that we populated here with our six paleo PFTs. As PFTs differ in physiology and structure, leaf and stem optical properties, aerodynamic parameters, root distribution parameters, and photosynthetic parameters must be defined for each type (Oleson et al., 2010). The PFT parameters cannot all be constrained from process-based ecosystem modeling and plant fossils, and thus paleo-PFTs are each modified from one of the 15 available modern PFTs that most closely reflect each extinct group. With unique vegetation types, interactions between the land surface and atmosphere are simulated as biogeophysical processes for each PFT independently within a grid cell, and these PFT properties are aggregated to the column level to calculate biogeophysical processes related to the soil. Likewise, the same atmospheric forcing used to force all PFTs surface variables and fluxes required by the atmosphere and the soil column within a grid cell are obtained by averaging the PFT and soil column quantities weighted by their fractional areas.

4.3.5 Paleo-floral plant functional types and their physiological characterization in CLM

The six broad taxonomic groups representing dominant Middle Pennsylvanian paleo-PFTs include lycopsids, cordaitaleans, walchian conifers, sphenopsids, marattialean tree ferns,

and medullosans (Figure 4.1). We approach paleo-PFT construction by starting with default modern PFTs distributed with CLM that most closely reflect each extinct group. To simulate lycopsids, cordaitaleans, sphenopsids, tree ferns, and medullosan, functional parameters are derived by modifying the tropical broadleaf evergreen tree PFT, whereas walchian conifers are simulated based on modification of the temperate needleleaf evergreen tree PFT. These tree types are default modern PFTs distributed with CLM that most closely reflect the ecophysiology each extinct group (Richey et al., 2020b; White et al., 2020). Although there is some evidence for deciduousness in the paleo-plants of interest, including deciduous lateral branches on the trunk and in the final-phase crown of some lycopsids (DiMichele, 2014), deciduous shoot dropping of ultimate branches in walchian conifers (Looy, 2013), and cordaitalean leaf beds (Schneider et al., 2016) that may indicate deciduousness, these plants were most likely dominantly evergreen and thus we chose evergreen trees as modern PFT analogs. In addition, we chose the broadleaf rather than the needleleaf tree PFT to accommodate the large leaf surface area of cordaitaleans, lycopsids, tree ferns, pteridosperms, and sphenopsids. Paleo-PFTs are defined by modifying four specific PFT parameters in CLM version 4: 1) leaf carbon-to-nitrogen ratio ($C:N_{leaf}$), 2) Departure of leaf angles from a random distribution (χ_L), 3) stomatal response to soil water potential (ψ_o, ψ_c), 4) a photosynthetic parameter (m) used in the calculation of leaf conductance, 5) fraction of leaf nitrogen in Rubisco (F_{LNR}), 6) specific leaf area (SLA) (Table 4.1).

PFT parameter	temperate NET	tropical BET	medullosan	sphenopsid	tree fern	cordaitalean	walchian	lycopsid	Units & Source	
χ_L	0.01	0.1	0	0.5	0.5	0	−0.4	−0.4	unitless	†
$\alpha_{leaf,vis}$	0.07	0.1	0.1	0.1	0.1	0.1	0.07	0.1	fraction	*
$\alpha_{leaf,nir}$	0.35	0.45	0.45	0.45	0.45	0.45	0.35	0.45	fraction	*
$\alpha_{stem,vis}$	0.16	0.16	0.16	0.16	0.16	0.16	0.16	0.16	fraction	*
$\alpha_{stem,nir}$	0.39	0.39	0.39	0.39	0.39	0.39	0.39	0.39	fraction	*
$\tau_{leaf,vis}$	0.05	0.05	0.05	0.05	0.05	0.05	0.05	0.05	fraction	*
$\tau_{leaf,nir}$	0.1	0.25	0.25	0.25	0.25	0.25	0.1	0.25	fraction	*
$\tau_{stem,vis}$	0.001	0.001	0.001	0.001	0.001	0.001	0.001	0.001	fraction	*
$\tau_{stem,nir}$	0.001	0.001	0.001	0.001	0.001	0.001	0.001	0.001	fraction	*
R_{z0m}	0.055	0.075	0.075	0.075	0.075	0.075	0.055	0.075	unitless	*
R_d	0.67	0.67	0.67	0.67	0.67	0.67	0.67	0.67	unitless	*

d_{leaf}	0.04	0.04	0.04	0.04	0.04	0.04	0.04	0.04	meters	*
r_a	7	7	7	7	7	7	7	7	unitless	*
r_b	2	1	1	1	1	1	2	1	unitless	*
m	6	9	12.8	5.3	5.7	56.8	4.5	38.1	unitless	‡
α	0.06	0.06	0.06	0.06	0.06	0.06	0.06	0.06	μmol CO_2 $μmol^{-1}$ photon	*
$C:N_{leaf}$	35	30	33	37	36	41	40	41	gC g^{-1} N	§
F_{LNR}	0.05	0.06	0.06	0.06	0.06	0.06	0.06	0.06	fraction	*
f(N)	0.72	0.83	0.83	0.83	0.83	0.83	0.72	0.83	unitless	*
SLA_0	0.01	0.012	0.012	0.012	0.012	0.012	0.012	0.012	m^2 g^{-1} C	‡
SLA_m	0.00125	0.0015	0	0	0	0	0	0	m^2 g^{-1} C	‡
$ψ_o$	−0.66	−0.66	−0.51	−0.51	−0.51	−0.51	−0.51	−0.51	MPa	#
$ψ_c$	−2.55	−2.55	−2.55	−2.55	−2.55	−2.55	−2.55	−2.55	MPa	#

Table 4.1 Plant functional type (PFT) parameters for the modern and paleo-PFTs in the Community Land Model version 4. Temperate NET = temperate needleleaf evergreen tree; Tropical BET = tropical broadleaf evergreen tree. Leaf and stem optical properties include the departure of leaf angles from a random distribution ($χ_L$), leaf and stem visible reflectance ($α_{leaf,vis}$, $α_{stem,vis}$), leaf and stem near-infrared reflectance ($α_{leaf,nir}$, $α_{stem,nir}$), leaf and stem visible transmittance ($τ_{leaf,vis}$, $τ_{stem,vis}$), and leaf and stem near-infrared transmittance ($τ_{leaf,nir}$, $τ_{stem,nir}$). Plant aerodynamic parameters are ratio of momentum roughness length to canopy top height (R_{z0m}), ratio of displacement height to canopy top height (R_d), and characteristic dimension of leaves in the direction of wind flow (d_{leaf}). Root distribution parameters (r_a, r_b) control the uptake of water from the soil. Photosynthetic parameters are represented by a PFT-dependent parameter (*m*) used in the calculation of leaf stomatal conductance based on the Ball-Berry conductance model, quantum efficiency (α), leaf carbon-to-nitrogen ratio ($C:N_{leaf}$), fraction of leaf nitrogen in Rubisco (F_{LNR}), a parameter that scales the maximum achievable photosynthetic rate in the absence of nitrogen limitation (f(N)), a value for specific leaf area at the top of the canopy (SLA_0), linear slope coefficient in the calculation of specific leaf area (SLA_m), and values of soil water potential when stomata are fully open and closed ($ψ_o$, $ψ_c$). For sources use to choose each PFT parameter, literature (†) refers to a value based on published reconstruction of plant morphology, modern (*) refers to using a "default" modern PFT parameter, *Paleo*-BGC & fossil (‡) refers to using a combination of *Paleo*-BGC output and fossil remains to constrain the parameter, *Paleo*-BGC (#) means that the value is directly taken from *Paleo*-BGC output, and fossil (§) means that plant-specific fossil measurements are used to constrain the parameter.

For all paleo-PFTs, the $C:N_{leaf}$ parameter values are derived from published C and N and isotopic analyses of a set of well-preserved leaf fossil cuticles representative of the six taxonomic groups simulated in this study (for more information, see Richey et al., 2020). In CLM, fossil-derived $C:N_{leaf}$ values are also used to initialize the C:N for other biomass pools of leaf litter ($C:N_{litter}$), fine roots ($C:N_{fineroot}$), live wood ($C:N_{livewood}$), and dead wood ($C:N_{deadwood}$). These

pools are important to consider given that living biomass C:N drives sink strength for soil uptake in the modeled growth, and C:N of non-living biomass drives environmental nitrogen cycling, including immobilization and mineralization rates, in the simulated soil pools. In the absence of tissue-specific samples, we used the ratio of C:N values of the different biomass pools (i.e., [C:N_{leaf}]:[C:N_{litter}]:[C:$N_{fineroot}$]:[C:$N_{livewood}$]:[C:$N_{deadwood}$]) for the modern PFT analogs in CLM, including the tropical broadleaf evergreen tree (1: 2: 1.4: 1.7: 16.7) to initialize the C:N values for each respective paleo PFT based on measured leaf fossil cuticle C:N_{leaf} (Richey et al., 2020b). For example, the fossil C:N_{leaf} of the cordaitalean group is 41.0, which using the above ratio produced C:N_{litter}, C:$N_{fineroot}$, C:$N_{livewood}$, and C:$N_{deadwood}$ values of 57.4, 82.0, 69.7, and 684.7, respectively (Table S4.1).

Leaf optical properties control the reflection, transmittance, and absorption of solar radiation of PFTs. The parameter χ_L, or the departure of leaf angles from a random distribution, is determined based on fossil-based reconstructions published in literature sources for relevant taxa (e.g., Andrews, 1945; Falcon-Lang and Bashforth, 2005; Taylor et al., 2009; Wilson et al., 2015). χ_L is equal to +1 for horizontal leaves, 0 for random leaves, and −1 for vertical leaves. Medullosans and cordaitaleans have completely random leaf angles (χ_L = 0), whereas sphenopsids and tree ferns have more horizonal leaf angles (χ_L = 0.5) and walchians and lycopsids have more vertical leaf angles (χ_L = −0.4). The stomatal response to soil water potential is derived from *Paleo*-BGC, with all paleo-PFTs having values of −0.51 MPa and −2.55 MPa when stomata are fully open (ψ_o) and closed (ψ_c), respectively.

One of the difficulties in implementing CLM family models for deep-time modeling is the use of the Ball-Berry model to solve for stomatal conductance (g_s). The Ball-Berry conductance model in CLM version 4 is described by Collatz et al. (1991) and implemented in a global climate model by Sellers et al. (1996). The model relates stomatal conductance (g_s, i.e., the inverse of resistance) to net leaf photosynthesis, scaled by the relative humidity at the leaf surface and the CO_2 concentration at the leaf surface, and is based on parameter fitting from gas-exchange measurements. For extinct species, this is impossible, and thus we must use available characteristics that can be reliably obtained from plant fossils. For reference, the Ball-Berry conductance model included in CLM version 4 is:

$$g_s = m\frac{A}{c_s}\frac{e_s}{e_i}P_{atm} + b \qquad \text{Eq. 4.1}$$

where m is a fitted parameter, A is leaf photosynthesis (μmol CO_2 m^{-2} s^{-1}), c_s is the CO_2 partial pressure at the leaf surface (Pa), e_s is the vapor pressure at the leaf surface (Pa), e_i is the saturation vapor pressure (Pa) inside the leaf at the vegetation temperature, P_{atm} is the atmospheric pressure (Pa), and b = 2000 is the minimum stomatal conductance (μmol m^{-2} s^{-1}) when A = 0. Because theoretical g_{smax} is typically estimated from leaf fossils based on stomatal density and size, we assume here that all conditions are optimized such that A is equivalent to the maximum carboxylation rate of the leaf (assuming a 25°C reference; V_{cmax25}). V_{cmax25} is a function of leaf nitrogen:

$$V_{cmax25} = N_a \cdot f_{LNR} \cdot f_{NR} \cdot a_{R25} \quad \text{Eq. 4.2}$$

$$N_a = \frac{1}{C{:}N_{leaf} \cdot SLA} \quad \text{Eq. 4.3}$$

$$SLA(x) = SLA_0 + SLA_m x \quad \text{Eq. 4.4}$$

where values of N_a (nitrogen per unit leaf area; g N m^{-2}) are derived from cuticle C:N (g C g^{-1} N) and estimated SLA (m^2 leaf area g^{-1} C) values (Table S1 and S3). SLA is assumed to increase linearly with greater cumulative leaf area index (x, m^2 m^{-2}), where SLA_0 is the value for SLA at the top of the canopy (m^2 leaf area g^{-1} C) and SLA_m is the linear slope coefficient. For all paleo-PFTs, we assume that SLA_m = 0 and thus SLA = SLA_0.

Proxy-based methods have been developed to estimate paleo-SLA (Soh et al., 2017; White and Scott, 2006), but we use the SLA values of modern PFT analogs for each paleo-PFT in the current study. We first estimated SLA values based on $C{:}N_{leaf}$ for each paleo-PFT (ranging from 0.024 to 0.035 m^2 leaf area g^{-1} C). However, these relatively high SLA values produce simulated LAI values that are too high (LAI > 10) compared to that of modern PFTs. As a result, we set SLA_0 for paleo-PFTs to the total SLA values of their modern PFT analog (i.e., 0.025 and 0.015 for the tropical broadleaf and temperate needleleaf evergreen trees, respectively). These SLA values also produce a reasonable agreement of low-latitude LAI between the CLM and *Paleo*-BGC simulations (Figure S4.2). That said, future studies could explore the impact of paleo-SLA estimates based on three alternative methods–cuticle thickness, adaxial epidermal cell density, or petiole thickness (Soh et al., 2017).

The parameter f_{LNR} is the fraction of leaf N partitioned by the plant into the Rubisco enzyme (g N in Rubisco g^{-1} leaf N). How ancient plants partitioned their leaf N into the Rubisco enzyme is not known, and thus f_{LNR} is set to 0.06 for each paleo-PFT based on the value of the

tropical broadleaf evergreen tree. The parameters f_{NR} (fraction of the total molecular mass of Rubisco that is N; g total mass of Rubisco g^{-1} N in Rubisco) and a_{R25} (and the mass-specific activity rate of Rubisco at 25°C; μmol CO_2 g^{-1} Rubisco s^{-1}) are assigned as constants with values of 7.16 g total mass of Rubisco g^{-1} N in Rubisco and 60.0 μmol CO_2 g^{-1} Rubisco s^{-1}. The C:N and V_{cmax25} values are inversely proportional (Table S3) as higher C:N means less leaf nitrogen, and thus less enzyme investment for carbon fixation.

Paleo-BGC estimates operational g_s based on Jarvis (1976), where a g_{smax} value directly measured from leaf fossils is reduced by environmental constrains, and thus provides a fossil-based standard to compare with the operational g_s produced by our CLM simulations. However, because CLM solves for g_s based on the Ball-Berry equation (Collatz et al., 1991; Sellers et al., 1996) estimation of the *m* parameter, usually derived from gas-exchange measurements, is required for the paleo PFTs. First, theoretical g_{smax} for the fossil leaves are converted the into μmol CO_2 m^{-2} s^{-1} from original units of mol H_2O m^{-2} s^{-1} (1×10^6 [44 g mol^{-1} CO_2/18 g mol^{-1} H_2O]) as shown (Table S4.2). Next, to solve for initial *m* values, we invert the Ball-Berry equation using the theoretical g_{smax} derived from the fossil data:

$$m = \frac{c_s}{A}\frac{e_i}{e_s}\frac{(g_{smax} - b)}{P_a} \qquad \text{Eq. 4.5}$$

where e_i e_s^{-1} = 1.0 (no vapor deficit), P_a = 101325 Pa, c_s = 56.7 Pa assuming an atmospheric CO_2 = 560 ppm and O_2 = 0.21 mol mol^{-1}. First, the assumption of no vapor pressure deficit is associated with utilization of the theoretical g_{smax} from the fossil data as under best case conditions, plants would have fully opened stomatal pores. Likewise, we use the minimum C:N (i.e. highest leaf nitrogen) from the fossil leaf cuticles to calculate V_{cmax25}, thus making the assumption that the maximum potential photosynthesis (*A*) is associated with the most conductance. Finally, while b is generally estimated experimentally, we adopt the CLM version 4 default stomatal conductance value, approximately equivalent to 2000 μmol CO_2 m^{-2} s^{-1} at sea level and 25°C.

In CLM version 4, for needle-leaved forests, *m* = 6, compared to all other plant types (except C_4 grass) for which *m* = 9 (Collatz et al., 1991; Sellers et al., 1996). We use *m* values calculated as a function of minimum C:N and g_{smax} for each paleo-PFT (Table S4.3) as these parameters result in simulated operational g_s values that compare best with the operational g_s

from *Paleo*-BGC (Figure S4.1; also see Section 4.4.1). For the medullosan PFT, we use the average *m* value of *Macroneuropteris* and *Neuropteris*. For a summary of all the parameters used for paleo PFTs and modern PFT analogs in CLM, see Table 4.1.

4.3.6 Ecosystem and Earth system model simulation sets

Two initial, baseline CESM simulations with modern PFTs (CESM–1×W–modern and CESM–2×W–modern) are produced to provide atmospheric input data with relatively low and high atmospheric CO_2, respectively, for *Paleo*-BGC and standalone CLM cases (Figure 4.3). The CESM–1×W and CESM–2×W simulations are run for ~1,500 years to equilibrate the surface ocean and have top-of-atmosphere energy balances of −0.19 Wm^{-2} and 0.002 Wm^{-2}, respectively. Results from these baseline simulations are not included in the current study. For detailed information on the model configuration and boundary conditions used in CESM–1×W–modern and CESM–2×W–modern, see the Supplemental Information. Daily minimum/maximum/average surface temperature, precipitation, incident solar radiation, day length, and specific humidity at each paleolatitude over the last 50 years of CESM–1×W–modern and CESM–2×W–modern are provided as atmospheric input data for the *Paleo*-BGC simulations.

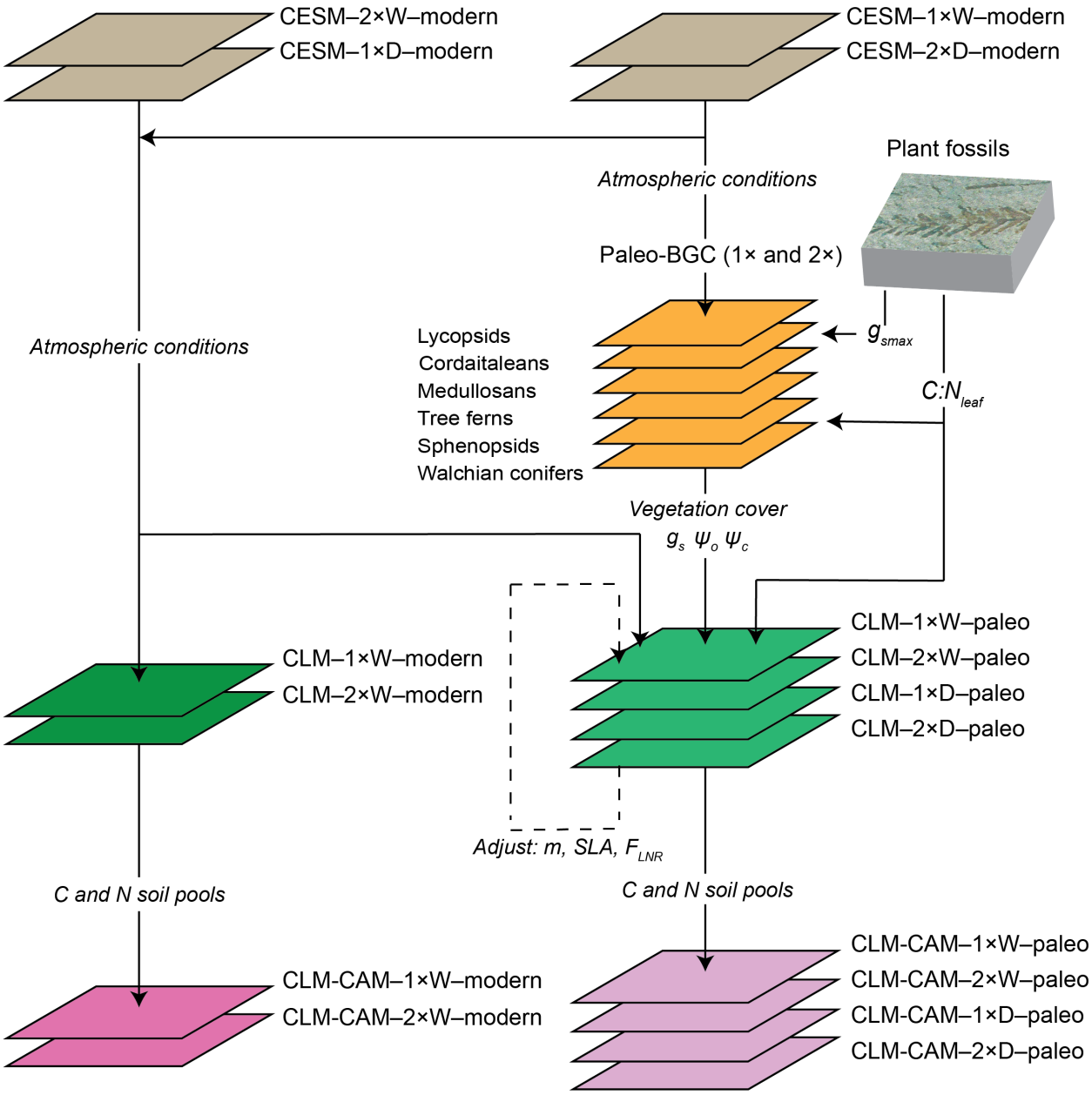

Figure 4.3 Simplified flowchart of the simulation configurations. Simulations include the fully coupled configuration of the Community Earth System Model version 1.2 (CESM), *Paleo*-BGC, standalone Community Land Model version 4 (CLM), and Community Land Model version 4 coupled to the Community Atmosphere Model version 5 (CLM-CAM) (see text and Table 4.2 for more information on each simulation).

Two global sets of *Paleo*-BGC point simulations are run for each paleo-PFT (i.e., collectively referred to as PaleoBGC–1×W–paleo and PaleoBGC–2×D–paleo, respectively; after Matthaeus et al., 2021) with the same atmospheric composition as CESM–1×W–modern and

CESM–2×W–modern to provide estimates of soil water potential, operational g_s, and LAI for comparison with CLM as well as areas of low LAI for prescribed areas of bare ground in CLM (Figure 4.3 and Table 4.2). For the meteorological inputs required by *Paleo*-BGC, values are extracted from the CESM–1×W–modern and CESM–2×W–modern simulation output for every paleo-latitude and paleo-longitude over land such that point simulations are run for every ice-free land grid cell. To simulate the same paleo-plant types as CLM in *Paleo*-BGC, general functional parameters were derived by modifying the evergreen broad-leaved forest PFT, a default modern plant type distributed with BIOME-BGC model. Paleo-PFTs are defined by modifying four specific fossil-derived parameters: 1) leaf conductance, involving g_{smax}, 2) $C:N_{leaf}$, 3) SLA, and 4) mesophyll path length (for more information, see White et al., 2020). After a model initialization routine of up to 10,000 years that allows ecosystem carbon and nitrogen pools to reach equilibrium (Thornton and Rosenbloom, 2005), forest stands are simulated using *Paleo*-BGC for each paleo-PFT based on 50-year model runs, in which the 50-year CESM-derived meteorological data are cycled once. To compare operational g_s and LAI point values from *Paleo*-BGC with two-dimensional (2D) fields from CLM simulations, we compute a weighted sum of each variable over all paleo-PFTs whose weighting depends on the PFT area relative to all PFTs within each grid cell, and then plot values on a 2D map with the same paleo-latitudes and paleo-longitudes as CLM. This cross-model validation of operational g_s and LAI is important because fossil-based estimates of g_s from *Paleo*-BGC provide a constraint on the photosynthetic paleo-PFT parameters in CLM (i.e., *m*) that influence stomatal conductance and cannot be directly derived from plants fossils.

Six standalone CLM simulations (i.e., CLM uncoupled from all other CESM components, with atmospheric forcing input) are run under the same atmospheric compositions, 0.21 mol mol^{-1} O_2 with 280 ppm or 560 ppm CO_2, to evaluate the sensitivity and response of the tropical wetland and dryland biomes to paleo-plant physiology and atmospheric CO_2. Standalone CLM simulations capture the land surface response to a given set of atmospheric conditions without any atmospheric feedback, and thus provide analogous values of operational g_s and LAI for comparison with *Paleo*-BGC. The standalone CLM simulations vary with respect to atmospheric CO_2 concentration (1× = 280 ppm; 2× = 560 ppm), the geographic distribution of tropical wetland and dryland biomes (W = wetland-dominated; D = dryland-dominated; Figure 4.2), and whether the tropical biomes contain modern or paleo-PFTs (modern or paleo; Figure

4.1). These simulations are referred to as CLM–1×W–modern, CLM–2×W–modern, CLM–1×W–paleo, CLM–2×W–paleo, CLM–2×D–modern, and CLM–2×D–paleo (Figure 4.3 and Table 4.2). Grid cells in PaleoBGC–1×W–paleo and PaleoBGC–2×D–paleo with low LAI (LAI < 0.1) are used to prescribe grid cells with 100% bare ground in the standalone CLM simulations. In the tropics, these non-vegetated grid cells correspond to a few cold mountainous locations at high elevation (>2,000 m) and dry locations at low elevation. Each of the six standalone CLM simulations are run for ~700 years to spin up the carbon and nitrogen pools in the biogeochemistry Carbon-Nitrogen Model such that land surface variables of interest (i.e., g_s, LAI) are near equilibrium. The land surface datasets with spun up C and N pools from CLM–1×W–modern, CLM–1×W–paleo, CLM–2×W–modern, CLM–2×W–paleo, CLM–2×D–modern, and CLM–2×D–paleo simulations are used to initialize subsequent simulations with CLM version 4 coupled to CAM version 5 (CLM-CAM).

Six CLM-CAM simulations are run under the same atmospheric compositions, 0.21 mol mol^{-1} O_2 with 1× or 2× CO_2, W or D biome distributions (Figure 4.2), and modern or paleo-PFTs (Figure 4.1) to evaluate the sensitivity to evaluate the response of tropical vegetation-climate interactions to paleo-plant physiology and atmospheric CO_2. These simulations are referred to as CLM-CAM–1×W–modern, CLM-CAM–1×W–paleo, CLM-CAM–2×D–modern, CLM-CAM–2×D–paleo, CLM-CAM–2×W–modern, and CLM-CAM–2×W–paleo (Figure 4.3 and Table 4.2). These simulations are identical to the standalone CLM simulations except for the incorporation of atmospheric feedbacks, with dynamical coupling between land and atmospheric processes, and a slab ocean model with prescribed ocean heat transport based on the baseline CESM–1×W–modern and CESM–2×W–modern simulations. Each of the four CLM-CAM simulations are run for ~70 years with results shown here averaged over the last 25 years.

Experiment	**Model**	**CO_2 (ppm)**	**Dominant tropical biome**	**Plant functional types**
CESM–1×W–modern	Fully coupled CESM	280	Wetland	Modern
CESM–2×W–modern	Fully coupled CESM	560	Wetland	Modern
PaleoBGC–1×W–paleo	*Paleo*-BGC	280	Wetland	Paleo
PaleoBGC–2×D–paleo	*Paleo*-BGC	560	Dryland	Paleo
CLM–1×W–modern	Standalone CLM	280	Wetland	Modern
CLM–2×D–modern	Standalone CLM	560	Dryland	Modern
CLM–2×W–modern	Standalone CLM	560	Wetland	Modern
CLM–1×W–paleo	Standalone CLM	280	Wetland	Paleo
CLM–2×D–paleo	Standalone CLM	560	Dryland	Paleo

CLM–2×D–paleo	Standalone CLM	560	Wetland	Paleo
CLM-CAM–1×W–modern	CLM coupled to CAM	280	Wetland	Modern
CLM-CAM–2×D–modern	CLM coupled to CAM	560	Dryland	Modern
CLM-CAM–2×W–modern	CLM coupled to CAM	560	Wetland	Modern
CLM-CAM–1×W–paleo	CLM coupled to CAM	280	Wetland	Paleo
CLM-CAM–2×D–paleo	CLM coupled to CAM	560	Dryland	Paleo
CLM-CAM–2×W–paleo	CLM coupled to CAM	560	Wetland	Paleo

Table 4.2 Summary of model experiments. The name of each experiment with format AAAA–#×BB–C corresponds to AAAA = model use to run experiment, # = multiplier of pre-industrial pCO_2 used in experiment (i.e., 280 ppm CO_2), BB = tropical biome distribution with wetland-dominant (W; Figure 4.2b) and dryland-dominant (D; Figure 4.2c), and C = modern or paleo plant functional types used in the tropical biomes. CESM = fully coupled configuration of the Community Earth System Model version 1.2; CLM = standalone Community Land Model version 4; CLM-CAM = Community Land Model version 4 coupled to the Community Atmosphere Model version 5.

We focus on five domains across the Euramerican and Cathaysian tropics (Figure 4.2b and c), including the Ancestral Rocky Mountains, western Pangaea, central Pangaea, eastern Pangaea, and Cathaysia, to capture regional variations in hydroclimate and vegetation-climate interactions. Although the Ancestral Rocky Mountains are a part of western Pangaea, we differentiate these highlands because they typically exhibit different hydroclimate dynamics from the rest of the region. We use modeled differences in LAI and canopy conductance between PaleoBGC–1×W–paleo and CLM–1×W–paleo as well as PaleoBGC–2×D–paleo and CLM–2×D–paleo to validate photosynthetic parameters in the Ball-Berry conductance model that cannot be constrained from fossilized remains. First, we describe general patterns of tropical temperature and monsoon circulation using CLM-CAM–1×W–paleo. Second, we compare the response of modern and paleo-PFTs to the same atmospheric conditions with CLM–1×W–paleo and CLM–1×W–modern and assess the vegetation-climate feedbacks under the same CO_2 with CLM-CAM–1×W–paleo and CLM-CAM–1×W–modern. Third, we compare differences in temperature, atmospheric and soil moisture, precipitation, and canopy transpiration between CLM-CAM–1×W–paleo and CLM-CAM–2×W–paleo as well as CLM-CAM–1×W–modern and CLM-CAM–2×W–modern to analyze the impact of paleo-plant physiology on tropical vegetation-climate interactions under elevated CO_2. Lastly, we compare differences in surface water fluxes between CLM-CAM–2×D–paleo and CLM-CAM–2×W–paleo as well as CLM-CAM–2×D–modern and CLM-CAM–2×W–modern to assess the impact of vegetation transitions between dryland-dominated and wetland-dominated tropical biomes on Pangaean surface climate

and runoff. For a summary of all model experiments included in this study, see Figure 4.3 and Table 4.2.

4.4 Results

4.4.1 Comparison of LAI, stomatal and canopy conductance between *Paleo*-BGC and CLM

Initial comparisons between *Paleo*-BGC and CLM simulations showed large differences in predicted g_s. As a result, we choose to calibrate CLM by modifying specific photosynthetic parameters of the paleo-PFTs that cannot be constrained directly by the fossil record (i.e., *m*). Once calibrated, g_s, LAI, and canopy conductance values from standalone CLM simulations agree well with analogous simulations of *Paleo*-BGC. Under high and low atmospheric CO_2, values of g_s are higher overall in the tropical wetland biome compared to the dryland biome in *Paleo*-BGC and standalone CLM simulations with paleo PFTs (Figure S4.1a, b, d, e). Equatorial g_s values are lower overall in the CLM–2×D–paleo simulation compared to PaleoBGC–2×D–paleo with the largest differences in wetland-dominated regions, such as −0.007 m s^{-1} in the Ancestral Rocky Mountains and −0.017 m s^{-1} in Cathaysia (Figure S4.1d, e), because the Ball-Berry conductance model of CLM cannot resolve the extremely high g_s values of lycopsid and medullosan PFTs simulated in *Paleo*-BGC. Nevertheless, g_s values are substantially lower in the standalone CLM simulations with modern PFT analogs compared to *Paleo*-BGC under high and low CO_2 (Figure S4.1c, f). The improved agreement in g_s values between *Paleo*-BGC and standalone CLM simulations with paleo PFTs suggests that the modified photosynthetic parameters (i.e., *m*, F_{LNR}, SLA, $C:N_{leaf}$) better capture the average g_s, and thus photosynthesis and transpiration, of each extinct plant compared to modern PFT analogs.

One important factor that could potentially affect comparisons of simulated g_s based on fossil-derived g_{smax} is whether operational g_{smax} (i.e., the highest measured value of g_s in natural field conditions, and similar to how g_{smax} values are determined for modern plants in the Jarvis model) is equivalent to theoretical g_{smax}. Modern studies indicate that the operational g_s of plants in normal field conditions rarely operate at the theoretical g_{smax} based on plant anatomy (e.g., Murray et al., 2020). This raises the question of whether fossil-derived g_{smax} values represent operational g_{smax} or theoretical g_{smax}. If fossil-derived g_{smax} values are equal to theoretical g_{smax}, then the development of a scaling relationship between operational g_{smax} and theoretical g_{smax}

would permit more direct comparisons between modern and paleo-plant g_s. This topic opens another potential opportunity for further research.

In addition to g_s, photosynthesis and transpiration are modulated by LAI at the canopy scale. LAI is not preserved in fossilized remains and is a critical parameter that scales the relative importance of other plant physiological traits between vegetated grid cells based on "per unit leaf area". For example, canopy conductance is calculated in CLM version 4 as g_{ssun}*LAI_{sun} + g_{ssha}*LAI_{sha}, where g_{ssun}, LAI_{sun}, g_{ssha}, and LAI_{sha} are sunlit g_s, sunlit LAI, shaded g_s, and shaded LAI, respectively. If two vegetated grid cells that have the same values of g_{ssun} and g_{sha} but different values of LAI_{sun} and LAI_{sha} under the same atmospheric conditions, the grid cell with higher LAI will produce higher canopy transpiration rates. CLM has also been found to overestimate LAI when compared to present-day satellite observations (e.g., Castillo et al., 2012). As a result of these factors, we ensure that LAI values are relatively similar across all CLM and *Paleo*-BGC simulations such that the modeled impacts of vegetation on climate are primarily driven by differences in plant physiology and not LAI.

Due to our calibration, equatorial LAI values are similar overall between the *Paleo*-BGC and CLM-only simulations. However, there are some exceptions in regions where vegetation is supported in *Paleo*-BGC but not in CLM (Figure S4.2). The largest differences in LAI occur in eastern Pangaea, where average LAI in PaleoBGC–1×W–paleo is 4.6 and CLM–1×W–paleo is 2.3 (50% lower LAI; Figure S4.2b). Unlike Paleo-BGC, overall dry conditions along the coast of eastern Pangaea inhibit the growth of vegetation in CLM. Relatively lower LAI in eastern equatorial Pangaea drives lower regional canopy conductance in CLM–1×W–paleo and CLM–2×D–paleo (Figure S4.2b and c). However, canopy conductance values compare well overall between Paleo-BGC and CLM-only simulations with paleo PFTs (Figure S4.3b and e). Relatively higher LAI values in the CLM-only simulations with modern PFT analogs (Figure S4.2c and f) drive higher canopy conductance values than what we would expect from patterns of stomatal conductance alone, yet the CLM–1×W–modern and CLM–2×D–modern simulations underestimate canopy conductance in the wetland biome compared to PaleoBGC–1×W–paleo and PaleoBGC–2×D–paleo, respectively (Figure S4.3c and f). In sum, the photosynthetic parameters of paleo PFTs that we modified (i.e., m, F_{LNR}, and SLA) based on Paleo-BGC produce reasonable values of canopy conductance. In addition, comparison of LAI values

between the CLM simulations with paleo PFTs and modern PFT analogs suggests that differences in canopy conductance arise primarily from g_s and not LAI.

4.4.2 General characteristics of low-latitude terrestrial surface climate under low CO_2

The low-latitudes of Pangaea are characterized by extreme continentality and equatorial highlands, including the Ancestral Rocky Mountains in the west and the southwest–northeast trending mountain chain (i.e., Central Pangaean Mountains), that produce high spatial gradients in temperature and precipitation patterns across the supercontinent. In the CLM-CAM–1×W–paleo simulation, lowland surface temperatures (<900 m elevation) decrease from ~25°C in western Pangaea to ~23.5°C in central Pangaea (Figure 4.4b). Seasonal surface temperature variations in the lowland regions are low overall (i.e., up to ~1.2°C in eastern Pangaea). The Central Pangaean Mountains create elevation-driven surface temperature decreases down to <6°C in central-eastern Pangaea where elevations >2500 m. Seasonal temperature variations in the Central Pangaean Mountains are slightly higher than in the lowlands, reaching up to ~2.3°C in central Pangaea, whereas mean seasonal temperatures remain ~24.5°C in the Ancestral Rocky Mountains. Surface temperatures over Cathaysia remain at a relatively constant value of ~25–26°C throughout the year. Although temporal variations in low-latitude surface temperature are relatively small, extreme seasonality in terrestrial rainfall is driven by monsoon systems.

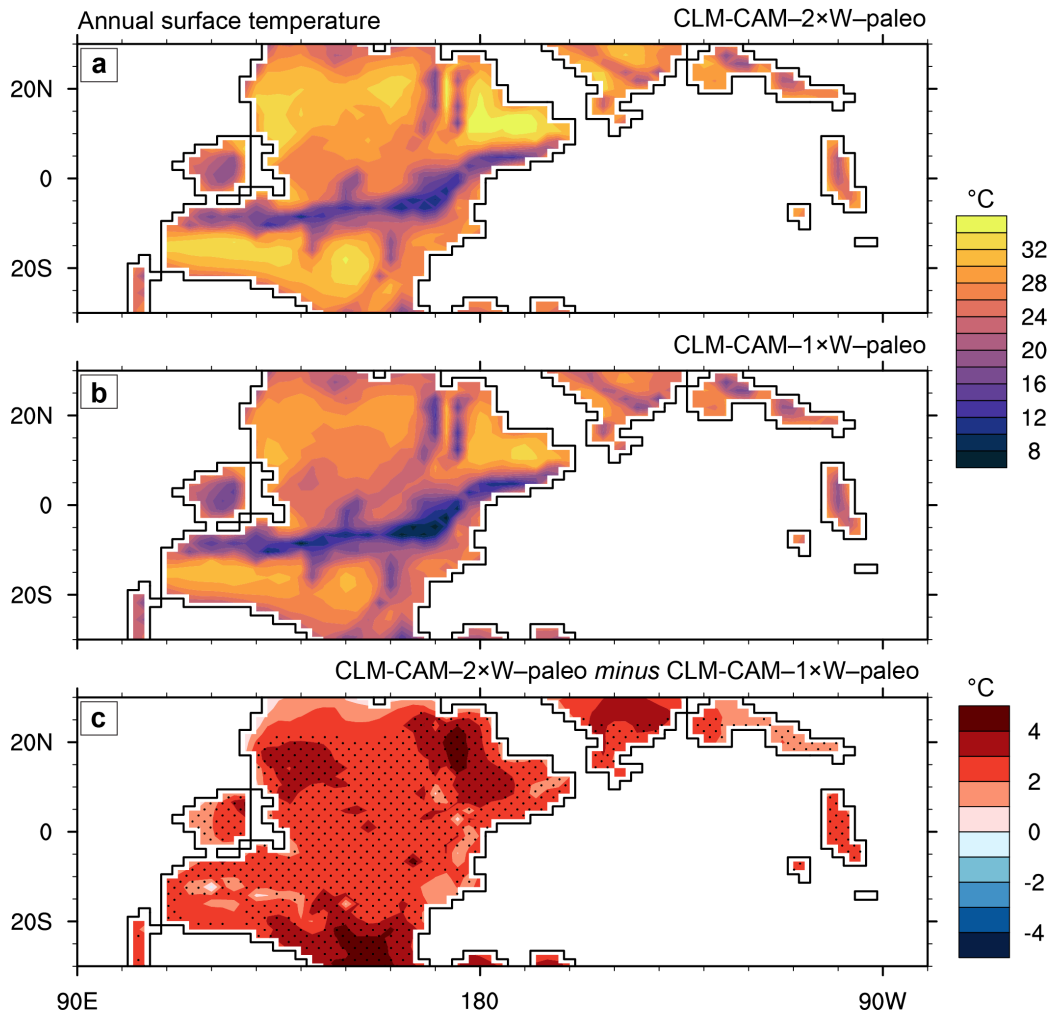

Figure 4.4 Mean annual surface temperature over land (°C) for the (a) CLM-CAM–2×W–paleo and (b) CLM-CAM–1×W–paleo simulations. (c) The difference in surface temperature between the two simulations. Stippled areas indicate significant differences at $p < 0.05$ using a student's t-test. Note that temperature patterns for the CLM-CAM–2×W–modern and CLM-CAM–1×W–modern cases are very similar. Only annual temperatures are shown here because temperature variations over ~10°S–N are small throughout the year under high and low CO_2.

The hydrological cycle over the Pangaean supercontinent has long been hypothesized to have been dominated by large-scale monsoonal circulation, referred to as the "megamonsoon" (Dubiel et al., 1991; Kutzbach and Gallimore, 1989; Parrish, 1993; Parrish et al., 1982). Under low atmospheric CO_2, megamonsoon systems exist in both hemispheres over low-latitude Pangaea and the Paleo-Tethys Ocean, producing highly seasonal precipitation across the tropics (Figure 4.5). During the summer months in the Northern Hemisphere (June-July-August; JJA), westerly winds carry moisture from the eastern equatorial Panthalassic Ocean over low-latitude

Pangaea (particularly from ~5°S–15°N) and create an overall decreasing west-east gradient of rainfall, with mean values of 6.3 mm day^{-1} in the Ancestral Rocky Mountains and 3.2 mm day^{-1} in the lowland regions of eastern Pangaea (Figure 4.5c). At the same time over the North Paleo-Tethys, strong cross-equatorial flow brings warm, moist airmasses from south of the equator and produces high precipitation over Cathaysia. During the summer months in the Southern Hemisphere (December-January-February; DJF), the inter-tropical convergence zone shifts southward and precipitation decreases across lowland Euramerica (e.g., 27% and 63% on average in western and central Pangaea). DJF terrestrial precipitation is concentrated over the Central Pangaean Mountains (Figure 4.5d). Southwesterly winds produce high amounts of precipitation, 7.5 and 6.3 mm day^{-1}, along the western and central portions of the Central Pangaean Mountains, respectively. A similar reversal of cross-equatorial winds occurs over the Paleo-Tethys and brings relatively higher precipitation to Cathaysia during DJF (7.9 mm day^{-1} compared to 6.3 mm day^{-1} during JJA), but rainfall remains high throughout the year relative to the lowland regions of Pangaea.

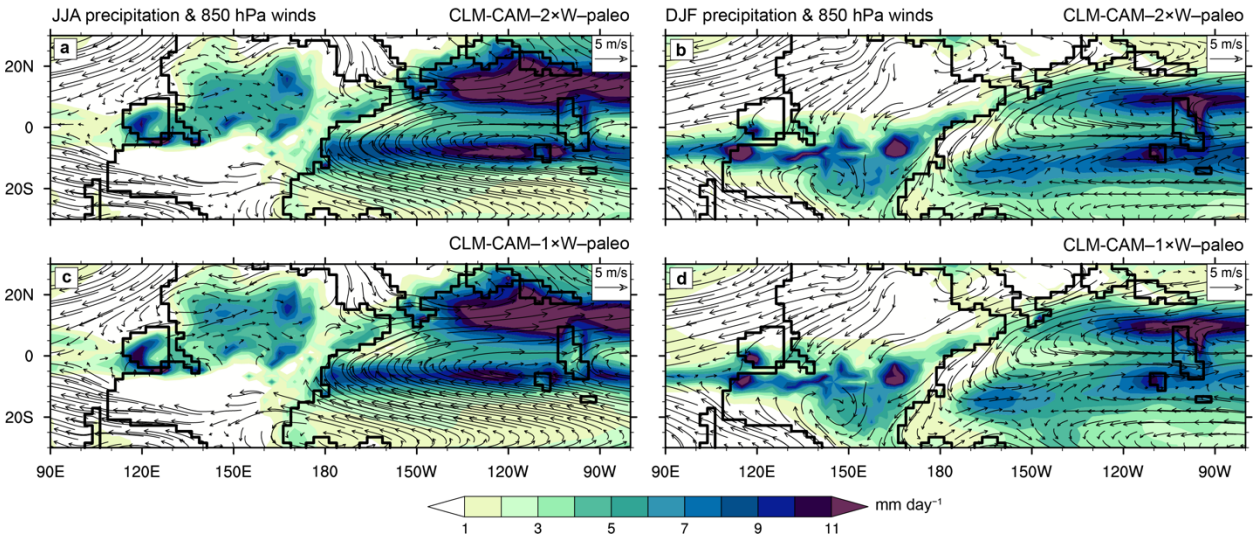

Figure 4.5 Seasonal precipitation (mm day^{-1}) and 850 hPa winds (m s^{-1}) over low-latitude Pangaea under high and low CO2 (same biome distribution and plant physiology). Mean June-July-August (JJA) and December-January-February (DJF) precipitation and winds are shown for the CLM-CAM–2×W–paleo (a, b) and CLM-CAM–1×W–paleo (c, d) simulations, respectively.

4.4.3 Influence of modern and paleo-plant physiology on vegetation-climate interactions under low CO_2

The same general patterns of low-latitude temperature and precipitation are captured with paleo-PFTs and modern PFTs under relatively low atmospheric CO_2, yet the higher canopy conductance of paleo-PFTs causes stronger vegetation-atmosphere feedbacks compared to modern PFTs (Figure 4.7). Under the same atmospheric conditions (without any atmospheric feedbacks) and biome distribution, the higher canopy conductance of paleo-PFTs compared to modern PFTs causes overall enhanced canopy transpiration that reduces soil moisture over nearly every region of paleotropical Euramerica and Cathaysia (Figure 4.6a, e, c, g). In lowland regions where seasonal precipitation is concentrated, such as portions of western and central Pangaea near the Central Pangaean Mountains during JJA (Figure 4.5c), soil moisture remains high in CLM–1×W–paleo and CLM–1×W–modern despite up to ~50% higher canopy transpiration with paleo-PFTs compared to modern PFTs. In these regions with initially high precipitation and soil moisture, positive atmospheric feedbacks (i.e., CLM-CAM–1×W–paleo) cause paleo-PFTs to dry atmospheric and soil conditions. High transpiration rates associated with initially high soil moisture in these regions eventually deplete soil moisture (Figure 4.6b), reduce precipitation, and increase VPD, which further enhance transpiration rates (Figure 4.6d). On the other hand, in some regions with lower precipitation, such as lowland regions of western and central Pangaea from ~5–10°N during JJA (northern edge of equatorial Euramerica) (Figure 4.5c), relatively high canopy transpiration with paleo-PFTs substantially lowers regional soil moisture in CLM–1×W–paleo compared to CLM–1×W–modern. With atmospheric feedbacks, paleo-PFTs either suppresses or keeps transpiration rates the same in response to relatively low initial soil moisture, leading to increased soil moisture and precipitation in these regions. Because transpiration rates are lower overall for modern PFTs, soil moisture remains relatively high across most of the paleotropics, and thus atmospheric feedbacks cause moderate increases in plant transpiration that do not alter precipitation substantially. Taken together, the high canopy transpiration rates of paleo-PFTs induce stronger paleotropical vegetation-climate feedbacks compared to modern PFTs given the same atmospheric conditions and biome distribution. Our future work will focus on the contribution of specific paleo-PFT parameters to relatively higher conductance compared to modern PFTs.

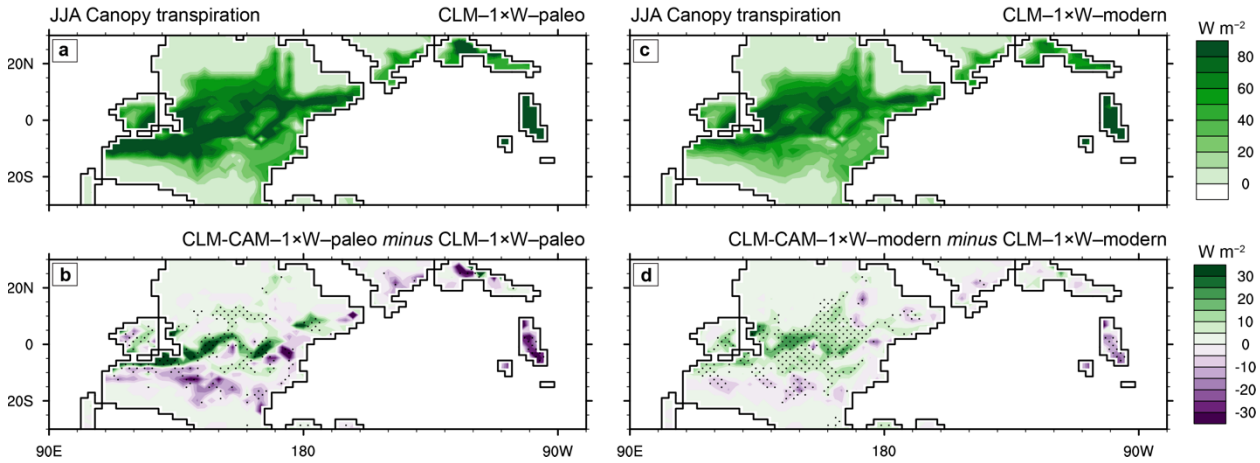

Figure 4.6 Contribution of atmospheric feedbacks to canopy transpiration of modern and paleo PFTs. Absolute values of mean June-July-August (JJA) canopy transpiration in the (a) CLM–1×W–paleo and (c) CLM–1×W–modern simulations. Differences in JJA canopy transpiration between (b) CLM-CAM–1×W–paleo and CLM–1×W–paleo as well as (d) CLM-CAM–1×W–modern and CLM–1×W–modern. Stippled areas indicate significant differences at $p < 0.05$ using a student's t-test.

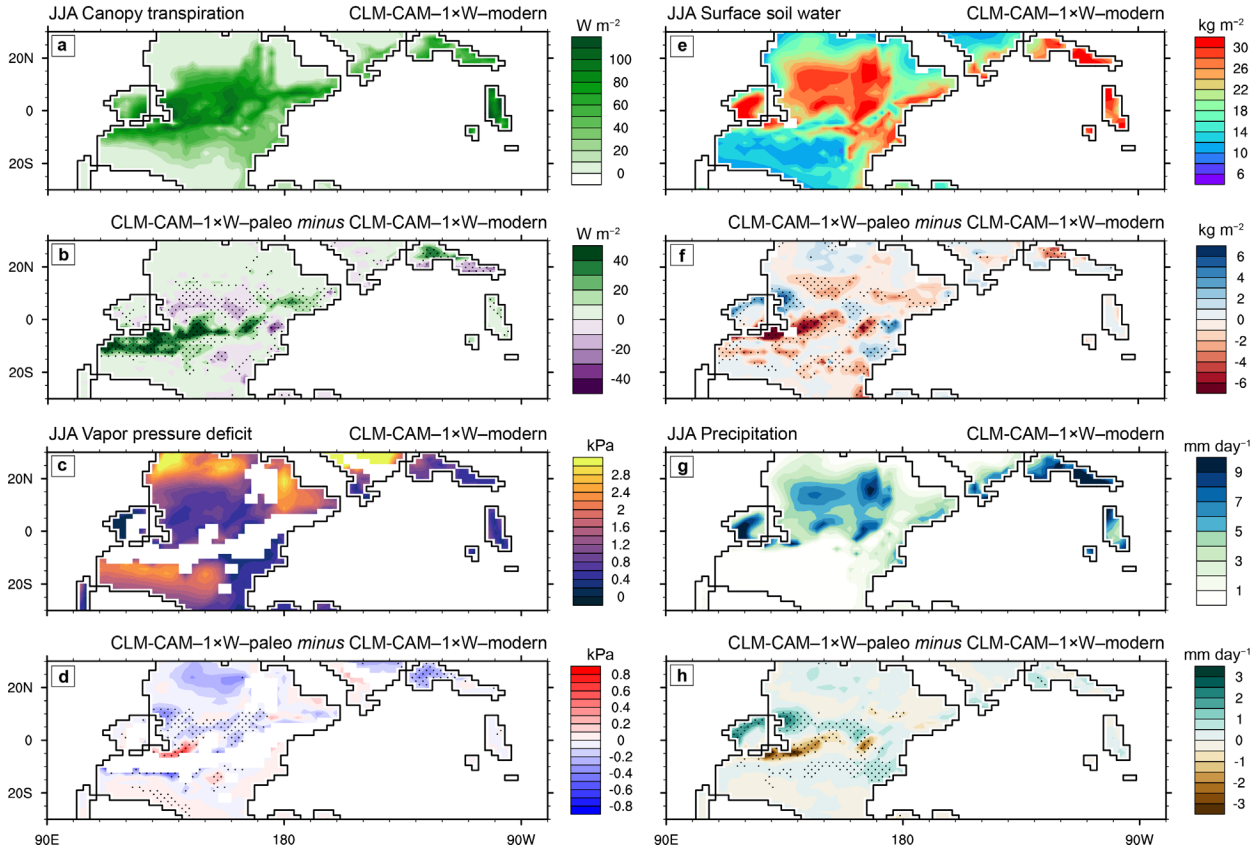

Figure 4.7 Differences in surface climate between modern and paleo-PFTs under low CO_2. Absolute values and differences in mean JJA (a, b) canopy transpiration, (c, d) vapor pressure

deficit, (e, f) surface soil water, and (g, h) total precipitation, respectively, between the CLM-CAM–1×W–paleo and CLM-CAM–1×W–modern simulations. Stippled areas indicate significant differences at $p < 0.05$ using a student's t-test.

4.4.4 Response of modern and paleo-plants to elevated atmospheric CO_2 across the low-latitudes

The surface temperature and VPD response to a doubling of atmospheric CO_2 is relatively similar with modern and paleo-PFTs. Surface temperatures increase by ~1.8–3.2°C across low-latitude Pangaea with a doubling of atmospheric CO_2 (Figure 4.4c). The seasonality of lowland surface temperatures remains relatively low with <1.0°C difference between JJA and DJF. Surface heating from increased pCO_2 leads to increases in VPD and decreases of low cloud cover (up to 15%) over most of low-latitude Pangaea, particularly on the northern and southern edges of the dryland tropics where LAI is low and thus heating drives large increases in ground evaporation (Figure 4.9b and f; Figure 4.8 e). Decreases in low cloud cover suppress precipitation and weaken shortwave cloud forcing, allowing more solar radiation to reach the surface (Figure 4.8c). Nevertheless, in some equatorial regions (e.g., lowland western and eastern Pangaea during JJA) CO_2-induced increases in specific humidity are relatively higher and thus VPD is similar or even slightly decreased. In these regions, relatively similar or slightly increased low cloud cover under higher pCO_2 strengthens shortwave cloud forcing and increases precipitation in these regions. In vegetated regions of equatorial Pangaea with high LAI, soil moisture and/or biome type determines the plant physiological response to increased pCO_2.

It is typically expected that stomatal conductance, and thus transpiration, decreases under elevated atmospheric CO_2 to promote water use efficiency, however stomatal behavior is also affected by environmental factors, such as water availability (e.g., soil moisture, vapor pressure deficit) and temperature (Purcell et al., 2018; Xu et al., 2016). In our simulations with paleo-PFTs, the response of stomatal conductance and canopy transpiration rates to a doubling of pCO_2 varies across low-latitude Pangaea (i.e., differences between CLM-CAM–1×W–paleo and CLM-CAM–2×W–paleo; Figure 4.9d). Lowland regions with decreased canopy transpiration rates coincide with similar or decreased VPD because low atmospheric moisture demand suppresses the evaporative force driving transpiration (e.g., central Pangaea during JJA; Figure 4.8a and

4.9b). Relatively high regional moisture and low VPD is accompanied by increases in low cloud cover and precipitation (Figure 4.8d and e), leading to strengthened shortwave cloud forcing (i.e., less solar radiation reaches the surface) and suppressed surface heating in these regions (Figure 4.8b and c). Increased precipitation coupled with decreased transpiration produces overall wetter atmospheric and soil conditions (i.e., more positive net surface water flux, or precipitation minus evapotranspiration; P–ET) (Figure 4.8f). Conversely, lowland regions with increased VPD and high soil moisture correspond with increased canopy transpiration rates (e.g., western Pangaea during JJA; Figure 4.9b and d). In these regions, relatively low atmospheric moisture and high VPD lead to decreases in low cloud cover of up to 15% and weakened shortwave cloud forcing, allowing more solar radiation to warm the surface (Figure 4.8e and c). Precipitation also decreases in the regions, leading to overall drier atmospheric and soil conditions (i.e., decreased P–ET; Figure 4.8f). These two main vegetation-climate feedbacks control regional increases and decreases in P–ET across lowland wetland and dryland regions where seasonal precipitation is high (Figure 4.10).

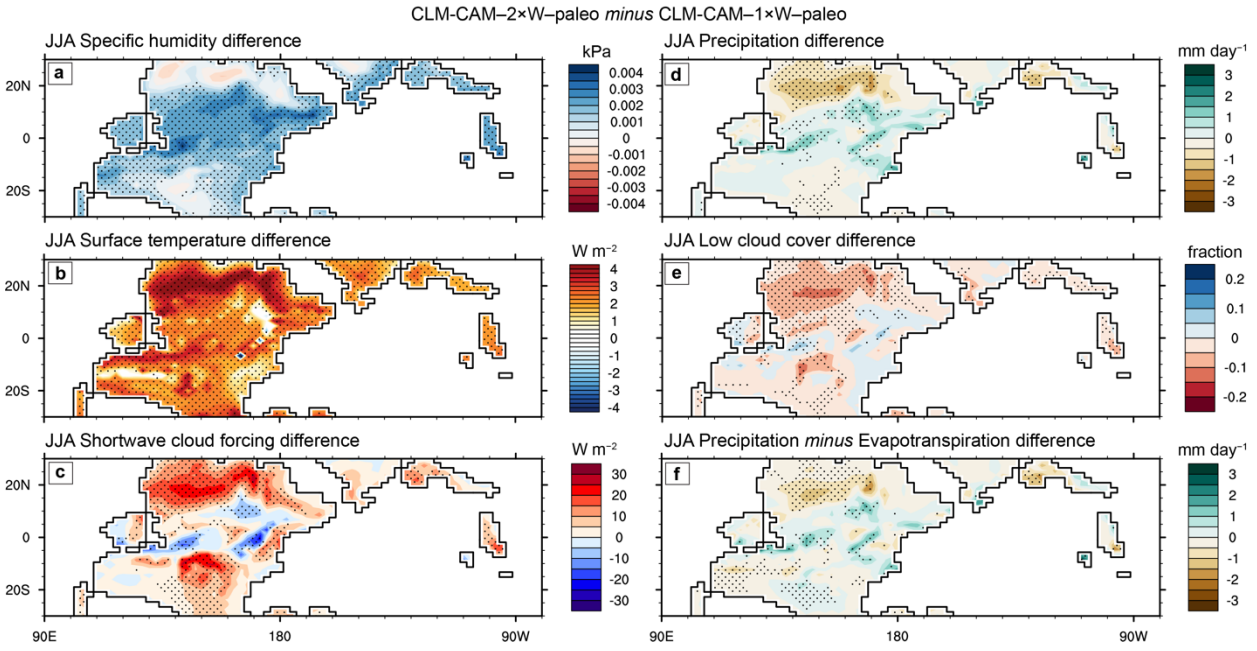

Figure 4.8 Differences in mean JJA surface climate between the CLM-CAM–2×W–paleo and CLM-CAM–1×W–paleo simulations. Differences in (a) specific humidity, (b) surface temperature, (c) shortwave cloud radiative forcing, (d) precipitation, (e) low cloud cover, and (f) precipitation minus evapotranspiration (P–ET) are shown. Stippled areas indicate significant differences at $p < 0.05$ using a student's t-test. An increase (decrease) in P–ET from CLM-

CAM–1×W–paleo to CLM-CAM–2×W–paleo, indicated with blue (brown) values, indicates wetter (drier) atmospheric conditions. Differences in soil moisture are similar that of P–ET.

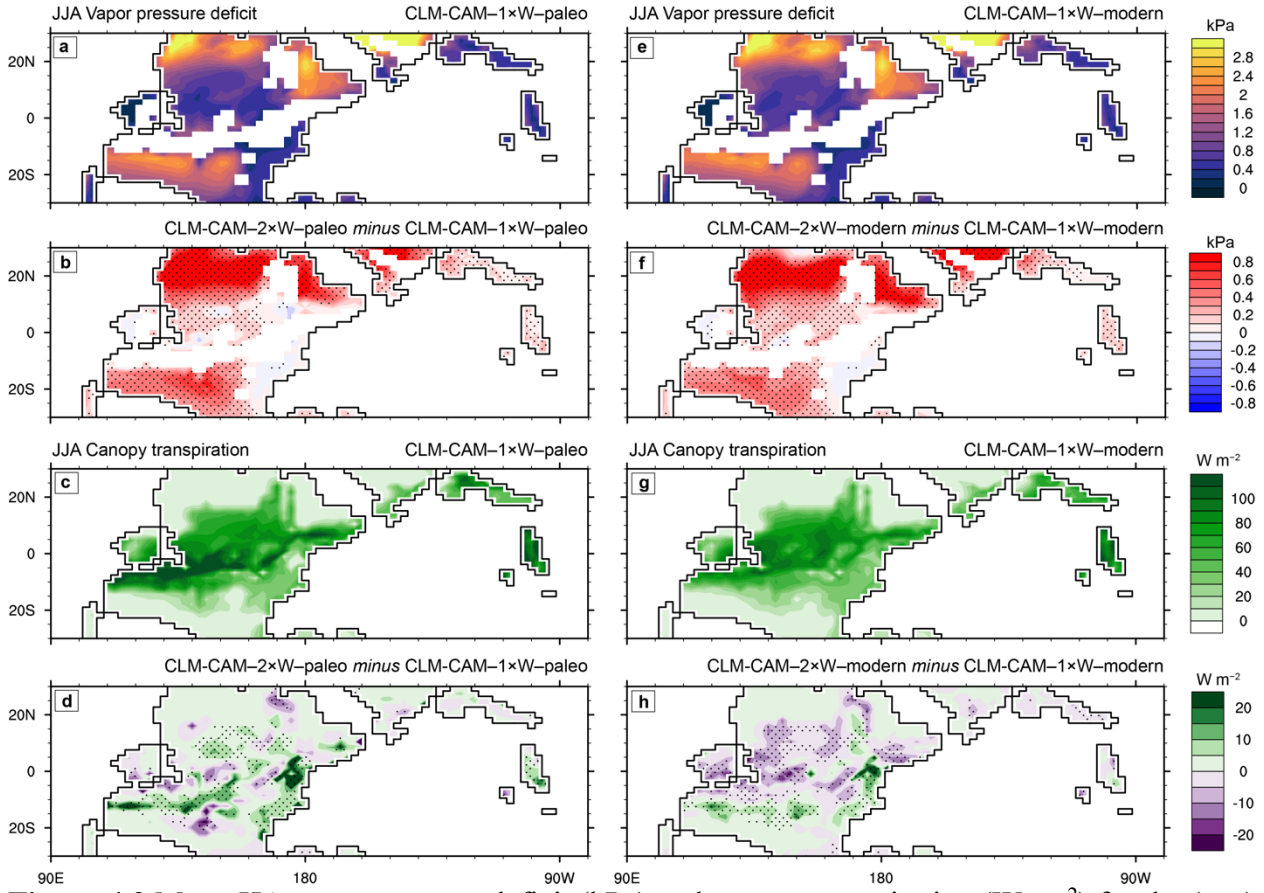

Figure 4.9 Mean JJA vapor pressure deficit (kPa) and canopy transpiration (W m^{-2}) for the (a, c) CLM-CAM–1×W–paleo and (e, g) CLM-CAM–1×W–modern simulations. Differences in JJA vapor pressure deficit and canopy transpiration between the (b, d) CLM-CAM–2×W–paleo and CLM-CAM–1×W–paleo simulations and the (f, h) CLM-CAM–2×W–modern and CLM-CAM–1×W–modern simulations, respectively. Stippled areas indicate significant differences at $p < 0.05$ using a student's t-test.

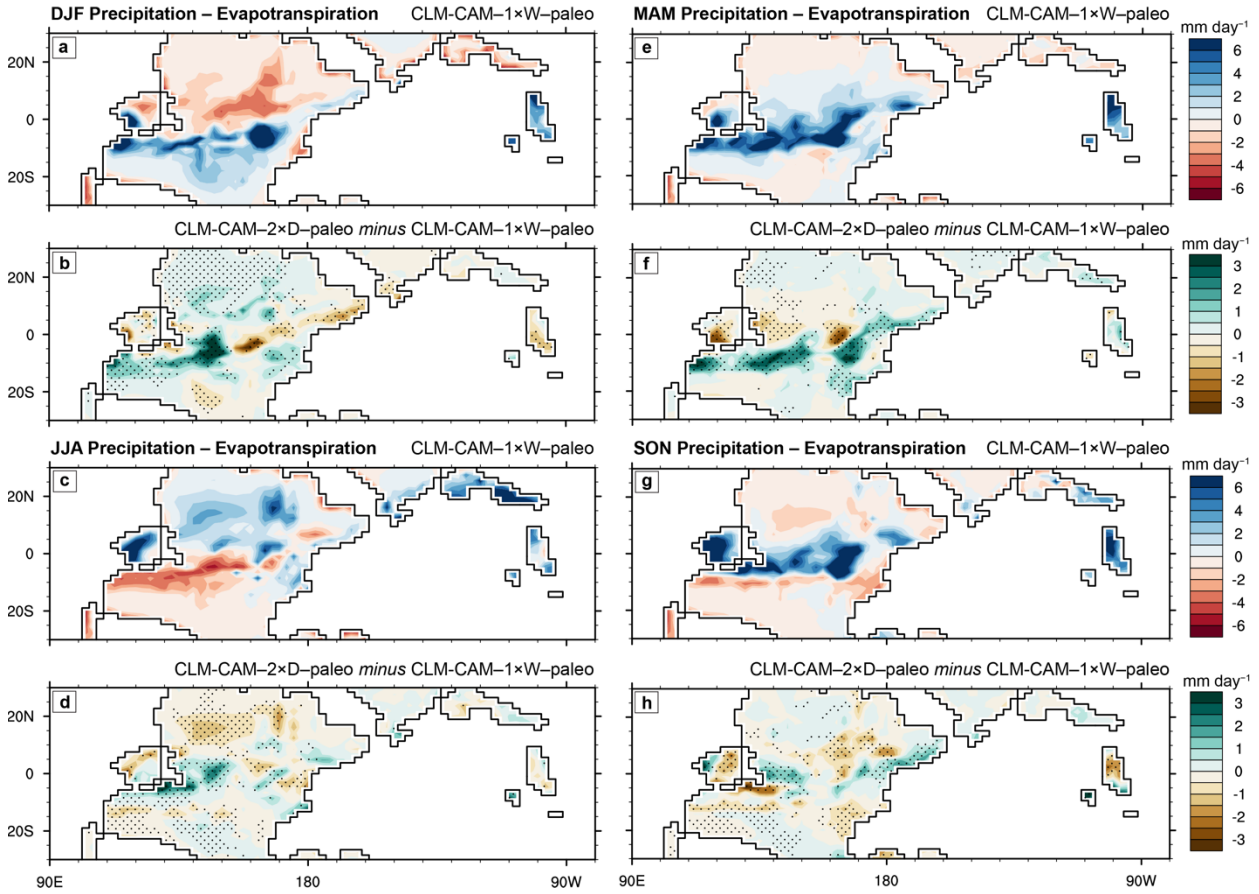

Figure 4.10 Seasonal net surface water flux indicated by precipitation minus evapotranspiration (mm day^{-1}; P–ET) for the CAM-CLM simulations with paleo PFTs. Absolute values of mean P–ET are shown for CLM-CAM–1×W–paleo during (a) DJF, (e) MAM, (c) JJA, and (g) SON. Differences in mean DJF (b), MAM (f), JJA (d), and SON (h) P–ET values between CLM-CAM–1×W–paleo and CLM-CAM–2×D–paleo. Stippled areas indicate significant differences at $p < 0.05$ using a student's t-test.

Modern PFTs exhibit a more spatially uniform response to a doubling of atmospheric pCO_2 (i.e., differences between CLM-CAM–1×W–modern and CLM-CAM–2×W–modern). Modern PFTs almost uniformly decrease stomatal conductance, and thus canopy transpiration rates, despite overall similar changes in VPD under increased pCO_2 (Figure 4.9h). Consequently, decreased transpiration coupled with increased precipitation produces wetter atmospheric and soil conditions where seasonal precipitation is high in lowland equatorial Pangaea (e.g., western Pangaea during JJA; Figure 4.11c). In regions where VPD and soil moisture is high, there are relatively small increases in canopy transpiration that lead to drier atmospheric and soil conditions (e.g., central Pangaea during JJA; Figure 4.11c). The overall enhanced stomatal conductance of paleo PFTs compared to that of the modern PFT analogs (Figure S4.1) results in

consistently higher canopy transpiration rates across the Pangaean tropics, particularly in wetland biome regions (Figure 4.9c and g). In lowland regions, the largest increases in canopy transpiration (i.e., 17.4 and 12.2 W m^{-2} or 26% and 28%) occur in western and eastern Pangaea during JJA. The transpiration rates of modern PFTs do not increase as much in response to high VPD and low atmospheric moisture, and thus decreases in P–ET and soil moisture are not as apparent (compare Figure 4.11c and Figure 4.8f). Taken together, modern PFTs produce overall wetter conditions in lowland regions of Pangaea under elevated CO_2, whereas paleo-PFTs cause regional wetting and drying in select lowland regions of Pangaea that are drier overall under elevated CO_2 (Figure 4.13).

A doubling of CO_2 primarily impacts surface runoff in highland regions of low-latitude Pangaea (Figure 4.12) and differs based on modern or paleo-PFT vegetation cover. During March-April-May (MAM) when the ITCZ is centered over the equatorial highlands (i.e., positive P–ET), paleo PFTs and modern PFTs produce a similar decrease in surface runoff (−0.37 mm day^{-1}) in the Ancestral Rocky Mountains under elevated CO_2 (Figure 4.12a; Figure S4.4a). In the western, relatively low elevation region of the Central Pangaean Mountains, paleo-PFTs cause increased P–ET and soil moisture under elevated CO_2, leading to regional increases in surface runoff of up to 0.57 mm day^{-1} during MAM (Figure S4.4). MAM and September-October-November (SON) exhibit the largest seasonal changes in Euramerican surface runoff because the ITCZ is centered over the equatorial highlands. On the other hand, modern PFTs lead to decreased MAM runoff in the Central Pangaean Mountains (Figure S4.4). Although MAM P–ET values in the region increase under elevated CO_2 with modern and paleo PFTs, the difference in surface runoff response is produced by lowered evapotranspiration and enhanced precipitation driving regional increases in P–ET, respectively. Consequently, CO_2-induced changes in net surface runoff over western Pangaea (including the Ancestral Rocky Mountains) are positive and negative with paleo-PFTs and modern PFTs, respectively. During times of low precipitation in the Central Pangaean Mountains (i.e., negative or close to zero P–ET) such as JJA, paleo-PFTs also induce 30–45% increases in canopy transpiration rates that lower regional P–ET and suppress surface warming by up to ~2°C relative to modern PFTs under elevated CO_2.

It is also important to note that a humid climate persists in Cathaysia regardless of modern or paleo-PFTs. Positive P–ET persist throughout the year in Cathaysia with paleo and

modern PFTs, as increases in canopy transpiration are largely balanced by enhanced rainfall under low and high CO_2.

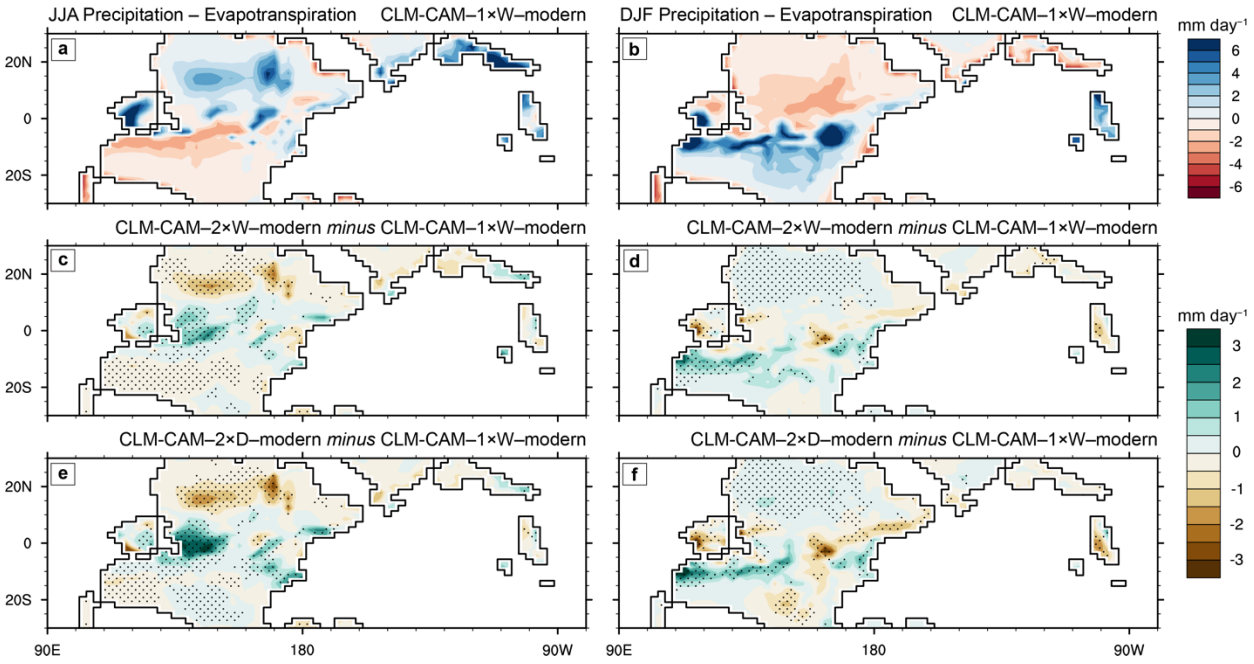

Figure 4.11 Seasonal net surface water flux indicated by precipitation minus evapotranspiration (mm day^{-1}; P–ET) for the CAM-CLM simulations with modern PFTs. Absolute values of mean P–ET are shown for CLM-CAM–1×W–modern during (a) JJA and (b) DJF. Differences in mean JJA and DJF P–ET values relative to CLM-CAM–1×W–modern are shown for (c, d) CLM-CAM–2×W–modern and (e, f) CLM-CAM–2×D–modern, respectively. Stippled areas indicate significant differences at $p < 0.05$ using a student's t-test.

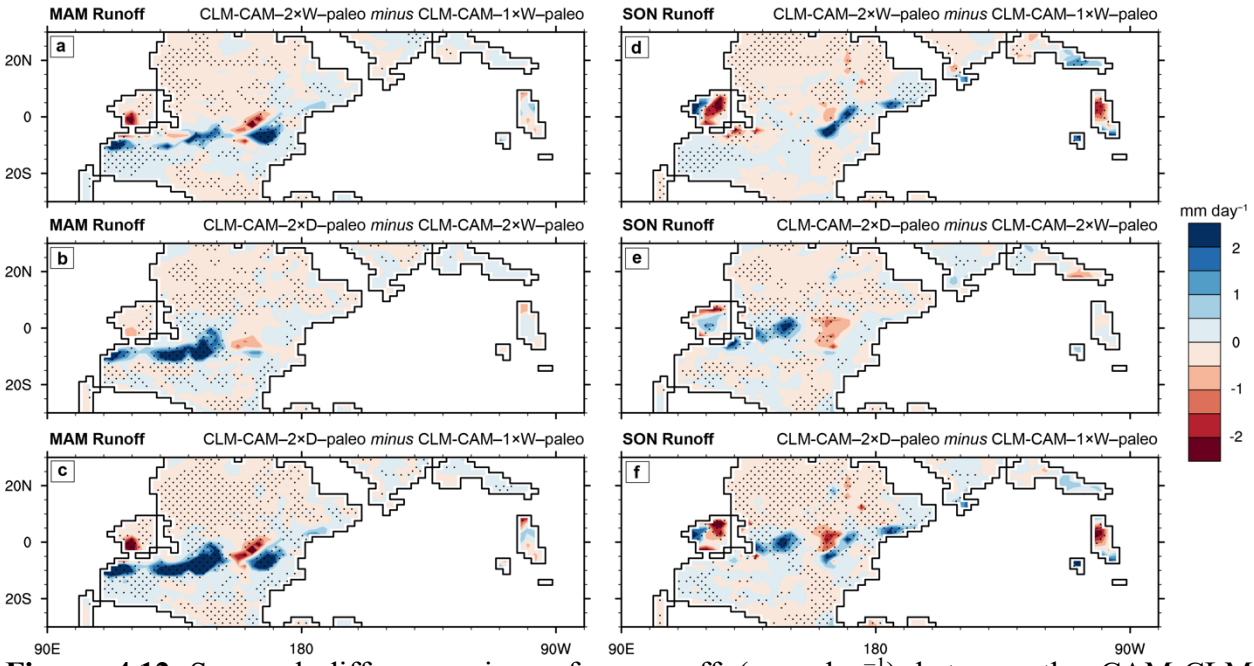

Figure 4.12 Seasonal differences in surface runoff (mm day^{-1}) between the CAM-CLM simulations with paleo PFTs. Differences in MAM and SON surface runoff are shown between (a, d) CLM-CAM–2×W–paleo and CLM-CAM–1×W–paleo, (b, e) CLM-CAM–2×D–paleo and CLM-CAM–2×W–paleo, (c, f) CLM-CAM–2×D–paleo and CLM-CAM–1×W–paleo, respectively. Stippled areas indicate significant differences at $p < 0.05$ using a student's t-test. Surface runoff changes in Euramerica are largest during MAM and SON because the inter-tropical convergence zone is centered over the equatorial highlands.

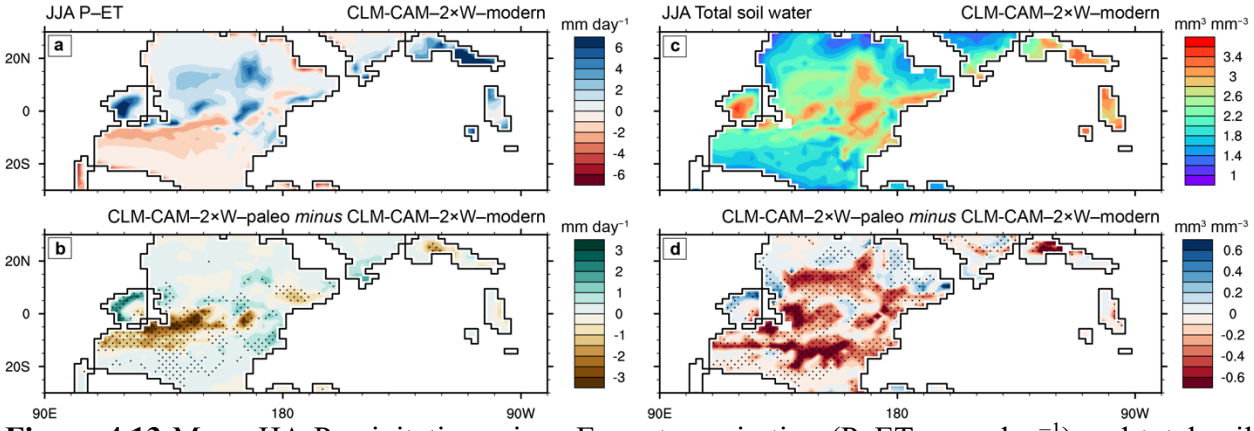

Figure 4.13 Mean JJA Precipitation minus Evapotranspiration (P–ET; mm day^{-1}) and total soil water (mm^3 mm^{-3}) for the (a, c) CLM-CAM–2×W–modern simulation. Differences in JJA P–ET and total soil water between the (b, d) CLM-CAM–2×W–paleo and CLM-CAM–2×W–modern simulations, respectively. Stippled areas indicate significant differences at $p < 0.05$ using a student's t-test.

4.4.5 Influence of paleotropical biome distributions on tropical vegetation-climate interactions

Our simulations capture an environmental transition from wetland-dominant tropics under low CO_2 (CLM-CAM–1×W–paleo) to wetland-dominant tropics under high CO_2 (CLM-CAM–2×W–paleo) to dryland-dominant tropics under high CO_2 (CLM-CAM–2×D–paleo). A doubling of atmospheric CO_2 with a wetland-dominant biome distribution produces two main vegetation-climate feedbacks: regional drying caused by low atmospheric humidity and high VPD that drives higher canopy transpiration rates and regional wetting induced by similar or decreased VPD with lower canopy transpiration rates. With the addition of vegetation shifts from wetland to dryland biomes in equatorial regions of western and central Pangaea (i.e., differences between CLM-CAM–1×W–paleo and CLM-CAM–2×D–paleo), the vegetation-climate feedback that causes wetter atmospheric and soil moisture conditions is strengthened (i.e., increases in P–ET and soil moisture are enhanced) while regional aridification is largely the same (Figure 4.10). Canopy transpiration rates decrease in regions of western and central Pangaea that transition from the wetland to dryland biome due to overall lower stomatal conductance values of dry-adapted plants (particularly regions with low JJA monsoonal precipitation). Consequently, decreased rates of canopy transpiration associated with similar or decreased VPD under elevated CO_2 are even lower in the dryland compared to the wetland biome, producing higher P–ET values in the region (Figure 4.10d). In portions of western and central Pangaea that are drier under elevated CO_2 (i.e., lower P–ET and soil moisture values), the net surface water flux is similar with a shift from the wetland to dryland biome because suppressed canopy transpiration is offset by slight increases in regional LAI (<1.0). Differences in low-latitude vegetation-climate interactions are similar between CLM-CAM–1×W–paleo and CLM-CAM–2×D–paleo versus CLM-CAM–1×W–paleo and CLM-CAM–1×W–modern because of the relatively lower stomatal conductance values of dry-adapted paleo-PFTs and modern PFTs compared to paleo PFTs in the wetland biome.

The combined effects of a shift from wetland to dryland-dominated tropics and increased pCO_2 cause an overall increase in surface runoff across low-latitude Pangaea (Figure 4.12c and f). In the western region of the Central Pangaean Mountains, increases in P–ET and soil moisture under elevated CO_2 produce regional increases in surface runoff of 0.88 and 0.29 mm day^{-1}

during MAM and SON, respectively. Regional increases in surface runoff in the lowlands of western Pangaea and Central Pangaean Mountains dominate runoff decreases in the Ancestral Rocky Mountains.

4.5 Discussion

4.5.1 Relationship between CO_2 and tropical hydroclimate over Pangaea during the Pennsylvanian

Proxy-based reconstructions document repeated and dynamic restructuring of paleotropical forests over a hierarchy of timescales (10^5–10^7 yr) during the Pennsylvanian–early Permian, roughly in step with climate and pCO_2 change (DiMichele, 2014; DiMichele et al., 2009). At the eccentricity scale, tropical wetland and dryland biomes were intercalated, yet wetland and dryland biomes dominated glacial and interglacial phases of each successive cycle, respectively (DiMichele, 2014; Falcon-Lang, 2004; Falcon-Lang et al., 2009). The spatial distribution of dry-adapted plant fossils and paleoclimate indicators across the low-latitudes suggest that the lowlands of western Pangaea were drier on average than that of central and eastern Pangaea (Cecil et al., 2003; Tabor and Montañez, 2002). Over million-year timescales, both the wetland and dryland biomes were broadly restructured with more drought-tolerant vegetation over a long-term trend of decreasing pCO_2 during the Pennsylvanian (DiMichele et al., 2009; Montañez et al., 2016; Pfefferkorn and Thomson, 1982; Phillips et al., 1974; Tabor et al., 2013). At the Carboniferous–Permian boundary, wetland biomes disappeared from the paleotropics and dryland biomes prevailed along with a long-term trend of increasing pCO_2 and aridification over the early Permian (Montañez et al., 2016; Tabor and Poulsen, 2008). Proxy records of humid tropical climate (e.g., coal, laterite, and bauxite) are common during the Pennsylvanian, but are virtually absent and replaced by records of dry climate (e.g., calcrete and evaporite) in the early Permian of western and central Pangaea (Gibbs et al., 2002; Tabor and Montanez, 2004; Tabor and Poulsen, 2008). The transition from relatively humid to arid climate was rapid in western equatorial Pangaea (Montanez et al., 2007; Tabor and Montanez, 2004), extended over considerably longer time-scales in central Pangaea (Roscher and Schneider,

2006), and likely absent in Cathaysia as regional paleoclimate records of humidity continue from Late Pennsylvanian–Early Permian (Gibbs et al., 2002; Rees et al., 2002).

A wide range of conceptual and numerical models have been used to explain Late Paleozoic climate change considering the detailed spatial and temporal proxy records from across near-equatorial Pangaea. The majority of environmental proxy data and modeling evidence indicate that hydroclimate over low-latitude Pangaea was relatively wetter during intervals of lower pCO_2 (Cecil et al., 2003; DiMichele, 2014; Horton et al., 2010, 2012; Montañez and Poulsen, 2013; Peyser and Poulsen, 2008). Modeling studies in line with this view indicate that higher pCO_2 warms continental temperatures, leading to high evaporation rates, and reductions in soil moisture that reduce precipitation across equatorial Pangaea (Horton et al., 2012; Otto-Bliesner, 2003; Peyser and Poulsen, 2008; Poulsen et al., 2007). Nevertheless, some modeling studies indicate that the Pangaean tropics were drier under low pCO_2 because CO_2-induced cooling reduces atmospheric moisture availability and tropical precipitation (Heavens et al., 2012, 2015). This view of paleotropical aridity under low pCO_2 is supported by some geologic indicators of drier climate, such as widespread deposits of loess and calcareous fossil soils (Falcon-lang and DiMichele, 2010; Soreghan, 1994; Soreghan et al., 2008). As previous climate modeling studies have acknowledged (Heavens et al., 2015; Horton et al., 2012), the paleotropical humidity/aridity paradigm has largely oversimplified the mechanisms driving Pangaean climate variability.

Our simulations support a more complex picture of paleotropical climate in which (1) both humid and seasonally-dry tropical climates characterized regions of low-latitude Pangaea under varying atmospheric pCO_2 and (2) paleo-plant physiology played an important role in amplifying CO_2-induced changes in the net surface water flux in the tropics. Overall higher VPD under elevated pCO_2 causes tropical wetland and dryland vegetation to transpire more and draw more water from the soil, leading to atmospheric and soil drying in these regions. In some regions and times of the year, such as western and eastern lowland Pangaea during JJA, relatively high atmospheric moisture and low VPD cause tropical wetland and dryland vegetation to transpire less under high CO_2, leading to atmospheric and soil wetting in these regions. Our simulations also indicate that western portion of lowland Pangaea experienced the largest fluctuations in hydroclimate with seasonal and CO_2 changes, supporting the persistence of dry-adapted plant fossils and proxy records of dry climate in this region compared to the central and

eastern portions of lowland Pangaea. Furthermore, the high stomatal conductance of paleo-PFTs reduces soil moisture across the low-latitudes, particularly in western lowland Pangaea, compared to modern PFTs. Importantly, overall lower stomatal conductance values cause modern PFTs to underestimate regional atmospheric and soil drying under elevated CO_2 that is observed in proxy records over low-latitude Pangaea. Regardless of modern or paleo-PFTs and pCO_2, Cathaysia experiences high precipitation throughout the year, supporting the idea that humid climate persisted in Cathaysia from Late Pennsylvanian–Early Permian.

4.5.2 Influence of paleo-plants on surface hydrology over tropical Euramerica

Recent studies using *Paleo*-BGC to better understand the physiology of Pennsylvanian plant types that dominated tropical lowland ecosystems have highlighted the impact of both ecophysiology and spatial distribution of paleo-vegetation on watershed hydrology (Richey et al., 2020b; White et al., 2020). Glacial-interglacial shifts in vegetation during the Middle Pennsylvanian from lycopsid- to cordaitalean-dominated tropical forests would have resulted in substantially greater surface runoff, and thus weatherability, erosion potential, and sediment yield, under sufficiently high levels of precipitation (e.g., ~3.2× higher runoff under 1600 mm yr^{-1} precipitation) (Richey et al., 2020b). Our simulations with paleo-PFTs confirm that a transition from the wetland to dryland biome in western Pangaea (under the same level of atmospheric CO_2) produces significant increases in runoff during MAM and SON when the region receives the highest amount of seasonal precipitation (Figure 4.11b and e). Modern PFTs underestimate these increases in runoff (Figure S4.4). Enhanced runoff in western Pangaea would also increase surface water discharge to the nearby ocean, influencing estuarine-like circulation patterns and widespread benthic anoxia in the North American Midcontinent Sea (Algeo and Heckel, 2008; Macarewich et al., 2021).

4.6 Conclusions

The CESM and *Paleo*-BGC modeling presented here reveals insight that directly addresses three fundamental questions regarding Pennsylvanian tropical vegetation-climate interactions: (1) How does replacing modern PFTs with paleo-PFTs in CESM alter tropical vegetation-climate interactions in Pennsylvanian simulations? (2) How did paleotropical biomes

influence Pangaean surface climate under elevated CO_2? (3) How did shifts in the distribution of tropical wetland and dryland biomes influence low-latitude hydroclimate over Pangaea?

Regarding question (1), our simulations indicate that relatively high canopy conductance and stomatal response to soil water potential causes paleo-PFTs to exert a stronger influence on surface hydroclimate compared to modern PFTs. Under the same atmospheric conditions (e.g., precipitation, pCO_2) paleo-PFTs transpire more water than modern PFTs across the tropics, leading to overall lower soil moisture and higher surface humidity. Soil water decreases are most prominent in western lowland Pangaea, where proxy records indicate relatively dry climate conditions compared to central and eastern lowland regions. In regions with relatively high (low) baseline precipitation and soil moisture, atmospheric feedbacks further enhance (do not affect or slightly suppress) transpiration, leading to decreases (slight increases) in soil moisture and precipitation that are up to 100% greater with paleo-PFTs than modern PFTs. In particular, the relatively low transpiration rates of modern PFTs are associated with a less sensitive responses to atmospheric feedbacks, and thus regional increases and decreases in soil moisture and precipitation are muted compared to paleo-PFTs.

Concerning question (2), our simulations suggest that increased atmospheric pCO_2 produces variable effects on vegetation-climate interactions across lowland equatorial Pangaea. We have identified two main vegetation-climate feedbacks that control the net surface water flux in regions of high seasonal precipitation across lowland Pangaea. Regions with high VPD and low atmospheric moisture cause paleo-vegetation to transpire more, and thus this vegetation-climate feedback amplifies atmospheric and soil drying. Conversely, regions with relatively similar or low VPD allow paleo-vegetation to transpire less. This vegetation-climate feedback enhances atmospheric and soil wetting. Importantly, modern PFTs underestimate or do not capture regional drying feedback compared to paleo-PFTs. Atmospheric and soil drying over equatorial Pangaea under elevated CO_2 is supported by the prevalence of dry-adapted plants in fossil plant assemblages during eccentricity scale intervals of sea level maxima and multimillion year replacement of paleoclimate records indicating humid tropical climates to that of dry climate (DiMichele, 2014; Montañez et al., 2016; Tabor and Poulsen, 2008). As a result, spatial variations in these ancient vegetation-climate feedbacks are not adequately captured by modern PFTs, and thus modeling extinct plant ecosystems necessitates the use of fossil data.

Our simulations also indicate that elevated atmospheric pCO_2 causes variable effects on hydroclimate across equatorial highlands of Pangaea and over Cathaysia. The Ancestral Rocky Mountains experience overall drier atmospheric and soil conditions, whereas the Central Pangaean Mountains are predominantly wetter under increased pCO_2. Precipitation over Cathaysia remains high throughout the year regardless of atmospheric pCO_2 and modern or paleo-PFTs, supporting the persistence of wet-adapted vegetation in this region through the Pennsylvanian.

Results concerning question (3) indicate that a shift from wetland to dryland biome in portions of western and central Pangaea enhance CO_2-induced increases in P–ET and runoff due to overall lower stomatal conductance values. This result supports previous modeling with *Paleo*-BGC that glacial-interglacial shifts in wet to dry-adapted vegetation during the Middle Pennsylvanian would have resulted in substantially greater surface runoff (Richey et al., 2020b). Taken together, this study highlights that representing the functional differences between extinct plant groups in Earth system models is essential to understanding the impact of vegetation on climate and erosional potential of land area over the course of geologic time.

4.7 Acknowledgements and funding

This work was supported by the National Science Foundation (NSF) award 1338200 (C.J.P.). We also acknowledge high-performance computing support from Cheyenne (doi:10.5065/D6RX99HX) provided by the National Center for Atmospheric Research's Computational and Information Systems Laboratory, sponsored by NSF.

4.8 References

Algeo, T. J. and Heckel, P. H.: The Late Pennsylvanian Midcontinent Sea of North America: A review, Palaeogeogr. Palaeoclimatol. Palaeoecol., 268(3–4), 205–221, doi:10.1016/j.palaeo.2008.03.049, 2008.

Andrews, H. N.: Contributions to our knowledge ofAmerican Carboniferous Floras. VII. Some pteridosperm stems from Iowa., Ann. Missouri Bot. Gard., 32, 323–360, 1945.

Andrews, H. N. and Agashe, S. N.: Some exceptionally large calamite stems, Phytomorphology, 15, 103–108, 1965.

Bashforth, A. R., Cleal, C. J., Gibling, M. R., Falcon-Lang, H. J. and Miller, R. F.: Paleoecology

of Early Pennsylvanian vegetation on a seasonally dry tropical landscape (Tynemouth Creek Formation, New Brunswick, Canada), Rev. Palaeobot. Palynol., 200, 229–263, doi:10.1016/j.revpalbo.2013.09.006, 2014.

Bashforth, A. R., DiMichele, W. A., Eble, C. F., Falcon-Lang, H. J., Looy, C. V. and Lucas, S. G.: The environmental implications of upper Paleozoic plant-fossil assemblages with mixtures of wetland and drought-tolerant taxa in tropical Pangea (In Press.), Geobios, 2021.

Basinger, J. F., Rothwell, G. W. and Stewart, W. N.: Cauline Vasculature and Leaf Trace Production in Medullosan Pteridosperms, Bot. Soc. Am., 61(9), 1002–1015 [online] Available from: http://www.jstor.org/stable/2441991, 1974.

Beerling, D. J.: The influence of Carboniferous palaeo-atmospheres on plant function: An experimental and modelling assessment, Philos. Trans. R. Soc. B Biol. Sci., 353(1365), 131–140, doi:10.1098/rstb.1998.0196, 1998.

Bonan, G. B., Lawrence, P. J., Oleson, K. W., Levis, S., Jung, M., Reichstein, M., Lawrence, D. M. and Swenson, S. C.: Improving canopy processes in the Community Land Model version 4 (CLM4) using global flux fields empirically inferred from FLUXNET data, J. Geophys. Res., 116(G2), 1–22, doi:10.1029/2010jg001593, 2011.

Boyce, C. K. and Knoll, A. H.: Evolution of developmental potential and the multiple independent origins of leaves in Paleozoic vascular plants, Paleobiology, 28(1), 70–100, doi:10.1666/0094-8373(2002)028<0070:eodpat>2.0.co;2, 2002.

Boyce, C. K. and Zwieniecki, M. A.: The prospects for constraining productivity through time with the whole-plant physiology of fossils, New Phytol., 223(1), 40–49, doi:10.1111/nph.15446, 2019.

Castillo, C. K. G., Levis, S. and Thornton, P.: Evaluation of the new CNDV option of the community land model: Effects of dynamic vegetation and interactive nitrogen on CLM4 means and variability, J. Clim., 25(11), 3702–3714, doi:10.1175/JCLI-D-11-00372.1, 2012.

Cecil, C. B., Dulong, F. T., West, R. R., Stamm, R., Wardlaw, B. and Edgar, N. T.: Climate Controls on the Stratigraphy of a Middle Pennsylvanian Cyclothem in North America, Clim. Control. Stratigr., 77, 151–180, doi:10.2110/pec.03.77.0151, 2003.

Cecil, C. B., DiMichele, W. A. and Elrick, S. D.: Middle and late pennsylvanian cyclothems, American midcontinent: Ice-age environmental changes and terrestrial biotic dynamics, Comptes Rendus - Geosci., 346(7–8), 159–168, doi:10.1016/j.crte.2014.03.008, 2014.

Cleal, C. J. and Thomas, B. A.: Palaeozoic tropical rainforests and their effect on global climates: Is the past the key to the present?, Geobiology, 3(1), 13–31, doi:10.1111/j.1472-4669.2005.00043.x, 2005.

Collatz, G. J., Ball, J. T., Grivet, C. and Berry, J. A.: Physiological and environmental regulation of stomatal conductance, photosynthesis and transpiration: a model that includes a laminar boundary layer, Agric. For. Meteorol., 54(2–4), 107–136, doi:10.1016/0168-1923(91)90002-8, 1991.

Delevoryas, T.: A Palaeostachya from the Pennsylvanian of Kansas, Am. J. Bot., 42(6), 481–488 [online] Available from: https://www.jstor.org/stable/2438683, 1955.

DiMichele, W. A.: Wetland-Dryland Vegetational Dynamics in the Pennsylvanian Ice Age Tropics, Int. J. Plant Sci., 175(2), 123–164, doi:10.1086/675235, 2014.

DiMichele, W. A. and Falcon-Lang, H. J.: Calamitalean "pith casts" reconsidered, Rev. Palaeobot. Palynol., 173, 1–14, doi:10.1016/j.revpalbo.2012.01.011, 2012.

DiMichele, W. A. and Phillips, T. L.: The ecology of Paleozoic ferns, Rev. Palaeobot. Palynol., 119(1–2), 143–159, doi:10.1016/S0034-6667(01)00134-8, 2002.

DiMichele, W. A., Tabor, N. J., Chaney, D. S. and Nelson, W. J.: From wetlands to wet spots: Environmental tracking and the fate of carboniferous elements in early permian tropical fl oras, Spec. Pap. Geol. Soc. Am., 399(11), 223–248, doi:10.1130/2006.2399(11), 2006.

DiMichele, W. A., Montanez, I. P., Poulsen, C. J. and Tabor, N. J.: Climate and vegetational regime shifts in the late Paleozoic ice age earth, Geobiology, 7(2), 200–226, doi:10.1111/j.1472-4669.2009.00192.x, 2009.

DiMichele, W. A., Chaney, D. S., Lucas, S. G., Nelson, J. W., Elrick, S., Falcon-lang, H. and Kerp, H.: Middle and Late Pennsylvanian fossil floras from Socorro County, New Mexico, U.S.A., Carboniferous-Permian Transit. Socorro County, New Mex., 77(2017), 25–99, 2017.

DiMichele, W. A., Bashforth, A. R., Falcon-Lang, H. J. and Lucas, S. G.: Uplands, lowlands, and climate: Taphonomic megabiases and the apparent rise of a xeromorphic, drought-tolerant flora during the Pennsylvanian-Permian transition, Palaeogeogr. Palaeoclimatol. Palaeoecol., 559(August), 109965, doi:10.1016/j.palaeo.2020.109965, 2020.

Dubiel, R. F., Parrish, J. T., Parrish, J. M. and Good, S. C.: The Pangaean megamonsoon; evidence from the Upper Triassic Chinle Formation, Colorado Plateau, Palaios, 6(4), 347–370, doi:10.2307/3514963, 1991.

Falcon-lang, A. H. J. and Dimichele, W. A.: What happened to the coal forests during Pennsylvanian glacial phases?, Soc. Sediment. Geol., 25(9), 611–617, 2010.

Falcon-Lang, H. J.: Pennsylvanian tropical rain forests responded to glacial-interglacial rhythms, Geology, 32(8), 689–692, doi:10.1130/G20523.1, 2004.

Falcon-Lang, H. J. and Bashforth, A. R.: Pennsylvania uplands were forested by giant cordaitalean trees, Geology, 32(5), 417–420, doi:10.1130/G20371.1, 2004.

Falcon-Lang, H. J. and Bashforth, A. R.: Morphology, anatomy, and upland ecology of large cordaitalean trees from the Middle Pennsylvanian of Newfoundland, Rev. Palaeobot. Palynol., 135(3–4), 223–243, doi:10.1016/j.revpalbo.2005.04.001, 2005.

Falcon-Lang, H. J., Nelson, W. J., Elrick, S., Looy, C. V., Ames, P. R. and DiMichele, W. A.: Incised channel fills containing conifers indicate that seasonally dry vegetation dominated Pennsylvanian tropical lowlands, Geology, 37(10), 923–926, doi:10.1130/G30117A.1, 2009.

Falcon-Lang, H. J., Lucas, S. G., Kerp, H., Krainer, K., Montañez, I. P., Vachard, D., Chaney, D. S., Elrick, S. D., Contreras, D. L., Kurzawe, F., DiMichele, W. A. and Looy, C. V.: Early Permian (Asselian) vegetation from a seasonally dry coast in western equatorial Pangea: Paleoecology and evolutionary significance, Palaeogeogr. Palaeoclimatol. Palaeoecol., 433, 158–173, doi:10.1016/j.palaeo.2015.05.010, 2015.

Feild, T. S., Brodribb, T. J., Iglesias, A., Chatelet, D. S., Baresch, A., Upchurch, G. R., Gomez, B., Mohr, B. A. R., Coiffard, C., Kvacek, J. and Jaramillo, C.: Fossil evidence for Cretaceous escalation in angiosperm leaf vein evolution, Proc. Natl. Acad. Sci., 108(20), 8363–8366, doi:10.1073/PNAS.1014456108, 2011.

Florin, R.: Evolution of cordaites and conifers., Acta Horti Berginal, 17, 259–388, 1951.

Franks, P. J. and Beerling, D. J.: Maximum leaf conductance driven by CO_2 effects on stomatal size and density over geologic time, Proc. Natl. Acad. Sci. U. S. A., 106(25), 10343–10347, doi:10.1073/pnas.0904209106, 2009.

Gibbs, M. T., Rees, P. M., Kutzbach, J. E., Ziegler, A. M., Pat, J., Rowley, D. B., The, S., January, N., Gibbs, M. T., Rees, P. M., Kutzbach, J. E., Ziegler, A. M., Behling, P. J. and Rowley, D. B.: Simulations of Permian Climate and Comparisons with Climate - Sensitive Sediments Published by : The University of Chicago Press Simulations of Permian Climate and Comparisons with Climate-Sensitive Sediments, , 110(1), 33–55, 2002.

Gupta, N. S., Collinson, M. E., Briggs, D. E. G., Evershed, R. P., Pancost, R. D., Paleobiology, S. and Summer, N.: Reinvestigation of the Occurrence of Cutan in Plants : Implications for the Leaf Fossil Record Published by : Cambridge University Press Stable URL : https://www.jstor.org/stable/4096960 REFERENCES Linked references are available on JSTOR for this article, , 32(3), 432–449, 2006.

Heavens, N. G., Mahowald, N. M., Soreghan, G. S., Soreghan, M. J. and Shields, C. a.: Glacial-interglacial variability in Tropical Pangaean Precipitation during the Late Paleozoic Ice Age: simulations with the Community Climate System Model, Clim. Past Discuss., 8(3), 1915–1972, doi:10.5194/cpd-8-1915-2012, 2012.

Heavens, N. G., Mahowald, N. M., Soreghan, G. S., Soreghan, M. J. and Shields, C. A.: A model-based evaluation of tropical climate in Pangaea during the late Palaeozoic icehouse, Palaeogeogr. Palaeoclimatol. Palaeoecol., 425, 109–127, doi:10.1016/j.palaeo.2015.02.024, 2015.

Hernandez-Castillo, G. R., Rothwell, G. W. and Mapes, G.: Thucydiaceae Fam . Nov, with a Review and Reevaluation of Paleozoic Walchian Conifers, Int. J. Plant Sci., 162(5), 1155–1185 [online] Available from: https://www.jstor.org/stable/10.1086/321920, 2014.

Hilton, J. and Cleal, C. J.: The relationship between Euramerican and Cathaysian tropical floras in the Late Palaeozoic: Palaeobiogeographical and palaeogeographical implications, Earth-Science Rev., 85(3–4), 85–116, doi:10.1016/j.earscirev.2007.07.003, 2007.

Le Hir, G., Donnadieu, Y., Goddéris, Y., Meyer-Berthaud, B., Ramstein, G. and Blakey, R. C.: The climate change caused by the land plant invasion in the Devonian, Earth Planet. Sci. Lett., 310(3–4), 203–212, doi:10.1016/j.epsl.2011.08.042, 2011.

Horton, D. E., Poulsen, C. J. and Pollard, D.: Influence of high-latitude vegetation feedbacks on late Palaeozoic glacial cycles, Nat. Geosci., 3(8), 572–577, doi:10.1038/ngeo922, 2010.

Horton, D. E., Poulsen, C. J., Montañez, I. P. and DiMichele, W. A.: Eccentricity-paced late Paleozoic climate change, Palaeogeogr. Palaeoclimatol. Palaeoecol., 331–332, 150–161, doi:10.1016/j.palaeo.2012.03.014, 2012.

Hurrell, J. W., Holland, M. M., Gent, P. R., Ghan, S., Kay, J. E., Kushner, P. J., Lamarque, J. F., Large, W. G., Lawrence, D., Lindsay, K., Lipscomb, W. H., Long, M. C., Mahowald, N., Marsh, D. R., Neale, R. B., Rasch, P., Vavrus, S., Vertenstein, M., Bader, D., Collins, W. D., Hack, J. J., Kiehl, J. and Marshall, S.: The community earth system model: A framework for collaborative research, Bull. Am. Meteorol. Soc., 94(9), 1339–1360, doi:10.1175/BAMS-D-12-00121.1, 2013.

Jarvis, P. G.: The Interpretation of the Variations in Leaf Water Potential and Stomatal Conductance Found in Canopies in the Field, Philos. Trans. R. Soc. London, 273(927), 593–610 [online] Available from: https://www.jstor.org/stable/2417554, 1976.

Kerp, H.: The Modernization of Landscapes during the Late Paleozoic-Early Mesozoic, Paleontol. Soc. Pap., 6, 79–114, doi:10.1017/s1089332600000723, 2000.

Kiehl, J. T. and Shields, C. A.: Climate simulation of the latest Permian : Implications for mass extinction, Geology, (9), 757–760, doi:10.1130/G21654.1, 2005.

Kutzbach, J. E. and Gallimore, R. G.: Pangaean climates: megamonsoons of the megacontinent, J. Geophys. Res., 94(D3), 3341–3357, doi:10.1029/JD094iD03p03341, 1989.

Kutzbach, J. E. and Ziegler, A. M.: Simulation of late Permian climate and biomes with an

atmosphere- ocean model: comparisons with observations, Philos. Trans. - R. Soc. London, B, 341(1297), 327–340, doi:10.1098/rstb.1993.0118, 1993.

Ladant, J. B., Poulsen, C. J., Fluteau, F., Tabor, C. R., Macleod, K. G., Martin, E. E., Haynes, S. J. and Rostami, M. A.: Paleogeographic controls on the evolution of Late Cretaceous ocean circulation, Clim. Past, 16(3), 973–1006, doi:10.5194/cp-16-973-2020, 2020.

Laveine, J. P.: The size of the frond in the genus Alethopteris Sternberg(Pteridospermopsida, Carboniferous), Geobios, 19(1), 49–59, doi:10.1016/S0016-6995(86)80035-3, 1986.

Laveine, J. P. and Belhis, A.: Frond architecture of the seed-fern Macroneuropteris scheuchzeri, based on Pennsylvanian specimens from the Northern France coal field, Palaeontogr. Abteilung B Palaeophytologie, 277(1–4), 1–41, doi:10.1127/palb/277/2007/1, 2007.

Lenton, T. M., Dahl, T. W., Daines, S. J., Mills, B. J. W., Ozaki, K., Saltzman, M. R. and Porada, P.: Earliest land plants created modern levels of atmospheric oxygen, Proc. Natl. Acad. Sci. U. S. A., 113(35), 9704–9709, doi:10.1073/pnas.1604787113, 2016.

Looy, C. V.: Natural history of a plant trait: branch-system abscission in Paleozoic conifers and its environmental, autecological, and ecosystem implications in a fire-prone world, Paleobiology, 39(2), 235–252, doi:10.1666/12030, 2013.

Looy, C. V., Kerp, H., Duijnstee, I. A. P. and DiMichele, W. A.: The late Paleozoic ecological-evolutionary laboratory, a land-plant fossil record perspective, Sediment. Rec., 2014.

Macarewich, S., Poulsen, C. J. and Montañez, I. P.: Simulation of oxygen isotopes and circulation in a late Carboniferous epicontinental sea with implications for proxy records, Earth Planet. Sci. Lett., 559, 116770, doi:10.1016/j.epsl.2021.116770, 2021.

Matthaeus, W. J., Macarewich, S. I., Richey, J. D., Wilson, J. P., McElwain, J. C., Montañez, I. P., DiMichele, W. A., Hren, M. T., Poulsen, C. J. and White, J. D.: Freeze tolerance influenced forest cover and hydrology during the Pennsylvanian, Proc. Natl. Acad. Sci., 118(42), e2025227118, doi:10.1073/pnas.2025227118, 2021.

McElwain, J. C., Yiotis, C. and Lawson, T.: Using modern plant trait relationships between observed and theoretical maximum stomatal conductance and vein density to examine patterns of plant macroevolution, New Phytol., 209(1), 94–103, doi:10.1111/nph.13579, 2016.

Mencl, V., Holeček, J., Rößler, R. and Sakala, J.: First anatomical description of silicified calamitalean stems from the upper Carboniferous of the Bohemian Massif (Nová Paka and Rakovník areas, Czech Republic), Rev. Palaeobot. Palynol., 197, 70–77, doi:10.1016/j.revpalbo.2013.05.001, 2013.

Montañez, I. P., Tabor, N. J., Niemeier, D., DiMichele, W. A., Frank, T. D., Fielding, C. R., Isbell, J. L., Birgenheier, L. P. and Rygel, M. C.: CO_2-Forced Climate and Vegetation

Instability During Late Paleozoic Deglaciation, Science., 315(5808), 87–91, doi:10.1126/science.1134207, 2007.

Montañez, I. P.: A Late Paleozoic climate window of opportunity, Proc. Natl. Acad. Sci., 113(9), 2334–2336, doi:10.1073/pnas.1600236113, 2016.

Montañez, I. P. and Poulsen, C. J.: The Late Paleozoic Ice Age: An Evolving Paradigm, Annu. Rev. Earth Planet. Sci., 41(1), 629–656, doi:10.1146/annurev.earth.031208.100118, 2013.

Montañez, I. P., McElwain, J. C., Poulsen, C. J., White, J. D., DiMichele, W. A., Wilson, J. P., Griggs, G. and Hren, M. T.: Climate, pCO_2 and terrestrial carbon cycle linkages during late Palaeozoic glacial–interglacial cycles (supplemental), Nat. Geosci., 9(11), 824–828, doi:10.1038/ngeo2822, 2016.

Mösle, B., Collinson, M. E., Finch, P., Stankiewicz, B. A., Scott, A. C. and Wilson, R.: Factors influencing the preservation of plant cuticles: A comparison of morphology and chemical composition of modern and fossil examples, Org. Geochem., 29(5–7), 1369–1380, doi:10.1016/S0146-6380(98)00080-1, 1998.

Murray, M., Soh, W. K., Yiotis, C., Spicer, R. A., Lawson, T. and McElwain, J. C.: Consistent relationship between field-measured stomatal conductance and theoretical maximum stomatal conductance in C3 woody angiosperms in four major biomes, Int. J. Plant Sci., 181(1), 142–154, doi:10.1086/706260, 2020.

Oleson, K. W., Lawrence, D. M., Gordon, B., Flanner, M. G., Kluzek, E., Peter, J., Levis, S., Swenson, S. C., Thornton, E., Dai, A., Decker, M., Dickinson, R., Feddema, J., Heald, C. L., Lamarque, J., Niu, G., Qian, T., Running, S., Sakaguchi, K., Slater, A., Stöckli, R., Wang, A., Yang, L., Zeng, X. and Zeng, X.: Technical Description of version 4.0 of the Community Land Model (CLM)., 2010.

Otto-Bliesner, B. L.: The role of mountains, polar ice, and vegetation in determining the tropical climate during the Middle Pennsylvanian: climate model simulations, in Climate Controls on Stratigraphy, pp. 227–238, SEPM Society for Sedimentary Geology., 2003.

Parrish, J. T.: Climate of the Supercontinent Pangea, J. Geol., 101(2), 215–233 [online] Available from: https://www.jstor.org/stable/30081148, 1993.

Parrish, J. T., Ziegler, A. M. and Scotese, C. R.: Rainfall Patterns and the Distribution of Coals and Evaporites in the Mesozoic and Cenozoic, Palaeogeogr. Palaeoclimatol. Palaeoecol., 40, 67–101, 1982.

Peck, S. L.: Simulation as experiment: A philosophical reassessment for biological modeling, Trends Ecol. Evol., 19(10), 530–534, doi:10.1016/j.tree.2004.07.019, 2004.

Peppe, D. J., Royer, D. L., Cariglino, B., Oliver, S. Y., Newman, S., Leight, E., Enikolopov, G.,

Fernandez-Burgos, M., Herrera, F., Adams, J. M., Correa, E., Currano, E. D., Erickson, J. M., Hinojosa, L. F., Hoganson, J. W., Iglesias, A., Jaramillo, C. A., Johnson, K. R., Jordan, G. J., Kraft, N. J. B., Lovelock, E. C., Lusk, C. H., Niinemets, Ü., Peñuelas, J., Rapson, G., Wing, S. L. and Wright, I. J.: Sensitivity of leaf size and shape to climate: Global patterns and paleoclimatic applications, New Phytol., 190(3), 724–739, doi:10.1111/j.1469-8137.2010.03615.x, 2011.

Peppe, D. J., Lemons, C. R., Royer, D. L., Wing, S. L., Wright, I. J., Lusk, C. H. and Rhoden, C. H.: Biomechanical and leaf-climate relationships: A comparison of ferns and seed plants, Am. J. Bot., 101(2), 338–347, doi:10.3732/ajb.1300220, 2014.

Peyser, C. E. and Poulsen, C. J.: Controls on Permo-Carboniferous precipitation over tropical Pangaea: A GCM sensitivity study, Palaeogeogr. Palaeoclimatol. Palaeoecol., 268(3–4), 181–192, doi:10.1016/j.palaeo.2008.03.048, 2008.

Pfefferkorn, H. W. and Thomson, M. C.: Changes in dominance patterns in upper Carboniferous plant-fossil assemblages, Geology, 10(12), 641–644, doi:10.1130/0091-7613(1982)10<641:CIDPIU>2.0.CO;2, 1982.

Pfefferkorn, H. W. and Wang, J.: Early Permian coal-forming floras preserved as compressions from the Wuda District (Inner Mongolia, China), Int. J. Coal Geol., 69(1–2), 90–102, doi:10.1016/j.coal.2006.04.012, 2007.

Phillips, T. L. and Peppers, R. A.: Changing patterns of Pennsylvanian coal-swamp vegetation and implications of climatic control on coal occurrence, Int. J. Coal Geol., 3, 205–255, doi:10.1016/0166-5162(84)90019-3, 1984.

Phillips, T. L., Peppers, R. A., Avcin, M. J. and Laughnan, P. F.: Fossil plants and coal: Patterns of change in Pennsylvanian coal swamps of the Illinois Basin, Science (80-.)., 184(4144), 1367–1369, doi:10.1126/science.184.4144.1367, 1974.

Poulsen, C. J., Pollard, D., Montanez, I. P. and Rowley, D.: Late Paleozoic tropical climate response to Gondwanan deglaciation, Geology, 35(9), 771–774, doi:10.1130/G23841A.1, 2007.

Purcell, C., Batke, S. P., Yiotis, C., Caballero, R., Soh, W. K., Murray, M. and McElwain, J. C.: Increasing stomatal conductance in response to rising atmospheric CO_2, Ann. Bot., 121(6), 1137–1149, doi:10.1093/aob/mcx208, 2018.

Raymond, A. and Sloan, E. D. J.: A new permineralized Alethopteris from the Kalo Formation and a simple method for distinguishing permineralized Alethopteris species, in Lucas, S.G., DiMichele, W.A., Barrick, J.E., Schneider, J.W., Speilmann, J.A. (Eds.), The Carboniferous-Permian Transition. New Mexico Museum of Natural History, pp. 338–342, Albuquerque, NM., 2013.

Raymond, A., Lambert, L., Costanza, S., Slone, E. J. and Cutlip, P. C.: Cordaiteans in

paleotropical wetlands: An ecological re-evaluation, Int. J. Coal Geol., 83(2–3), 248–265, doi:10.1016/j.coal.2009.10.009, 2010.

Rees, P. M., Ziegler, A. M., Gibbs, M. T., Kutzbach, J. E., Behling, P. J. and Rowley, D. B.: Permian Phytogeographic Patterns and Climate Data/Model Comparisons Permian Phytogeographic Patterns and Climate, J. Geol., 110(January), 1–31, 2002.

Richey, J. D., Montañez, I. P., Goddéris, Y., Looy, C. V., Griffis, N. P. and Dimichele, W. A.: Influence of temporally varying weatherability on CO_2-climate coupling and ecosystem change in the late Paleozoic, Clim. Past, 16(5), 1759–1775, doi:10.5194/cp-16-1759-2020, 2020a.

Richey, J. D., Montañez, I. P., White, J. D., DiMichele, W. A., Matthaeus, W. J., Poulsen, C. J., Macarewich, S. I. and Looy, C. V.: Modeled physiological mechanisms for observed changes in the late Paleozoic plant fossil record, Palaeogeogr. Palaeoclimatol. Palaeoecol., doi:10.1016/j.palaeo.2020.110056, 2020b.

Roscher, M. and Schneider, J. W.: Permo-Carboniferous climate: Early Pennsylvanian to Late Permian climate development of central Europe in a regional and global context., 2006.

Rößler, R. and Noll, R.: Sphenopsids of the Permian (I): The largest known anatomically preserved calamite, an exceptional find from the petrified forest of Chemnitz, Germany, Rev. Palaeobot. Palynol., 140(3–4), 145–162, doi:10.1016/j.revpalbo.2006.03.008, 2006.

Rothwell, G. W. and Mapes, G.: Vegetation of a Paleozoic Conifer Community, Reg. Geol. Paleontol. Up. Paleoz. Hamilt. Quarr. Area Southeast. Kansas Kansas Geol. Surv. Guideb., 6(1988), 213–223, 1988.

Rothwell, G. W., Mapes, G. and Mapes, R. H.: Late Paleozoic conifers of North America: structure, diversity and occurrences, Rev. Palaeobot. Palynol., 95, 95–113 [online] Available from: https://www.jstor.org/stable/10.1086/321920, 1997.

Royer, D. L. and Hren, M. T.: Carbon isotopic fractionation between whole leaves and cuticle, Palaios, 32(4), 199–205, doi:10.2110/palo.2016.073, 2017.

Schneider, J. W., Lucas, S. G., Trumper, S. and Krainer, K.: Carrizo Arroyo, Central New Mexico - A New Late Paleozoic Taphotype of Arthropod Fossillagerstätte, New Mex. Geol. Soc. Guideb., 67, 377–386, doi:10.19080/ofoaj.2018.07.555710, 2016.

Sellers, P. J., Randall, D. A., Collatz, G. J., Berry, J. A., Field, C. B., Dazlich, D. A., Zhang, C., Collelo, G. D. and Bounoua, L.: A Revised Land Surface Parameterization (SiB2) for Atmospheric GCMs. Part I: Model Formulation, J. Clim., 9, 676–705, 1996.

Shields, C. A. and Kiehl, J. T.: Monsoonal precipitation in the Paleo-Tethys warm pool during the latest Permian, Palaeogeogr. Palaeoclimatol. Palaeoecol., 491(August 2017), 123–136, doi:10.1016/j.palaeo.2017.12.001, 2018.

Soh, W. K., Wright, I. J., Bacon, K. L., Lenz, T. I., Steinthorsdottir, M., Parnell, A. C. and McElwain, J. C.: Palaeo leaf economics reveal a shift in ecosystem function associated with the end-Triassic mass extinction event, Nat. Plants, 3(July), 1–8, doi:10.1038/nplants.2017.104, 2017.

Soreghan, G. S.: The impact of glacioclimatic change on Pennsylvanian cyclostratigraphy, Can. Soc. Pet. Geol., (Memoir 17), 523–543, 1994.

Soreghan, G. S., Soreghan, M. J., Poulsen, C. J., Young, R. A., Eble, C. F., Sweet, D. E. and Davogustto, O. C.: Anomalous cold in the Pangaean tropics, Geology, 36(8), 659–662, doi:10.1130/G24822A.1, 2008.

Spatz, H. C., Rowe, N., Speck, T. and Daviero, V.: Biomechanics of hollow stemmed sphenopsids: II. Calamites - To have or not to have secondary xylem, Rev. Palaeobot. Palynol., 102(1–2), 63–77, doi:10.1016/S0034-6667(98)00014-1, 1998.

Stewart, W. and Delevoryas, T.: Bases for Determining Relationships Among the Medullosaceae, Am. J. Bot., 39(7), 505–516 [online] Available from: https://www.jstor.org/stable/2438335, 1952.

Tabor, N. J. and Montanez, I. P.: Morphology and distribution of fossil soils in the Permo-Pennsylvanian Wichita and Bowie Groups, north-central Texas, USA: Implications for western equatorial Pangean palaeoclimate during icehouse-greenhouse transition, Sedimentology, 51(4), 851–884, doi:10.1111/j.1365-3091.2004.00655.x, 2004.

Tabor, N. J. and Montañez, I. P.: Shifts in late Paleozoic atmospheric circulation over western equatorial Pangea: Insights from pedogenic mineral $\delta^{18}O$ compositions, Geology, 30(12), 1127–1130, doi:10.1130/0091-7613(2002)030<1127:SILPAC>2.0.CO;2, 2002.

Tabor, N. J. and Poulsen, C. J.: Palaeoclimate across the Late Pennsylvanian-Early Permian tropical palaeolatitudes: A review of climate indicators, their distribution, and relation to palaeophysiographic climate factors, Palaeogeogr. Palaeoclimatol. Palaeoecol., 268(3–4), 293–310, doi:10.1016/j.palaeo.2008.03.052, 2008.

Tabor, N. J., DiMichele, W. A., Montañez, I. P. and Chaney, D. S.: Late Paleozoic continental warming of a cold tropical basin and floristic change in western Pangea, Int. J. Coal Geol., 119, 177–186, doi:10.1016/j.coal.2013.07.009, 2013.

Taylor, E. L. and Taylor, T. N.: Seed ferns from the late Paleozoic and Mesozoic: Any angiosperm ancestors lurking there?, Am. J. Bot., 96(1), 237–251, doi:10.3732/ajb.0800202, 2009.

Taylor, E. L., Taylor, T. N. and Krings, M.: Paleobotany: The Biology and Evolution of Fossil Plants, 2nd ed., New York, USA: Academic Press, Oxford, UNITED STATES. [online] Available from:

http://ebookcentral.proquest.com/lib/umichigan/detail.action?docID=421040, 2009.

Thornton, P. E. and Rosenbloom, N. A.: Ecosystem model spin-up: Estimating steady state conditions in a coupled terrestrial carbon and nitrogen cycle model, Ecol. Modell., 189(1–2), 25–48, doi:10.1016/j.ecolmodel.2005.04.008, 2005.

Thornton, P. E., Lamarque, J. F., Rosenbloom, N. A. and Mahowald, N. M.: Influence of carbon-nitrogen cycle coupling on land model response to CO_2 fertilization and climate variability, Global Biogeochem. Cycles, 21(4), 1–15, doi:10.1029/2006GB002868, 2007.

Tidwell, W. D. and Ash, S. R.: Revision and description of two new species of Charliea Mamay from Pennsylvanian strata in New Mexico and Utah, USA, Rev. Palaeobot. Palynol., 124(3–4), 297–306, doi:10.1016/S0034-6667(02)00253-1, 2003.

Wade, D. C., Luke Abraham, N., Farnsworth, A., Valdes, P. J., Bragg, F. and Archibald, A. T.: Simulating the climate response to atmospheric oxygen variability in the Phanerozoic: A focus on the Holocene, Cretaceous and Permian, Clim. Past, 15(4), 1463–1483, doi:10.5194/cp-15-1463-2019, 2019.

White, J. D. and Scott, N. A.: Specific leaf area and nitrogen distribution in New Zealand forests: Species independently respond to intercepted light, For. Ecol. Manage., 226(1–3), 319–329, doi:10.1016/j.foreco.2006.02.001, 2006.

White, J. D., Montanez, I. P., Wilson, J. P., Poulsen, C. J., Mcelwain, J. C., DiMichele, W. A., Hren, M. T., Macarewich, S., Richey, J. D. and Matthaeus, W. J.: A process-based ecosystem model (*Paleo*-BGC) to simulate the dynamic response of Late Carboniferous plants to elevated O2 and aridification, Am. J. Sci., 320(September), 122–136, doi:10.2475/09.2020.01, 2020.

Wilson, J. P.: Modeling 400 Million Years of Plant Hydraulics, Paleontol. Soc. Pap., 19, 175–194, doi:10.1017/s1089332600002734, 2013.

Wilson, J. P. and Fischer, W. W.: Geochemical support for a climbing habit within the Paleozoic seed fern genus Medullosa, Int. J. Plant Sci., 172(4), 586–598, doi:10.1086/658929, 2011.

Wilson, J. P., Knoll, A. H., Holbrook, N. M. and Marshall, C. R.: Modeling Fluid Flow in Medullosa, an Anatomically Unusual Carboniferous Seed Plant, Paleobiology, 34(4), 472–493 [online] Available from: https://www.jstor.org/stable/20445610, 2008.

Wilson, J. P., White, J. D., DiMichele, W. A., Hren, M. T., Poulsen, C. J., McElwain, J. C. and Montañez, I. P.: Reconstructing extinct plant water use for understanding vegetation-climate feedbacks: Methods, synthesis, and a case study using the Paleozoic-era Medullosan seed ferns, Paleontol. Soc. Pap., 21, 167–195, doi:10.1017/S1089332600003004, 2015.

Wilson, J. P., Montañez, I. P., White, J. D., DiMichele, W. A., McElwain, J. C., Poulsen, C. J. and Hren, M. T.: Dynamic Carboniferous tropical forests: new views of plant function and potential for physiological forcing of climate, New Phytol., 215(4), 1333–1353, doi:10.1111/nph.14700, 2017.

Wilson, J. P., White, J. D., Montañez, I. P., DiMichele, W. A., McElwain, J. C., Poulsen, C. J. and Hren, M. T.: Carboniferous plant physiology breaks the mold, New Phytol., 227(3), 667–679, doi:10.1111/nph.16460, 2020.

Wnuk, C. and Pfefferkorn, H. W.: The Life Habits and Paleoecology of Middle Pennsylvanian Medullosan Pteridosperms Based on an In Situ Assemblage from the Bernice Basin (Sullivan County, Pennsylvania, U.S.A.), Rev. Palaeobot. Palynol., 41, 329–351, 1984.

Wullschleger, S. D., Epstein, H. E., Box, E. O., Euskirchen, E. S., Goswami, S., Iversen, C. M., Kattge, J., Norby, R. J., Van Bodegom, P. M. and Xu, X.: Plant functional types in Earth system models: Past experiences and future directions for application of dynamic vegetation models in high-latitude ecosystems, Ann. Bot., 114(1), 1–16, doi:10.1093/aob/mcu077, 2014.

Xu, Z., Jiang, Y., Jia, B. and Zhou, G.: Elevated-CO2 response of stomata and its dependence on environmental factors, Front. Plant Sci., 7(MAY2016), 1–15, doi:10.3389/fpls.2016.00657, 2016.

4.9 Supplementary information

Model configuration and boundary conditions for baseline simulations

Baseline simulations (CESM–1×W–modern and CESM–2×W–modern) are performed with the fully coupled Community Earth System Model version 1.2 (CESM), including the Community Atmosphere Model version 5 (CAM), Community Land Model version 4 (CLM), Parallel Ocean Model version 2 (POP), and Sea Ice Model version 4 (CICE) components (Hurrell et al., 2013). CAM and CLM have a 1.9° × 2.5° horizontal resolution with 30 vertical levels. We use a configuration of CLM in all simulations that includes prescribed vegetation with a fully prognostic treatment of the terrestrial carbon and nitrogen (i.e., biogeochemistry model is active), and thus the composition and abundance of PFTs within a model grid cell is defined as time-invariant fields, whereas plant phenology (i.e., LAI and stem area index; m^2 leaf/stem area m^{-2} ground area) and structure (i.e., canopy top and bottom height; m) are calculated prognostically based on carbon and nitrogen availability in the grid cell.

The CESM–1×W–modern and CESM–2×W–modern baseline simulations are identical except for atmospheric CO_2 levels, which are specified as 280 and 560 ppm, respectively, based on a multi-proxy (10^3–10^4 yr resolution) CO_2 reconstruction (Montañez et al., 2016; Richey et al., 2020a). In the absence of proxy data, other greenhouse gas concentrations are set to their pre-industrial values. The simulations have a modern pO_2 of 0.21 mol mol^{-1} as an approximate level for Early-Middle Pennsylvanian atmospheric conditions. The simulations include a Late Pennsylvanian (~300 Ma) paleogeographic reconstruction from the PALEOMAP Project (Scotese, 2004). Aerosol distributions are zonally averaged separately for land and ocean from pre-industrial levels following the procedure outlined by Heavens et al. (2012). We use a modern Earth orbital configuration, and the total incoming solar irradiance is reduced to an appropriate Late Pennsylvanian value of 1333 Wm^{-2} (97.5% of present), following (Gough, 1981). The distribution of prescribed vegetation follows the Middle Pennsylvanian biomes for glacial phases (Wilson et al., 2017), where the closest possible composition of modern PFTs is chosen to represent each biome. Ice sheets in southern Gondwana based on regional highlands, where elevations >500 m are prescribed as ice. The CESM–1×W and CESM–2×W simulations are run for ~1,500 years to equilibrate the surface ocean and have top-of-atmosphere energy balances of −0.19 Wm^{-2} and 0.002 Wm^{-2}, respectively.

	C:N			V_{cmax25}		
Taxa	Min	Max	Median	Min	Max	Median
Macroneuropteris	27.5	31.7	29.6	35.2	32.2	33.6
Neuropteris	32.7	39.8	36.3	31.7	28.7	29.9
Sphenophyllum	31.7	42.6	37.2	32.2	27.9	29.6
Lepidodendron	34.8	47.2	41.0	30.6	27.1	28.3
Cordaites	38.7	44.2	41.5	29.0	27.6	28.2
Tree Fern	29.3	43.1	36.2	25.1	20.4	22.1
Walchia	37.5	43.2	40.3	32.3	31.2	31.6

Table S4.1 Values of C:N and V_{cmax25} used in the estimation of photosynthetic parameter *m*.

	g_s (µmol CO_2 m^{-2} s^{-1})		
Taxa	Min	Max	Median
Macroneuropteris	166120.4	509660.6	373294.4
Neuropteris	118050.8	982072.7	363624.1
Sphenophyllum	27346.6	303467.7	122534.3
Lepidodendron	277356.7	2082626.9	901888.9
Cordaites	13983.2	2945516.6	138387.6
Tree Fern	11585.4	256423.8	64733.7
Walchia	53978.3	261401.6	90217.6

Table S4.2 Stomatal conductance values for each plant group used in the estimation of photosynthetic parameter *m*.

	m **(unitless)**			
Taxa	Min C:N, Max g_s	Max C:N, Min g_s	Median C:N, g_s	**Average**
Macroneuropteris	8.1	2.9	6.2	5.7
Neuropteris	17.4	2.3	6.8	8.8
Sphenophyllum	5.3	0.5	2.3	2.7
Lepidodendron	38.1	5.7	17.8	20.5
Cordaites	56.8	0.3	2.7	19.9
Tree Fern	5.7	0.3	1.6	2.5
Walchia	4.5	1.0	1.6	2.4
Average	19.4	1.9	5.6	8.9

Table S4.3 Photosynthetic parameter *m* values for each paleo-plant group.

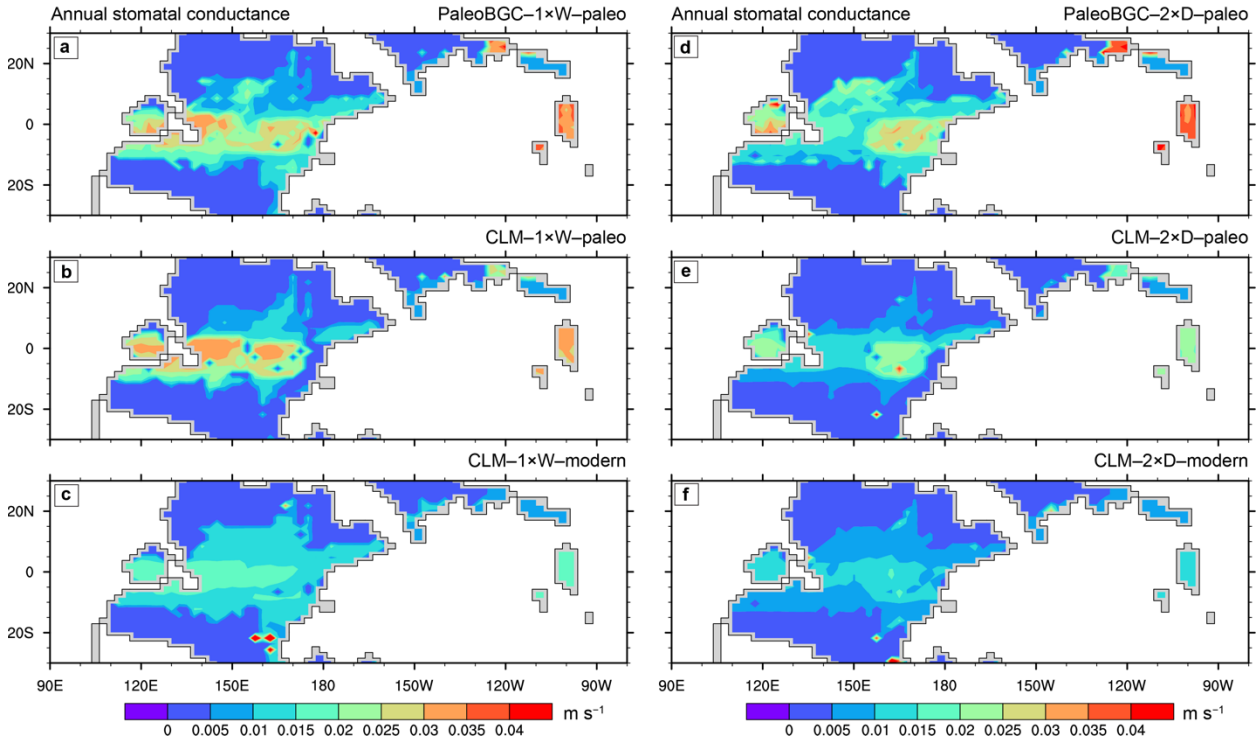

Figure S4.1 Mean annual stomatal conductance (m s^{-1}) in the Paleo-BGC and standalone CLM simulations. The cases shown are (a) PaleoBGC–1×W–paleo, (b) CLM–1×W–paleo, (c) CLM–1×W–modern, (d) PaleoBGC–2×D–paleo, (e) CLM–2×D–paleo, and (f) CLM–2×D–modern. In the standalone CLM simulations, grid cells with LAI < 1.0, which are located in the desert biome and along the edges of the tropical dryland biome, have stomatal conductance set to 0 to remove anomalously high stomatal conductance for visualization purposes.

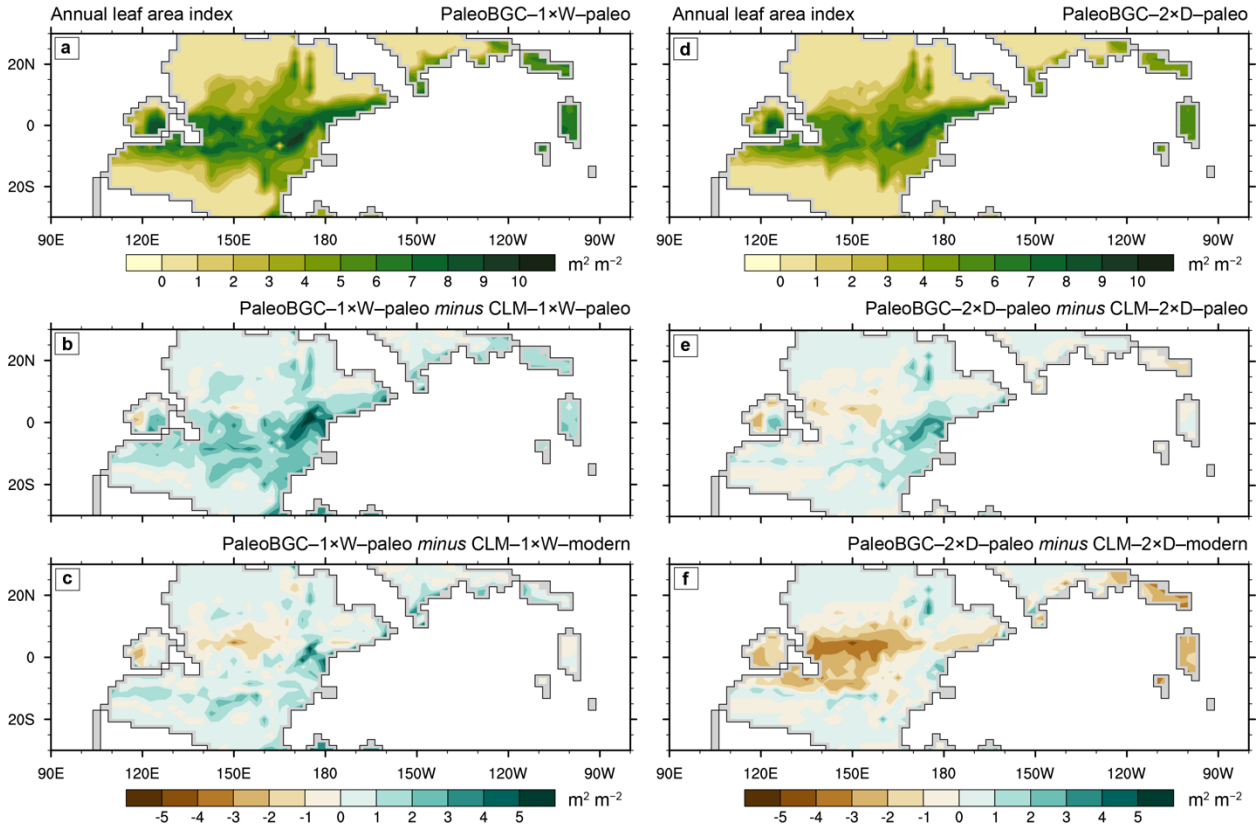

Figure S4.2 Mean annual total leaf area index (LAI; m^2 leaf area m^{-2} ground area) for the *Paleo*-BGC and standalone CLM simulations. Absolute values of LAI are shown for the (a) PaleoBGC–1×W–paleo and (d) PaleoBGC–2×D–paleo simulations. Differences in LAI are shown for the CLM-only simulations relative to the Paleo-BGC simulations with (b) PaleoBGC–1×W–paleo minus CLM–1×W–paleo, (c) PaleoBGC–1×W–paleo minus CLM–1×W–modern, (e) PaleoBGC–2×D–paleo minus CLM–2×D–paleo, and (f) PaleoBGC–2×D–paleo minus CLM–2×D–modern.

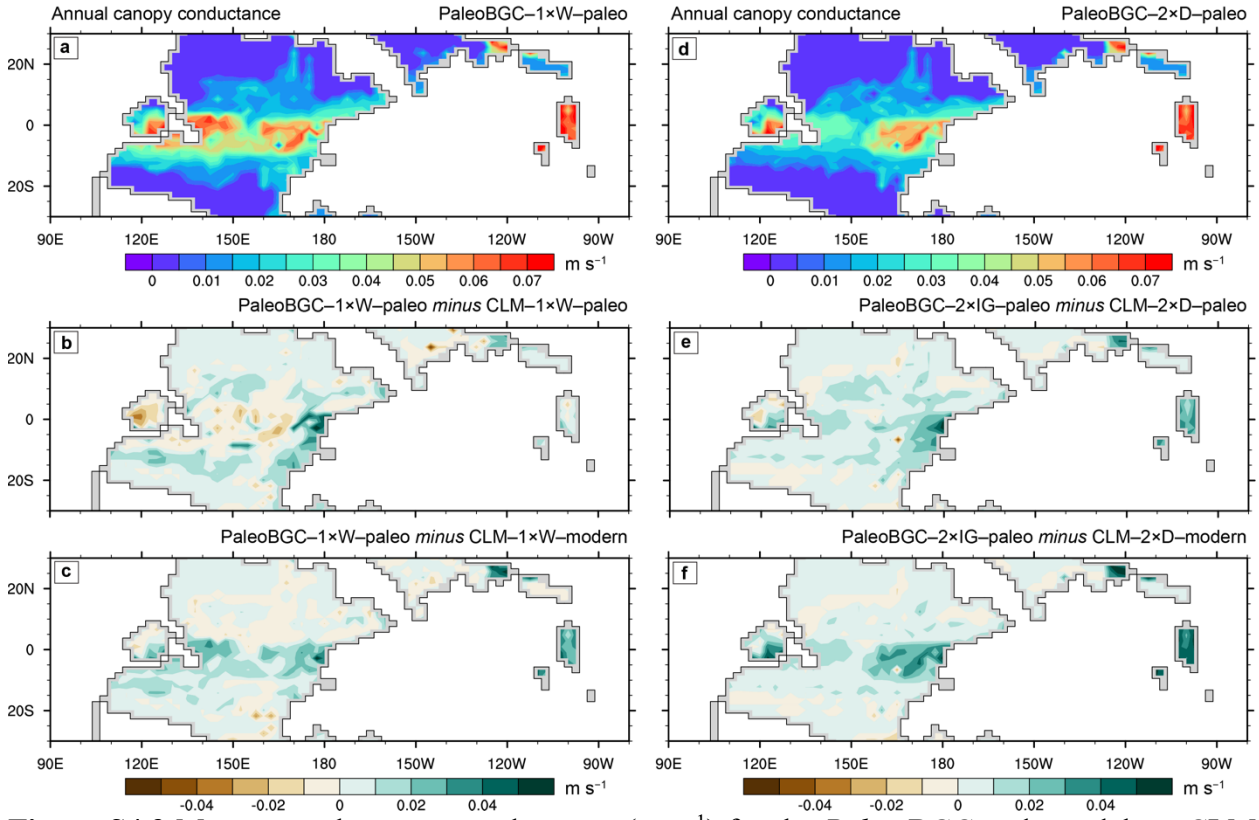

Figure S4.3 Mean annual canopy conductance (m s^{-1}) for the *Paleo*-BGC and standalone CLM simulations. Absolute values of canopy conductance are shown for the (a) PaleoBGC–1×W–paleo and (d) PaleoBGC–2×D–paleo simulations. Differences in LAI are shown for the CLM-only simulations relative to the Paleo-BGC simulations with (b) PaleoBGC–1×W–paleo minus CLM–1×W–paleo, (c) PaleoBGC–1×W–paleo minus CLM–1×W–modern, (e) PaleoBGC–2×D–paleo minus CLM–2×D–paleo, and (f) PaleoBGC–2×D–paleo minus CLM–2×D–modern.

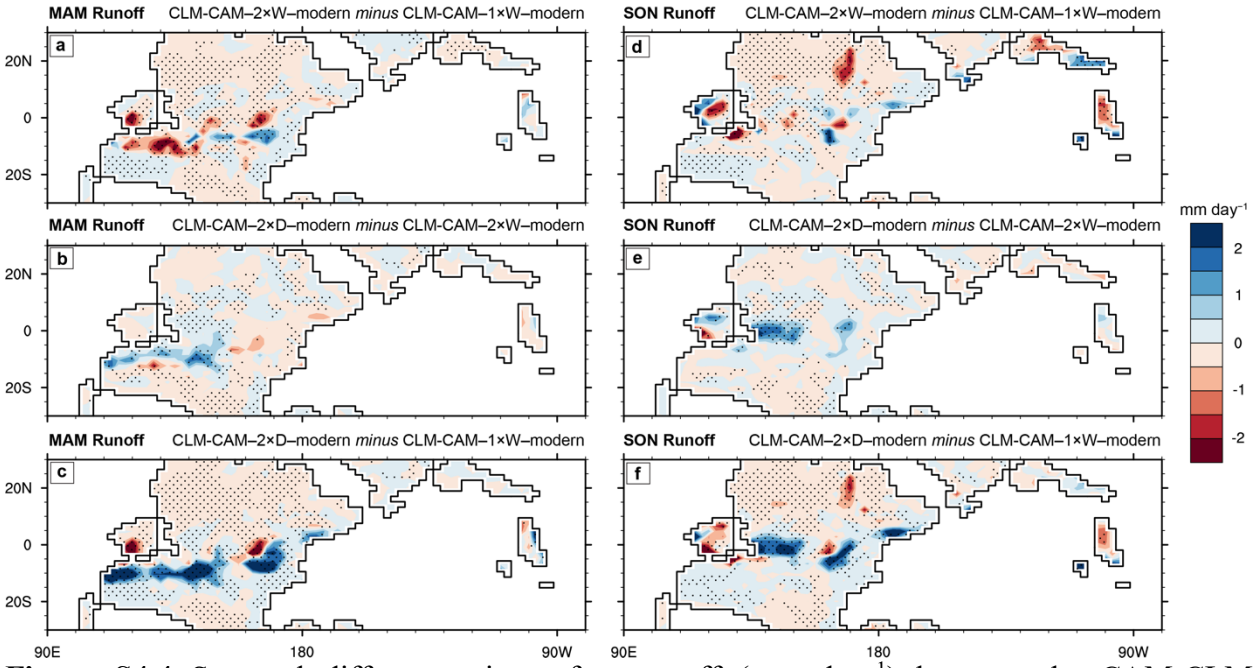

Figure S4.4 Seasonal differences in surface runoff (mm day^{-1}) between the CAM-CLM simulations with modern PFT analogs. Differences in MAM and SON surface runoff are shown between (a, d) CLM-CAM–2×W–modern and CLM-CAM–1×W–modern, (b, e) CLM-CAM–2×D–modern and CLM-CAM–2×W–modern, (c, f) CLM-CAM–2×D–modern and CLM-CAM–1×W–modern, respectively. Stippled areas indicate significant differences at $p < 0.05$ using a student's t-test. MAM and SON indicate the larger seasonal changes in runoff.

References

Gough, D. O.: Solar interior structure and luminosity variations, Sol. Phys., 74(1), 21–34, doi:10.1007/BF00151270, 1981.

Heavens, N. G., Shields, C. A. and Mahowald, N. M.: A paleogeographic approach to aerosol prescription in simulations of deep time climate, J. Adv. Model. Earth Syst., 4(11), doi:10.1029/2012MS000166, 2012.

Hurrell, J. W., Holland, M. M., Gent, P. R., Ghan, S., Kay, J. E., Kushner, P. J., Lamarque, J. F., Large, W. G., Lawrence, D., Lindsay, K., Lipscomb, W. H., Long, M. C., Mahowald, N., Marsh, D. R., Neale, R. B., Rasch, P., Vavrus, S., Vertenstein, M., Bader, D., Collins, W. D., Hack, J. J., Kiehl, J. and Marshall, S.: The community earth system model: A framework for collaborative research, Bull. Am. Meteorol. Soc., 94(9), 1339–1360, doi:10.1175/BAMS-D-12-00121.1, 2013.

Montañez, I. P., McElwain, J. C., Poulsen, C. J., White, J. D., DiMichele, W. A., Wilson, J. P., Griggs, G. and Hren, M. T.: Climate, pCO_2 and terrestrial carbon cycle linkages during late Palaeozoic glacial–interglacial cycles, Nat. Geosci., 9(11), 824–828, doi:10.1038/ngeo2822, 2016.

Richey, J. D., Montañez, I. P., Goddéris, Y., Looy, C. V., Griffis, N. P. and Dimichele, W. A.: Influence of temporally varying weatherability on CO_2-climate coupling and ecosystem change in the late Paleozoic, Clim. Past, 16(5), 1759–1775, doi:10.5194/cp-16-1759-2020, 2020.

Scotese, C. R.: A Continental Drift Flipbook, J. Geol., 112(6), 729–741, 2004.

Wilson, J. P., Montañez, I. P., White, J. D., DiMichele, W. A., McElwain, J. C., Poulsen, C. J. and Hren, M. T.: Dynamic Carboniferous tropical forests: new views of plant function and potential for physiological forcing of climate, New Phytol., 215(4), 1333–1353, doi:10.1111/nph.14700, 2017.

Chapter 5 Conclusion

This dissertation is a compilation of three chapters that use new Earth system model simulations and published proxy records to identify the response of ocean dynamics and vegetation-climate interactions to atmospheric pCO_2 during the Pennsylvanian–early Permian. Each of these chapters provide new insights and understanding into icehouse climate dynamics that we did not or could not know without the integration of Earth system models and proxy records. This concluding section summarizes the most important results of each data chapter, provides a brief synthesis of the major contributions of this dissertation to our understanding of climate change during the Late Paleozoic Ice Age (LPIA), and proposes new research directions motivated by this work.

5.1 Summary of dissertation and key findings

Our view of the LPIA has transformed, primarily since the turn of the 21st century, from a period of long-term stability to one of dynamic change that documents the climate and ecosystem response to repeated glacial-interglacial transitions (Montañez and Poulsen, 2013). Initially, the LPIA was interpreted as a period of protracted supercontinental-scale glaciation (Crowley and Baum, 1991; Veevers and Powell, 1987). However, increasing precision of Carboniferous–Permian chronostratigraphy, which permits the regional-to-global correlation of high-resolution stratigraphic, paleobiologic, geochemical, and tectonic records, has revealed the dynamic synchronicity of Gondwanan glaciation, sea level, atmospheric pCO_2, and ecosystem change during the LPIA (Montañez and Poulsen, 2013). Due to these recent scientific advancements, we now understand the LPIA as a dynamic interval that archives the climate and ecosystem response to repeated glacial-interglacial cycles that were likely driven by CO_2.

Efforts to relate climate change with marine and terrestrial ecosystems during the LPIA have revealed major changes in paleotropical forest composition and marine faunal distribution in sync with pCO_2 and Gondwanan glaciation. Plant fossil remains have been used reconstruct repeated and dynamic changes of wet- and dry-adapted floras in paleotropical forests over a

hierarchy of timescales during the Pennsylvanian–early Permian (Montañez, 2016; Montañez et al., 2016). Climate models have revealed that pCO_2, Gondwanan ice extent, and sea level modulated precipitation over low latitude Pangaea and likely influenced the composition and distribution of paleotropical forests over time (Heavens et al., 2012, 2015; Peyser and Poulsen, 2008; Poulsen et al., 2007). In the ocean, the paleogeographic distribution and geochemistry of some climate-sensitive marine fauna in shallow, coastal settings support seawater cooling and a contraction of warm, subtropical surface currents during the Carboniferous–Permian transition into the LPIA apex of glaciation (Angiolini et al., 2007; Grossman et al., 2008; Waterhouse and Shi, 2010). This dissertation expands on previous work by providing mechanistic linkages between proxy-based inferences of marine and terrestrial change with regional and global climate change.

This dissertation leverages new climate model simulations and novel insights from environmental proxy data to better understand the role of ocean dynamics and the terrestrial biosphere in Pennsylvanian–early Permian climate change under different levels of pCO_2. Chapter 2 focuses on global ocean temperature and circulation patterns for glacial and interglacial conditions. Chapter 3 constrains the local processes and oxygen isotopic composition of an epicontinental sea. Chapter 4 addresses the role of paleo-plant physiology in modulating paleotropical vegetation-climate interactions. All three of these chapters reveal the importance of pCO_2 in driving past icehouse climate dynamics.

The most important novel findings from this dissertation are that continental runoff significantly influences the oxygen isotopic composition of proxy records from the North American Midcontinent Sea (Chapter 3) and that paleo-plant physiology modulates the regional response of low latitude precipitation over Pangaea (Chapter 4). Neither of these findings would be possible without leveraging the complementary strengths of Earth system modeling and proxy records. In Chapter 3, simulations from a fully coupled, isotope-enabled Earth system model provide mechanistic constraints on local processes in ancient epicontinental seas. This work helps paleoclimatologists differentiate isotopic changes in marine proxy records associated with global paleoceanographic events from epicontinental sea-specific processes, and thus improve reconstructions of global seawater chemistry in deep time. In Chapter 4, the integration of empirically and experimentally constrained paleo-floral plant functional types in an Earth system model captures paleotropical vegetation-climate drying feedbacks that have been inferred from

proxy records and not adequately captured by traditional modern plants. This finding highlights the importance of accounting for the influence of paleo-plant physiology in vegetation-climate interactions in deep time.

The most important contributions from this dissertation are relatively high-resolution, global scale estimates of ocean circulation, oxygen isotopic composition, and temperature for the Permo-Carboniferous (Chapter 2 and 3) and a road map for integrating fossil-based paleo-plant physiology into fully coupled Earth system models (Chapter 4). Chapter 2 highlights that Earth system models with time-specific boundary conditions can be used to connect environmental inferences from spatially discontinuous proxy records to large-scale climate dynamics in deep time. Chapter 4 primarily focuses on method development and provides a testing ground for future work on vegetation-climate feedbacks over a variety of geologic intervals.

The conclusions and implications of from this dissertation improve our understanding of the climate dynamics underlying environmental inferences from marine and terrestrial proxy records over the LPIA. Taken together, the chapters in this dissertation provide novel approaches to integrating Earth system models and proxy data that can be applied beyond the LPIA and demonstrate the immense potential of Earth system modeling to improve our understanding of deep time climate change.

5.2 Remaining questions

This final section outlines several additional scientific questions that have emerged from this work. The questions listed below are among the most important unanswered questions that have emerged or are highlighted from my dissertation.

1) **What role did the superocean play in the global carbon cycle during the LPIA?** Long-term trends in atmospheric pCO_2 over the LPIA have been attributed to the emergence and fluctuation of the earliest paleotropical forests, weathering of the Central Pangaean Mountains, and widespread eruptive volcanism (Richey et al., 2020; Soreghan et al., 2019). Nevertheless, our understanding of the carbon sources and sinks controlling atmospheric CO_2 concentration during the LPIA is incomplete. Changes in ocean circulation and stratification have been found to play a key role in modulating ocean carbon storage and thus atmospheric CO_2 concentrations during the Quaternary glacial state (Brovkin et al., 2007; Watson et al., 2015), yet the role of superocean dynamics in

the late Paleozoic carbon cycle has not been explored. As shown in Chapter 2, major changes in Panthalassic overturning circulation occur between glacial and interglacial states. Therefore, additional work on the physical and biological mechanisms of superocean carbon content during the LPIA would be a worthwhile area of future study.

2) **How do local processes in ancient epicontinental seas influence the Phanerozoic oxygen isotope secular curve?** Records of marine calcite $\delta^{18}O$ reveal an ~8‰ increase over the past half billion years (e.g., Meuhlenbachs and Clayton, 1976; Gregory and Taylor, 1981; Veizer and Prokoph, 2015; Bergmann et al., 2018; Ryb and Eiler, 2018). Two first-order and long debated hypotheses for the origin of this long-term $\delta^{18}O$ trend are the progressive increased influence of diagenesis over time (e.g., Land, 1995) and a secular increase in global seawater $\delta^{18}O$ driven in large part by high-temperature isotopic exchange between seawater and seafloor at mid-ocean ridges (Gregory and Taylor, 1981; Veizer and Prokoph, 2015). Moving back through the Phanerozoic, the range of calcite $\delta^{18}O$ values from low-latitude regions increases substantially at ~200 Mya, with the maximum value remaining ~0‰ through time. Oceanic crust older than ~200 Mya is not preserved, and thus pre-Jurassic records of calcite $\delta^{18}O$ are primarily from low-latitude epicontinental seas (Veizer & Prokoph, 2015). In Chapter 3, we show that high freshwater runoff accounts for a substantial portion of the spatial variability in oxygen isotope records from a low-latitude epicontinental sea during the LPIA. This result suggests that the growing range of calcite $\delta^{18}O$ and more negatives values (prior to ~200 Mya) may also reflect the outsized influence of low-latitude epicontinental seas in marine records that have been impacted by freshwater runoff and diagenetic overprinting. Isotope-enabled modeling of ancient epicontinental seas from additional geologic intervals is needed to evaluate the contribution of local epicontinental processes to the Phanerozoic oxygen isotope secular curve.

3) **How did climate forcings other than atmospheric CO_2 influence tropical vegetation-climate interactions during the LPIA?** Environmental factors such as high-latitude glaciation, sea level, Earth's orbital configuration, and pCO_2 have been found to modulate tropical precipitation during the LPIA (Heavens et al., 2012, 2015; Horton et al., 2012; Peyser and Poulsen, 2008; Poulsen et al., 2007). However, the phasing of tropical precipitation with glacial and interglacial conditions remains debated. In Chapter

4, we show that paleo-plant physiology alters the response of paleotropical precipitation to a doubling of pCO_2, indicating that vegetation dynamics also play an important role in precipitation over Pangaea. Additional climate modeling on the response of paleotropical vegetation-climate interactions to changes in high-latitude glaciation, sea level, and Earth's orbital configuration with the representation of paleo-plant physiology would permit a more comprehensive understanding of glacial-interglacial controls on tropical precipitation variability during the LPIA.

5.3 References

Angiolini, L., Mangiagalli, V., Muttoni, G., Stephenson, M. H. and Zanchi, A.: Tethyan oceanic currents and climate gradients 300 m.y. ago, Geology, 35(12), 1071–1074, doi:10.1130/G24031A.1, 2007.

Bergmann, K. D., Finnegan, S., Creel, R., Eiler, J. M., Hughes, N. C., Popov, L. E. and Fischer, W. W.: A paired apatite and calcite clumped isotope thermometry approach to estimating Cambro-Ordovician seawater temperatures and isotopic composition, Geochim. Cosmochim. Acta, 224, 18–41, doi:10.1016/j.gca.2017.11.015, 2018.

Brovkin, V., Ganopolski, A., Archer, D. and Rahmstorf, S.: Lowering of glacial atmospheric CO_2 in response to changes on oceanic circulation and marine biogeochemistry, Paleoceanography, 22(4), 1–14, doi:10.1029/2006PA001380, 2007.

Crowley, T. J. and Baum, S. K.: Estimating Carboniferous sea-level fluctuations from Gondwanan ice extent, Geology, (October), 975–977, 1991.

Gregory, R. T. and Taylor, H. P.: An Oxygen Isotope Profile in a Section of Cretaceous Oceanic Crust, Samail Ophiolite, Oman: Evidence for $\delta^{18}O$ Buffering of the Oceans by Deep (>5 km) Seawater-Hydrothermal Circulation at Mid-Ocean Ridges, J. Geophys. Res. Solid Earth, 86(B4), 2737–2755, doi:10.1029/jb086ib04p02737, 1981.

Grossman, E. L., Yancey, T. E., Jones, T. E., Bruckschen, P., Chuvashov, B., Mazzullo, S. J. and Mii, H.: Glaciation, aridification, and carbon sequestration in the Permo-Carboniferous: The isotopic record from low latitudes, Palaeogeogr. Palaeoclimatol. Palaeoecol., 268(3–4), 222–233, doi:10.1016/j.palaeo.2008.03.053, 2008.

Heavens, N. G., Mahowald, N. M., Soreghan, G. S., Soreghan, M. J. and Shields, C. a.: Glacial-interglacial variability in Tropical Pangaean Precipitation during the Late Paleozoic Ice Age: simulations with the Community Climate System Model, Clim. Past Discuss., 8(3), 1915–1972, doi:10.5194/cpd-8-1915-2012, 2012.

Heavens, N. G., Mahowald, N. M., Soreghan, G. S., Soreghan, M. J. and Shields, C. A.: A

model-based evaluation of tropical climate in Pangaea during the late Palaeozoic icehouse, Palaeogeogr. Palaeoclimatol. Palaeoecol., 425, 109–127, doi:10.1016/j.palaeo.2015.02.024, 2015.

Horton, D. E., Poulsen, C. J., Montañez, I. P. and DiMichele, W. A.: Eccentricity-paced late Paleozoic climate change, Palaeogeogr. Palaeoclimatol. Palaeoecol., 331–332, 150–161, doi:10.1016/j.palaeo.2012.03.014, 2012.

Land, L. S.: Comment on "Oxygen and carbon isotopic composition of Ordovician brachiopods: Implications for coeval seawater" by H. Qing and J. Veizer, Geochim. Cosmochim. Acta, 59(13), 2843–2844, doi:10.1016/0016-7037(95)00176-Z, 1995.

Meuhlenbachs, K. and Clayton, R. N.: Oxygen Isotope Composition of the Oceanic Crust and Its Bearing on Seawater., J. Geophys. Res., 81(23), 4365–4369, doi:10.1029/JB081i023p04365, 1976.

Montañez, I. P.: A Late Paleozoic climate window of opportunity, Proc. Natl. Acad. Sci., 113(9), 2334–2336, doi:10.1073/pnas.1600236113, 2016.

Montañez, I. P. and Poulsen, C. J.: The Late Paleozoic Ice Age: An Evolving Paradigm, Annu. Rev. Earth Planet. Sci., 41(1), 629–656, doi:10.1146/annurev.earth.031208.100118, 2013.

Montañez, I. P., Mcelwain, J. C., Poulsen, C. J., White, J. D., Dimichele, W. A., Wilson, J. P., Griggs, G. and Hren, M. T.: Climate, pCO_2 and terrestrial carbon cycle linkages during late Palaeozoic glacial–interglacial cycles, Nat. Geosci., 9(November), doi:10.1038/NGEO2822, 2016.

Peyser, C. E. and Poulsen, C. J.: Controls on Permo-Carboniferous precipitation over tropical Pangaea: A GCM sensitivity study, Palaeogeogr. Palaeoclimatol. Palaeoecol., 268(3–4), 181–192, doi:10.1016/j.palaeo.2008.03.048, 2008.

Poulsen, C. J., Pollard, D., Montanez, I. P. and Rowley, D.: Late Paleozoic tropical climate response to Gondwanan deglaciation, Geology, 35(9), 771–774, doi:10.1130/G23841A.1, 2007.

Richey, J. D., Montañez, I. P., Goddéris, Y., Looy, C. V., Griffis, N. P. and Dimichele, W. A.: Influence of temporally varying weatherability on CO_2-climate coupling and ecosystem change in the late Paleozoic, Clim. Past, 16(5), 1759–1775, doi:10.5194/cp-16-1759-2020, 2020.

Ryb, U. and Eiler, J. M.: Oxygen isotope composition of the Phanerozoic ocean and a possible solution to the dolomite problem, Proc. Natl. Acad. Sci., 115(26), 1–6, doi:10.1073/pnas.1719681115, 2018.

Soreghan, G. S., Soreghan, M. J. and Heavens, N. G.: Explosive volcanism as a key driver of the

late Paleozoic ice age, Geology, 47(7), 600–604, doi:10.1130/G46349.1, 2019.

Veevers, J. J. and Powell, C. M.: Late Paleozoic glacial episodes in Gondwanaland reflected in transgressive- regressive depositional sequences in Euramerica, Geol. Soc. Am. Bull., 98(4), 475–487, doi:10.1130/0016-7606(1987)98<475:LPGEIG>2.0.CO;2, 1987.

Veizer, J. and Prokoph, A.: Temperatures and oxygen isotopic composition of Phanerozoic oceans, Earth-Science Rev., 146, 92–104, doi:10.1016/j.earscirev.2015.03.008, 2015.

Waterhouse, J. B. and Shi, G. R.: Evolution in a cold climate, Palaeogeogr. Palaeoclimatol. Palaeoecol., 298(1–2), 17–30, doi:10.1016/j.palaeo.2010.08.022, 2010.

Watson, A. J., Vallis, G. K. and Nikurashin, M.: Southern Ocean buoyancy forcing of ocean ventilation and glacial atmospheric CO_2, Nat. Geosci., 8(11), 861–864, doi:10.1038/ngeo2538, 2015.